

**HYDROTREATING OF GAS OILS USING Ni-Mo CATALYST SUPPORTED ON
CARBON NANOHORNS AND ASSOCIATED CARBON MATERIALS**

A Thesis Submitted to the College of Graduate and Postdoctoral Studies
in Partial Fulfilment of the Requirements for the
Degree of Doctor of Philosophy
in the Department of Chemical and Biological Engineering
University of Saskatchewan
Saskatoon, SK, Canada

By
Emma Naa Adukwei Aryee

© Copyright Emma Naa Adukwei Aryee, July, 2019. All rights reserved.

PERMISSION TO USE

In presenting this thesis in partial fulfillment of the requirements for a Doctor of Philosophy Degree from the University of Saskatchewan, I agree that the Libraries of the University of Saskatchewan may make this thesis freely available for inspection. I further agree that permission for copying of this thesis in any manner, in whole or in part, for scholarly purposes may be granted by Dr. Ajay Dalai and Dr. John Adjaye, who supervised my PhD thesis work or, in their absence, by the Head of Department or the Dean of the College of Engineering. It is understood that any copying or publication or use of this thesis as a whole or parts thereof for financial gain shall not be allowed without any written permission. It is also understood that due recognition shall be given to me and to the University of Saskatchewan in any scholarly use which may be made of any material in my thesis.

Requests for permission to copy or to make other use of material in this thesis in whole or parts shall be addressed to:

Head of the Department of Chemical & Biological Engineering
University of Saskatchewan, 57 Campus Drive
Saskatoon, Saskatchewan S7N 5A9, Canada.

OR

Dean
College of Graduate and Postdoctoral Studies
University of Saskatchewan, 116 Thorvaldson Building,
110 Science Place
Saskatoon, Saskatchewan S7N 5C9, Canada.

ABSTRACT

For many decades, crude oil refinery companies and catalysis research establishments worldwide are being challenged to develop new hydrotreating processes aimed at producing cleaner fuel. Use of an active and stable catalyst in hydrotreating is one way of improving catalytic activity of hydrotreating reactions such as hydrodesulfurization (HDS) and hydrodenitrogenation (HDN). Hence, this research primary goal is to develop a NiMo catalyst supported on carbon nanohorns (CNH) and associated carbon materials for hydrotreating. CNH is the support of choice used in this research due to its inert nature and excellent textural properties (mesoporosity, high surface area and desirable pore volume) which are known to enhance hydrotreating activities. The research plan is divided into five phases, and the research goals, experimental methods and outcomes pertaining to each of the phases are summarized in this thesis.

For phase one, the goal was to maximize the production of CNH in the lab for hydrotreating application by investigating the effects of, current settings, processing time and equipment design on CNH production. A current setting of 90 A and 30 minutes processing time were determined to be the best conditions for laboratory scale maximization of CNH production. In phase two, the primary aim was to incorporate functionality in an otherwise inert CNH material using, 30 wt% HNO₃ under reflux for 15 minutes to 4 hours at 110°C. Production of CNH concurrently generates other carbon particles (OCP) as by-products that can be differentiated into fine (OCP_f) and chunk (OCP_c) forms. Due to the superior quality of the CNH material in phase three, the goal was to test the influence of four different supports (i.e. gamma-alumina (γ -Al₂O₃), CNH, OCP_f, and carbon nanotubes (CNT)) on hydrotreating performance, and to determine how the physico-chemical properties of each support has on the hydrotreating performance. In comparison to the remaining carbon-supported catalysts, NiMo/CNH catalyst exhibited higher HDS (89%) and HDN (42%) activities for light gas oil containing 3 wt% sulfur and 0.18 wt% nitrogen and this is ascribed to, the high textural properties of the NiMo/CNH catalyst as well as its ability to induce, high metal dispersion plus reduction of metal oxides at a lower temperature in comparison to the remaining carbon-supported catalysts. The yield of OCP material from the laboratory synthesis of CNH was more than 45% of the CNH yield. Moreover, from phase three, OCP_f support was also found to be a viable support in hydrotreating hence, the main focus of phase four work was to improve the hydrotreating performance of NiMo/OCP_f catalyst by varying Ni and Mo compositions on the functionalized OCP_f support. To this effect, a series of hydrotreating experimental runs with

varying Ni (2.5, 3.5, 5.0 wt%) and Mo (13, 19, 26 wt%) compositions with light gas oil indicated that 5.0wt%Ni19wt%Mo/OCP_f catalysts exhibited the highest HDS and HDN activity.

The last phase (phase 5) of the research plan focused on the development of the best NiMo/CNH catalyst for hydrotreating by varying Ni loadings (2.5 wt%, - 5 wt%) at constant Mo loading of 19 wt%. Hydrotreating results from these catalysts showed that, the 3.5wt%Ni19wt%Mo/CNH catalyst exhibited the highest HDS and HDN activity. This catalyst was further modified by adding 2 wt% P to the 3.5 wt% Ni and 19 wt% Mo concentrations via a co-impregnation method to study the effects of phosphorus as a secondary promoter on HDS and HDN activity. Optimization of the operating parameters, kinetic and stabilization studies were further carried out using the 3.5wt%Ni19wt%Mo/CNH catalyst. The results from this phase are also presented in this thesis. The overall results from all phases demonstrated that CNH is not only a material that have superior physicochemical properties as compared to CNT and OCP material but, also a potential catalyst support with great benefit in hydrotreating.

ACKNOWLEDGEMENTS

My first and foremost thanks goes to the almighty God for taking me through this journey. Indeed, “Christ in me the hope of glory.” I am indebted to my supervisors Dr. Ajay K. Dalai and Dr. John Adjaye for giving me the opportunity to advance my education and compliment my knowledge in the area of petroleum upgrading. Dr. Dalai and Dr. Adjaye played an instrumental role in the successful completion of this research by providing me with the resources, help, guidance, constructive criticism, contributions and encouragement at every stage of my work. Words alone cannot describe how grateful I am to them. My sincere gratitude also goes to each of my graduate supervisory committee members; Dr. M. Paige, Dr. R. Evitts, Dr. J. Soltan and Dr. M. Nemati for their supervision, time, comments and all the valuable suggestions that contributed to the quality of this PhD work. I also treasure the invaluable support and motivation of Dr. I. Oguocha and Dr. A. Odeshi. It was always a privilege to interact with them. Profound appreciation to Mr. RLee Prokopishyn for assistance with the building and maintenance of the arc discharge setup, and for support with maintenance, repairs and troubleshooting of the hydrotreater. The priceless input of Mr. Richard Blondin and Ms. Heli Eunike with samples characterizations and the hydrotreater can never go unnoticed. I am so thankful to them. Special appreciation goes to University of Saskatchewan, Natural Science and Engineering Research Council of Canada (NSERC), Syncrude Canada Limited and MITACS for funding this study.

I am truly indebted to my dad, Mr. Frans K. Bruce, my mum, Ms. Florence A. Ashitey, my aunt Ms. Juliana A. Ashitey, my brother, Mr. Egbert K. Bruce and my sister, Mrs Matilda A. Dzakwasi for their continuous prayers, support, understanding and encouragement. You have always been my rock, you stood by me through every part of this journey, and you always lifted me up, put a smile on my face and gave me hope when I needed it most. To my hubby, Mr. Felix Aryee, I am sincerely thankful for all the sacrifices, suggestions, encouragements and support you offered. Holding our chin up in this roller coaster ride throughout the years truly defines our journey. To my beloved children, Jaedon and Jeanne Aryee you ushered me into another phase of multitasking that I was clueless about. Together we all made it, and I am proud about its consequences. My sincere gratitude to both of you for your patience, time, and unconditional love to your mama. Furthermore, I would also like to appreciate Dr. Christian Botcheway, Dr. Joseph Essilfie-Dughan, Dr. P. Boahene, Majak Mapiour, and Dr. S. Badoga for contributing to this feat through various discussions, laboratory support, and insightful moments with me. Sincere thanks

to my good friend Dr. W. Alabi, I appreciate you for inspiring and motivating me. You encouraged me to stay positive even in tough times. I am grateful to you for consistently checking on me and I also treasure our moments of great laughter. My heartfelt appreciation goes to Otema Ohene-Asare, Bibi Olomola, Ankeeta Kurhade, Rachita Rana and Afees Ayodeji for helping me in diverse ways as I pursue this dream. Special recognition also to catalysis and chemical reaction engineering laboratories fellow members, thanks so much for all your kindness. Finally, my genuine gratitude goes to faculty, colleagues, families, friends and everyone whose name has not been mentioned but, who cheered me on to complete this program. I am extremely grateful to you all. Thank you and be blessed.

DEDICATION

I dedicate this thesis to:

My heavenly father who saw me through it all and especially at the crossroad. Truly in Him, I
live and have my being.

My husband for all the support, love, valuable discussions and for enduring both the good and
bad times with me.

My kids, you challenged me for good deeds, refined me throughout this journey and brought me
profound joy.

My parents and siblings for believing in me, sharing my journey and for all the concerns.

My aunt, you have always been there for me since I was a child and showered me with countless
blessings.

My maternal grandma you departed this world at the age of 96 years, the same date and
approximately the same time my daughter was born. You instilled so much into me and cared for
me a lot. Even in your last days you never ceased to ask whether my reactor has started working.

I miss you dearly.

TABLE OF CONTENTS

PERMISSION TO USE	i
ABSTRACT	ii
ACKNOWLEDGEMENTS	iv
DEDICATION	vi
TABLE OF CONTENTS	vii
LIST OF TABLES	xiii
LIST OF FIGURES	xiv
NOMENCLATURE and ABBREVIATIONS	xx
CHAPTER 1 : Introduction and Thesis Outline	1
1.1 Introduction.....	1
1.2 Knowledge Gaps.....	2
1.3 Hypothesis.....	3
1.4 Research Objective and Sub-objectives.....	4
1.4.1 Research Objective	4
1.4.2 Sub-objectives.....	4
1.5 Research Phases	5
1.6 Organization of this thesis	6
1.7 Gas oil feedstocks	8
1.8 The hydrotreating reactor.....	8
CHAPTER 2 : Literature Review	13
2.1 Hydroprocessing	13
2.2 Hydrotreating process variables.....	14
2.3 Reactivity of sulfur compounds in feedstock.....	15
2.4 Reactivity of nitrogen compounds in feedstock.....	17
2.5 Reactivity of oxygen compounds in feedstock	18
2.6 Olefins saturation	19
2.7 Aromatic saturation.....	20
2.8 Metals removal in feedstocks.....	20
2.9 Inhibitors to hydrotreating reactions	21
2.10 Hydrotreating catalyst.....	22
2.11 Catalyst life cycle during hydrotreating.....	23

2.12 Effect of secondary promoters on HDS and HDN.....	25
2.13 The role of the catalyst support.....	26
2.14 Catalyst preparation	28
2.15 Carbon and its allotropes	28
2.16 Carbon nanohorns (CNH).....	29
2.17 Application of CNH.....	31
2.18 Synthesis methods for CNH.....	32
2.18.1 Laser ablation method of carbon nanomaterial synthesis	32
2.18.2 Arc discharge method of carbon nanomaterial synthesis	32
2.18.3 Chemical vapour deposition method for synthesising carbon nanomaterial	34
2.19 Functionalization.....	35
CHAPTER 3 : Characterization Techniques and Sample Analyses	39
3.1 Brunauer-Emmett-Teller (BET) surface area, pore size and pore volume analyzer.....	40
3.1.1 BET sample analysis.....	41
3.2 High resolution transmission electron microscopy (HRTEM)	41
3.2.1 HRTEM sample analysis	42
3.3 Fourier transform infrared (FTIR) spectroscopy	42
3.3.1 FTIR sample analysis.....	43
3.4 Pyridine Fourier transform infrared spectroscopy (Py-FTIR)	43
3.4.1 Pyridine FTIR sample analysis	44
3.5 Raman spectroscopy	44
3.5.1 Raman spectroscopy sample analysis	46
3.6 X-ray diffraction (XRD)	47
3.6.1 XRD sample analysis.....	48
3.7 Thermogravimetric analysis (TGA).....	48
3.7.1 TGA sample analysis	49
3.8 Boehm titration	49
3.8.1 Boehm titration analysis	50
3.9 CO chemisorption	50
3.9.1 CO chemisorption analysis	52
3.10 Temperature programmed reduction (TPR).....	52
3.10.1 TPR sample analysis	52

3.11 Nitrogen-Sulfur (NS) analyzer.....	53
3.11.1 N-S sample analysis.....	53
3.12 X-ray absorption spectroscopy (XAS).....	55
3.12.1 XAS sample analysis	56
CHAPTER 4 : Maximization of Carbon Nanohorns Production via the Arc-discharge Method for Hydrotreating	58
4.1 Abstract.....	59
4.2 Introduction.....	60
4.3 Experimental method.....	61
4.3.1 Production of CNH	61
4. 4 Characterizations.....	63
4.5 Results and discussion	63
4.5.1 Mass balance for arc discharge experiments	63
4.5.2 Effects of current setting on CNH production	64
4.5.3 Effects of time on CNH production	67
4.5.4 Effect of current variation on morphology of CNH.....	68
4.5.5 Effect of current variation on textural properties of CNH.....	69
4.5.6 Effect of current variation on thermal stability of CNH	72
4.5.7 FTIR analysis of CNH synthesized under different current conditions.....	73
4.5.8 XRD analysis of CNH synthesized under different current conditions.....	74
4.5.9 Raman spectroscopy analysis of CNH synthesized under different current conditions	75
4.6 Conclusions.....	77
CHAPTER 5 : Functionalization and Characterization of Carbon Nanohorns (CNH) for Hydrotreating of Gas Oil.....	78
5.1 Abstract.....	79
5.2 Introduction.....	80
5.3 Experimental method.....	81
5.3.1 CNH functionalization, catalyst preparation and hydrotreating experiment	81
5.4. Characterizations.....	83
5.5 Results and discussion	83
5.5.1 BET analysis of pristine and functionalized CNH and NiMo/CNH catalyst.....	83
5.5.2 Morphology of pristine and functionalized CNH and NiMo/CNH catalyst	86
5.5.3 Thermal stability of pristine and functionalized CNH and NiMo/CNH catalyst.....	87

5.5.4 XRD analysis of pristine CNH and NiMo/CNH catalyst	89
5.5.5 FTIR analysis of pristine and functionalized CNH.....	90
5.5.6 Raman spectroscopy of pristine and functionalized CNH.....	91
5.5.7 Catalytic activity of NiMo/CNH catalyst	93
5.6 Conclusions.....	95
CHAPTER 6: Comparative Studies of Carbon Nanomaterial and Gamma-alumina as Supports for Ni-Mo Catalyst in Hydrotreating of Gas Oils.....	96
6.1 Abstract.....	97
6.2 Introduction.....	98
6.3 Experimental method.....	100
6.3.1 Catalyst preparations and hydrotreating experiments.....	100
6.4. Characterizations.....	101
6.5 Results and discussion	102
6.5.1 Morphology of arc-discharge materials.....	102
6.5.2 Textural properties of catalysts.....	102
6.5.3 Thermal stability of catalysts.....	104
6.5.4 Examination of XRD patterns.....	105
6.5.5 Dispersion behaviour of catalysts	107
6.5.6 Reducibility of catalysts.....	108
6.5.7 Acidity measurements.....	110
6.5.8 XAS analysis.....	112
6.5.9 Determination of catalytic activity.....	116
6.6 Conclusions.....	120
CHAPTER 7 : Determination of a suitable NiMo/OCP_f catalyst with varying Ni and Mo loadings for hydrotreating of light gas oils.....	122
7.1 Abstract.....	123
7.2 Introduction.....	124
7.3 Experimental method.....	127
7.3.1 Catalyst preparations and hydrotreating experiments.....	127
7.4. Characterizations.....	128
7.5 Results and discussion	129
7.5.1 BET analysis of pristine OCP _f , functionalized OCP _f and OCP _f -supported NiMo catalysts	129

7.5.2 TGA analysis of the OCP _f -supported NiMo catalysts	130
7.5.3 XRD analysis of the OCP _f -supported NiMo catalysts	132
7.5.4 CO chemisorption analysis of the OCP _f -supported NiMo catalysts	134
7.5.5 HRTEM examination of the morphology of the various OCP _f -supported NiMo catalysts	135
7.5.6 TPR analysis of the various OCP _f -supported NiMo catalysts	135
7.5.7 HDS and HDN activities of the various OCP _f -supported NiMo catalysts.....	137
7.6 Conclusions.....	140
CHAPTER 8 : Development of the NiMo/CNH catalyst for hydrotreating:	
Characterization, statistical, hydrodynamics and mass transfer studies ..	
8.1 Abstract	142
8.2 Introduction.....	143
8.3 Experimental Method.....	144
8.3.1 Catalyst preparations, hydrotreating experiments and statistical analysis method.....	144
8.4 Characterization	146
8.5 Results and discussion	146
8.5.1 Textural properties of pristine CNH, functionalized CNH and NiMo/CNH and P-doped NiMo/CNH catalysts	146
8.5.2 Examination of XRD patterns.....	147
8.5.3 CO-chemisorption analysis of catalysts.....	148
8.5.4 TPR analysis of catalysts	149
8.5.5 HDS and HDN activities.....	150
8.5.6 Statistical analysis.....	153
8.5.7 Hydrodynamics of a trickle-bed reactor	160
8.5.8 Mass transfer resistances for the HDS/HDN reactions.....	161
8.5.8.1 External mass transfer.....	162
8.5.8.2 Internal mass transfer.....	164
8.5.9 Kinetics	166
8.5.10 Catalyst Stability Study.....	171
8.6 Conclusions.....	172
CHAPTER 9 : Conclusions and Recommendations	
9.1 Overall conclusions.....	174
9.2 Recommendations for future research work.....	176

References.....	179
Appendix A: Arc discharge production and filtration station.....	208
Appendix B: Determination of best condition for OCP and OCP _f functionalization.	211
Appendix C: Raman and BET results of different carbon-supported catalysts and gamma- alumina supported catalyst (Phase 3 of research or Chapter 6).....	213
Appendix D: Statistical analysis	215
Appendix E: Hydrodynamics calculations for hydrotreating of light gas oil using 3.5wt%Ni19wt%Mo/CNH catalyst.	219
Appendix F: External mass transfer calculation	221
Appendix G: Internal mass transfer calculation.....	230
Appendix H: Hydrotreating performance on heavy gas oil using the best catalyst (3.5wt%Ni19wt%Mo/CNH) established from phase 5.	235
Appendix I: Permissions to Use Papers, Tables and Figures.....	236

LIST OF TABLES

Table 1.1 Feed characteristics of light and heavy gas oils.....	8
Table 2.1 A hydrotreating catalysts typical physical properties (Adapted from Robinson and Dolbear, 2006).....	23
Table 4.1 Effect of time on the quantity of CNH produced.....	68
Table 4.2 Textural properties of pristine CNH samples based on current settings of (50 -100A).....	70
Table 4.3 Examination of pristine CNH quality based on ID/IG ratio.	77
Table 5.1 Textural properties of pristine and functionalized CNH and NiMo/CNH catalyst.....	84
Table 5.2 Examination of pristine and functionalized CNHs quality based on I_D/I_G ratio.	93
Table 6.1 Textural properties of all the different supported Ni-Mo catalysts.....	103
Table 6.2 CO chemisorption results of different NiMo-supported catalysts.	108
Table 7.1 BET analysis of pristine OCPf, functionalized OCPf, and NiMo/OCPf catalysts.....	129
Table 7.2 CO-chemisorption analysis of OCPf-supported NiMo catalysts.	134
Table 8.1 Design levels (coded and uncoded) for design of experiment.	146
Table 8.2 Textural properties of pristine CNH, functionalized CNH and NiMo/CNH and P-doped NiMo/CNH catalysts.	147
Table 8.3 CO chemisorption results of various NiMo/CNH catalysts.....	149
Table 8.4 Results of nitrogen removal and sulfur removal percentages based on DOE.....	154
Table 8.5 ANOVA analysis results for response surface quadratic model of % sulfur removal with 3.5Ni19Mo/CNH catalyst.....	156
Table 8.6 ANOVA analysis results for response surface quadratic model of % nitrogen removal with 3.5Ni19Mo/CNH catalyst.	156
Table 8.7 Optimum operating condition for maximization of sulfur and nitrogen removal.....	160
Table 8.8 Hydrodynamics of a trickle-bed reactor using a carbon (CNH)-supported catalyst..	161
Table B.1 Effects of functionalization on OCP (BET results).....	211
Table B.2 Effects of functionalization on OCP _f (BET results).....	211

LIST OF FIGURES

Figure 1.1 Schematic of the trickle bed hydrotreater used for hydrotreating of gas oil.	9
Figure 1.2 Schematic of the tubular microreactor showing the various loadings	12
Figure 2.1 General reactions of some sulfur compounds in feedstock (Adapted from Guria, 2008).....	16
Figure 2.2 HDS of DBT showing two reaction pathways (Adapted from Knudsen et al. 1999).....	17
Figure 2.3 Nitrogen reactions in feedstock (Adapted from Gruia, 2008).....	18
Figure 2.4 Nitrogen removal mechanism (Adapted from Gruia, 2008).....	18
Figure 2.5 De-oxygenation reaction during hydrotreating of feedstock (Adapted from Gruia,2008).....	19
Figure 2.6 Olefin saturation in hydroprocessing (Adapted from Gruia, 2008).....	19
Figure 2.7 Aromatic saturation in hydroprocessing (Adapted from Gruia, 2008).....	20
Figure 2.8 Life cycle of NiMo/Al ₂ O ₃ catalyst during hydrotreating (Eijsbouts, 1997).....	24
Figure 2.9 Examples of carbon allotropes a) Diamond, b) Graphite, c) Amorphous carbon d) Spherical fullerene, C ₆₀ e) Ellipsoidal fullerene, C ₇₀ and f) Tubular fullerene, SWCNT (Ren et al. 2012).....	29
Figure 2.10 a) TEM image of the CNH, b) conceptual image of CNH (Iijima et al.1999; Fan et al. 2007).....	30
Figure 2.11 Five possibilities of graphitic cones and experimental representation (Krishnan et al. 1997; Ebbesen 1998).	31
Figure 2.12 Schematic drawing showing a proposed physical model of the arc discharge method using liquid (Xing et al. 2007).....	34
Figure 2.13 Examples of surface oxygen group structures; a) carboxyl group, b) carboxylic anhydride, c) lactone group, d) lactols, e) single hydroxyl group, f) isolated carbonyl group, g) quinone-group h) substitution of oxygen for edge carbon atoms (e.g. xanthan) (Boehm, 1994).....	36
Figure 3.1 Diagram of adsorption-desorption isotherms and some hysteresis loop; a) IUPAC classification of adsorption-desorption isotherms (note the appearance of hysteresis in Types IV and V), b) correlation between the pore shape plus adsorption-desorption isotherm (Sing et al. 2008).	41

Figure 3.2 Energy diagram illustration of Rayleigh and Raman scattering (Tu and Chang, 2012).	45
Figure 3.3 Diagram showing the regions of an X-ray absorption spectrum (Penner-Hahn, 2003).	56
Figure 4.1 Schematic of experimental setup for producing CNH.....	62
Figure 4.2 Mass balance of the arc discharge process.	63
Figure 4.3 Effect of increasing current (50 A to 100 A) on the yield of CNH produced from an arc-discharge experiment.	64
Figure 4.4 Effects of baffle incorporation and extension of length of electrode rod at higher current (80A, 90A and 100A) settings on the yield of CNH.	66
Figure 4.5 Effect of increasing process duration (10 mins to 60 mins) on the yield of CNH produced from arc-discharge experiment.	67
Figure 4.6 TEM of pristine CNH at; a) Low magnification synthesized at 70 A, b) High magnification synthesized at 70 A, c) Low magnification synthesized at 80 A, d) High magnification synthesized at 80 A.....	69
Figure 4.7 BET Isotherms of CNH synthesized at various currents; a) 90A, b-e) 60A, 70A, 80A, 100A, f) 50A.	71
Figure 4.8 Pore size distribution of CNH synthesized at various currents; a) 90A, b) 70A, c) 100A, d) 80A, e) 60A, f) 50A.....	72
Figure 4.9 TGA analysis of pristine CNH synthesized at 80A.....	73
Figure 4.10 FTIR analysis of pristine CNH synthesized at; a) 100A, b) 90A, c) 80A, d) 70A, e) 60A, f) 50A.....	74
Figure 4.11 XRD analysis of pristine CNH synthesized at 80A.....	75
Figure 4.12 Raman spectra of pristine CNH produced at different currents; a) 80A, b) 70A, c) 90A, d) 100A, e) 50A, f) 60A.	76
Figure 5.1 BET Isotherms of; a) 90A CNH, b) 90A CNH_4 h, c)90A CNH_2 h, d) 90A CNH_1 h, e) NiMo/CNH, f)90A CNH_30 min, g) 90A CNH_15 min.....	85
Figure 5.2 Pore size distribution of; a) 90A CNH_4 h, b) 90A CNH_2 h, c) 90A CNH_1 h, d) NiMo/CNH catalyst, e) 90A CNH_30 min, f) 90A CNH_15 min, g) 90A CNH.....	86
Figure 5.3 TEM images of; a) 90A CNH, b) 90A CNH_30 min, c) 90A CNH_1 h,	

d) NiMo/CNH (low magnification), e) NiMo/CNH (high magnification).....	87
Figure 5.4 TGA analysis of; a) 90A CNH_30 min, b) 90A CNH and c) NiMo/CNH catalyst. ..	88
Figure 5.5 XRD analysis of; a) NiMo/CNH catalyst, b) 90A CNH.	90
Figure 5.6 FTIR analysis of; a) 90A CNH_4 h, b) 90A CNH_15 min, c) 90A CNH_2 h, d) 90A CNH_1 h, e) 90A CNH_30 min, f) 90A CNH.	91
Figure 5.7 Raman spectra of pristine CNH produced at different currents; a) 90A CNH_1 h, b) 90A CNH, c) 90A CNH_2 h, d) 90A CNH_30 min, e) 90A CNH_4 h, f) 90A CNH_15 min.	92
Figure 5.8 HDN and HDS activities of NiMo/CNH catalyst using Bitumen derived LGO at various temperatures. (Catalyst volume = 5cm ³ , P= 8.8 MPa LHSV = 2h ⁻¹ and H ₂ /oil ratio = 600 (v/v)).....	94
Figure 6.1 TEM images of different carbon materials from arc-discharge experiment; a) pristine CNH, b) pristine OCP _f , and c) pristine OCP.	102
Figure 6.2 TGA thermograms of the different supported catalysts; a) NiMo/OCP, b) NiMo/CNT, c) NiMo/OCP _f , d) NiMo/CNH, and e) NiMo/γ-Al ₂ O ₃	105
Figure 6.3 XRD patterns of different supported catalysts: a) NiMo/γ-Al ₂ O ₃ , b) NiMo/CNH, c) NiMo/OCP _f , and d) NiMo/CNT.	106
Figure 6.4 TPR profiles of different supported catalysts; a) NiMo/γ-Al ₂ O ₃ , b) NiMo/OCP, c) NiMo/CNH, d) NiMo/OCP _f , and e) NiMo/CNT.	109
Figure 6.5 Pyridine FTIR images of samples; a) NiMo/CNH, b) NiMo/OCP _f , and c) NiMo/CNT.....	111
Figure 6.6 Pyridine FTIR image of NiMo/γ-Al ₂ O ₃	112
Figure 6.7 Mo K-edge XANES spectra of: Mo foil, Na ₂ MoO ₄ , [(NH ₄) ₆ Mo ₇ O ₂₄ ·4H ₂ O], NiMo/γ-Al ₂ O ₃ , MoO ₃ , NiMo/OCP _f , and NiMo/CNH.....	113
Figure 6.8 (a) Mo K-edge k ³ -weighted EXAFS, and (b) Fourier transform (FT) spectra for a k interval of 2-12 Å ⁻¹ of (NH ₄) ₆ Mo ₇ O ₂₄ ·4H ₂ O, NiMo/γ-Al ₂ O ₃ , MoO ₃ , NiMo/OCP _f , and NiMo/CNH.	115
Figure 6.9 HDS activities of carbon and gamma alumina-supported NiMo catalysts using LGO at 370, 350, and 330 °C (Catalyst = 5 cm ³ , LHSV = 2 hr ⁻¹ , P = 9.0 MPa, and H ₂ / oil ratio = 600 (v/v)).	117
Figure 6.10 HDN activities of carbon and gamma alumina-supported NiMo catalysts	

using LGO at 370, 350, and 330 °C (Catalyst = 5 cm ³ , LHSV = 2 hr ⁻¹ , P = 9.0 MPa, and H ₂ / oil ratio = 600 (v/v)).	117
Figure 7.1 TGA profile of OCP _f -supported NiMo catalysts; a) 5.0wt%Ni19wt%Mo/OCP _f , b)3.5wt%Ni19wt%Mo/OCP _f , c) 3.5wt%Ni13wt%Mo/OCP _f , d) 2.5wt%Ni13wt%Mo/OCP _f , e) 2.5wt%Ni19wt%Mo/OCP _f , f) 5.0wt%Ni13wt%Mo/OCP _f , g) 5.0wt%Ni126wt%Mo/OCP _f	131
Figure 7.2 Low angle XRD pattern of OCP _f -supported NiMo catalysts; a) 5.0wt%Ni26wt%Mo/OCP _f b) 5.0wt%Ni19wt%Mo/OCP _f c) 5.0wt%Ni13wt%Mo/OCP _f d) 3.5wt%Ni19wt%Mo/OCP _f e) 3.5wt%Ni13wt%Mo/OCP _f f) 2.5wt%Ni19wt%Mo/OCP _f g) 2.5wt%Ni13wt%Mo/OCP _f	133
Figure 7.3 High angle XRD pattern of OCP _f -supported NiMo catalysts; a) 5.0wt%Ni26wt%Mo/OCP _f b) 5.0wt%Ni19wt%Mo/OCP _f c) 5.0wt%Ni13wt%Mo/OCP _f d) 3.5wt%Ni19wt%Mo/OCP _f e) 3.5wt%Ni13wt%Mo/OCP _f f) 2.5wt%Ni19wt%Mo/OCP _f g) 2.5wt%Ni13wt%Mo/OCP _f	133
Figure 7.4 Morphology of different NiMo/OCP _f catalysts; a) 2.5wt%Ni13wt%Mo/OCP _f , b) 2.5wt%Ni19wt%Mo/OCP _f , c) 3.5wt%Ni13wt%Mo/OCP _f , d) 3.5wt%Ni19wt%Mo/OCP _f , e) 5.0wt%Ni13wt%Mo/OCP _f , f) 5.0wt%Ni19wt%Mo/OCP _f , g) 5.0wt%Ni26wt%Mo/OCP _f	135
Figure 7.5 TPR results of NiMo/OCP _f catalysts; a) 5.0wt%Ni19wt%Mo/OCP _f , b) 5.0wt%Ni26wt%Mo/OCP _f , c) 5.0wt%Ni13wt%Mo/OCP _f , d) 3.5wt%Ni19wt%Mo/OCP _f , e) 3.5wt%Ni13wt%Mo/OCP _f , f) 2.5wt%Ni19wt%Mo/OCP _f , g) 2.5wt%Ni13wt%Mo/OCP _f	136
Figure 7.6 HDS activities of NiMo/OCP _f catalysts with LGO at 370, 350, and 330 °C (Catalyst = 5 cm ³ , LHSV = 2 hr ⁻¹ , P = 9.0 MPa, and H ₂ / oil ratio = 600 (v/v)). ...	139
Figure 7.7 HDN activities of NiMo/OCP _f catalysts with LGO at 370, 350, and 330 °C (Catalyst = 5 cm ³ , LHSV = 2 hr ⁻¹ , P = 9.0 MPa, and H ₂ / oil ratio = 600 (v/v)).	139
Figure 8.2 XRD patterns of NiMo/CNH and P-doped NiMo/CNH catalysts.....	148
Figure 8.3 TPR profiles of a) 3.5wt%Ni19wt%Mo/CNH, b) 2.5wt%Ni19wt%Mo/CNH,	

c) 5.0wt%Ni19wt%Mo/CNH and d) 3.5wt%Ni19wt%Mo2.0wt%P/CNH.	150
Figure 8.4 HDS activities of a) 2.5wt%Ni19wt%Mo/CNH, b) 3.5wt%Ni19wt%Mo/CNH, c) 5.0wt%Ni19wt%Mo/CNH and d) 3.5wt%Ni19wt%Mo2.0wt%P/CNH and e) 3.5wt%Ni19wt%Mo/CNH (pel) catalysts using LGO at 370, 350, and 330 °C (Catalyst = 5 cm ³ , P = 9.0 MPa, LHSV = 2 hr ⁻¹ , and H ₂ / oil ratio = 600 (v/v)).....	151
Figure 8.5 HDN activities of a) 2.5wt%Ni19wt%Mo/CNH, b) 3.5wt%Ni19wt%Mo/CNH, c) 5.0wt%Ni19wt%Mo/CNH and d) 3.5wt%Ni19wt%Mo2.0wt%P/CNH and e) 3.5wt%Ni19wt%Mo/CNH (pel) catalysts using LGO at 370, 350 and 330 °C (Catalyst = 5 cm ³ , P = 9.0 MPa, LHSV = 2 hr ⁻¹ , and H ₂ / oil ratio = 600 (v/v)).	152
Figure 8.6 Main effects plot for % sulfur removal.	158
Figure 8.7 Main effects plot for % nitrogen removal.	158
Figure 8.8 Contour Plots for % sulfur removal.....	159
Figure 8.9 Contour plots for % nitrogen removal.....	159
Figure 8.10 Determination of R ² for HDS of light gas oil with n =1.4	169
Figure 8.11 Determination of R ² for HDN of light gas oil with n = 1.0.....	170
Figure 8.12 Determination of activation energy for HDS reaction with n = 1.4	171
Figure 8.13 Determination of activation energy for HDN reaction with n = 1.0.....	171
Figure 8.14 HDS and HDN long-term stability study with 3.5wt%Ni19wt%Mo/CNH catalyst using LGO at 370 °C (Catalyst = 5 cm ³ , P = 9.0 MPa, LHSV = 2 hr ⁻¹ , and H ₂ / oil ratio = 600 (v/v)).	172
Figure A.1 Arc discharge setup and filtration area in the pilot plant.	208
Figure A.2 Part of arc discharge setup showing mounted electrodes and some tools.	209
Figure A.3 Filtration, air drying of samples and sample collection.....	210
Figure B.1 HDN and HDS activities of 2.5wt%Ni13wt%/CNH catalysts using LGO at 370, 350, and 330 °C (Catalyst = 5 cm ³ , P = 9.0 MPa, LHSV = 2 hr ⁻¹ , and H ₂ / oil ratio = 600 (v/v)). CNH support was functionalized for 15 mins.	212
Figure C.1 Raman Spectroscopy of: a) NiMo/OCP _{f1} b) NiMo/OCP _{f2} c) NiMo/ γ Al ₂ O ₃ d) NiMo/CNT e) NiMo/CNH.	213

Figure C.2 Adsorption capabilities of carbon-supported catalysts and gamma-alumina supported catalyst: a) NiMo/ γ -Al ₂ O ₃ , b) NiMo/CNH, c) NiMo/CNT, d) NiMo/OCP _f , e) NiMo/OCP.	214
Figure D.1 Pareto Chart of the Standardized Effects (response is % Sulfur removal, $\alpha = 0.05$).	215
Figure D.2 Pareto Chart of the Standardized Effects (response is % Nitrogen removal, $\alpha = 0.05$).	215
Figure D.3 Interaction plot for % sulfur removal.	216
Figure D.4 Interaction plot for % nitrogen removal.	217
Figure D.5 Parity Plot for Sulfur Removal	217
Figure D.6 Parity Plot for Nitrogen Removal	218
Figure H.1 HDN and HDS activities of 3.5wt%Ni19wt%Mo/CNH catalysts using HGO at 370, 380, and 390 °C (Catalyst = 5 cm ³ , P = 9.0 MPa, LHSV = 1 hr ⁻¹ , and H ₂ / oil ratio = 600 /v)).	235

NOMENCLATURE and ABBREVIATIONS

4, 6-DMDBT	4, 6-dimethyl dibenzothiophene
4-MDBT	4-methyl dibenzothiophene
γ -Al ₂ O ₃	Gamma alumina
[(NH ₄) ₆ Mo ₇ O ₂₄ ·4H ₂ O]	ammonium heptamolybdate tetrahydrate
[Ni(NO ₃) ₂ ·6H ₂ O]	nickel nitrate hexahydrate
%M _{Disp}	percentage metal dispersion
a _s	Liquid/solid interfacial surface area
As	Arsenic
BET	Brunauer-Emmett-Teller
BJH	Barrett-Joyner-Halenda
C	Solubility of a gas in solvent
C _{H₂}	Hydrogen concentration in the liquid phase at equilibrium, mol/mL
[C _i] _s	Catalyst surface concentration of sulfur/nitrogen species, mol/mL
CCD	Central composite design
CNH	Carbon nanohorns
CNT	Carbon nanotubes
Co	Cobalt aluminate
Cu	Copper
CVD	Chemical vapour deposition
d _p	Average diameter of the catalyst particles
d _{pe}	Effective catalyst particle diameter
D _L	Liquid/Gas diffusion coefficient (cm ² /s)
D _R	Internal inside diameter of reactor
D _i	Bulk diffusivity of organosulfur compounds, cm ² /g
E _i	Activation energy, J/mol
EPR	Enhanced permeability and retention
EXAFS	Extended X-ray absorption fine structure
Fe	Iron

FTIR	Fourier transform infrared
g	Acceleration due to gravity (981 cm/s ²)
H_{H_2}	Henry's constant for hydrogen in LGO, MPa.m ³ /mol
H ₂ O ₂	Hydrogen peroxide
H ₂ S	Hydrogen sulphide
H ₂ SO ₄	Sulfuric acid
HPS	High-pressure separator
HRTEM	High resolution transmission electron microscopy
HDA	Hydrodearomatization
HDM	Hydrodemetallization
HDN	Hydrodenitrogenation
HDO	Hydrodeoxygenation
HDS	Hydrodesulfurization
HGO	Heavy gas oil
HNO ₃	Nitric acid
I _o	Incident intensity
I _t	Transmitted intensity
K	Proportionality constant
k _L	H ₂ /LGO mass transfer coefficient - gas/liquid side, cm/s
k _{OVr}	Overall mass transfer coefficient for hydrogen, cm/s
k _s	H ₂ /LGO mass transfer coefficient – liquid/solid side, cm/s
k _t	Thermal conductivity of the NiMo/CNH catalyst pellet powder particle, W/(m. K)
KBR	Potassium bromide
KMnO ₄	Potassium permanganate
L	Length of the catalyst bed
L _A	Liquid mass flow over cross-sectional area, g/(s.cm ²)
LHSV	Liquid hourly space velocity

LUMO	Lowest unoccupied molecular orbital
M	Metallic surface area (m ² /g)
m ₁	Empirical constant*
m ₂	Empirical constant*
M _{AVE}	Average molecular weight of LGO, g/mol
mins	minutes
Mo	Molybdenum
MoS ₂	Molybdenum disulfide
n	Reaction order
Nd: YAG	Neodymium-doped yttrium aluminum garnet
N	Nitrogen
Na	Sodium
Ni	Nickel
Ni(Al ₂ O ₄)	Nickel aluminate
NiO	Nickel oxide
NS	Nitrogen-sulfur
Ni ₃ S ₂	Nickel (III) sulfide
N _S	Entire number of metal atoms that are on the surface
N _T	Entire number of metal atoms (both bulk and surface)
NTA	Nitriiotriacetic acid
OCP	Other carbon particles
OCP _c	Chunk fraction of other carbon particles
OCP _f	Fine fraction of other carbon particles
<i>P</i>	Specific mass of the metal (g/cm ³)
P	Operating pressure, MPa
P _{gas}	Partial pressure of the gas above the solution
P _{eL}	Peclet number
pyL	Pyridine coordinated species
pK _B	Base dissociation constant
Py-FTIR	Pyridine Fourier transform infrared spectroscopy
pyH ⁺	Pyridinium ions

r_{HDN}	Molar rate of nitrogen removal achieved from the hydrotreating catalyst (mol/s)
r_{HDS}	Molar rate of sulfur removal achieved from the hydrotreating catalyst (mol/s)
R	Universal gas constant, J/(mol.K)
{ R_i }	Global reaction rate, mol/(s.mL)
S	Sulfur
SF _{calc}	Calculated stoichiometry factor
SiC	Silicon carbide
STEM	Scanning transmission electron microscopy
SWCNT	Single wall carbon nanotube
T	Operating temperature, °R
T_b	Average boiling point of LGO
T_s	Pellet catalyst or powder catalyst particle surface temperature, K
TEM	Transmission electron microscopy
TiO ₂	Titania
TPR	Temperature programmed reduction
V	Vanadium
V ₃ S ₄	Trivanadium tetrasulfide
V ₃ S ₂	Vanadium (III) Sulfide
V_c	Volume of the loaded catalyst, mL
V_b	Hydrogen molar volume at the normal boiling point
W	Tungsten
$W_{Atomic, Mo}$	Atomic weight of first metal, Mo (g/mole)
$W_{Atomic, Ni}$	Atomic weight of second metal, Ni (g/mole)
x	Conversion of sulfur and nitrogen species for HDS and HDN reactions
x_{HDN}	Stoichiometric values for HDN
x_{HDS}	Stoichiometric values for HDS
X	Association parameter

XANES	X-ray absorption near-edge structure
XAS	X-ray absorption spectroscopy
Zn	Zinc
μ_L	Liquid-phase viscosity (cP)
μ (E)	Energy-dependent x-ray absorption coefficient.
ρ_L	Liquid-phase density (g/cm ³)
v_L	Liquid superficial velocity (cm/s)
$(-1/V_c \cdot dn/dt)$	Rate of hydrogen conversion in the reaction, mol/(s.mL)
a_L	Interfacial surface area over unit volume (cm ⁻¹)
ε	Bed porosity
μ_L	Viscosity of LGO at the operating temperature, g/ (s.cm)
ρ_L	Density of LGO at the operating conditions, g/mL
α_1	Constant based on the catalyst particle properties*
α_2	Constant based on the catalyst particle properties*
°API	American petroleum institute gravity
$\rho_{15.6}$	Density of LGO at 15.6°C
$\Delta_{\rho T}$	Temperature density correlation, lbs/ft ³
$\Delta_{\rho P}$	Pressure density correlation, lbs/ft ³
v_N	Hydrogen molar volume at standard conditions, L/mol
λ_{H_2}	Hydrogen solubility in LGO, mL/(kg·MPa)
ρ_{20}	Density of LGO at 20 °C, g/mL
$\Delta H_{R,i}$	Heat of HDS/HDN reaction, kJ/mol
ε_p	Porosity of the catalyst pellets or powder particles, dimensionless
γ_p	Tortuosity of the catalyst pellets or powder particle, dimensionless
v_i	Molar volume of sulfur/nitrogen molecules under standard conditions, mL/mol
v_L	Molar volume of LGO under standard conditions, mL/mol
v_c^m	Critical specific mass volume, mL/g or ft ³ /lb
$SG_{15.6}$	Specific gravity at 15.6 °C

β_{HDS}

Isothermality ratio

β_{HDN}

Isothermality ratio

CHAPTER 1

Introduction and Thesis Outline

Contribution of this chapter to overall study

This chapter gives information about what hydroprocessing is about, the problem at stake that requires the need for hydrotreating, the plan that would be followed to improve the hydrotreating performance based on identified knowledge gaps and associated hypothesis. In addition, the objectives of this research and the organization of this entire thesis is provided.

1.1 Introduction

Hydrotreating is a catalytic driven hydrogenation process which is widely used in oil and gas applications to convert hydrocarbon gas oils and liquids from petroleum residues into products with less sulfur (S), nitrogen (N), metals and asphaltenes contents. Hydrotreating is therefore aimed at ensuring that the upgraded product has a safe impact on public health and the environment. As an example, in Canada a mandate was passed in 2006 to limit the amount of sulfur in diesel fuels to 15 ppm. The extent of hydrotreating is influenced by the reactor design, catalyst, process parameters, source and quality of feedstock, nitrogen and aromatic compounds in the feedstock, reactivities of sulfur compounds, as well as inhibition effects from hydrogen (H_2S) (Frag, 2007; Zeuthen et al. 2001; Song et al. 2006). Among the factors that affect hydrotreating performance, the use of an active and stable catalyst is the preferred option since, product quality could be improved in a cost-effective manner. Some approaches that could be used to develop an active catalyst include; changing the active molybdenum (Mo) or tungsten (W) component, using different supports such as titania (TiO_2) or carbon (C) and varying the method of preparation (Okamoto et al. 2003). Adding secondary promoters like boron and phosphorus to the catalyst also plays a significant impact on the catalyst performance by aiding active metals dispersion and modifying the existing interaction between the support and Mo oxides (Maity et al. 2011; Prins 2001).

In this research work, the approach to achieving an enhanced hydrotreating catalyst was to develop an active catalyst based on carbon and specifically carbon nanohorns (CNH), other carbon particles (OCP), fine fraction of other carbon particle (OCP_f). Gamma alumina (γ -Al₂O₃) is the traditional support of interest used in industries because of its large surface area, strong mechanical strength, high temperature resistance plus appropriate pore structure. However, the major problem with γ -Al₂O₃ is that, a strong metal-support-interaction occurs between the metallic precursor and support at the onset of catalyst preparation and, this causes a decrease in hydrotreating activity due to the inability of the supported metal oxide to undergo complete sulfidation during hydrotreating. In view of this, use of carbon was considered as an alternative for γ -Al₂O₃ support since, carbon exhibits excellent properties including; large surface area, controlled pore volume and size, variable surface functional group. Additionally, the inert nature of carbon could result in a minimization of metal-support-interaction and consequent improvement in hydrodenitrogenation (HDN) and hydrodesulfurization (HDS) activities (Lee et al. 2003, Abotsi and Scaroni, 1989). CNH material is the carbon support of interest being used in this research. CNH can be described as horn-like shaped graphene sheets that are radially aggregated into a spherical structure with diameter ranging from 50-100 nm. The length and average diameter of an individual horn is 30 - 50 nm and 2 - 5 nm, respectively. Each horn has an apex angle of 20° as a result of the conical shape of its tip (Iijima et al. 1999).

1.2 Knowledge Gaps

Following, a comprehensive literature review on both hydrotreating and hydrotreating catalyst articles the following knowledge gaps were identified:

- i. There is limited information on the maximization of CNH production on a laboratory scale.
- ii. There is no known studies on improving the functionalities of CNH with nitric acid for hydrotreating.
- iii. No known information exists on the evaluation of CNH and/or OCP (i.e. chunk fraction of other carbon particles ((OCP_c) and OCP_f) properties and their use as catalyst support for hydrotreating. Until now, activated carbon, carbon nanotubes and carbon black are some of the carbon supports that have been used for hydrotreating purposes.
- iv. Investigation on the effects of varying metal compositions on OCP_f by-product as catalyst support for hydrotreating has not been researched.

v. Limited information exist on the effects of varying metal compositions as well as the use of secondary promoters such as phosphorous on CNH-supported catalyst in hydrotreating. Examination of the optimum hydrotreating process condition and hydrotreating kinetic studies of NiMo/CNH catalyst have not been studied in open literature.

1.3 Hypothesis

The following hypotheses were made based on the above knowledge gaps, and each of the enlisted hypothesis and knowledge gaps are linked consecutively. The hypothesis are as follows:

1. Variation of current, voltage, electrode dimension, processing time can maximize CNH production.
2. Carbon materials (e.g. CNH) with nanowindows created on them via oxidative treatment have enhanced surface area, porosity and surface chemistry than carbon materials with no acid treatment. In addition, carbon material with enhanced surface chemistry will provide more binding sites for anchorage of metals, increase the number of active sites and consequently increase the hydrotreating performance of the carbon-supported catalyst.
3. Carbon-supported catalyst (CNH, OCP, OCP_f, carbon nanotubes (CNT)) will have desirable physio-chemical properties that will improve hydrotreating performance. Also, the use of carbon-supported catalysts with lower metal-support interaction compared to the traditional NiMo/ γ -Al₂O₃ catalyst will increase HDS and HDN activities.
4. OCP_f-supported NiMo catalyst with different or increasing metal loading compositions will improve hydrotreating (HDS and HDN) activities. This will help to determine if NiMo/OCP_f catalyst can be a potential hydrotreating catalyst.
5. CNH-supported catalyst developed with different Ni and Mo combinations will increase or decrease hydrotreating activities. Also, in hydrotreating, the use of a CNH-supported catalyst that contains a secondary additive such as phosphorus will further enhance HDS and HDN activities. Another hypothesis is that various combination of hydrotreating operating variables (pressure, temperature and LHSV) will cause an increase or decrease in HDS and HDN activities and a specific combination of these operating variables will lead to optimal HDS and HDN activities. Also, the best CNH-supported catalyst used for hydrotreating will have negligible mass transfer limitations and subsequently generate reliable kinetic data.

1.4 Research Objective and Sub-objectives

1.4.1 Research Objective

The overall research goal is to develop a NiMo catalyst supported on CNH and associated carbon materials for hydrotreating of light gas oil (LGO), and this objective is broken down into sub-objectives listed below.

1.4.2 Sub-objectives

1. To build a setup that can produce CNH in the laboratory, and to maximize the production of CNH by identifying and using the best process conditions.
2. To improve the functionality of CNH by creation of oxygen functionalities (e.g. hydroxyl and carboxyl groups) on both inner and outer walls of CNH support material, and to determine the morphology and characteristics of pristine and functionalized CNH.
3. To find out if other carbon materials (i.e., by products of CNH production) could be used as a hydrotreating catalyst. In this regard Ni-Mo catalyst supported on CNH, OCP, OCP_f, and CNT will be formulated and fully characterized. Then, experiments will be conducted to compare the performance of carbon-supported (CNH, OCP, OCP_f, CNT) catalyst vs γ -Al₂O₃-supported catalyst in hydrotreating.
4. To develop the best NiMo/OCP_f catalyst for hydrotreating of gas oils by conducting catalyst screening on OCP_f with varying Ni and Mo compositions.
5. To develop the best NiMo/CNH catalyst for hydrotreating of gas oils by using a combination of Ni and Mo compositions and incorporating a secondary additive such as phosphorus (P). Also, to investigate how variation in hydrotreating operating conditions affects the activity of NiMo/CNH catalyst and finally to determine the kinetics and deactivation studies on the best NiMo/CNH catalyst.

1.5 Research Phases

The research was broken down into five phases to help with better co-ordination of the action items in a clear and specific way. The phases are as follows:

Phase 1: Maximization of CNH production using the submerged arc in liquid nitrogen method

This required building a setup in the laboratory and improving on the yield of the synthesized CNH products as specified in patented literature by varying process conditions (e.g. time and current). Calculation of the yield of CNH produced and sample characterizations were done. The goal was to generate a substantial amount of CNH support material to cover the entire research work.

Phase 2: Functionalization of as-synthesized CNH using nitric acid

Nitric acid was used to functionalize the CNH generated from the arc discharge method. Functionalization was considered as a result of the inertness (lack of acid or basic properties) of CNH carbon material, and the importance of making the CNH material reactive for catalysts formulation and hydrotreating experiments. Effect of time on functionalization was tested and various techniques were used to characterize both pristine and functionalized samples. A hydrotreating experimental run was conducted and liquid products were analyzed.

Phase 3: Compare the effects of using different carbon-supported catalysts and gamma alumina catalyst on hydrotreating performance

Four carbon-supported catalysts were prepared, characterized and used for hydrotreating. A gamma-alumina catalyst was also prepared alongside and used for hydrotreating. The intent was to compare the activity of carbon-supported catalysts with the traditional Ni-Mo supported catalyst. All support materials were impregnated with the constant Ni and Mo compositions. Hydrotreated liquid samples were characterized.

Phase 4: Development of the best NiMo/OCP_f catalyst: effect of metal compositions on the catalyst

As synthesized OCP_f by-products from CNH synthesis were functionalized and used in making seven catalysts for hydrotreating. These OCP_f supported catalysts differed by the amount of Ni and Mo compositions used in impregnating the OCP_f support. These catalysts were further screened by running a series of hydrotreating test to ascertain the best catalyst. Both solid and liquid samples were characterized.

Phase 5: Development of the best NiMo/CNH catalyst

A combination of Ni and Mo compositions were used in formulating three CNH-supported catalysts and these catalysts were used in hydrotreating an untreated light gas oil. The catalyst that gave the best hydrotreating activities was further impregnated with a secondary promoter (phosphorus) to test the effects of this secondary promoter on hydrotreating performance. An experiment was designed to evaluate how pressure, temperature and liquid hourly space velocity (LHSV) affects the hydrotreating performance with the best catalyst. The liquid and solid samples were characterized. Mass transfer, kinetic and deactivation studies were also done using the best catalyst.

1.6 Organization of this thesis

This thesis document is made up of nine chapters, followed by a list of references and an appendix section. The thesis style is a “Manuscript-based Thesis Format” prescribed by the University of Saskatchewan. Chapters 1 to 3 begin with a sub-section which provides information about the contribution of the chapter towards the overall study. Chapter 1 is the introduction and includes thesis outline, knowledge-gaps, hypothesis and objectives concerning this research. Chapter 2 (literature review) summarizes information about hydrotreating, what constitute a catalyst and catalyst preparation methods (e.g. incipient wetness impregnation, co-impregnation) carbon, carbon production and functionalization options, hydrotreating operating conditions, some research studies and outcomes. The information provided in Chapter 2 therefore helps in defining the objectives and providing a better understanding about hydrotreating catalyst and processes. In Chapter 3 the techniques employed to characterize the supports (pristine and functionalized), catalysts, treated and untreated gas oil samples from the five phases of the research are presented. Additionally, the principles behind each characterization technique, some key information and sample analysis procedures are described in this chapter.

Chapters 4 to 8 are independently linked to each of the five phases of this research and since this is a paper-based thesis format, advanced notification is provided at the beginning of these chapters as to whether the content of the chapter has already been published and/or communicated in the form of oral or poster presentation to the scientific community. For the published chapters (Chapter 4 and 5) the full citation information is also shared. A completed manuscript on Chapter 6 has been sent to a scientific journal for review and publication.

Although Chapter 7 and 8 have not been published, the content of these chapters has been presented in a manuscript-style format with the intent of sending it to a suitable journal. Chapters 4-8 also contain two subsections which highlights the contribution of the Ph.D. candidate and other individuals to each respective phase, as well as the contribution of the chapter to the overall Ph.D. work. Thereafter, the remaining content of the chapters are apportioned in this order; abstract, introduction, experimental methods, characterization, results and discussion, conclusions and acknowledgement. Due to the likelihood of having certain similar characterizations running through each of the phases, the characterization part under Chapters 4-8 only mentions the technique but, refers to Chapter 3 where detailed or further information could be found to eliminate any repetition of techniques or wordings that could result in plagiarism.

Availability of enough CNH material for all experimental work relating to the entire research project was a necessity hence, the results of the study conducted to maximize CNH production by varying factors such as time, current settings and baffle type are discussed in Chapter 4. Chapter 5 focuses on the possibility of adding some functionality to the inert CNH material using nitric acid (HNO_3) treatment to alter its surface chemistry and enhance its properties for catalyst formulation and subsequent hydrotreating application. The catalyst support is a key component of the catalyst since amongst others, it controls; the way the active metals are dispersed on the support, the reducibility of the catalyst, the metal-support-interaction and their consequent effect on hydrotreating performance. Hence, chapter 6 presents a summary on how the different supported-catalysts impact HDN and HDS activities. The findings reported in Chapter 7, are based on investigations that were carried out to determine if the OCP_f by-product from CNH synthesis could be enhanced further by varying the compositions of Mo and Ni species on the support material. In Chapter 8, the variation of Ni compositions (2.5, 3.5, and 5.0 wt%) at a fixed Mo composition (19 wt%) were examined on the CNH support based on the screening work done with the OCP_f material. This chapter also contains information about the effects of a secondary promoter on hydrotreating activity and the design of experiment work that was done to optimize the hydrotreating operating conditions. Evaluation of mass transfer and estimation of kinetic parameters based on the power law model can be found in Chapter 8. Chapter 9 emphasizes on this research project overall findings and recommendations that could be beneficial in improving the entire work. Enlisted references plus supporting information relating to this research can be found under the Reference and Appendix part of the thesis.

1.7 Gas oil feedstocks

All hydrotreating experiments under phases 2-5 were carried out using light gas oil. A feasibility study with heavy gas oil (HGO) was also conducted using the best catalyst (3.5wt%Ni19wt%Mo/CNH), and the results are shown in Appendix H. Information about the feed characteristics of the gas oils used in this research are shown in Table 1.1.

Table 1.1 Feed characteristics of light and heavy gas oils.

Parameter	Light gas oil (LGO)	Heavy gas oil (HGO)
Sulfur content (ppm)	30000	43000
Nitrogen content (ppm)	1800	3900
Density (g/ml)	0.90	0.98
Aromatic content (%)	33.6	45.5
Simulated distillation		
IBP (°C)	159	208
FBP (°C)	502	625

1.8 The hydrotreating reactor

A schematic of the hydrotreater used in carrying out all hydrotreating experiments is shown in Figure 1.1. The setup consisted of a: 304 stainless steel tubular microreactor, twin-furnace system, temperature controller, mass flow meter and controller (Brooks Instrument) feed tank, high pressure metering pump (Eldex laboratories), high pressure gas-liquid separator, water scrubber, ¾ filled NaOH bottle, back pressure regulator and pressure relieve valve.

The micro-reactor was a trickle-bed reactor and therefore a three-phase chemical reactor in which the liquid and gas phase flow concurrently downward over a packed bed of catalyst. The processing method was continuous. The length and internal diameter of the microreactor were 240 mm and 14 mm, respectively. The microreactor was loaded with the catalyst bed prior to any experimental run. A schematic of the catalyst bed is shown in Figure 1.2. The temperature for the reaction was provided by a twin-furnace system shielding/encasing the reactor. A K-type stainless steel thermocouple fixed at the side of the furnace was used in taking temperature readings of the furnace. The average temperature of the catalyst bed inside the reactor was noted as the operating temperature, and the temperature controller was used in monitoring and maintaining the operating temperature.

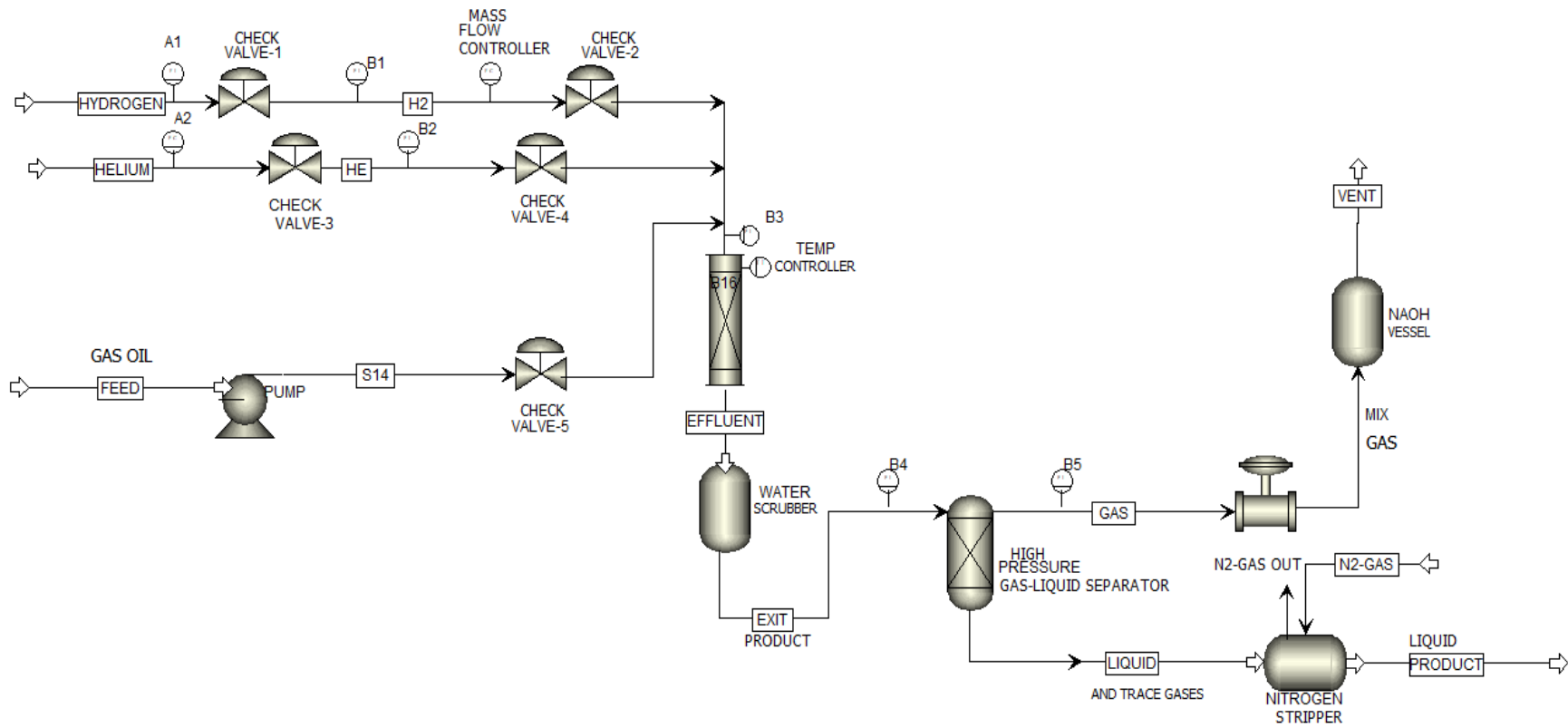


Figure 1.1 Schematic of the trickle bed hydrotreater used for hydrotreating gas oil.

The high-pressure metering pump was used in pumping the gas oil feed into the reactor, and the pump was closely monitored to ensure that it was in good working condition. Hydrogen flow rate for the reaction was regulated using the mass flow controller. Gas oil was fed into the reactor from a 1 litre feed tank through a metering pump with the aid of helium carrier gas running at low pressure (0.3 MPa). The feed tank was topped up twice within the course of an experimental run to ensure that there was constant flow of feed into the reactor. A weighing scale was also placed underneath the feed tank to aid with the measurements of the liquid volumetric flowrates as well as LHSV calculations. The scrubber was filled with approximately 50 ml of distilled water before pressurizing the system in order to, absorb ammonium salts resulting from denitrogenation reactions taking place in the reactor. This helps in preventing downstream lines from being blocked. High pressure gas-liquid separator enabled the separation of liquid products from gases. The back-pressure regulator was used to control and maintain the reactor operating pressure at the set point condition by, venting excess gases through NaOH contained in a bottle and filled to $\frac{3}{4}$ level. This procedure also absorbs H_2S in the exit gas stream before venting any excess hydrogen into the atmosphere. A pressure relief valve served as a safety measure to ensure that the pressure within the system was controlled without exceeding the set condition.

Loading of the reactor preceded any hydrotreating experiment once the reactor had been cleaned with Voltesso TM 35 oil (Marsollier Petroleum, Canada) or Hexane (Fisher Scientific, Canada) depending on the severity of the cleaning process. This procedure removes residual gas oil and dirt that could possibly lead to coke formation during, the catalyst pretreatment stage and running of the various hydrotreating experiments. For each hydrotreating experiment, the length of the catalyst bed loaded into/within the reactor was kept constant at about 10 cm to ensure that the bed was within the heating zone of the reactor and was supplied with/subjected with consistent heat from the reactor furnace system. The bottom part of the microreactor was closed with a 60-micron filter so that the catalyst bed stayed intact throughout the run. Following this, Loctite nickel anti-seize gel was applied around the bottom threads before, finally securing the filter by placing and tightening a 316-stainless steel VCR face seal fitting with reducing adapter body on top of the 60-micron filter. The closed reactor was mounted vertically on a clamp to facilitate loading and during loading, the reactor was slightly vibrated periodically to allow compact packing. Once loading was over, Loctite nickel anti-seize gel was applied to the top threads on the reactor before fitting a 60 micron Swagelok stainless steel ferrule and finally closing and tightening the top end

of the reactor with a 316-stainless steel VCR face seal fitting with reducing adapter body. The entire assembly was then placed and secured inside the reactor furnace. At this point, all joints connecting the lines within the reactor are tightened to make way for a leak test before the hydrotreating reaction begins.

Apart from the 60-micron filter, which ensured the powder catalyst was not washed off, the catalyst loading pattern in Figure 1.2 also helped to retain the powder catalyst sample in the reactor during the experiment. The loading pattern was done in such a way that the 10 cm catalyst bed consisted of ~ 5 ml (~ 2 g) of powdered catalyst mixed with equal ratios of ~ 12 ml of 90 mesh silicon carbide in 10-12 layers, and sandwiched between a set of different mesh sizes (16, 46, 60) of silicon carbide (SiC) (Ritchey Supply Ltd., Canada) and 3 mm glass bed. For the set of different mesh sizes and glass beads loaded at the top and bottom of the catalyst bed, the order in which they were loaded resulted in particle sizes consistently decreasing from the bottom of the reactor to the base of the catalyst bed, whereas a reverse order of loading was applied from the top of the catalyst bed to the top of the reactor.

The loading configuration and the use of inert silicon carbide particles helped in satisfying hydrodynamic conditions of the system by preventing channeling of fluids, eliminating wall effect, increasing liquid hold-up and improving catalyst wetting during the hydrotreating process. Negligible wall effect enhances the catalyst performance. An enhanced wetting effect resulted in better usage of catalyst. Liquid hold-up and higher catalyst wetting affected the performance of trickle bed reactor by preventing external effects that could affect the rates of reaction even at low liquid and gas flow rates. Axial dispersion or backmixing of liquid in microreactors was reduced when the catalyst bed was diluted with SiC and this leads to an achievement of plug flow behaviour. The presence of SiC in the reactor resulted in preheating and distribution of the feed before encountering the catalyst bed. The use of diluents also helps in maintaining a stable temperature across the catalyst bed which consequently improves the rate of heat transfer in the catalyst bed. A near trickle flow in the catalyst bed can be assumed based on this loading configuration as well. The variation in SiC particle size can therefore improve liquid hold-up and ensure that the reactants attained the set temperature before encountering the catalyst (Ramirez et al. 2004; Bej et al. 2001; Bej et al. 2000; Giermen, 1988; Mears, 1971).

For the leak test, the reactor was pressurized to about 9.3 - 9.7 MPa and then a short preliminary leak check was conducted by monitoring if a drop in pressure will occur within 10

min. Swagelok liquid detector in the form of Snoop solution (VWR, Canada) was used in identifying fittings with leak. Small leaks were identified and resolved after isolating the reactor system in sections and monitoring which pressure gauges registered a drop in pressure within 10 to 30 mins. After the possibility of any leak had been cleared, the reactor was pressurized again and left to stand for 24 hrs. At the end of this duration, once there was no leakage the backpressure regulator was adjusted to slowly reduce the system pressure to a desired operating pressure for the hydrotreating reaction.

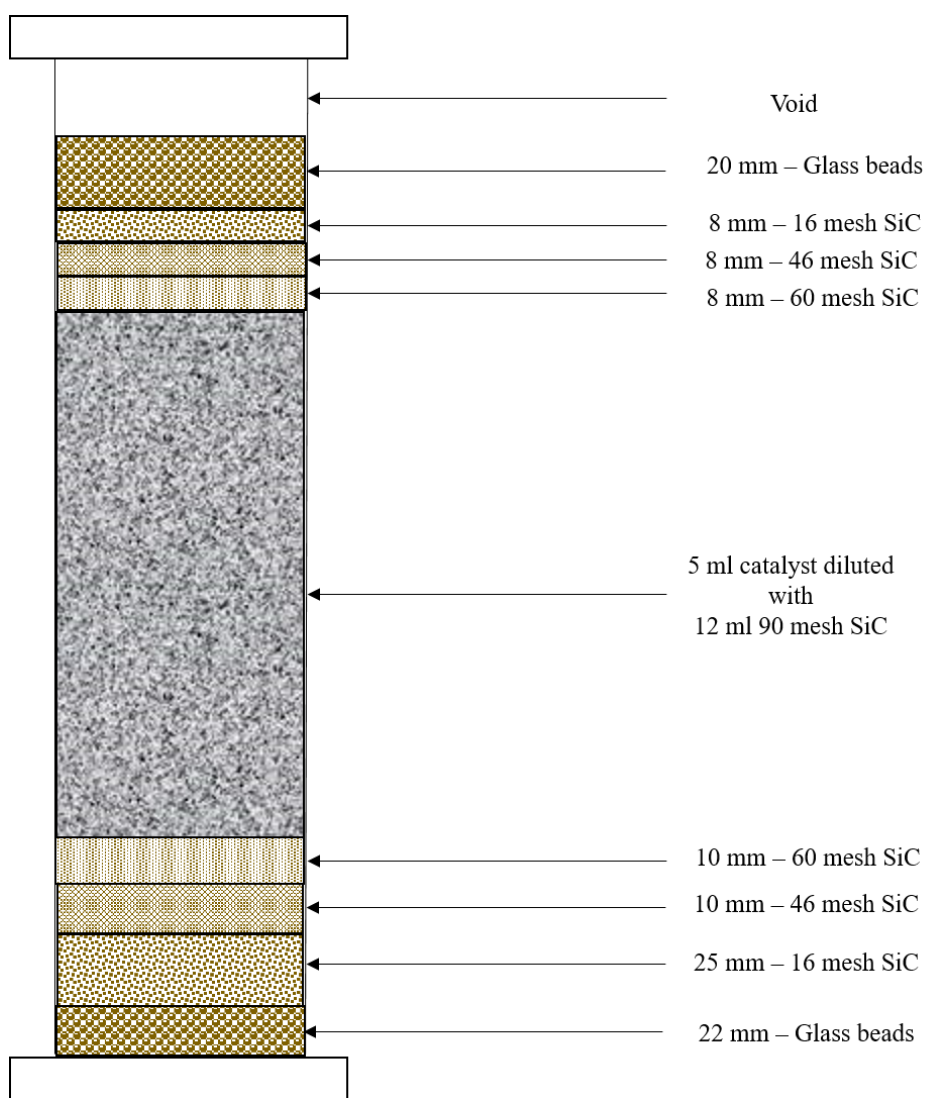


Figure 1.2 Schematic of the tubular microreactor showing the various loadings.

CHAPTER 2

Literature Review

Contribution of this chapter to the overall Ph.D. work

This chapter describes the hydrotreating process, hydrotreating catalyst, carbon allotropes, carbon nanohorns, carbon nanohorns production methods and functionalization of carbon materials, and enables readers to understand why certain directives were taken to accomplish the phases under this thesis based on what is known and what is being investigated.

2.1 Hydroprocessing

Crude oil hydroprocessing falls under two different categories i.e. hydrotreating and hydrocracking. Hydrotreating comprises of four main reactions namely, hydrodesulfurization (HDS), hydrodenitrogenation (HDN), hydrodemetallization (HDM) as well as hydrodeoxygenation (HDO). During hydrotreating, these reactions occur simultaneously after the feed has reacted with hydrogen under catalytic conditions. Normally, HDS specifically removes sulfur contaminants in the feedstock. In the case of HDN, HDM and HDO, nitrogen, metals and oxygen contaminants are specifically removed from the feedstock, respectively. The hydrotreating process also results in aromatics and olefins saturation present in the crude feed stock. Hydrogenation of aromatics or hydrodearomatization is also denoted as HDA. On the other hand, hydrocracking is a process whereby a catalyst is used to break down complex hydrocarbons into simpler ones at elevated hydrogen partial pressure (Jones 1995; Satterfield, 1991). Overall, the demand for crude oil from heavier fractions have been on the ascendency as a result of a general decline in light oil reserves and an increase in heavier oil reserves. A worldwide degradation in the quality of available petroleum feedstocks coupled with, stringent environmental regulations that are being enforced in many countries have also led to considerable efforts to develop a better catalyst for hydrotreating activities. Hydrotreating reactions are normally run at temperatures from 290 - 390 °C and pressures from 8.8-10MPa to attain ultra-low sulfur diesel (< 10 ppm) production. Process parameters, catalyst type and quality of feedstock are some of the factors that can affect the hydrotreating performance (Marafi et al. 2007; Rana et al. 2007).

2.2 Hydrotreating process variables

During hydrotreating, five main process variables that influence reaction conversion, selectivity, activity and stability of the catalyst are: hydrogen partial pressure, total pressure, reaction temperature, H₂ gas/oil ratio and the liquid hourly space velocity (LHSV). A hydrotreating reactor operating at high hydrogen partial pressures leads to longer catalyst life cycle, higher conversion, better distillate quality and ability to process heavier feeds. Hydrogen partial pressure is important during nitrogen removal since it influences the hydrogenation of aromatic ring structures that are rate limiting steps in nitrogen removal. It is therefore advisable to operate the hydrotreating reactor at a hydrogen partial pressure which is similar to what is recommended in its original design (Gruia, 2008; Mehra and Al-Abdulal, 2005; Stanislaus and Cooper, 1994). Since equipment limitations prohibit the operation of the reactor near the recommended design value, the best way the H₂ partial pressure can be increased is to raise the purity of the recycle gas by increasing the makeup H₂ purity, releasing gas from the high-pressure separator (HPS) or lowering the HPS temperature (Mapiour et al. 2010; Gruia, 2008). Removal of impurities are normally easier at high hydrogen partial pressures however, this condition is a major cost problem for refineries since it makes the reactor more expensive and increases hydrogen consumption. Hydrogen also helps to inhibit coke deposition on catalysts due to hydrogenation of coke precursor and removal of heteroatoms (Rana et al. 2007; Gruia, 2008).

The total pressure of a hydrotreating unit is dependent on the reactor design, and it is controlled with the back-pressure regulator at the exit of the high-pressure liquid separator. Both HDS and HDN conversions can be increased with high hydrogen pressures. High reactor pressure mitigates or prevents coke formation, thus a decrease in catalytic deactivation rate occurs, and the life cycle of the catalyst is also preserved. Under high operating pressures, conventional sulfided catalyst can be used to achieve aromatic saturation since, this condition is favorable for overcoming the thermodynamic limitation of aromatic saturation. On the other hand, use of excessive pressure can saturate the catalyst to an extent that any further increase in pressure would not have any positive effect on the activity. This implies that there are limitations on the pressure usage (Gruia, 2008; Mehra and Al-Abdulal, 2005; Speight, 2000; Stanislaus and Cooper, 1994). The lifetime of a catalyst and the type of compounds removed from the feedstock during hydrotreating are dependent on temperature. A temperature surge during hydrotreating usually cause an increase in reaction rates and the rate at which impurities are removed from the feedstock.

Increasing temperature therefore enhances hydrotreating kinetics. Conversion can be improved with temperature because of the Type II Co-Mo-S or Ni-Mo-S structures which are formed with temperature increase. Hydrogenation reaction usually increases with increasing temperature. Since most hydrotreating reactions are exothermic in nature, there is a limit to the maximum allowable operation temperature in order to prevent thermal cracking. The ability to form coke also increases with increasing temperature and consequently leads to a reduction in active catalyst sites. In the event of catalyst deactivation, it is generally common to preserve the quality of the product and compensate for catalyst deactivation by increasing the temperature (Candia et al. 1984; Speight, 2000). Increase in H₂ gas/oil ratio promotes conversion and removal of impurities since it ensures that the hydrogen, catalyst and feed are in maximum physical contact. Coke deposition is also minimized with increase in H₂ gas/oil ratio, and by so doing the rate of catalyst deactivation minimizes as well. An increase in the H₂ gas/oil ratio controls the temperature rise during reactions by increasingly removing heat as reaction proceeds. The H₂ gas/oil ratio aids in stripping off volatile products from the reactant liquid feed, and therefore the concentrations of these components are affected in the liquid reactive phase. In hydrotreating, space velocity is termed as LHSV and it is inversely proportional to the residence or contact time. This implies that an increase in LHSV results in less contact time and low conversion of a reaction. Higher degree of saturation also accompanies longer contact times (Stanislaus, 2010; Ancheyta and Speight, 2007; Robinson and Dolbear, 2007; Satterfield, 1991; Aeres, 1980).

2.3 Reactivity of sulfur compounds in feedstock

Sulfur removal or hydrodesulfurization (HDS) is a type of hydrotreating reaction that removes organic sulfur compounds in feedstock by converting them to hydrogen sulfide (H₂S). The intermediate olefins that are formed are also saturated. These organic sulfur compounds exist in different boiling range of petroleum fractions and can be categorized into 6 (six) sulfur compounds i.e. mercaptans, sulfides, di-sulfides, thiophenes, benzothiophenes and dibenzothiophenes. Figure 2.1 shows examples of some simplified HDS reaction schemes. These reactions are easier as compared to HDS reactions involving sulfur compounds which are very hard to desulfurize. Dealing with such complex compounds during hydrotreating poses a challenge when the aim is to reach ultra low-level diesel fuels. Higher molecular weight dibenzothiophenes (i.e. 4, 6-dimethyl dibenzothiophene (4, 6-DMDBT) and 4-methyl dibenzothiophene (4-MDBT))

that contain side chains that are close in proximity to the sulfur atom are examples of such difficult compounds.

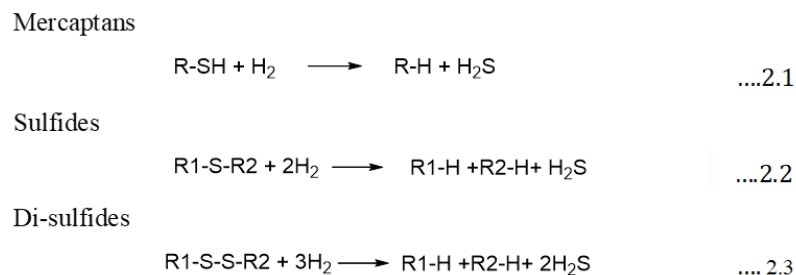
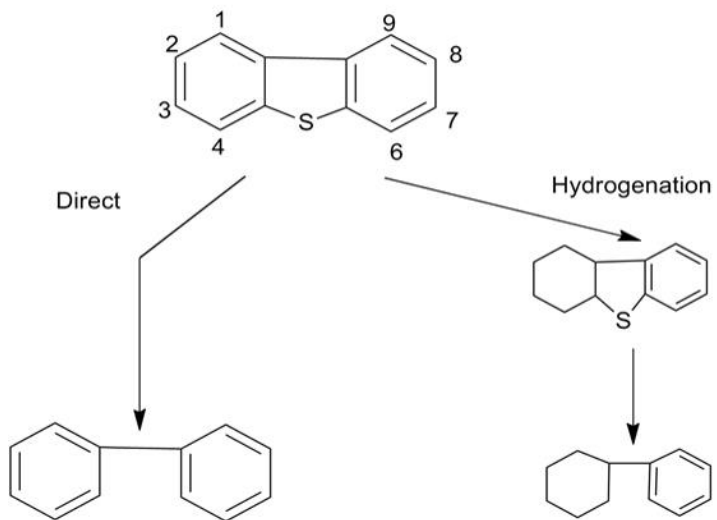


Figure 2.1 General reactions of some sulfur compounds in feedstock (Adapted from Guria, 2008).

These sulfur compounds with higher molecular weight are considered as refractory sulfur compounds and consist of aromatic sulfur species. Their level of reactivity was found to be dependent on their steric hindrance. HDS of thiophenic compounds takes place by two main pathways which include; ring opening to remove sulfur and then saturation of the olefin that occurs. Thus, from Figure 2.2, sulfur removal from alkylated dibenzothiophenes and dibenzothiophene can be achieved through two possible pathways. For the first pathway sulfur atom is directly extracted (hydrogenolysis) from the molecule whereas, in the second pathway one atomic ring must be prehydrogenated before the sulfur atom can be extracted. The ease of sulfur removal from a feedstock is therefore dependent on type of sulfur present in the hydrocarbon fraction (Deliyanni et al. 2009; Gruia, 2008; Knudsen et al. 1999; Girgis and Gates, 1991).



....2.4

Figure 2.2 HDS of DBT showing two reaction pathways (Adapted from Knudsen et al. 1999).

2.4 Reactivity of nitrogen compounds in feedstock

Nitrogen removal by hydrodenitrogenation (HDN) is a hydrotreating reaction that removes organic nitrogen compounds by converting them to ammonia. Nitrogen compounds are present in five- and six-member rings and are made of complex molecules. Their quantity increases as the boiling range increases and they are very difficult to remove due to their complexity. HDN reactions are more complicated than HDS reactions hence, it is important to hydrogenate the numerous heterocyclic aromatic molecules with strong C-N bonds to, transform them into weaker aliphatic C-N bonds before nitrogen can be removed. Besides nucleophilic substitution, nitrogen extraction from the intermediate alkylamines arises as a result of Hofmann β -H elimination. Higher temperatures and pressures are required for HDN reactions as compared to HDS reactions and more hydrogen are consumed during nitrogen removal. In addition, the strongest inhibitors to HDS reactions are ascribed to basic organo-nitrogen compounds that are present in the crude feedstock. Removal of nitrogen is therefore essential during hydrotreating to achieve an efficient HDS process. Figure 2.3 shows some typical examples of reactions involving nitrogen compounds in heavier crude fractions. Figure 2.4 shows a demonstration of the nitrogen removal mechanism (Prado et al. 2017; Gruia, 2008; Prins et al. 2006; Nelson and Levy, 1979).

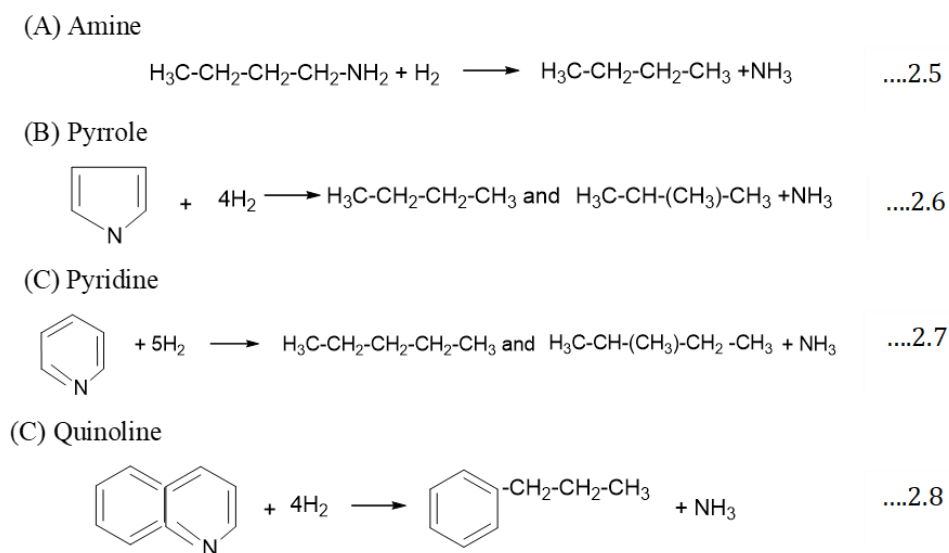


Figure 2.3 Nitrogen reactions in feedstock (Adapted from Gruia, 2008).

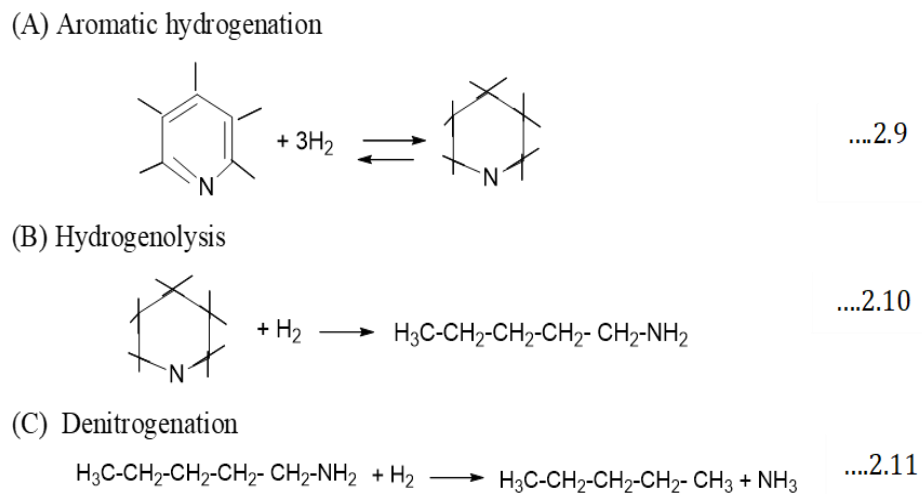


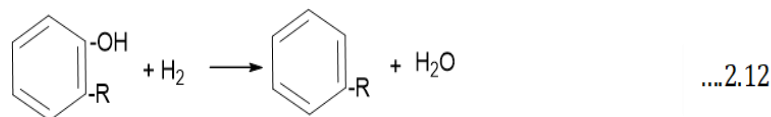
Figure 2.4 Nitrogen removal mechanism (Adapted from Gruia, 2008).

2.5 Reactivity of oxygen compounds in feedstock

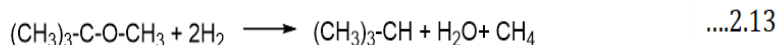
The quantity of oxygen in majority of crude feedstock is low. Hydrogenation of oxygen-containing compounds present in crude oil produces hydrocarbon and water. The severity of hydrogenating oxygen containing compounds is high with higher molecular weight compounds

like furans than with lower molecular compounds (Gruia, 2008; Girgis and Gates, 1991). Figure 2.5 shows examples of de-oxygenation reactions in hydrotreating.

(A) Phenols



(B) Oxygenates



(C) Napthenic Acids

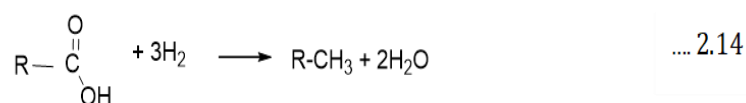


Figure 2.5 De-oxygenation reaction during hydrotreating of feedstock (Adapted from Gruia, 2008).

2.6 Olefins saturation

Olefins occur when the petroleum fractions are processed in catalytic or thermal units. Thus, olefins are commonly found in feedstocks obtained from thermal cracking operations like ethylene production and coking. Prior to hydrotreating, it is advisable to prevent petroleum fractions containing olefins from being in contact with oxygen in order to avoid the occurrence of polymer gums. Olefins saturation involves the hydrogenation of unsaturated products to form more stable hydrocarbons. Olefins saturation reactions are highly exothermic and very fast hence, they must be handled with care to prevent extreme coking that can result in a build up of pressure drop and/or maldistribution of liquid feed through the catalyst bed. Figure 2.6 highlights some examples of olefin saturation (Ancheyta and Speight, 2007; Gruia, 2008).

(A) Hexene



(B) Cyclohexene



Figure 2.6 Olefin saturation in hydroprocessing (Adapted from Gruia, 2008).

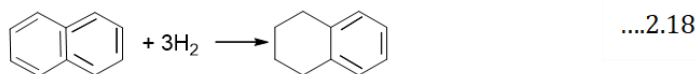
2.7 Aromatic saturation

Aromatic saturation or hydrodearomatization (HDA) is important in hydroprocessing since, it enhances fuel quality and reduces the creation of unwanted emissions in exhaust gases. Aromatics present in middle distillates and high boiling petroleum fractions usually consist of four groups i.e. monoaromatics, diaromatics, triaromatics and polycyclic aromatics depending on how many (1, 2, 3, ≥ 4) aromatic rings are present. The polycyclic aromatics have at least four benzene rings and are mostly present in high boiling petroleum fractions. Maximum aromatic saturation occurs within temperatures of 320 – 360 °C. To achieve complete aromatic saturation more severe process conditions than normal hydrotreating conditions are applied. Saturation of polycyclic aromatics takes place by a stepwise mechanism. Examples of some aromatic saturation reactions are shown in Figure 2.7 (Gruia, 2008; Stanislaus and Cooper, 1994).

(A) One ring – Toluene



(B) Two ring –Naphthalene



(C) Three ring- Phenanthrene

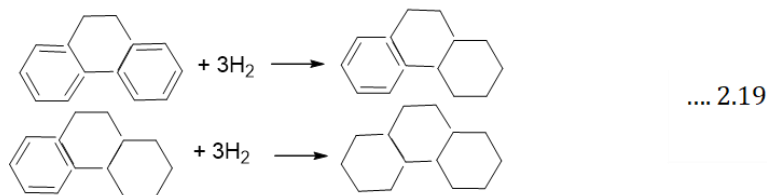
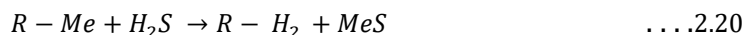


Figure 2.7 Aromatic saturation in hydroprocessing (Adapted from Gruia, 2008).

2.8 Metals removal in feedstocks

In hydrotreating, hydrodemetallization or HDM reactions that takes place are aimed at removing metals in heavy boiling fractions of crude. The predominant metal contaminants in heavy crudes are vanadium (V) and nickel (Ni) however, other metal contaminants that are present include copper (Cu), iron (Fe), arsenic (As), zinc (Zn) and sodium (Na). These metals exist in the form of salts or organo-metallic compounds. During hydrotreating, these metals settle on the catalyst as metal sulfides (Ni_3S_2 , V_3S_2 , V_3S_4) and block the pores due to their large size.

The effect of this pore mouth blockage of the catalyst include; reduced number of active catalytic sites, drastic decrease of catalyst hydrogenation activity and inability to access reactant molecules. Metallic contaminants in the crude, therefore, causes catalyst fouling and poisoning. Deactivation by metal deposits are not reversible unlike, the reversible catalyst deactivation by coke during catalyst regeneration. Liquid products get contaminated by metals as well resulting to a deterioration in their physical properties. Additionally, the presence of these metal contaminants leads to extreme coke and gas formation. Ni, V, and Na have been known to cause extensive corrosive damage to hydroprocessing units, boilers and furnaces. These metal particles also pollute the environment since they contribute to particulates emission and exist in the submicron size range. Removal of V from the crude oil has an impact on environmental pollution control since this reduces the occurrence of acid rain. Arsenic and mercury are the primary contaminants in naphtha and condensates, respectively. Arsenic and mercury contaminants easily form alloy (e.g. aluminum alloy) with active metals and creates an inactive catalyst surface. Thereby, this causes a reduction in the effective surface area for reactivity. Other problems posed by Hg in the refinery include, toxic waste generation, corrosion of equipment's, health impacts, catalyst poisoning and reduced catalyst life. The decomposition reaction to form metal sulfides is shown below. (Abbas et al. 2010; Maity et al. 2013; Elliot, 1996; Guria, 2008; Wilhelm, 2001).



2.9 Inhibitors to hydrotreating reactions

Hydrogen sulfide (H₂S) is a common inhibitor in HDS process. H₂S produced during HDS compete for similar catalytic active sites during the catalytic removal of sulfur in feedstock. Elimination of H₂S as an inhibitor is inevitable since it is a key by-product in hydrotreating. Difficulties in hydrotreating also occurs as a result of inhibition effect of nitrogen-containing compounds on HDS. Egorova and Prins, 2004 noted that nitrogen and sulfur containing molecules have similar hydrogenation sites, but nitrogen-containing compounds strongly suppress the hydrogenation of sulfur containing compounds (Yoshimuru et al. 2004; Egorova and Prins 2004).

2.10 Hydrotreating catalyst

A hydrotreating catalyst consists of transition metals like Mo and W dispersed on a support and promoted by Co and Ni. These promoters enhance the activity of the hydrotreating catalyst and provide a synergetic effect on the metals. At specified conditions, the catalyst's activity for a reaction is defined in terms of the rate of reaction over the catalyst. The catalyst with a higher activity therefore shows higher rate of reaction at the given conditions. Chemisorption is a factor that influences the catalyst activity because, for the catalyst to be active the adsorption of reactants on the catalyst surface should not be too weak or strong. Activity can also be defined in terms of an achievement in the conversion of a reactant. This implies that at specified conditions the higher the conversions, the higher the activity of the catalyst for that reaction. For metal-supported catalysts activity is usually defined in terms of metal sites since the metal sites are the active sites for chemical reactions. As a result, the activity is mostly expressed in terms of turnover frequency (TOF). TOF can be expressed at the number of molecules reacting per active sites per second. Reaction increases with increasing activity since, the activity of a catalyst is its tendency to increase the rate of a reaction (Fogler, 2006; Satterfield, 1991).

Table 2.1 shows general physical properties of hydrotreating catalysts. (Zhu et al. 2016; Robinson and Dolbear 2007; Chianelli et al. 1994). A plethora of research uses transition metals sulfides (TMS) from group VIII elements of the periodic table to prepare hydrotreating catalysts. Additionally, MoS₂ or WS₂ is a common TMS used in hydroprocessing and there is a surge in their use since, extremely high intrinsic activity for HDS of organic sulfides can be achieved with them. Use of TMS catalysts in hydroprocessing is also advantageous because, they are more resistant to catalyst poisoning and carbon deposition than other metals outside the TMS group. Common catalytically driven TMS reactions include (HDS), (HDN) hydrodemetallization (HDM), dealkylation, as well as ketones, olefins and aromatics hydrogenation (Chianelli et al. 2002; Chianelli et al. 1994).

Table 2.1 A hydrotreating catalysts typical physical properties (Adapted from Robinson and Dolbear, 2006).

Property	Low	High
Surface area, m ² /g	150	250
Pore volume, mL/g	0.5	1.0
Pore diameter (Average), nm	7.5	25
Bulk density, kg/m ³	480	960
Co or Ni (as CoO or NiO), wt%	3	8
Mo or W (as MoO ₃ or WO ₃), wt%	10	30

In general, TSM catalysts are made by decomposition of a sulfur-containing precursor or by direct sulfidation of the metal salt (e.g. oxide). Ni and Co promoted MoS₂/Al₂O₃ are frequently used as industrial catalyst for HDN and HDS reactions. NiMo catalysts are selective for nitrogen removal whereas, CoMo catalyst are selective for sulfur removal. (Zhang et al. 1998). The major problem with heterogenous catalysts is the decrease in catalysts activity with time. Recent approaches for attaining deep hydrodesulfurization (HDS) in hydrotreating include; single stage hydrotreating of light gas oils with highly active HDS catalysts such as NEBULA and CENTINEL (Eijsbouts et al. 2007; Plantenga et al. 2002) or a two-stage integrated hydrotreating approach whereby, in the first stage a traditional NiMo or CoMo sulfide catalysts is utilized and then for the second stage use is made of a noble metal catalyst with sulfur-tolerance. The draw back to the addition of second reactor is that it leads to high cost of equipments and complicated operational problems (Yoshimura et al. 2004).

2.11 Catalyst life cycle during hydrotreating

During hydrotreating, the life cycle of Ni-Mo (Co-Mo) catalyst supported on the traditional Al₂O₃ support varies by changes in structure and the way the active phase is dispersed. The various transformations are shown in Figure 2.8. As can be seen in step (a), the oxidic catalyst consist of oxidic Mo and Ni species that are bound to Al₂O₃. The oxide catalyst must be sulfided in order to make it active for hydrotreating. Sulfidation of this catalyst takes place in stages and proceeds with sulfidation of the Ni species. Therefore, in step (b) the sulfided Ni species is no longer bound to the Al₂O₃ support, and the oxide catalyst is partially sulfided due to the link between Al₂O₃ and Mo oxysulfide. As sulfidation continues in step (c), the catalyst is still partially sulfided and therefore, part of the Mo species become sulfided whereas the non sulfided Mo species still

remains bound to the support. In step (d) the oxide catalysts remain in its partial sulfided state and as a result some slabs of MoS₂ that appear with Ni decoration remains attached to Al₂O₃.

The sulfided catalyst in its partial state becomes completely sulfided in step (e) and because of the occurrence of fully sulfide species of Mo at this point, the slabs of MoS₂ with sulfidic Ni decoration attain mobility. In the process of catalyst deactivation, i.e. step (f) small slabs of MoS₂ with sulfidic Ni decoration gets sintered into large slabs, stacks and crystals. Also, formation of separate Ni sulfide crystals occur since the crystal surface is not large enough to accommodate all Ni species. Regeneration of the deactivated catalyst as in step (g) causes part of the MoS₂ crystals decorated with Ni sulfide crystals to be partially redispersed. Step (h) illustrates that in regeneration Ni (Co) do not redisperse on oxidation but, only large MoS₂ crystals becomes oxidized on the surface. Small structures in the catalyst are however, oxidized completely during regeneration and return to their initial state in step (i). Rapid and complete sulfidation of Mo occurs under high sulfidation temperatures like step (j) and therefore does not involve the intermediate steps. Addition of a chelating agent such as NTA in step (k) forms –Ni-Mo-NTA complexes that are fully sulfided and have no linkages with the support (Eijsbouts, 1997).

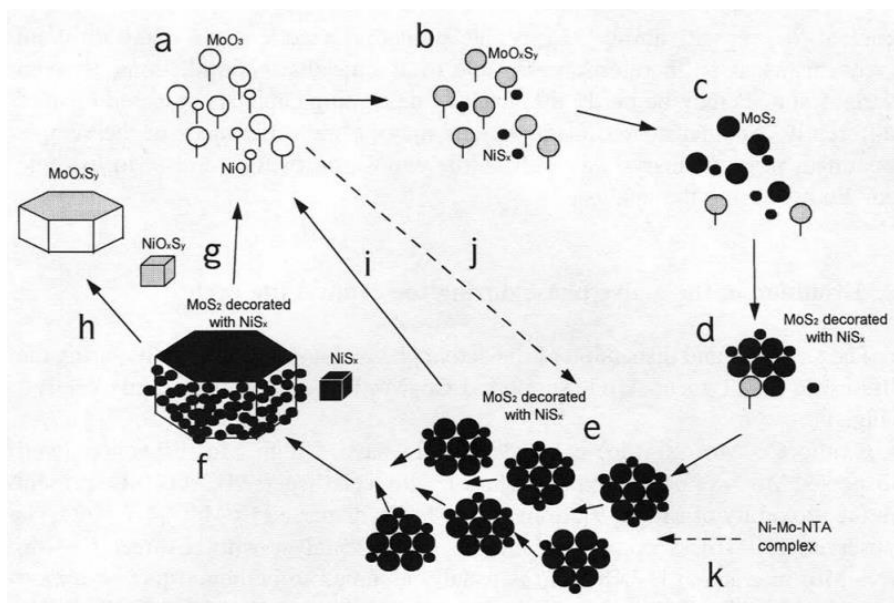


Figure 2.8 Life cycle of NiMo/Al₂O₃ catalyst during hydrotreating (Eijsbouts, 1997).

2.12 Effect of secondary promoters on HDS and HDN

Secondary promoters such as phosphorous, fluorine and boron are incorporated into the synthesis of a hydrotreating catalyst to enhance the acidity of the catalysts. Addition of boron likely changes the strength and type of alumina acidity. Based on co-precipitation, some Al atoms may be substituted by Boron to form B^{3+} , and both Lewis plus Bronsted acidic sites are possibly formed when H_2O is also present. This implies that increasing boron content subsequently enhances the quantity of acid sites. Furthermore, HDS and HDN catalytic activities also increases since, increase in $NiMo/Al_2O_3$ catalysts acidities facilitates C-S or C-N bond scissions of nitrogen and sulfur species in the feedstock. On the contrary, other researches have shown that addition of boron has a detrimental effect on HDS and HDN activities (Yao, et al. 2012; Ding et al. 2007; Perot, 2003; Delmastro et al. 1992). Usman *et al.* (2007) found out that catalyst performance is improved after boron addition since, it results in the weakening of surface interactions that exist between the Al_2O_3 support and molybdenum oxides. In so doing, the type of acid sites changes from a less type I Co-Mo-S active phase to a more type II Co-Mo-S active phase.

Although there are controversial studies as to whether addition of phosphorus to $NiMo/\gamma-Al_2O_3$ catalyst have a promotional or detrimental effect on HDS and HDN activities, Sigurdson *et al.* (2008) discovered an increase in sulfur and nitrogen conversion as phosphorus content was raised from 0.5 to 2.0 wt%. An enhancement in HDN and HDS activities at these phosphorus concentrations was attributed to higher metals dispersion on the surface of the catalyst. Moreover, upon phosphorus addition available metal sulfides clusters that could have been formed on the catalyst surface and restricted accessibility to active sites are eliminated. With higher dispersion more transition metals appear on the catalyst surface and therefore increases the amount of accessible sulfided active metal sites for molecules in the feed. Additionally, the work by Sigurdson *et al.* (2008) showed that conversions were higher for HDN activities than HDS activities as a result of the rate determining step and mechanism of the simultaneous HDS and HDN reactions. Since the C-N bond breaking step appears to be the slowest in the HDN reaction, it was noted that addition of phosphorous facilitated the breaking of C-N bond (rate determining step) due to the formation of new Bronsted acid sites (from Drift spectroscopy analysis) that subsequently increased the HDN activity. Alternatively, the minimal increase in HDS activity after phosphorous addition could be ascribed to the fact that C-S bonds are not the rate limiting step because, they mainly originated from organic sulfur compounds that are less weak compared to

bonds involving C-N. Meanwhile, the rate limiting step for HDS hydrogenation takes place on metal sulfide species with sulfur vacancies (Sigurdson et al. 2008; Yang and Satterfield, 1983).

Molecular-level research work to ascertain the effect of promoters in hydrotreating suggest that, there is a correlation between the structure of a promoted catalyst and its catalytic functionality. In general, for the well known “Co-Mo-S” or “Ni-Mo-S” phase, its hydrotreating activity is dependent on MoS₂ nanoparticles edges while, its promotional effect is linked to the presence of Ni or Co atoms that are at the edges of MoS₂-like structures in these aforementioned phases. The Co-Mo-S structure is also referred to as a Type I phase if it is made up of single-layer MoS₂ nanoparticles. On the other hand, it is called a Type II phase if it consists of multi-layer MoS₂ nanoparticles. The Type II phase is normally more active than the type I phase (Topsoe et al. 1981). Certain model studies show that an un-promoted MoS₂ nanoparticle is in the form of a triangular shape and terminated with (100) Mo-edge termination however, in a sulfided state the presence of Co and Ni improves the stability of hexagonally shaped MoS₂ nanocrystals by preferably attaching to lower indexed (-100) S-edge termination of MoS₂ nanocrystals (Zhu et al. 2016).

2.13 The role of the catalyst support

The ultimate purpose of the support is to disperse and maintain the active catalyst metals in a stable state, and consequently the benefits of an enhanced dispersion is that, catalytic activities are improved due to the tendency to maximize the degree of exposure of the catalytic active sites to reactants. Furthermore, the activity of the catalyst can be influenced by the support material as a result of the interaction between the support and active sites (metal catalyst). This interaction effects are in two parts; electronic and geometric effects. In terms of the electronic effects, the support material modifies the catalyst particles electronic characteristics and thereby affect the reactivity of active sites available on the surface of the catalyst. On the other hand, the geometric effect causes a modification of the catalyst particles shape by the support material. Both (electronic and geometric) effects likely changes catalytic sites activities on the metal surface and results in the modification of available number of active sites. Another benefit of using a support is that during catalyst preparation, the overall cost of the catalyst is reduced by diluting the active metals and promoters with the support that results in enormous cost saving venture for catalyst manufacturers (Antolini, 2009; Satterfield 1991).

Despite the successful commercial use of the traditional catalyst (cobalt or nickel promoted with molybdenum or tungsten on alumina support) some challenges encountered with this catalyst are difficulties in sulfurization and strong interaction effect between the active species and support material. Use of alternate supports such as carbon (especially activated carbon), zirconia, titania, and silica have stimulated research interest over the years. The type of support used is important since catalytic activity could be affected depending on the interaction existing between the active phase and the support. Desirable characteristics of a selected support include; inertness, high mechanical properties, stability under reaction and regeneration conditions, high textural properties and its chemical nature. Carbon has been found to be a good replacement for conventional alumina since studies involving carbon supported Mo, CoMo, or NiMo catalyst had shown excellent HDS activity in comparison with the metal or metal compounds on alumina. Carbon supports has been known to provide good catalytic performance in industrial processes (Shu and Oyama, 2005; Rodriguex-Reinoso, 1998). Additionally, use of carbon in place of alumina has led to lower coke deposition, and an ease in recovering the carbon from the spent catalysts by burning off the carbonaceous support. Another advantage of using carbon materials as support is that, carbon materials can be used under high pressure conditions with no damages. Due to this, porosity loss and the consequent negative effect on adsorption performance are not an issue when carbon is used under high pressure conditions (Casco et al. 2015). The use of nanomaterials such as carbon nanohorns (CNH) and carbon nanotubes (CNT) in research has soared over the years due to their remarkable properties (e.g. physical, chemical, mechanical, thermal, electrical or optical) which makes them available for use in numerous applications like drug delivery, hydrogen storage, and fuel cell (Shang et al. 2007; Rodriguex-Reinoso, 1998).

In an HDS study done by Lee *et al.* (2003) they discovered that use of a new type of nanoporous carbon that had large mesoporosity and surface area enhanced the overall activity of CoMoS catalyst as compared with activated carbon and alumina. Out of the three support types it was discovered that although the surface area of activated carbon was the largest, there was a drastic reduction its surface area after metal loading. For the nanoporous carbon and alumina, their surface areas were almost preserved once metal loading was done. The intrinsic activity of the catalyst on activated carbon support was also low compared with the intrinsic activity when nanoporous carbon and alumina were used as support. This may be due to the limitation of reactants to diffuse into the catalyst pores. Results from their studies therefore showed that using

nanoporous carbon as a support has promising effect in HDS studies as a result of its high mesoporosity and large surface area. Besides large surface area, a high mesoporosity is also advantageous in dispersing the metal catalyst on the support during catalyst preparation as this prevents significant pore blocking (Lee et al. 2003). It has been realized that the alumina support cannot be termed inert since the Ni and Co promoter ions occupy octahedral and tetrahedral sites in the outer layers of the support after reaction. In addition, Ni (Al_2O_4) and Co (Al_2O_4) could be formed based on the conditions under which the catalyst was prepared (Breysse et al. 2003).

2.14 Catalyst preparation

The supported metal catalyst used in hydrotreating or hydrocracking can be prepared using two main methods i.e. precipitation and impregnation. For the precipitation method, at least two solutions are combined and form the solid product after filtration, washing, drying, and forming. The formed precursor catalyst is further activated via physical (e.g. heating via calcination) and chemical (e.g. reduction of metallic catalysts) means. On the other hand, impregnation is the commonly used method for catalyst preparation. In this method, the active metals are distributed within a porous catalyst support after contacting the support with an aqueous solution containing at least one active metal of choice. The procedure is mainly dependent on the suck up of aqueous solution onto the porous catalyst by capillary action. After impregnation the catalyst is dried and activated just like the precipitation method. Impregnation can be divided into two types that is wet impregnation and dry or incipient wetness impregnation method. For wet impregnation, the support is contacted with excess aqueous solution such that the uptake by capillary action comprises of uptake from the sum of solution clogged in the pores and the solution adsorbed on the pore surfaces. This procedure ensures that pores are fully saturated. The incipient wetness impregnation method, which is typically used in industries involves contacting the support with aqueous solution of concentrations equivalent to the exact pore volume of support or less. The support is therefore left in a just dry state (Robinson and Dolbear, 2007; Satterfield, 1991).

2.15 Carbon and its allotropes

Carbon exists in distinct crystalline and molecular forms known as allotropes. Carbon allotropes have specific properties that stems from their unique structures. The most common carbon allotropes are diamond (sp^3 hybridized carbon atoms), graphite (sp^2 hybridized carbon

atoms), amorphous carbon and fullerenes (e.g. buckyballs, ellipsoidal fullerenes, carbon nanotubes (sp^2 bonds)) and though they both have the same carbon chemistry they differ in structure and properties. As an example, diamond is the hardest material that is well known whereas, graphite is very soft. CNH falls under fullerenes. Figure 2.9 shows examples of some carbon allotropes (Georgakalis et al. 2015; Ren et al. 2012; Bera et al. 2006; Robertson and O'Reilly, 1987).

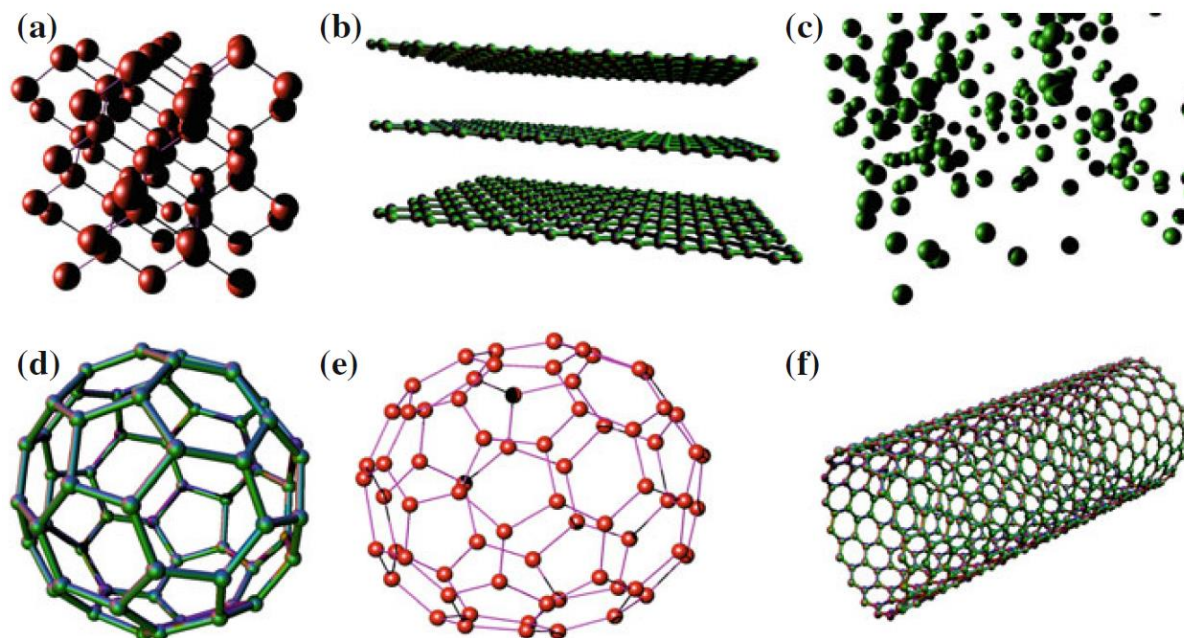


Figure 2.9 Examples of carbon allotropes a) Diamond, b) Graphite, c) Amorphous carbon d) Spherical fullerene, C_{60} e) Ellipsoidal fullerene, C_{70} and f) Tubular fullerene, SWCNT (Ren et al. 2012).

2.16 Carbon nanohorns (CNH)

CNH is composed of horn-shaped sheath of approximately 30-50 nm in length and 2-5 nm in diameter that groups together (about 2000 horns) to form a spherical aggregate that is 80-100 nm in diameter. CNH consists of both mesopores and micropores. Carbon nanohorns exist in two main forms i.e. dahlia-like and bud-like CNH. For the dahlia type CNH, the horns protrude out to the surface of its aggregated spherical structure whereas, for bud-like nanohorns the horns are present within its aggregated spherical structure. CNH appears as single walled carbon nanohorns unlike, CNT that can be in the form of either single-walled or double-walled CNT (Azami et al. 2008; Bandow et al. 2000; Iijima et al. 1999). A TEM image of the CNH produced by Iijima *et al.*

(1999) is shown in Figure 2.10a. Figure 2.10 b shows a conceptual diagram of a CNH agglomerate by Fan *et al.* (2007). Each of CNH horn-shaped sheath comprises of a cone angle of approximately 20° which is equivalent to five pentagonal rings at its tip. The sharper the opening angle, the greater the number of pentagonal rings. Thus 113° , 84° , 60° , and 39° corresponds to one, two, three and four pentagonal rings as shown in Figure 2.11 (Treacy and Kilian, 2001; Ebbesen, 1998).

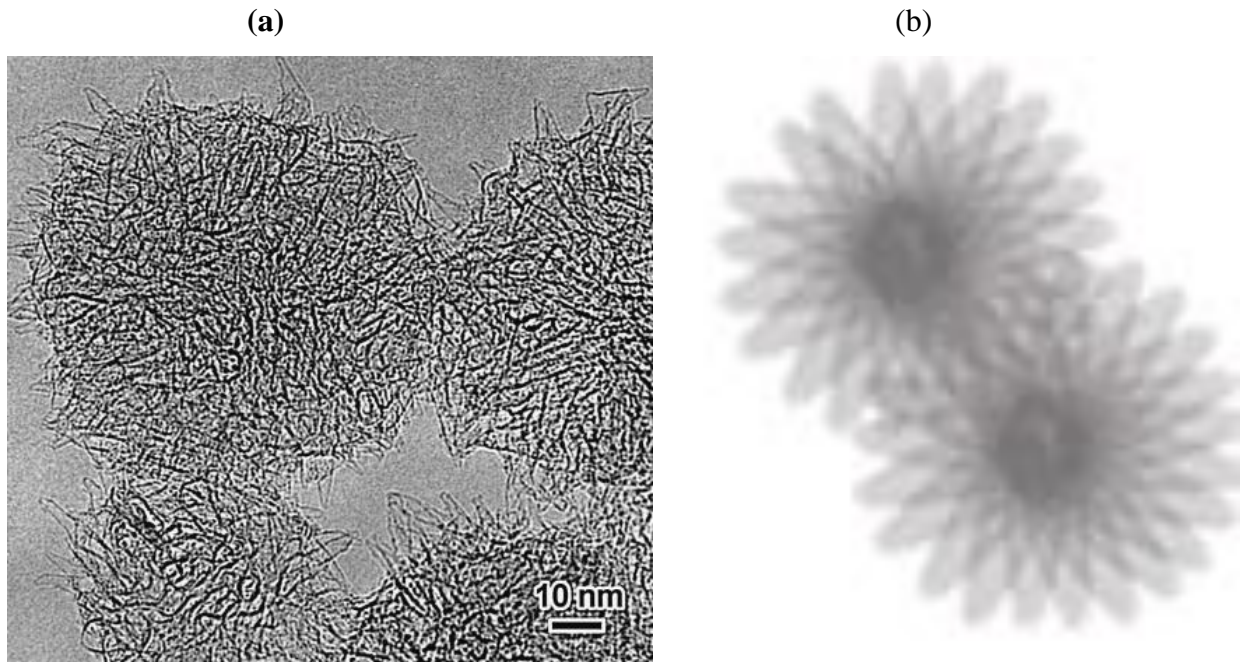


Figure 2.10 a) TEM image of the CNH, b) conceptual image of CNH (Iijima et al.1999; Fan et al. 2007).

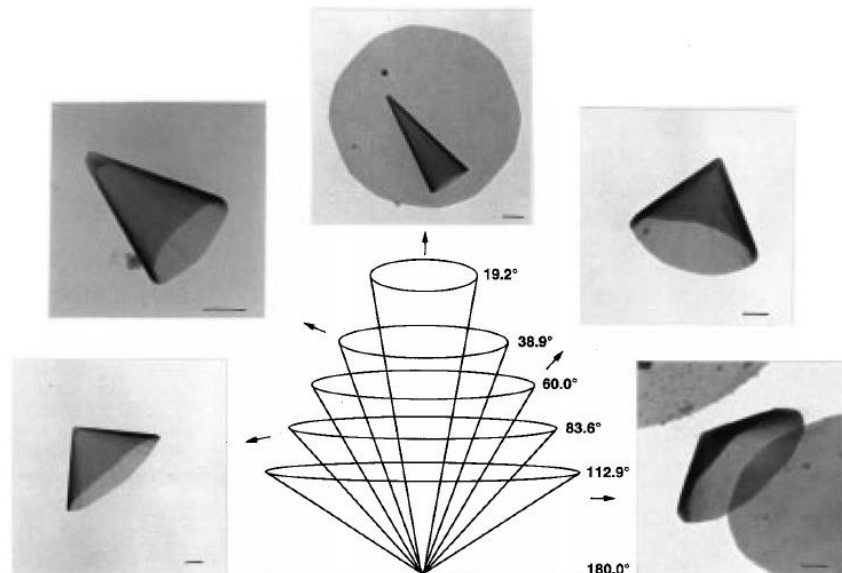


Figure 2.11 Five possibilities of graphitic cones and experimental representation (Krishnan et al. 1997; Ebbesen 1998).

2.17 Application of CNH

CNH is used for drug delivery purposes due to its shape (shell structure). As such their large surface area and numerous horn interstices enhances the adsorption of guest molecules on them. Additionally, the robust-spherical CNH aggregated size is beneficial since, it makes way for enhanced permeability and retention (EPR) effect. This implies that after CNH had permeated through damaged tumour tissue vessels, they stay intact due to limited lymphatic drainage. The 2-5 nm diameter of CNH horn is also suitable for slow release and incorporation of materials and drugs. During drug delivery, slow release is important because it reduces the amount of drug that could be lost before hitting its target (Aijima et al. 2005). The high specific surface areas of CNH material make them novel candidate for gas (methane) storage purposes and energy saving devices. In fuel cells application CNH is used as a support material for catalysts (e.g. Pt). Good composite materials can also be made using CNH as a result of its high conductivity and dispersibility in addition to its distinctive tubular structure. The strong oxidative property of CNH makes them highly sensitive in detecting ozone (O_3) in gas (Sano et al. 2007; Yang et al. 2007; Tanaka et al. 2005; et al. 2003; Yoshitake et al. 2002). Use of CNH for hydrotreating have not been reported in open literature.

2.18 Synthesis methods for CNH

Carbon nanomaterials (e.g. CNH and CNT) can be synthesized using three key methods namely, laser ablation, arc discharge and chemical vapour deposition (CVD).

2.18.1 Laser ablation method of carbon nanomaterial synthesis

The laser ablation method is a process whereby a laser beam (mostly CO₂ laser or Nd:YAG) is used to vaporize a material after hitting a solid target (e.g. graphite). The laser method is operated under inert (argon (Ar), helium (He), nitrogen (N) and neon (Ne) gas) and high temperature (1200 °C) conditions. The pressure is also kept under control at approximately 101.33 kPa. Reaction is run in a quartz tube equipped with a cooled collector end. Absorption of the laser beam at the targeted area causes chemical bonds to break. Consequently, high velocity injection and evaporation of the targeted material occurs due to the intensity of the laser beam as it heats the localized surface. As a result, carbon species that are produced are transported to a copper-cooled collector end with the aid of the inert carrier gas (Purohit et al. 2014; Arepalli 2004). The vaporized species then cool and causes minute carbon atoms and molecules to condense into larger clusters such as CNH or fullerene. Spiral rotation of the target at approximately 2 rpm and 90 minutes can result in continuous CNH production, and no catalysts is needed for CNH production. Factors such as, laser conditions (intensity, wavelength and pulse duration) and the nature of the targeted material affects the extent and rate of ablation. The laser can be run in continuous or pulse mode. Although the laser method produces carbon nanomaterials in high yield, it is a very expensive method of choice (Purohit et al. 2014; Arepalli 2004; Bekyarova et al. 2003).

2.18.2 Arc discharge method of carbon nanomaterial synthesis

Arc discharge is the generation of plasma after an electrical breakdown of a gas. During arc discharge two carbon rods (anode and cathode rods) facing each other and separated by a 1mm gap gets vaporized after a current has passed through them. Usually the reaction is conducted in an inert environment (liquid or gas) to create an oxygen free environment for the reactions (Arora and Sharma, 2014; Antisari et al. 2003). This arc vaporization process creates a high temperature (~ 4000-6000K) between the anode (positive) and cathode (negative) rods and, causes the anode rod to consume and settle on the face of the cathode rod as the anode rotates along its orbit towards the cathode. From literature the deposit comprises of carbon nanohorns, carbon nanotubes, carbon

onions, amorphous carbon, multi-shells and some dislodged graphene sheets (Bera et al. 2006). It is important to keep the voltage (15-30 V) across the electrodes constant to maintain a stable plasma. A uniform plasma arc and temperature is also required to meet huge production demands. Also, the quantity and quality of the carbon nanomaterial have been found to be dependent on the current, voltage, pressure, cathode shape, temperature, setup modification. Graphite is commonly used as a carbon precursor in arc discharge because of it is readily available on the market in a pure state, and moreover graphite is an excellent conductor of electrons and heat. The arc discharge method is simple to setup and produces high yield CNH material (Das et al. 2016; Arora and Sharma, 2014; Akiladevi and Basak, 2010).

Figure 2.12 depicts a proposed physical model to explain how carbon-nanomaterials are formed using the arc discharge in liquid method. The liquid medium (liquid nitrogen or deionized water) aids in cooling the high temperature electrodes after arcing and provides a unique boundary for nanomaterials nucleation and growth. During arcing the ablated carbon ions and atoms from the anode and arc region combine into smaller particles as they move to lesser temperatures near the relatively cold bubble wall. The cooling effect close to the bubble wall produces adequate temperature gradients that aids with the nucleation and growth of carbon nanostructures (Xing et al. 2007). Typically, liquid nitrogen is used to synthesize CNH whereas, deionized water is used to produce CNT and carbon onions. Considering liquid nitrogen and water, the extremely low temperature of liquid nitrogen compared to water creates a higher temperature gradient which causes carbon fragments migrating to cooler liquid nitrogen area around the liquid nitrogen bubble wall to bend abruptly and agglomerate into CNH as a result of an intense quenching effect. Contrarily in the case of water, the nucleation, growth and agglomeration of the ablated carbon fragments are impeded since, the lesser quenching effect allows the fragments to grow into spherical perfect carbon onions. CNT formation also takes place as a result of directional movement of ablated carbon species from the anode to the cathode. Temperature gradient and consistent supply of carbon species were found to be key factors for nanomaterials fabrication (Xing et al. 2007, Sano et al. 2004; Wang et al. 2004; Sano et al. 2002).

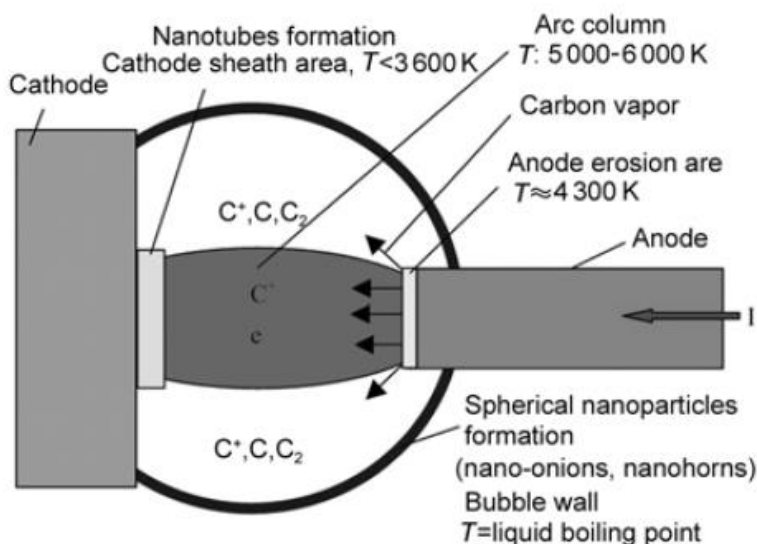


Figure 2.12 Schematic drawing showing a proposed physical model of the arc discharge method using liquid (Xing et al. 2007).

2.18.3 Chemical vapour deposition method for synthesising carbon nanomaterial

Chemical vapour deposition method can be used to produce carbon nanomaterials. It involves the decomposition of carbon containing source (in gaseous form) at elevated temperatures over a transition metal catalyst to form carbon nanomaterials. As a result, it is important to have a catalyst surface since it plays an important role by allowing both the decomposition of the carbon precursor and the formation of carbon nanomaterial. The steps involved can be broken down into two with the first step being the catalyst preparation step. Transition metals like Ni, Au, Fe, and Co are suitable for making these metal catalysts. The metal catalyst which can be prepared by either physical vapor deposition, dip coating or sputtering is deposited on a substrate and thereafter, catalyst nucleation proceeds using thermal annealing or chemical etching. The clustered catalysts on the substrate are mainly the sites for the growth of the carbon nanomaterial. Ammonia is a common etchant used in the CVD method. Ni, Silicon (Si), (SiO₂), Copper (Cu), stainless steel or glass are frequently used as substrates in CVD (Akiladevi et al. 2010; Purohit et al. 2014; Prasek et al. 2011; Hafner et al. 1998).

The substrate-coated-catalyst must be heated in a gaseous environment rich in carbon to aid with nanomaterial synthesis. Thus, a carbon source (acetylene, carbon monoxide, methane) is

introduced into a reaction chamber in a gaseous form, and heat from an energy source such as a heated coil or plasma is applied to convert the carbon molecule into carbon atom. The hydrocarbon is therefore decomposed by heat. Following this, the carbon atom diffuses towards the substrate-coated-catalyst to allow nanomaterials to grow over the metal catalyst. The synthesized nanomaterial is finally collected after the system had been cooled to room temperature using nitrogen. Temperatures ranging from 600 to 1200 °C are used to decompose the hydrocarbon. Vaporized reactants are transported in the reaction chamber using a carrier gas like Ar or N₂. Reaction can be run in a quartz tub furnace that has a temperature controller. CVD is a simple and versatile method since varieties of hydrocarbons in any state (gas, liquid or solid) can be used. The main drawback with this method is that the carbon nanomaterial produced from CVD method is structurally more defective than those produced by the laser or arc method (Akiladevi et al. 2010; Purohit et al. 2014; Li et al. 2009; Koziol et al. 2010).

2.19 Functionalization

Functionalization is commonly utilized in the area of nanotechnology, chemistry and material science and the aim is to add a new function, feature or property onto a material in order to alter its surface chemistry. Carbon nanomaterials (e.g. CNH, CNT) must be functionalized in order to create surface defects which acts as active or anchoring sites for metals that are added on the support. Functionalization of carbon nanomaterial results in the attachment of molecules or functional groups (e.g. carboxylic acid) to the surface of the material by chemical bonding or simply by adsorption. This treatment option is aimed at changing certain characteristics on the surface of the material which include; adhesion, hydrophilicity, surface charge, reactivity and roughness. Functionalization therefore aids in fine tuning the properties of carbon nanomaterial for other applications (catalyst formulation or hydrotreating reactions) by enhancing; the surface functional groups, surface area, porosity, pore volume, chemical bonding properties (due to the addition of oxygen atoms to the surface) and electro properties. The wetting and adsorption behaviour of carbon can be improved with functionalization. In catalysis enhanced wetting and adsorption are key properties required for a good catalyst. Functionalization can be controlled by varying temperature, acid concentration and duration of treatment. Choice of the right surface treatment technique is essential in maintaining the strength of the carbon nanomaterial for further reactions (Utsimi et al. 2007; Boehm, 2002; Stein et al. 2009).

Surface treatment can be accomplished by using oxidizing agents and gases such as nitric acid (HNO₃), sulfuric acid (H₂SO₄), hydrogen peroxide (H₂O₂), potassium permanganate (KMnO₄), air, ozone (O₃), and carbon dioxide (CO₂) (Pagona et al. 2009). With gas phase oxidation the carbonyl and hydroxyl functional group are enhanced whereas, liquid phase oxidation mainly improves the carboxylic groups. Among the liquid oxidants, functionalization with HNO₃ is usually preferred since, HNO₃ is not toxic, does not form secondary impurities and is inexpensive. Moreover, use of HNO₃ results in easier control of its oxidizing properties via temperature, time and concentration. The oxidized carbon surface can have acidic or basic functionalities depending on the functionalization method, and acidic surfaces having cation exchange properties are often formed when liquid oxidation is opted for or when oxygenated groups are created on the surface at high temperature (or through ageing). Acidic surface properties are created on the surface at high temperature (or through ageing). Acidic surface properties also occur as a result of carboxyl, hydroxyl and lactone groups that are generated during the oxidation treatment (Karousis et al. 2016; Stein et al. 2009; Boehm, H. 2002; Figueiredo et al. 1999). Examples of some likely oxygen surface groups are shown in Figure 2.13 (Boehm, H. 1994).

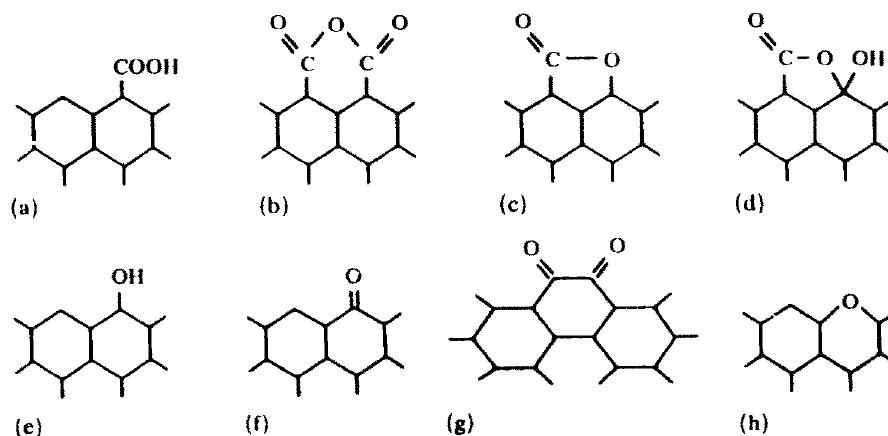


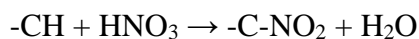
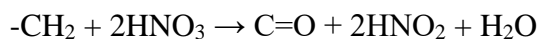
Figure 2.13 Examples of surface oxygen group structures; a) carboxyl group, b) carboxylic anhydride, c) lactone group, d) lactols, e) single hydroxyl group, f) isolated carbonyl group, g) quinone-group h) substitution of oxygen for edge carbon atoms (e.g. xanthan) (Boehm, 1994).

In relation to CNH, prior to functionalization the closed structure of CNH makes it difficult to allow any materials to penetrate its interior nanospaces. However, after functionalization possible entry points are generated which allow access to potential adsorption sites in the interior

of the nanohorns (Raffi-Tabar, 2004). Xu et al. 2011 emphasized that creation of holes on CNH aggregate via functionalization exposes three adsorption sites for other applications i.e. the external CNH surface, interstitial spaces between adjacent nanohorns and internal spaces within CNH at its edges (Xu et al. 2011).

Nitric acid is an oxidant and may be referred to as oxygenation reagent since it contains oxygen. After a reaction between nitric acid and carbon the products are made of carboxyl, nitrogen dioxide or nitrogen functional groups and water. For carbon materials, the characteristics of their surface (acidic or basic character) have a major impact on their surface chemistry. The porous carbons used in catalytic applications have graphitic structures and therefore contain, basal plain defects and unsaturated carbon atoms at the edges of the graphene layers which are prone to react with water, oxygen, nitrogen, or sulfur precursor compounds to form varieties of surface functional groups. The surface properties of carbon materials are influenced by their structure and consequently this also determines the way the carbon materials behave in catalysis. As mentioned earlier, acid treatment of carbon materials introduces oxygenated functional groups like carboxyl, phenols, alcohols, lactones and ketone on the surface, and enhances the hydrophilicity and surface charge density of the carbon material. The oxygenated functional groups, which are normally present at defective sites can be used to anchor metal precursors during catalyst formulation since, they have the ability to chemisorb reactants and form intermediate surface groups having adequate strength (Figueiredo et al., 2010, Moreno-Castilla et al. 2000; Figueiredo et al. 1999).

Unlike the chemical properties of carbon, which is associated with their surface functional groups, the physical properties of carbon are determined by factors such as porosity, size and specific surface area. Acid treatment does not only change the surface properties of carbon but at times it removes impurities and changes the porosity and specific surface area as well. The functional groups that are formed are dependent on the concentrations of nitric acid being used for the treatment. As a result, nitro groups and ketones are formed when low concentrations of nitric acid are used, and the following reactions are likely to be observed:



However, using high concentrations of nitric acid produces carboxyl groups according to the reaction below:



(Zhang et al. 2017; Ternero-Hidalgo et al. 2016; Figueiredo et al., 2010).

CHAPTER 3

Characterization Techniques and Sample Analyses

Contribution of this chapter to the overall Ph.D. work

Characterization of the catalyst is important since it provides information on the catalysts physico-chemical properties and gives a better understanding about how these properties affect hydrotreating reactions. For instance, knowledge on the textural properties (surface area, pore volume, pore diameter) of a catalyst is important since, it helps to control how the active components of catalysts are accessible for reactions. Thus, textural properties information from Brunauer-Emmett-Teller (BET) helps to determine whether the catalysts has; adequate surface area to improve dispersion, high pore volume to improve metal loading capacity, and optimum pore diameter to ensure that reactant molecules can diffuse in and out of the pore diameter for reactions. Prior knowledge about the catalyst pore size can also help to prevent operational challenges like clogging especially if the pore diameter is very small and a heavy crude oil has to be hydrotreated. Transmission electron microscopy (TEM) stacking information (i.e. Molybdenum disulfide (MoS_2) slab stacking degree and slab length) about a sulfided NiMo supported catalyst would reveal if a Type-I or Type-II NiMo phase was formed and would provide a clear understanding about the morphology and distribution of MoS_2 and how the phase impacted the hydrotreating activity results.

Knowledge of the elements present on a catalyst can help in troubleshooting operational problems such as corrosion. Verification of the catalysts chemical composition is necessary in situations where modification of the catalyst chemical composition for improved hydrotreating is important. Additionally, a technique such as electron microscopy reveals information about how the elements used in formulating the catalyst are distributed within the catalysts grains whereas, chemisorption techniques give insight on the catalyst surface reactivity. In the case of liquid (untreated and treated gas oil) samples, characterization techniques help to ascertain if the environmental protection agency (EPA) sulfur limit of 15 ppm mandated in Canada is being met and therefore, helps to improve upon the catalyst or hydrotreating process depending on the results of the treated sample. Overall, characterization is important in product and process development

In the following subsections under this chapter, the various characterization techniques used in this research are described.

3.1 Brunauer-Emmett-Teller (BET) surface area, pore size and pore volume analyzer

The BET method is used to evaluate the textural properties (specific surface area, specific pore volume, pore diameter and pore size distribution) of materials. The BET theory depends on the physical adsorption of gas molecules onto a solid surface, and in the case of physical adsorption the forces between the adsorbate (gas) and adsorbent (solid) are Van der Waals. The most commonly used adsorbate gas is nitrogen, however argon (microporous samples with pore size < 2nm) and krypton (precise measurements of tiny adsorbed quantities with specific surface area < 1m²/g) can also be used as probe molecules for the BET analysis. At constant temperature, the relationship between the quantity of gas adsorbed and the relative partial pressure (P/P_0) can be described by an adsorption isotherm. An adsorption-desorption isotherm therefore signifies the measured quantity of gas adsorbed and desorbed on the surface of the solid at a fixed temperature (approximately 77K using nitrogen).

Six isotherms i.e. Type I-Type VI (Figure 3.1a) exist according to IUPAC classification whereas, four types of hysteresis loops i.e. HI-H4 (Figure 3.1b) are also associated with the mesoporous materials. The breakdown of the isotherms are as follows; microporous adsorbents are classified as Type I, mesoporous adsorbents are of Types IV and V, and nonporous and macroporous ones are classified as Types II, III and VI. The standardized BET technique is based on the idea that, a gas condenses at a relative partial pressure (P/P_0) less than unity in a small size pore (Satterfield, 1991; Sing et al. 1985; Sing et al. 2008; Broekhoff, 1979; Shields et al. 2004).

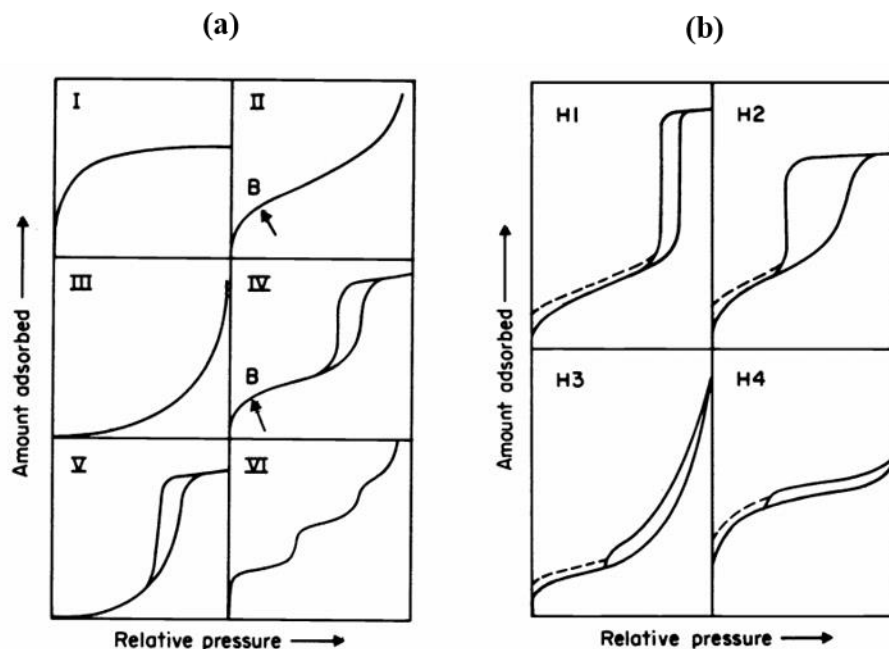


Figure 3.1 Diagram of adsorption-desorption isotherms and some hysteresis loop; a) IUPAC classification of adsorption-desorption isotherms (note the appearance of hysteresis in Types IV and V), b) correlation between the pore shape plus adsorption-desorption isotherm (Sing et al. 2008).

3.1.1 BET sample analysis

BET- Micromeritics ASAP 2020 surface area and porosity analyzer was used to measure the surface area and pore structure of the supports and catalysts used in this research. The pore size distributions of samples were however obtained using the Barrett-Joyner-Halenda (BJH) model. Prior to each analysis, 0.1 g of the sample was outgassed at 200 °C to a residual pressure of $< 6.6 \times 10^{-4}$ Pa for 4 hrs to get rid of moisture and adsorbed gases. Liquid nitrogen at 77 K was used for the analysis. The relative pressure range used in calculating the surface area was between 0.05 and 0.35. Both the adsorption and desorption isotherm branches were considered in the analysis.

3.2 High resolution transmission electron microscopy (HRTEM)

High resolution transmission electron microscopy was employed to enlarge the original object's image in order to examine its external and internal structure. The advantage of using HRTEM over light microscope is that, a detailed and clear information about the sample's microstructure can be provided. TEM provides information about the morphology (size and

shape), topography and composition of samples. Usually, HRTEM analysis involves the use of a focused beam of electrons to examine a sample and project an image. Additionally, its magnification and resolution ($\sim 0.1 - 1 \text{ nm}$) are higher than an optical microscope due to the lower wavelength of radiation for electrons.

3.2.1 HRTEM sample analysis

The morphology of support and catalyst samples were determined using a JEOL 2011 scanning transmission electron microscope (STEM). An accelerating voltage of 200 keV was used in operating the instrument. In preparation for HRTEM analysis, all support and catalyst samples were ground before analysis in order to reduce their size to a fine size for electrons to be transmitted through the resulting thin particle thickness ($\sim 100\text{-}200 \text{ nm}$). Following this, the homogenous fine powder was sonicated in ethanol before dipping a 200-mesh holey carbon-coated TEM support grid into the resulting solution to stick samples on the grid for analysis. 5-10 representative images were captured at low to high magnification ranging from 20 – 250 k times magnification.

3.3 Fourier transform infrared (FTIR) spectroscopy

FTIR spectroscopy is the preferred technique used in collecting infrared absorption or emission spectrum of a sample (solid, liquid or gas). It is used to identify chemical compounds and chemical bonds in a molecule. FTIR is therefore a very useful tool in detecting functional groups. After a sample has been exposed to infrared radiation, some of the radiation is transmitted through the sample whereas some is absorbed. High-spectral-resolution data are thereby collected over a wide spectral range based on the resulting signal at the detector. The infrared spectrum then gives a fingerprint information of the sample with absorption peaks representing molecular vibrational frequencies that make up the sample material. Due to the uniqueness of the combination of atoms present in each specific material or compound, FTIR analysis of different materials produces different infrared spectra that relates to the different materials being analyzed. The basic theory about this technique is that light is absorbed by most molecules in the infra-red region of the electromagnetic spectrum, and this absorption is exactly linked to bonds present in the molecule. In infrared absorption spectroscopy the spectral range of $4000\text{-}400 \text{ cm}^{-1}$ is frequently used since, most organic compounds and inorganic ions have absorption radiations that falls within this region (Lynch, 2003; Berthomieu and Hienerwadel, 2009).

3.3.1 FTIR sample analysis

The presence of functional groups in CNH samples was determined using Spectrum GX FTIR spectrometer from Perkin Elmer Inc. Both as-synthesized CNH and acid-treated CNH samples were analyzed. The instrument has a mid-IR KBr beamsplitter. Sample analysis with FTIR was done using the potassium bromide (KBR) pellet method hence, it was required that each respective sample and KBR was ground and mixed in an agate mortar at the onset of the analysis. The finely pulverized mixture was then pelletized using a hydraulic press to make sample disc for the analysis. Thereafter, the prepared disc was transferred and placed in the instrument for analysis. All analysis was run at room temperature and the spectrum covered a range of 400 to 4000 cm^{-1} with a total of 32 scans at spectral resolution of 4 cm^{-1} . FTIR absorption spectra were measured in the transmittance mode.

3.4 Pyridine Fourier transform infrared spectroscopy (Py-FTIR)

Infrared (IR) spectroscopy in the form of Py-FTIR method is also used in heterogenous catalysis to examine the characteristics of the acid sites that occur on the surface of the catalyst for reactions. Two types of acid sites exist i.e. Lewis acid sites where the acid sites accept electrons, as well as a Bronsted acid sites where a proton is donated to an unsaturated hydrocarbon from the acid sites. Py-FTIR method uses a gaseous base molecule (pyridine) to be adsorbed on the catalyst's surface acid sites for identification. This method provides a strong measure of the acid strength since, the conditions of the catalyst under study is close to reaction conditions. Basic probe molecules are of two types i.e. weak and strong probe molecules. Examples of weakly probe molecules that are used for detection of the solid catalyst strongest acid sites include ethylene, H_2S , deuterated acetonitrile and carbon monoxide (CO). Although protonation does not usually occur with these molecules, they are able to form species associated with hydrogen bonding. Ammonia, pyridine, 2, 6-dimethyl-pyridine and tri-methyl-pyridine are the most frequently used strong basic probe molecules (Satterfield, 1991; Lynch, 2003; Knozinger 1993).

The advantage of using Pyridine ($\text{C}_5\text{H}_5\text{N}$) ($\text{pK}_\text{B} = 8.8$) over 2, 6-dimethyl-pyridine is that it has dual functionality and thus, capable of adsorbing on both Lewis and Bronsted acid sites. As a result, the catalysts acid-base complex type is specifically identified. 2, 6 -dimethyl pyridine hardly differentiates the different types of Lewis acid sites present. Moreover, the bands ascribed to Lewis acidity when 2, 6 -dimethyl pyridine is used are linked with some physically adsorbed

species or hydrogen bonds and therefore it is not possible to associate the 1599 cm^{-1} band to just a Lewis acid site. Also, the location of Lewis acid sites as well as steric hindrance by methyl groups adjacent to the nitrogen atom on 2, 6 -dimethyl pyridine inhibits the formation of coordination complexes on the catalyst surface. Adsorption of 2, 6 -dimethyl pyridine is highly dependent on the solid surface topography. The drawback with NH_3 is that its strong basicity makes it possible for NH_3 to form very strong bonds with a variety of sites. By so doing, NH_3 cannot be used specifically as a probe molecule because, it might not usually provide the ideal properties needed for surface acidity studies. Pyridine forms coordinated pyL species on Lewis acid sites whereas, pyridinium ions, pyH^+ are formed on protonic sites. For, enhanced diffusion of the probe on small-sized channel surfaces, pyridine adsorption should be conducted at $150\text{ }^\circ\text{C}$ rather than ambient temperature (Lynch, 2003; Healy, 1989; Zecchina et al. 1998; Knözinger, 1993; Barzetti et al. 1996).

3.4.1 Pyridine FTIR sample analysis

The objective of utilizing pyridine adsorbed FTIR analysis on the catalysts was to ascertain the nature of its existing acid properties (i.e. Lewis and/or Bronsted type acid sites). As a first step of the analysis, a catalyst sample (0.1 g) was dried in an oven overnight at $110\text{ }^\circ\text{C}$. Thereafter, $50\text{ }\mu\text{L}$ of pyridine was used to soak the resulting product, before heating for 30 minutes at $150\text{ }^\circ\text{C}$. Pyridine-adsorbed IR spectra were then recorded with the aid of a Perkin-Elmer type spectrophotometer. The FTIR analysis was conducted at a resolution of 8 cm^{-1} , and the frequency range of choice was from 400 to 4000 cm^{-1} .

3.5 Raman spectroscopy

Raman spectroscopy technique is useful for studying carbon materials and is dependent on inelastic scattering of monochromatic light that originates from a laser source. Usually, the interaction of a sample (gas, liquid or solid) with monochromatic radiation causes the incident light to interact with the sample in various ways. This is because the incident light can either be scattered, absorbed or reflected. In the case of the light that is scattered, if all the incident light is scattered by the sample then there is no energy difference and the wave number is the same. This form of scattering is said to be elastic and is known as Rayleigh scattering. On the other hand, another form of scattering occurs which is denoted as inelastic scattering. For inelastic scattering,

there is some difference in energy or change in wavenumber between the incident light and the scattered light. This inelastic scattering is termed Raman scattering or Raman effect (Keresztury, 2006; Brumbah and Sharma, 2016). The energy diagram in Figure 3.2 shows an illustration of the Rayleigh and Raman scattering process. From this diagram, as the incident light from monochromatic radiation interacts with a molecule, it distorts the cloud of electrons in the vicinity of the molecule to a virtual state. Due to the instability of this state, the photon quickly re-emits as scattered light. It is worth knowing that, the frequency of the reemitted photons can be shifted down or up relative to the original monochromatic frequency.

For Rayleigh scattering, the electron falls back to the original ground level after being excited from the ground state. This brings about no change in energy hence, both the Rayleigh scattered light and the incident light have the same energy. However, Raman scattering is in two parts i.e. Stokes Raman scattering and anti-Stokes Raman scattering. For Stokes Raman scattering, the electrons fall to a vibrational level after being excited from the ground level. The result is that the molecule absorb energy and therefore the energy of Stokes Raman scattered light is less than the incident light. Less energy is equivalent to longer wavelength. Contrarily to this, the anti-Stokes Raman scattering describes the process whereby the electron is excited from the vibrational level and falls back to the ground level. Energy transfer therefore takes place to the scattered photon and the anti-Stokes Raman scattered light consequently has more energy (shorter wavelength) compared to the incident light (Tu and Chang 2012; Keresztury, 2006; Brumbah and Sharma, 2016).

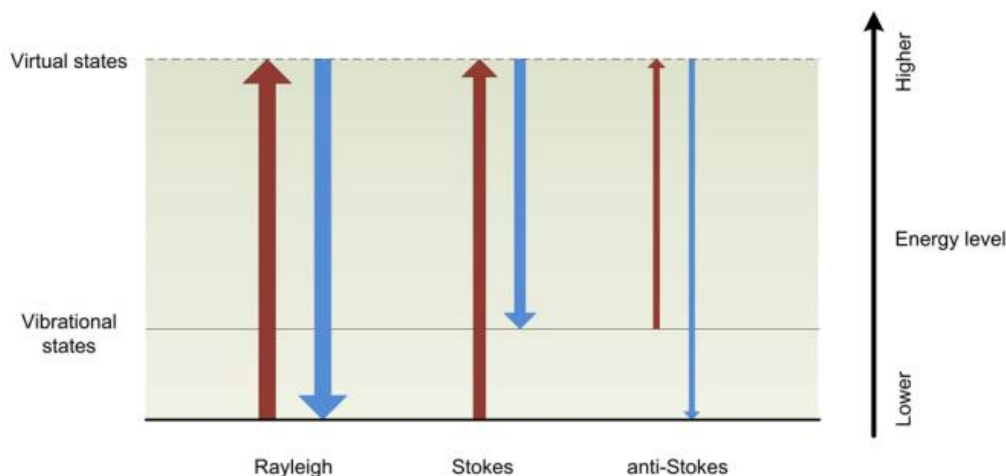


Figure 3.2 Energy diagram illustration of Rayleigh and Raman scattering (Tu and Chang, 2012).

Additionally, Raman scattering is known to occur as a result of coupling between the vibrational energy levels of molecules and incident radiation. The key effect of a Raman active vibration mode is that it should have the ability to change the polarizability of the molecules it encounters. Polarizability is dependent on the nature of bonds and molecular vibration. An observable peak in a Raman spectrum therefore originates from, a specific molecular or lattice vibration. The position of the peak is, attributed to vibrational modes of specific molecular functional group in the sample. The shape or width of the Raman peak can determine if there is little or much crystallinity in the sample. Presence of residual stress in the crystal can be estimated based on the direction and the difference in shift of the Raman peak. A shift in peak position would be observed from similar vibrational modes as a result of the influence of the close environment surrounding the functional group. Information regarding rotational, vibrational, and low frequency transitions in molecules can be obtained from this shift. The resulting Raman spectrum obtained after analysis also gives a distinct chemical fingerprint pertaining to a specific molecule or material, and therefore is a quick way of identifying materials or distinguishing one material from the other. Unlike light which is characterized by wavelength, wavenumber is preferably used in Raman spectroscopy because of its linear relation with energy hence, the resulting Raman spectrum becomes independent of excitation energy (Brumbah and Sharma, 2016; Tu and Chang, 2012; Cancado et al. 2006; Keresztury, 2006).

3.5.1 Raman spectroscopy sample analysis

Raman spectroscopy is an important tool used for characterizing carbon nanoparticles as a result of its sensitivity in detecting nanostructured materials (Jorio, 2012). Thus, the identity and/or quality of carbon nanomaterial (CNH, OCP_f and CNT) samples used for this research was validated with Raman spectroscopy. A Renishaw inVia Raman Microscope equipped with WiRE 3.3 software was used to perform the analysis. An argon (green) ion laser was also used at a laser excitation wavelength of 514 nm with a corresponding line grating of 1800 L/mm. Spectra measurements were taken using a 20x objective lens, and a laser power set to 100% allowed 3.6 mW of laser to be impinged on the sample under investigation. The laser spot size was about 1-2 μm , and an exposure time of 10 s was applied. Spectrum measurements within the range of 150-3500 cm^{-1} were examined for each sample. During analysis, the focus was mainly on the D and G

prominent band. The D to G band intensity ratio (I_D/I_G) is also used to access the quality of carbon nanomaterial.

3.6 X-ray diffraction (XRD)

XRD analysis is used to obtain information about a cell structure geometry as well as to identify the crystalline phase of a material. X-rays are produced from a cathode ray tube after a filament had been heated to create electrons. The generated X-rays are usually filtered to obtain monochromatic radiation, and then concentrated using a collimator before, they are used to bombard a targeted sample prepared for analysis. The incident x-ray on the sample may either be transmitted (by following its original path) or be scattered by electrons around the atoms of the material. All atoms along the X-ray beam path scatter X-rays, and constructive interference with a peak in intensity occurs when the diffracted patterns are in phase. This effect results in well defined X-ray beams exiting the sample at various angles. Most importantly, for this constructive interference and diffracted ray to occur, Braggs Law must be satisfied and is given by the relation:

$$n\lambda = 2d\sin\theta \quad \dots 3.0$$

where:

n = integer (1, 2, 3.....), λ = wavelength, d = distance between atomic planes in the crystal lattice and θ = angle of diffraction (Epp, 2016; Cullity and Stock 2001).

The diffracted X-rays that occur are detected, collected and processed. Possible diffraction patterns can also be obtained by using a range of 2 (theta) angles to scan through the samples. Additionally, to enable material identification, the diffraction peaks are converted to d-spacing and compared with standard reference patterns since, each material has its specific d-spacing or unique “fingerprint” of the available crystals in the sample. X-ray diffraction can also be used to determine the average crystallite size in a catalyst sample by using the Debye-Scherrer equation given below:

$$D = \frac{0.9\lambda}{\beta\cos\theta} \quad \dots 3.1$$

where;

λ = wavelength of the incident X-ray (1.5418 Å), β = full width at half maximum for the maximum intensity peak (radians) and θ = angle at which the most intense peak occurs (Jeseentharani et al. 2018). Additionally, from XRD, the degree of crystallinity can be calculated by integrating all the area under the peaks and calculating the ratio of the total area of crystalline peaks to the total area of all (both crystalline and broad) peaks (Murthy and Minor 1990). The equation below can be used (Murthy and Minor, 1990).

$$\% \text{ Crystallinity} = \frac{\text{total area of crystalline peaks}}{\text{total area of all peaks (crystalline and amorphous)}} \dots 3.2$$

3.6.1 XRD sample analysis

Wide and low angles XRD patterns were acquired using a Bruker D8 Advance powder X-ray diffractometer with $\text{CuK}\alpha$ radiation ($\lambda = 0.1541 \text{ nm}$) to ascertain the structure, crystallinity and phase of the catalysts. The instrument was operated under a Bragg-Brentano configuration, and also had a LynxEye detector plus a Ge monochromator which enables x-rays to be diffracted and focused. XRD power source was run at 30 mA and 40 kV. Smooth catalyst powdered samples (approximately 0.25 g) were analyzed after loading and pressing in a sample holder. Low angle X-ray diffraction scans were collected from 1.5° to 10° at a step time and 2θ (θ) step size of 2 seconds and 0.02, respectively. Wide angle diffraction data were also collected at 2θ ranges of 10 - 80° at a scanning rate of $0.05^\circ/\text{scan}$. The peaks that were present were identified with the aid of known Joint Committee on Powder Diffraction Standards (JCPDS) patterns to determine the type of chemical compound or elements available in the samples.

3.7 Thermogravimetric analysis (TGA)

TGA was used to study the thermal stability and behaviour of a sample (e.g. catalyst). TGA is a form of quantitative analysis whereby mass variation measurements of a heat-treated sample are taken in order to study the physical, chemical or physico-chemical property of the sample. A controlled environment is usually used, and the weight variations are measured as the temperature changes over time. The temperature variation of a heat-treated sample can also be obtained by differential thermal analysis (DTA). DTA measurements are made possible by comparing the variation in temperature of a reference material with that of the sample under equal treatment

conditions. Thermal effects data on the heated samples can be obtained after analysis, and DTA analysis also helps to determine whether the thermal behaviour is either exothermic or endothermic.

3.7.1 TGA sample analysis

TA Q500 series instrument with simultaneous thermogravimetry (TGA) / differential scanning calorimeter (DSC) application was used to determine the thermal stabilities of samples. About 15 mg of the sample to be analyzed was put in platinum-HT pans and subjected to heat from room temperature to 700 °C at 10 °C/minute ramp rate, and under nitrogen flow rate of 60 ml/min. The weight loss of samples as a function of temperature was evaluated using the analyzer.

3.8 Boehm titration

Surface properties of carbon materials can be affected by elements like oxygen (O₂) present on the surface. In aqueous solution carbon can also exhibit either acidic or basic behaviour. An established correlation exists between pH, and the oxygen content on carbon. Thus, higher oxygen content on carbon had been attributed to acidic surface groups with cation exchange properties whilst, low oxygen content on carbon are due to basic surface properties with anion exchange properties (Boehm, 1994; Studebaker, 1957). Usually, formation of surface oxides using liquid oxidants results in acidic surface properties that are due to the presence of lactones or lactols, carboxyl, and phenolic type hydroxyl groups. These groups have varying acidities and therefore can be differentiated by neutralizing with 0.05N of sodium carbonate (Na₂CO₃), sodium bicarbonate (NaHCO₃) as well as sodium hydroxide (NaOH), respectively. A simple procedure therefore involves, agitating the carbon with the respective base in excess, and determination of the excess using, back titration at the end of equilibration (Boehm, 2002; Scheibe et al. 2010). The quantity of acidic functional group present is calculated based on the knowledge that; carboxylic, phenolic and lactonic groups are neutralized by NaOH, carboxylic groups are only neutralized with NaHCO₃, and carboxylic and lactonic groups are neutralized by Na₂CO₃ (Boehm 2002; Boehm 2004; Scheibe et al. 2010).

3.8.1 Boehm titration analysis

Boehm titration method was utilized to evaluate the concentration of acidic character surface groups. Determination of the acidic strength of carboxylic acid groups, required addition of 25 mL of 0.05 N sodium bicarbonate (NaHCO_3) to 0.2 g of functionalized CNH samples (90A CNH_30 min) contained in a vial. The vial and its content were sealed, and then transferred onto a shaker device (VWR orbital shaker incubator) to enable 24 hr continuous mixing under mechanical agitation. This was done at room temperature and after completion of this duration, the resulting solution was filtered and then, 5 ml of each filtrate was pipetted and titrated against 0.05N HCl using methyl orange indicator. The quantity of carboxylic acid groups that reacted with NaHCO_3 was calculated based on the volume of HCl consumed (Boehm, 1964; Scheibe et al. 2010; Boehm 2002).

3.9 CO chemisorption

CO chemisorption is a quantitative method that can be used to evaluate the number of surface-active sites that are available to enhance catalytic chemical reactions. This process is selective, and therefore allows certain probe molecules (e.g. CO and H_2) to be chemisorbed on some adsorbents to cause significant interaction. Chemisorption studies can be conducted under conditions of pressure and temperature as a result of the formation of a monolayer on the metal surface. During chemisorption, a chemical reaction takes place between the active phase and the gas molecule that involves the sharing or transfer of electrons. Chemisorption may be associative or dissociative depending on the probe molecule and temperature. Additionally, the bonding could be linear or bridged although in most cases linear bonding is noted. Besides the percentage metal dispersion, chemisorption also aids in determining the average crystallite size of a supported metal catalyst. Metal dispersion can be defined as the ratio of the entire number of metal atoms that are available to the adsorbate species on the surface of the metal to the entire number of metal atoms present in the sample. Hence in its simplest term, metal dispersion (D) can be defined by Equation 3.3. CO chemisorption can be used to study the effects of catalyst loss, catalyst agglomeration and poisoning on the overall rate of reaction based on the number of active sites present for CO chemisorption. (Karakaya and Deutschmann, 2012; Lynch 2003; Satterfield, 1991).

$$D = \frac{N_S}{N_T} \quad \dots 3.3$$

where;

N_S = entire number of metal atoms that are on the surface and N_T = entire number of metal atoms (both bulk and surface) (Bergeret and Gallezot, 2008).

For bimetallic catalysts, the percentage metal dispersion can be calculated as follows:

$$\%M_{Disp} = \frac{1}{22414^*} \times \frac{V \times SF_{calc}}{\frac{wt. fract. Mo}{W_{Atomic, Mo}} + \frac{wt. fract. Ni}{W_{Atomic, Ni}}} \quad \dots 3.4$$

where;

$\%M_{Disp}$ = percentage metal dispersion, SF_{calc} = calculated stoichiometry factor, $W_{Atomic, Mo}$ = atomic weight of first metal, Mo (g/mole), $W_{Atomic, Ni}$ = atomic weight of second metal, Ni (g/mole), V = volume intercept that was obtained from the line of best fit to the differences in volume between the selected points of the first analysis and the repeated analysis ($\text{cm}^3/\text{g STP}$), *The volume occupied by one mole of gas ($\text{cm}^3 \text{ STP}/\text{mole of gas}$) (Micromeritics ASAP 2020 Chemi Manual, Appendix C).

In catalysis, particles are within the size range of 10^{-9} to 10^{-5} m. Particles such as zeolites, carbon, Raney metals are termed grains and their size is greater than 10^{-6} m. However smaller particles that are less than 2 nm are normally referred to as nanoparticles, clusters (oxides, metals), aggregates (metals). A small single crystal is termed crystallite, and one or more crystallites forms a particle. Dispersion and average size of metal particles are two main parameters often used to characterize the catalyst (Bergeret and Gallezot, 2008; Borodziński and Bonarowska, 1997).

The average diameter (nm) of the crystallites (assumption-spherical) is given by the equation:

$$d = \frac{6 \cdot 10^3}{\rho M} \quad \dots 3.5$$

where;

M = metallic surface area (m^2/g), ρ = the specific mass of the metal (g/cm^3), (Lynch, 2003).

3.9.1 CO chemisorption analysis

CO chemisorption analysis was conducted using an ASAP 2020 micrometrics instrument, and the goal was to calculate the percentage metal dispersion in relation to carbon monoxide uptake measured on each catalyst. Once, 0.1 g of the sample had been mounted on the instrument analysis port, an initial pre-treatment step was done at 110 °C for 60 minutes to get rid of the presence of moisture in the sample. After this step, 2 hours in situ reduction of sample at 350 °C under hydrogen (H₂) flow was allowed before, cooling to 35 °C. The resulting sample was evacuated after less than 1.3×10^{-5} Pa static pressure had been reached. CO chemisorption analysis then proceeded, and this involved measuring the total CO uptake at 35 °C after CO pulses had passed over the sample. The percentage metal dispersion of the available active metals that could interact with the adsorbate was then calculated.

3.10 Temperature programmed reduction (TPR)

The reducibility of the catalyst as a function of temperature and degree of oxidation can be determined using TPR. During reduction, hydrogen is added to the compound or oxygen is removed from the compound. H₂-reduction is vital since, the catalyst becomes activated for reaction(s) (Gervasini, 2013). Reducibility of the catalyst creates oxygen vacancies around the metal particle to aid with reactions. Use of a TPR technique allows reducibility studies on the catalyst to be conducted in real time by, closely monitoring the consumption of a reducing gas such as H₂ or CO on the catalyst as a linear heat program method is being applied (Gervasini 2013; Stagg-Williams et al. 2000; Brito and Laine, 1989). Thus, hydrogen consumption as a function of temperature is studied in TPR. The technique is also sensitive to chemical changes caused by the presence of a support or catalyst promoter. The extent of reduction can be evaluated by measuring the hydrogen content (composition) of the reducing gas mixture exiting the reactor, and the area under the peak is used to evaluate the entire amount of hydrogen consumed as well as in calculating the degree of reduction and average oxidation state of the catalyst at the end of reduction (Gervasini, 2013; Lynch, 2003).

3.10.1 TPR sample analysis

H₂-temperature programmed reduction (H₂ – TPR) analysis was conducted in a TPD/TPR Quantachrome AutosorbiQ (USA) equipment to evaluate how the reducibility of the metal species

in the catalyst behaves. The analysis progressed after a catalyst sample (0.1 g) placed in a U-shape quartz sample tube had been purged for an hour using helium (He) at 400 °C. This was done to eliminate traces of impurities present on the catalyst surface. Following this, cooling of the sample to room temperature proceeded by passing He. Then, TPR analysis was conducted at a ramp rate of 10 °C/min from room temperature to 800 °C with a 3 % H₂/N₂ (v/v) reducing gas mixture at 30 ml/min flow rate. TPR profiles of hydrogen consumption during analysis were recorded with the aid of a thermal conductivity detector, and an online data acquisition system was used in logging the TPR plots. Usually, an integration of the peak area under the concentration versus temperature gives the total amount of hydrogen consumed, and the amplitude of each peak is proportional to the rate of reaction (Chen et al. 2016; Gervasini, 2013).

3.11 Nitrogen-Sulfur (NS) analyzer

The total nitrogen and sulfur in the liquid hydrocarbon petroleum products were examined with an Antek nitrogen/sulfur analyzer (i.e. Antek Model 9000 NS Combustion analyzer with additional 4 modules. The sulfur concentrations in the hydrotreated liquid samples and feed were analyzed based on the combustion/fluorescence technique in agreement with ASTM 5463 standard procedure. On the other hand, the ASTM D4629 method which is dependent on a combustion/chemiluminescence technique was used to analyze the total nitrogen concentrations in the feedstock and hydrotreated liquid products. For both N and S analysis, an instrumental error of approximately $\pm 3\%$ was recorded which was based on, the calibration and analyzation of standard solutions with known compositions.

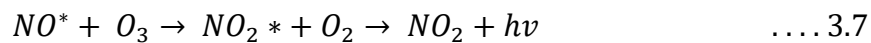
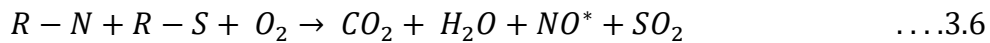
3.11.1 N-S sample analysis

NS analysis was done in order to find out about the concentrations of both S and N in gas oil. Treated and untreated light and heavy oil samples were analyzed after diluting with xylene. For light and heavy gas oils prior to analysis approximately 7 and 3 drops, respectively of oil sample was mixed with 1000 μ L of xylene, respectively. The weights of the drops were taken before diluting with xylene so that, the weight measurements could be used for further calculations relating to sulfur and nitrogen conversions. A mixture of argon carrier gas and an inlet oxygen gas are flowed into a pyrolysis tube where liquid samples are injected, exposed and treated to heat. Thus, at the onset of N-S procedure, the prepared oil samples are exposed to a high combustion

temperature (~1050 degrees C) to allow oxidation to take place. More oxygen gas is also routed to the pyrolysis tube to ensure that complete combustion and oxidation of entire sample matrix is attained.

Due to the oxidation reaction, any nitrogen and sulfur found in the sample are converted to their oxide form (mainly, nitric oxides and, sulfur dioxide respectively). The nitric oxide species that are formed are then contacted with ozone (O₃) from an ozone generator inside the Antek 9000NS to form, meta-stable nitrogen dioxide (NO₂) species. Decay of these meta-stable NO₂ species causes a photon of light to be emitted and detected by a photomultiplier tube that is integrated within the setup at certain wavelengths. This resulting chemiluminescence emission is specifically for nitrogen and is related to the original amount of nitrogen that exist in the sample. In the case of sulfur analysis, the oxidized sulfur species (SO₂) gets exposed to UV radiation of a certain wavelength, and this results in the UV radiation being absorbed and some electrons shifting to high energy levels. A fall back of the electrons to their original state releases the extra energy in the form of photons of light which is detectable at specific wavelengths by another photomultiplier tube integrated within the setup. In this situation, the emission type is fluorescence and is specific to sulfur, and proportion to the amount of sulfur in the original sample.

Equations 3.5, 3.6, 3.7 (Antek, 1998) are summarized descriptions of the basic chemistry that governs N-S operation.



At the end of the analysis, percentage nitrogen and sulfur conversion can be calculated using the equation below:

$$\% Conversion = \frac{C_{i,Feed} - C_{i,Product}}{C_{i,Feed}} \times 100\% \quad \dots 3.9$$

where;

$C_{i,Feed}$ and $C_{i,Product}$ = nitrogen or sulfur concentrations in feed and hydrotreated liquid products, respectively.

3.12 X-ray absorption spectroscopy (XAS)

X-ray absorption spectroscopy (XAS) is a type of characterization technique that uses X-rays to investigate the structure of materials (solids and liquids). XAS permits the study of local structure of the desired element without any interference from water or air, and XAS also characterizes the environment and chemical nature of atoms in molecules. Two methods fall under XAS i.e. X-ray absorption near-edge structure (XANES) as well as extended X-ray absorption fine structure (EXAFS). Usually for an element, XAS evaluates the energy-dependent fine structure of the X-ray absorption coefficient close to the absorption edge. In XANES analysis, the metal transitions from core electronic states to excited electronic states i.e. lowest unoccupied molecular orbital (LUMO) are measured whereas, EXAFS involves measurements from core electronic states to the continuum or free state. This occurs because, at energies that are higher than the LUMO level, X-Ray absorption provides enough energy to release electron (ionize) from the absorbing atom (Yano and Yachandra, 2009; Koningsberger and Prins, 1988; Teo, 1986).

The XANES region provides information concerning the oxidation state, and coordination chemistry (tetrahedral or octahedral) or the metal atom local site symmetry whereas, the EXAFS region can be used to quantitatively determine the local structure (e.g. bond distance, number, type of neighbor) of the element or molecule due to, its sensitivity to the radial distribution of electron density around the absorber atom. Structurally, XANES and EXAFS methods both compliment each other because, the XANES spectra reports the metal site's electronic structure and symmetry whereas, EXAFS reports numbers, types, and distances to neighboring atoms and ligands from the absorber atom (Yano and Yachandra, 2009; Teo, 1986; Koningsberger and Prins, 1988). A desired X-ray energy is used based on the specific element that needs to be probed. X-ray absorption spectra of any atomic or molecular material are identified by sudden increases in absorption at specific X-ray photon energies typical of the absorbing element. The abrupt increases in absorption are known as absorption edges and are associated with the energy that is needed to eject a core electron into either the LUMO or continuum to produce a photoelectron. K-edge absorption discontinuity refers to instances where the photoelectron is from a 1s core level, whereas L-edge absorption discontinuity refers to absorption discontinuity where ionization is either from 2s or 2p.

For simplicity purposes, X-ray absorption spectrum measurements only measures incident and transmitted X-ray flux. Thus, for an X-ray of intensity I_0 incident on a sample, the extent of absorption is dependent on the sample thickness, t and photon energy, E and based on Beer-Lambert's Law the transmitted intensity, I_t can be estimated as follows:

$$I_t(t) = I_0 e^{-\mu(E)t} \quad \dots 3.10$$

where;

$\mu(E)$ = energy-dependent x-ray absorption coefficient.

Figure 3.3 shows an illustration of the regions of a XAS spectrum (Penner-Hahn, 2003).

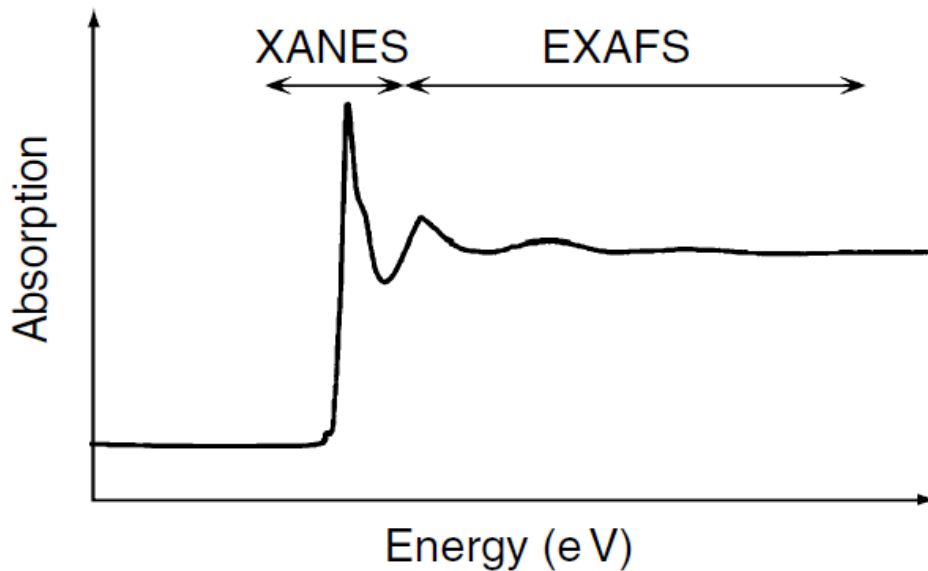


Figure 3.3 Diagram showing the regions of an X-ray absorption spectrum (Penner-Hahn, 2003).

3.12.1 XAS sample analysis

X-ray absorption spectroscopy (XAS) experiments were used to investigate NiMo/ γ -Al₂O₃, NiMo/CNH, and NiMo/OCP_f catalysts using the Hard X-ray Microanalysis Beamline (HXMA-061D-1) at, the University of Saskatchewan's Canadian Light Source (CLS) in Canada. CLS is among the first of third generation synchrotron facilities and its storage ring runs at 250 mA injection current and 2.9 GeV electron energy. The HXMA beamline consisted of Rh-coated upstream collimating and downstream focusing mirror with a split aperture of 0.55 mm as well as, an internal Kohzu double-crystal Si (220) monochromator. Detuning of the second

monochromator was paramount to allow 50% of the fully tuned beam intensity by suppressing any high harmonics in the beam. All experiments were conducted under ambient conditions, and in preparation for the XAS experiments, 200 mg of finely ground sample powder of each respective catalyst was packed into a Teflon® sample holder having a thickness of 0.5 mm with a sample window of 20 mm x 4 mm. A Kapton® tape was also used to keep the prepared sample secured before any XAS analysis. XAS data were also collected on these reference compounds (i.e. pure Ammonium heptamolybdate $[(\text{NH}_4)_6\text{Mo}_7\text{O}_{24}\cdot 4\text{H}_2\text{O}]$, Na_2MoO_4 , and MoO_3) to assist in characterizing the Mo bonding environment in the catalysts. Prior to the XAS experiment, boron nitride was used to dilute each of the reference compounds before they were put into the sample holders. Additionally, standard nitrogen gas filled ionization chamber (IC) detectors were used in acquiring Mo K-edge XAS measurements in transmission mode from, -200 to +800 eV close to the Mo K-edge (20,000 eV). For both the X-ray absorption near edge spectroscopy (XANES) and extended X-ray absorption fine structure (EXAFS) regions, the monochromator step size was reduced to 0.4 eV and 0.05 Å, respectively. 3 XAS scans were acquired for each catalyst sample whereas, 2 XAS scans were acquired for each of the reference compounds. Averaging of these repeated XAS scans were taken into consideration to increase the signal-to-noise ratio. For energy calibration purposes, reference Mo foil spectra were simultaneously collected for each spectrum during data analysis.

The Demeter suite (ATHENA & ARTEMIS) of XAS data analysis package aided with the data reduction as well as analyses of Mo K-edge XAS data for the various reference compounds and catalysts. Data reduction was accomplished using ATHENA, and this included the standard energy calibration procedures, background subtraction, per atom normalization, multiple scans averaging, and extraction for EXAFS analysis. The EXAFS oscillations were extracted in ATHENA using AUTOBK algorithm with a cut-off of $\text{Rbkg} = 1$ and $\text{k-weight} = 3$ before, Fourier transformation. By using the Hanning window and a k-range of about 2 - 12 Å⁻¹, the radial structure function (RSF) in R-space (Å) was produced after the k^3 - weighted $\chi(\text{k})$ function ($\chi(\text{k})\text{k}^3$) in k-space (Å⁻¹) had been Fourier transformed (FT) (Das et al. 2016; Ravel and Newville, 2005).

CHAPTER 4

Maximization of Carbon Nanohorns Production via the Arc-discharge Method for Hydrotreating

Most of the content in this chapter have been published in, Journal of Nanoscience and Nanotechnology and the citation is; Aryee, E.; Dalai, A. K.; Adjaye, J. “Maximization of Carbon Nanohorns Production via the arc discharge method for hydrotreating application” Journal of Nanoscience and Nanotechnology, 17 (2017) 4784 – 4791.

Excerpts of this study were presented at the following conferences:

- E. Aryee, A. K. Dalai, J. Adjaye, “Synthesis and characterization of carbon nanohorns for hydrotreating of gas oils,” Oral presentation at 62nd Canadian Chemical Engineering Conference, Vancouver, British Columbia, Canada, October 14-17, 2012.
- E. Aryee, A. K. Dalai, J. Adjaye, “Synthesis and characterization of carbon nanohorns for hydrotreating of gas oils,” Oral presentation at 245th American Chemical Society Conference, New Orleans, United States, April 7-11, 2013.

Contributions to this phase of work

The Ph.D. candidate, Emma Aryee developed the experimental plan and synthesized all CNH material used for this study. Emma Aryee also designed the arc-discharge setup and created a standard operating procedure (SOP) for CNH synthesis via the arc-discharge technique. The physical set up was built with the help of RLee Prokopishyn, who is an electrical technician in our department. Occasional repairs and maintenance of arc discharge setup was done by RLee Prokopishyn. All experiments, characterization, data processing, interpretation of results, writing and revision of this manuscript were done by Emma Aryee. During the course of the work my supervisors; Dr. A. K. Dalai and Dr. J. Adjaye critically reviewed experimental plan and results, provided some guidance and suggestion during discussions. Drs. Dalai and Adjaye also reviewed the manuscript and rebuttals prior to its final publication.

Contribution of this chapter to the overall Ph.D. work

This phase of research comprises of building an arc-discharge set up and enhancing the CNH generated from this technique for all CNH related hydrotreating experiments. Due to the low yield of the generated CNH, the intent was to further determine the best process conditions that would maximize CNH production. This chapter therefore give a better understanding about how reaction (arc-discharge) conditions impact maximum CNH production. Information from this study would also provide knowledge about whether variation of reaction condition affect the physico-chemical properties of CNH. Ability to drastically enhance the yield would be beneficial since, enough quantity of material would be available for the desired end use hydrotreating application. Additionally, this would also provide some flexibility as to the number of experiments to run to bring an idea into fruition or to back any experimental findings. Maximizing CNH production would also enable researchers to prepare enough catalyst from the same batch for both characterization and hydrotreating experiments. Consequently, this would be beneficial by providing clearer interpretation of results since, the support material used in making the catalyst would have similar properties from the onset. In that regard, the root cause of problems would also be narrowed down during troubleshooting. Availability of enough material would also ensure that experiments are run smoothly in a timely manner especially in the wake of unfortunate incidents like catalyst deactivation.

4.1 Abstract

The submerged arc in liquid nitrogen method was used to produce carbon nanohorns (CNH) for hydrotreating application. In this paper the effects of current, time and system design modification were investigated to maximize CNH production. A current setting of 90 A was found to be the best condition for CNH production. Additionally, CNH production was impacted by processing time and design setup used in synthesizing the samples. For each batch, 0.12 g of CNH was obtained for 30 mins of processing time. The properties of CNH were evaluated using Brunauer - Emmett - Teller (BET) method, transmission electron microscopy (TEM), Fourier transform infrared (FTIR), Raman Spectroscopy and X-ray diffraction (XRD). BET results revealed mesoporous pore diameters for all pristine CNH samples under the different current (50 - 100 A) settings. Dahlia-like and budlike structures with aggregate diameters ranging from ~ 50 - 110 nm were observed in the TEM images. Although current and processing times were found to

be two crucial parameters affecting the yield of CNH production, the entire equipment design was a major key factor in improving the yield by being capable of retaining more CNH particles during production.

4.2 Introduction

Manufacturing substantial quantities of carbon nanostructured materials for industrial and research applications will provide the necessary flexibility as efforts are being made worldwide to explore the use of nanotechnology in improving existing technologies and enhancing the effectiveness of new application (Azami et al. 2008; Wang et al. 2007). Examples of carbon nanostructured materials used in different applications include carbon nanohorns (CNH), carbon nanotubes (CNT), and carbon nanofibers (CNF) (Sigurdson et al. 2009; Sano and Ukita, 2006; Bessel et al. 2001). CNH can be produced by three main methods namely, laser ablation, arc discharge and chemical vapor deposition (Li et al. 2009; Sano, 2004; Iijima et al. 1999). Variables that alter the production (quality, type, quantity, yield, production rate) of carbon nanostructured materials include; current, electrode rod dimensions, catalyst (e.g. Fe, Co, Ni, Pt, Pd, Mo), gas atmosphere (e.g. ambient air, argon, helium), gas pressure, liquid media (liquid nitrogen, water, de-ionized water). The work of Iijima *et al.* (1999) saw the emergence of a new carbon allotrope, CNH of ~ 80 nm. No metal catalyst was used and the Nd: YAG laser type normally used for CNT production was replaced with CO₂ laser. The yield and purity were 75% and 95% respectively and the average production rate was 10 g/hr (Duncan et al. 2007; Sano, 2004; Yudasaka et al. 1999; Maser et al. 1998).

Gang *et al.* (2007) reported that in an arc discharge method, the liquid medium in which the arc was submerged influenced the type of carbon nanostructured materials produced. From their work MWCNT of about 15 layers with 10 - 20 nm diameter was mostly formed by arc discharge in de-ionized water using pure graphite rods as anode and cathode. Cobalt encapsulated carbon onions were obtained using pure graphite anode rods in CoSO₄ solution whereas, SWCNH of 80 – 100 nm diameter were produced in liquid nitrogen medium. Li *et al.* (2009) used CVD to produce multi-walled CNH of 40 - 50% purity with individual horn diameter and length of 20 nm and 50 - 500 nm respectively. High; surface area, mechanical strength, thermal stability, thermal conductivity, dispersibility, adsorption, porosity and electrical conductivity are properties that renders CNH useful in many applications such as drug delivery, catalyst support, hydrogen

storage, fuel cell, molecular sieves and field emission (Nakamura et al. 2011; Sano and Ukita, 2006; Ajima et al. 2005; Murata et al. 2002; Yoshitake et al. 2002; Nisha et al. 2000). Hydrotreating of gas oil is an area that requires the use of a catalyst in upgrading the gas oil to products containing less or no amount of sulfur, nitrogen, oxygen, metal atoms and other contaminants. In addition, the process leads to the saturation of aromatics and unsaturated hydrocarbons (Jarullah et al. 2011; Grange and Vanhaeren, 1997; Joo and Guin, 1996). Based on the positive outcome of the use of CNH in the aforementioned applications, the main aim of our work was in two folds: 1) to maximize CNH production in order to obtain substantial quantity for catalyst development and use in hydrotreating experimental runs using a trickle bed reactor and 2) to examine the unique properties of the CNH produced in order to determine the best synthesis condition required to develop an ideal CNH catalyst for hydrotreating (an area which has not been researched into). Current, time and system modification are the main parameters considered in this work to increase CNH production (i.e. quality, quantity, yield, production rate) via the arc discharge in liquid nitrogen method.

4.3 Experimental method

4.3.1 Production of CNH

The setup for production of CNH consisted of a 4.5 L Dewar flask (Fisher Scientific Canada), DC power supply, ammeter, voltmeter, control box, baffles, and electrode rod holders for both anode and cathode electrode rods (Figure 4.1). The electrode rod holders were made of aluminum with a total length of 254 mm. The length and diameter of the anode electrode rod was approximately 72.2 mm and 6.50 mm respectively whereas, that of the cathode electrode rod was approximately 38.7 mm and 14.0 mm respectively. These electrodes made from graphite were purchased from Mersen USA Greenville - MI Corp. (formerly Graphite Engineering & Sales Co.). Due to the larger cathode diameter relative to the anode diameter, the cathode has a lower current density than the anode (Arora and Sharma, 2014).

The arc discharge process was a batch process. In order to produce CNH, the two graphite rods (i.e. anode and cathode rods) of 99.9% purity were submerged in ~ 2 liters of liquid nitrogen and the distance between the two rods maintained at ~ 1 mm. An arc struck once the specific current has been set and this led to vaporization of the anode tip due to the high temperature (> 4000 K) at the arc discharge zone where carbon materials sublime (Sano et al. 2008). Arc voltages

ranging from 20 - 45 V were recorded. The products from the anode rod deposited on either the cathode rod or into the Dewar flask containing liquid nitrogen. On completion of an arc discharge experimental run, the entire contents of the Dewar flask were left for at least 12 hours (hrs) to allow any remaining liquid nitrogen to evaporate prior to particle separation and collection. Deionized water was then added to the product in the Dewar flask to facilitate natural segregation of particles. Subsequently, the contents of the Dewar flask were emptied into a beaker where three phases (floating, suspended, and settled) of particle separation were observed. The water and particles in the beaker were allowed to stand for ~ 5 minutes (mins) before filtering out the floating and suspended particles which were identified as CNH (Wang et al. 2004). Filtration of particles was done using MF-Millipore membrane filters of 0.65 μm pore size (Millipore, Canada). Both CNH samples and the settled particles in the beaker (denoted as other carbon particles, OCP), were air dried for at least 24 hrs. Thereafter, particles were collected and stored in designated sample vials. Current range of 20 – 100 A and process durations of 10 - 60 mins were investigated to determine their effect on CNH production. Furthermore, the effect of a modified system was also considered. This was done by extending the length of the electrode holders, h (Figure 4.1) from approximately 152 mm to 254 mm and adding baffles with same external diameters but different internal holes of diameters 4 and 8 mm. The baffles were made from FR4 fiber glass resin. Images of the arc discharge set up and filtration station are displayed in Appendix A.

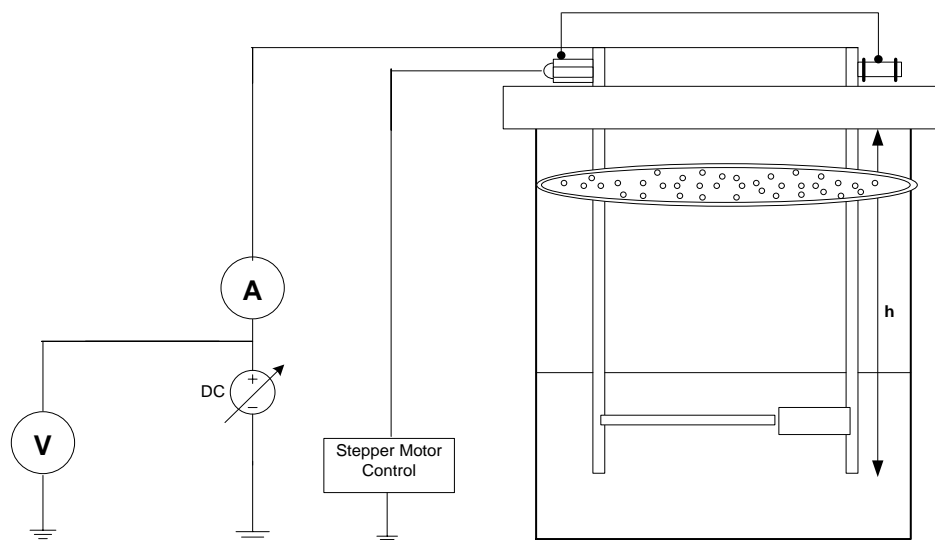


Figure 4.1 Schematic of experimental setup for producing CNH.

4.4 Characterizations

Characterization techniques that were used to determine the physico-chemical properties of CNH include; BET, HRTEM, FTIR, Raman Spectroscopy, XRD and TGA. Information about these techniques and sample analysis procedures are reported in Chapter 3 of this thesis.

4.5 Results and discussion

4.5.1 Mass balance for arc discharge experiments

A typical mass balance for the arc discharge production of CNH using an arc current of 90 A is shown in Figure 4.2. It shows that after a pure graphite rod of about 4 g had been processed, the yield of the OCP by-product is about 45 wt% more than the CNH material of interest. Upon sieving this OCP by-product with US No. 60 standard sieve series, OCP_f material of about 0.3 g could be obtained that was also more than the CNH material of interest. The unaccounted particles may have been lost through rapid turbulence or gasification as they are entrained by liquid nitrogen gas bubbles and become extremely difficult to capture (Charinpanitkul et al. 2009).

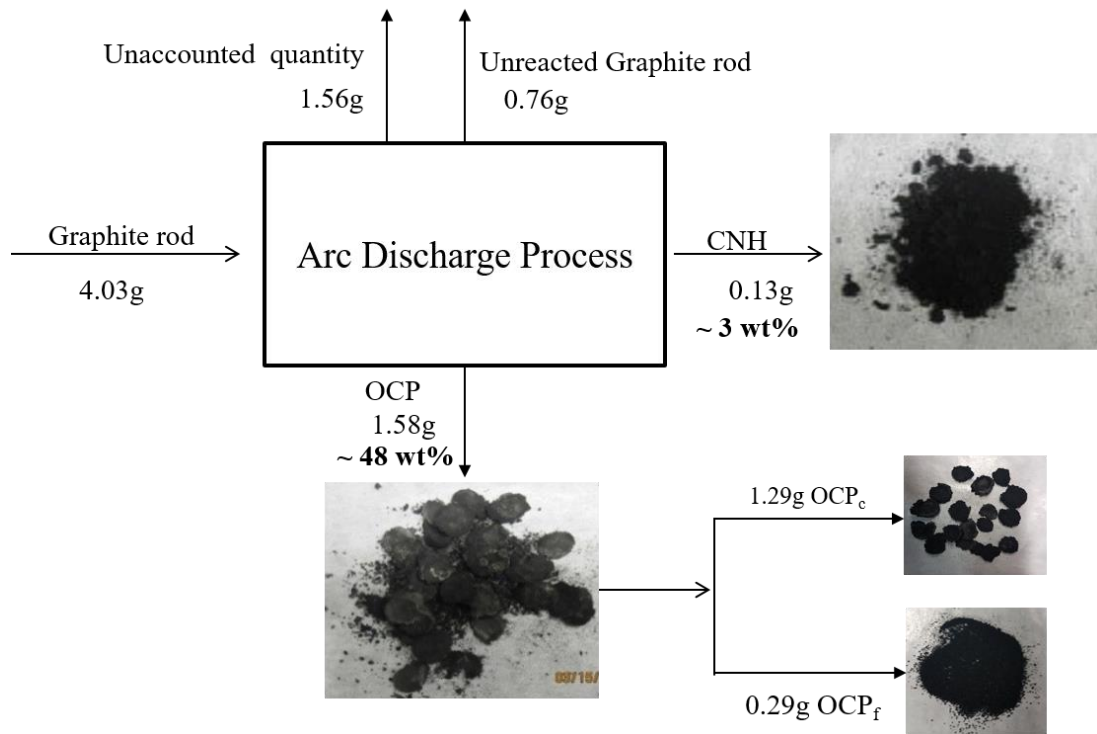


Figure 4.2 Mass balance of the arc discharge process.

The yield of each experimental run was calculated using Equation 4.1, which is based on the initial weight (I_w) of the anode rod before the start of experiment, final weight (F_w) of the unconsumed anode rod at the end of the experiment and the weight (X_w) of CNH or OCP separated and collected at the end of the run.

$$Yield = \frac{X_w}{I_w - F_w} \times 100\% \quad \dots 4.1$$

4.5.2 Effects of current setting on CNH production

Current settings in the range of 50 to 100 A were explored to study the effect of current on the yield and production rate of CNH. All experiments under this section were conducted at a constant anode rod length of 75 mm and process duration of 1 hr. The production rates were therefore measured based on the weight of CNH or OCP separated and collected per hour of run. Figure 4.3 shows a steady increase in yield as the current changed from 50 to 70 A. However, no appreciable increase in yield was observed as the current was varied from 80 to 100 A. Additionally, the yield increased to more than twice its value as higher currents (> 70 A) were experimented.

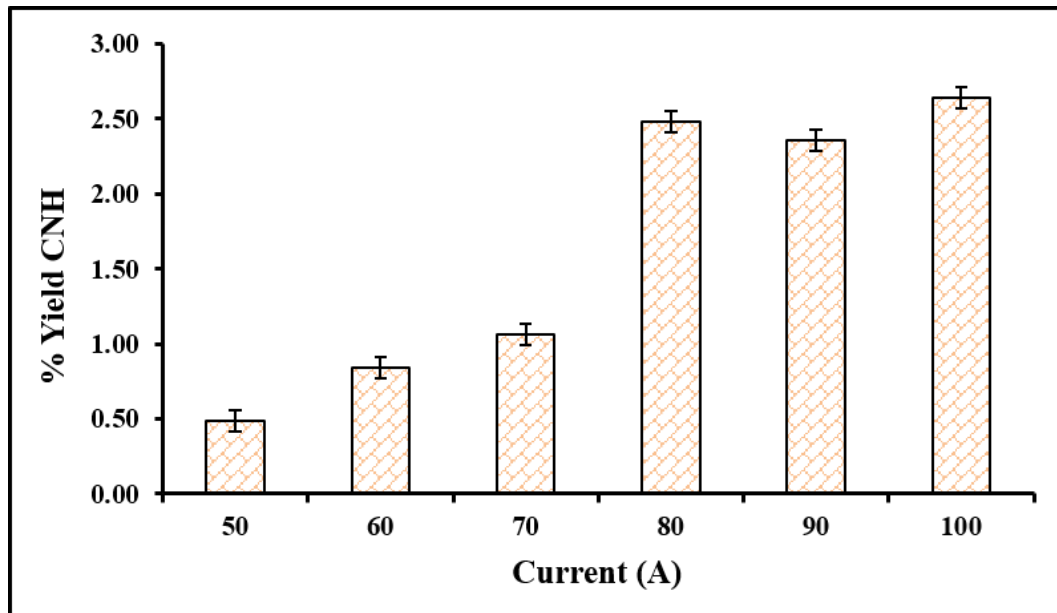


Figure 4.3 Effect of increasing current (50 A to 100 A) on the yield of CNH produced from an arc-discharge experiment.

The arcing period for all experiments carried out from 50 to 100 A was between 10 - 25 seconds. Increase in yield with increasing current is attributed to an increase in sublimation rate of carbon atoms from the anode as current increases (Gang et al. 2007; Gattia et al. 2007). This explains why experiments carried out at 20 A, 30 A and 40 A (results not shown) generated virtually no particles despite a much longer arcing duration of 5 - 6 mins. It was observed that beyond 70 A, although carbon nanoparticles formation was enhanced, the intensity of turbulence in the system was also high. Thus, a lot of particles escaped the Dewar system in the form of a plume or particles entrained by liquid nitrogen gas bubbles (Charinpanitkul et al. 2009). Overall, a yield of no more than 3% CNH was obtained by changing the current from 50 A to 100 A. From Figure 4.3, a minimum yield (~ 0.50%) was obtained at 50 A, and its equivalent production rate was 0.018 g/hr. The lower temperature at the arc zone at lower current tends to lower the evaporation rate of carbon from the anode and subsequent re-aggregation of CNH particle formation (Sano et al. 2011; Zhao et al. 2011). Varying current also had impact on the time taken to consume a rod. As such, the process duration decreased from 120 mins to 40 mins as current increased from 50 A to 100 A. Gattia *et al.* (2007) also made a similar observation about the effect of current on the process duration trend.

Results of repetitive experiments on the effect of current (i.e. 80 A, 90 A and 100 A) on the yield (Figure 4.4) after the system had been modified by extending the electrodes rod holders (h in Figure 4.0) from approximately 152 to 254 mm, and using a baffle with internal holes diameter of 4 and 8 mm have also been reported in this section. These currents were chosen because of their high CNH throughput as observed from Figure 4.2. Experiment using the 4 mm internal holes baffle were discontinued after a few runs since it resulted in pressure build-up within the Dewar flask accompanied by an explosive sound that subsequently disrupted the arc by frequently quenching it as it struck. From Figure 4.4, increasing current from 80 A to 90 A resulted in a slight increase in the yield but a drop in the yield occurred as the current was increased from 90 A to 100 A. More turbulence at higher temperatures results in particle loss. This explains why the production rate increased from 80 A to 90 A, and then dropped as the current was further increased from 90 A to 100 A. Extreme gasification at higher currents could also be a reason for particle loss (Charinpanitkul et al. 2009). For clarification purposes, the results displayed in Figure 4.3 were obtained prior to setup modification (i.e. inclusion of baffle and extension of the anode and cathode electrode rod holders) and at a different current setting.

The experiments were run for 1 hr. The results showed that a current setting of 80 A gave the highest yield. However, after setup modification had been completed repeating the experiments on the 80 A, 90 A and 100 A current settings (Figure 4.4) showed that the yield was higher for the CNH generated at 90 A. The production rate before and after setup modification for the 80 A current setting was 0.090 g/hr and 0.095 g/hr respectively. The overall results from Figure 4.4 shows that a maximum CNH yield of 1.86% was achieved using a current setting of 90 A and this resulted in an equivalent production rate of 0.13 g/hr. With the old setup the production rate was 0.075 g/hr at a current setting of 90 A therefore, system modification resulted in ~73% increase in the production rate. Based on this, all subsequent arc discharge experiments for the remaining phases of work were carried out using a current setting of 90 A.

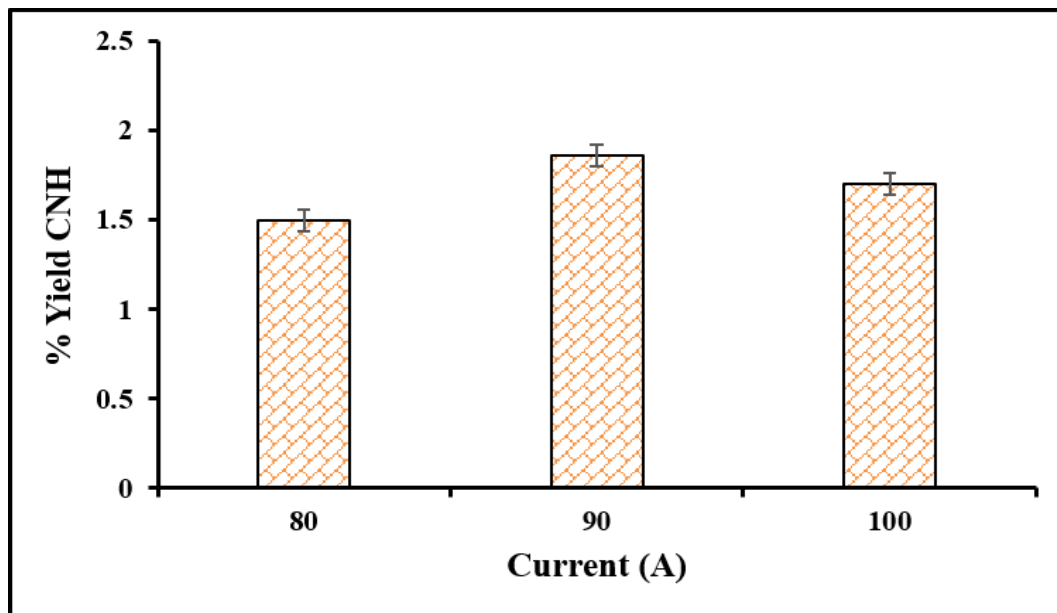


Figure 4.4 Effects of baffle incorporation and extension of length of electrode rod at higher current (80A, 90A and 100A) settings on the yield of CNH.

Setup modification did contribute to the increase in production rate because, with the extension of the electrodes rod support holder, the Dewar flask had to be filled to $\frac{1}{4}$ of its volume (unlike $\frac{3}{4}$ of its volume with the old setup design) in order to keep the cathode and anode rod adequately submerged in liquid nitrogen. The $\frac{1}{4}$ filled Dewar therefore, created more space for particles to condense on the Dewar wall and rods above the liquid nitrogen level and minimized the possibility of losing floating particles that are, closer to the top of the Dewar flask and had

greater potential of escaping as the flask was refilled with liquid nitrogen in the course of an experiment. Incorporating a baffle helped in trapping particles into the system as the experiments proceeded. Loss of CNH during particle generation was a challenge.

4.5.3 Effects of time on CNH production

The effect of time on the yield of CNH produced at a fixed current setting of 90 A is presented in Figure 4.5. From Figure 4.5, a yield of about 2.5% was obtained after 10 mins experimental run and this was more representative of the actual amount of CNH generated and retained in the setup since the exit plume was clearer at this initial stage of run.

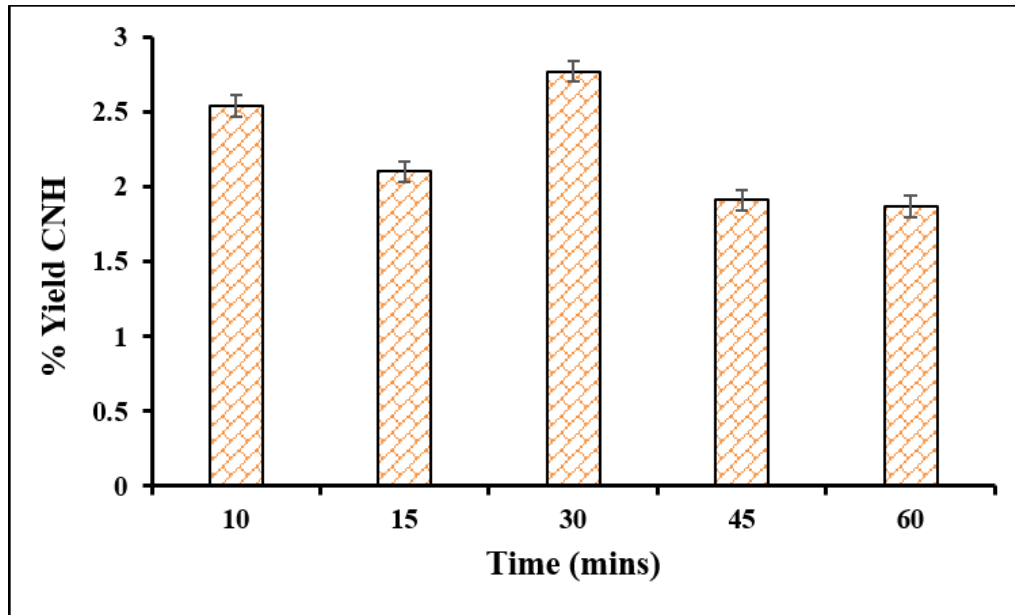


Figure 4.5 Effect of increasing process duration (10 mins to 60 mins) on the yield of CNH produced from arc-discharge experiment.

A decrease in CNH yield to about 2.1% was realized after increasing the run time from 10 to 15 mins. This is because as the run time was increased there was a greater probability of losing particles in the plume or entrained by nitrogen gas bubbles as the Dewar flask was refilled. However, at 30 mins run time though particle loss was also noticeable, this time frame was long enough to retain some additional CNH within the system. The retention rate was more of a contributing factor than particle loss for a run time of 30 mins. From 45 mins onwards, particle loss then became a contributing factor than particle retention and this was obvious since the exiting

plume became darker due to particle (carbon) enrichment. This observation is also supported by the amount of particles that settled on the laboratory bench, fume hood wall and floor during and after a run. Likewise, as shown in Table 4.1, the amount of CNH collected increased by 183% as the processing time increased from 10 to 30 mins. On the other hand, there was a 9% decrease in the quantity of CNH collected as the processing time increased from 30 to 45 mins. The method used in collecting CNH after synthesis was consistent. The same weighing balance was used, and the measurement procedure was also consistent regardless of the current settings. Difficulties and fluctuations in the amount of CNH collected over time are attributed to the rate of particle retention during the process.

Table 4.1 Effect of time on the quantity of CNH produced.

Time (mins)	CNH quantity (g)
10	0.04 ± 0.01
15	0.05 ± 0.02
30	0.12 ± 0.02
45	0.11 ± 0.03
60	0.13 ± 0.03

Based on our results in Figure 4.4 and Table 4.1, a run time of 30 mins was found to be the best condition for maximizing the yield of CNH. Also from Table 4.1, even though a process time of 60 mins generated the maximum amount of CNH, it is ideal to run the experiment for 30 mins since the quantity of CNH collected only increased by 12% for 60 mins and therefore, not too significant as compared to the energy consumption and time spent when doubling the processing time from 30 to 60 mins. The results presented thus far were based on the use of one Dewar flask. Hence, the throughput of CNH was maximized again for hydrotreating application by increasing the number of Dewar flasks to a total of 6 per day instead of the usual 1 flask/day. As such at these best conditions, i.e. current setting of 90 A and 30 mins processing time per Dewar flask, at least 0.6 g/day CNH could be produced using six Dewar flasks. For further discussions, pristine CNH are represented as: X CNH, where X denotes the current setting used in producing CNH.

4.5.4 Effect of current variation on morphology of CNH

Figure 4.6 (a) to (d) corresponds to low and high magnification TEM images of pristine CNH produced at 70 A and 80 A. The TEM aggregate size of all pristine samples synthesized from

50 to 100 A were in the range of 50 - 110 nm and were similar in morphology as those in Figure 4.5 (a) to (d). Both dahlia-like and bud-like CNH are revealed in the TEM images.

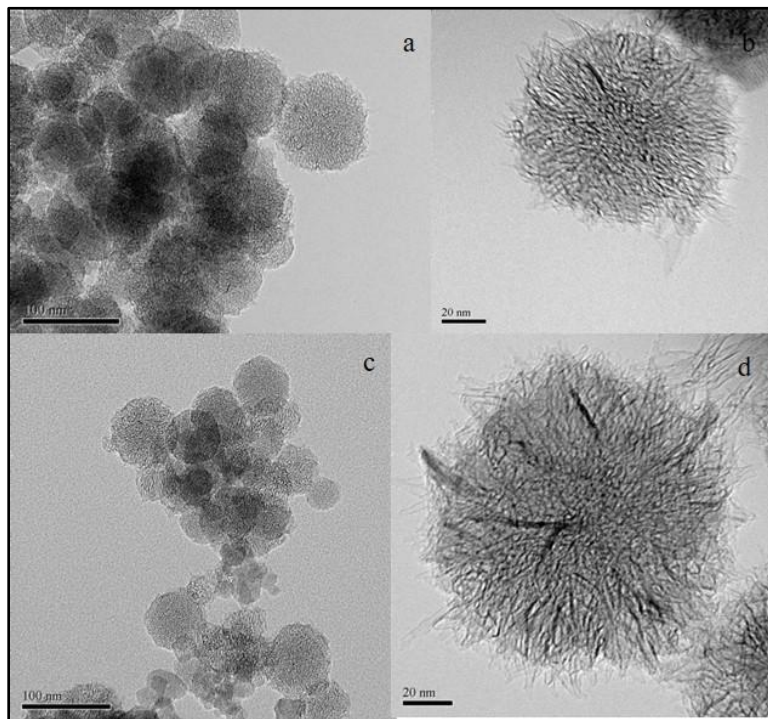


Figure 4.6 TEM of pristine CNH at; a) Low magnification synthesized at 70 A, b) High magnification synthesized at 70 A, c) Low magnification synthesized at 80 A, d) High magnification synthesized at 80 A.

4.5.5 Effect of current variation on textural properties of CNH

BET results of all pristine samples synthesized at various current (50 to 100 A) are shown in Table 4.2, Figure 4.7, and Figure 4.8. From Table 4.2, it can be noted that all the samples synthesized under current settings ranging from 50 to 100 A had mesoporous pore diameters according to IUPAC pore diameter classification (Satterfield, 1991). It was also observed that as the current increased from 50 to 90 A, there was a corresponding increase in the surface area and pore volume. In the case of the pore diameter, synthesis at 50 A generated the minimum pore diameter of ~ 17 nm. However, changing the current settings from 60 A to 80 A resulted in similar pore diameters of about 19 nm. CNH generated at 90 A exhibited the highest pore diameter of about 22 nm. Overall, the best textural properties (surface area, pore diameter, pore volume) for

the pristine CNH was obtained at a current setting of 90 A. A drop in optimum properties was also observed as the current increased from 90 A to 100 A.

Table 4.2 Textural properties of pristine CNH samples based on current settings of (50 -100A).

Sample	Surface Area (m²/g)	Pore Diameter (nm)	Pore Volume (cm³/g)
50A CNH	82 ± 1	16.8 ± 0.1	0.30 ± 0.01
60A CNH	104 ± 1	18.7 ± 0.1	0.40 ± 0.01
70A CNH	109 ± 1	18.4 ± 0.1	0.45 ± 0.01
80A CNH	114 ± 1	18.8 ± 0.1	0.46 ± 0.01
90A CNH	126 ± 1	22.2 ± 0.1	0.61 ± 0.01
100A CNH	106 ± 1	19.8 ± 0.2	0.30 ± 0.02

All the pristine CNH samples showed Type IV isotherms with H3 hysteresis loop typical of solids having mesopores diameters, and with aggregates forming pores like slits shape that are non-uniform in size (Figure 4.7) (Sing et al. 1985). The isotherms for CNH produced at 60 A, 70 A, 80 A and 100 A closely overlap due to the similarity in surface area and pore diameter and signified, almost similar adsorption capabilities under those current conditions. The isotherm generated at 90 A had the highest adsorption capability thereby, confirming that the CNH samples generated at 90 A have the best textural properties (e.g. higher surface area and pore diameter) than the other samples. On the contrary, CNH samples generated at 50 A showed the lowest adsorption capability in agreement with the lowest textural properties obtained for CNH generated at 50 A.

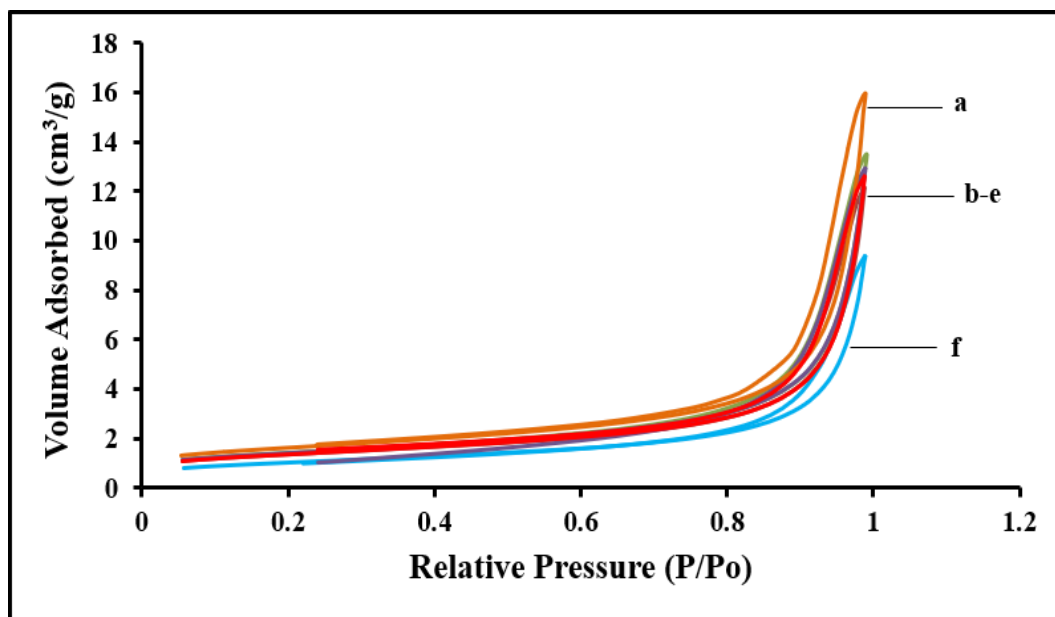


Figure 4.7 BET Isotherms of CNH synthesized at various currents; a) 90A, b-e) 60A, 70A, 80A, 100A, f) 50A.

Figure 4.8 displays the pore size distribution of CNH synthesized from 50 - 100 A. The pore size distribution was narrower for CNH synthesized at higher currents (70 - 100 A) and was in the range of 150 – 450 (Å). The highest and lowest mesopore volumes were achieved with current settings of 90 A and 50 A, respectively. CHN synthesized at 60 A exhibited broader pore size distribution whereas a bimodal pore size distribution was obtained for CNH synthesized at the lowest current setting of 50 A.

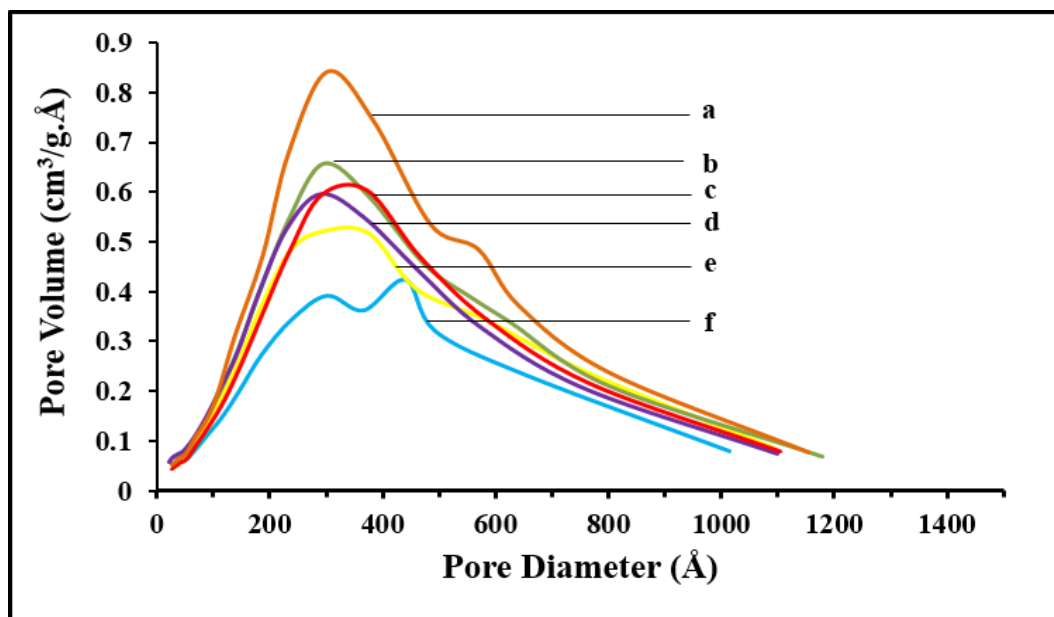


Figure 4.8 Pore size distribution of CNH synthesized at various currents; a) 90A, b) 70A, c) 100A, d) 80A, e) 60A, f) 50A.

4.5.6 Effect of current variation on thermal stability of CNH

TGA graphs of the pristine samples synthesized from 50 to 100 A were similar to the profile in Figure 4.9 corresponding to CNH synthesized at 80 A, and the overall results indicated a total weight loss of about 3% from room temperature (26 °C) to 400 °C. This agreed with literature value which showed that CNH exhibits good thermal stability (Nisha, 2000). The initial weight loss from 26 °C to 120 °C was due to evolution of OH groups. Reduction of weight up to about 120 °C was due to dehydration of water molecules that was physically adsorbed on the sample. Beyond 120 °C, any weight loss is attributed to bonded OH group or impurities. Therefore, at higher temperatures, loss of strongly bound water and OH occurred due to dehydration and/or dehydroxylation. Physical, chemical, thermal and reaction stability can be evaluated using the TGA (Che et al. 2011; Somanathan and Pandurangan, 2010, Hou, 2008).

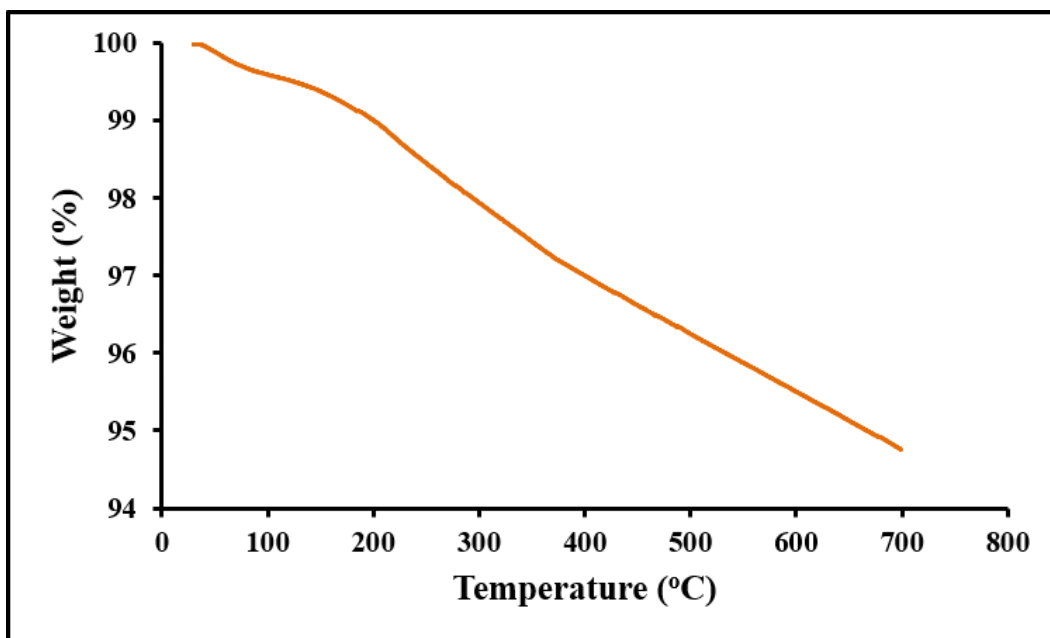


Figure 4.9 TGA analysis of pristine CNH synthesized at 80A.

4.5.7 FTIR analysis of CNH synthesized under different current conditions

The FTIR spectra of the pristine samples are shown in Figure 4.10. All the spectra were similar regardless of current setting. The bands that appeared in each spectrum at $1330 - 1350 \text{ cm}^{-1}$ and $3550 - 3600 \text{ cm}^{-1}$ correspond to C-C and OH groups respectively. The band that appeared around $\sim 1600 \text{ cm}^{-1}$ was due to olefinic C=C bonds (Hussain et al. 2011; Stobinski et al. 2010). The FTIR results imply that the chemical properties of CNH do not vary with change in current settings during synthesis.

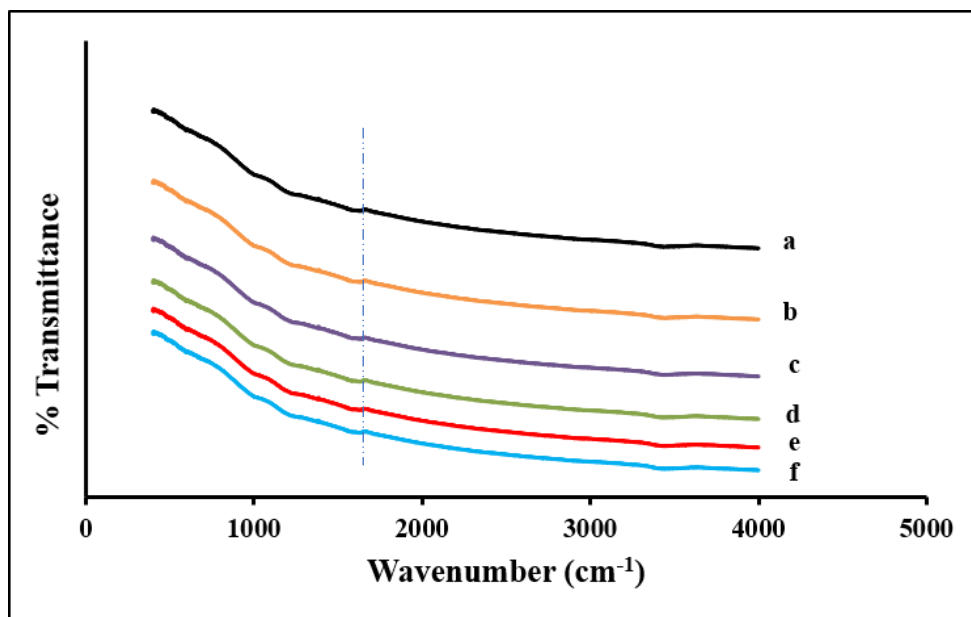


Figure 4.10 FTIR analysis of pristine CNH synthesized at; a) 100A, b) 90A, c) 80A, d) 70A, e) 60A, f) 50A.

4.5.8 XRD analysis of CNH synthesized under different current conditions

XRD patterns of all the pristine samples generated in this study at varying current (50 to 100 A) setting were like the x-ray diffraction patterns for sample generated at 80 A (see Figure 4.11). The narrowness of the XRD peaks are characteristic of crystalline phases. The peak at $2\theta = 26^\circ, 41^\circ, 42^\circ,$ and 56° is in close agreement with literature results and signifies well defined graphitic structures which are still maintained regardless of the different current settings used to produce CNH. This also confirms that CNH are made up of graphite structures that originates from their single graphene sheet framework (Georgakilas et al. 2015; Li et al. 2009; Tao et al. 2007). Usually, the powder XRD will be different among allotropes due to their different atomic arrangement. Thus, the diffraction peaks for a densely packed sp^3 hybridized diamond arrangement, would differ from that of a loosely packed sp^2 hybridized amorphous carbon within certain ranges of 2θ . However, for the CNH produced under different currents and displayed in Figure 4.11, the XRD diffraction patterns were the same since, the arc discharge method is a physical process and all the CNH produced are made from a single graphenic layer (i.e. a simple one atomic layer of graphite with an sp^2 bonded carbon atoms arrangement) (Georgakilas et al. 2015; Cullity and Stock, 2001). Hence for clarification, CNH are made of graphenic layer but not covered with graphenic layer outside as can be misrepresented.

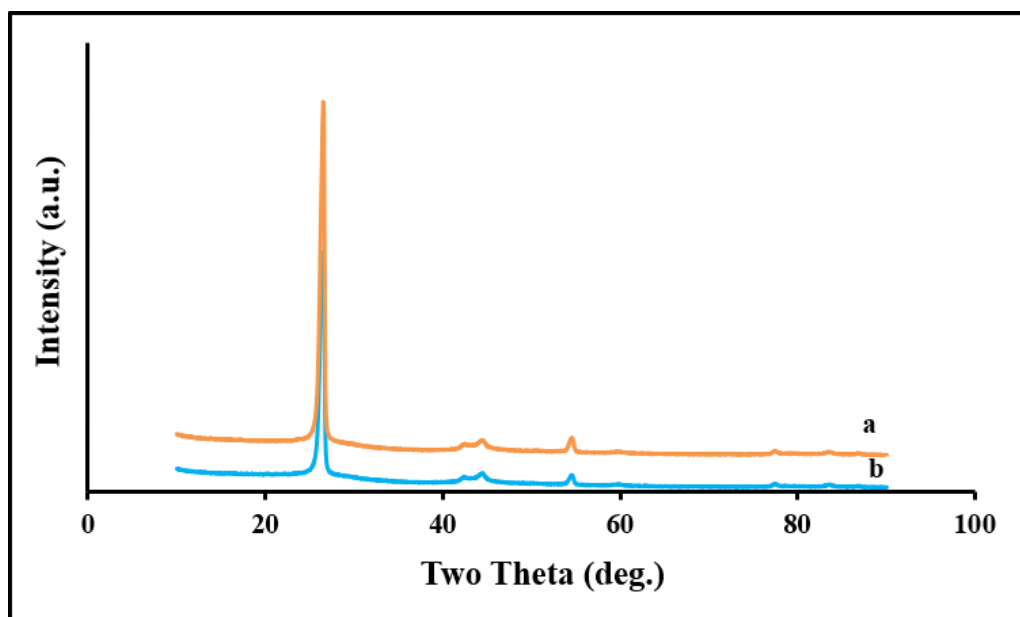


Figure 4.11 XRD analysis of pristine CNH synthesized at 80A.

4.5.9 Raman spectroscopy analysis of CNH synthesized under different current conditions

The Raman spectra and defect evaluation results of CNH samples synthesized from 50 to 100 A is shown in Figure 4.12 and Table 4.2, respectively. From Figure 4.12, it can be observed that all the samples reveal two prominent bands (i.e. D and G) that are characteristic of CNH. The D band reflects the degree of disorderliness or defects in graphitic structures and occurs between the wavenumbers of 1330 to 1380 cm^{-1} . The G band signifies the stretching mode of sp^2 graphite bonds and occur between the wavenumbers of 1580 - 1600 cm^{-1} (Tao et al. 2007; Cancado et al. 2006).

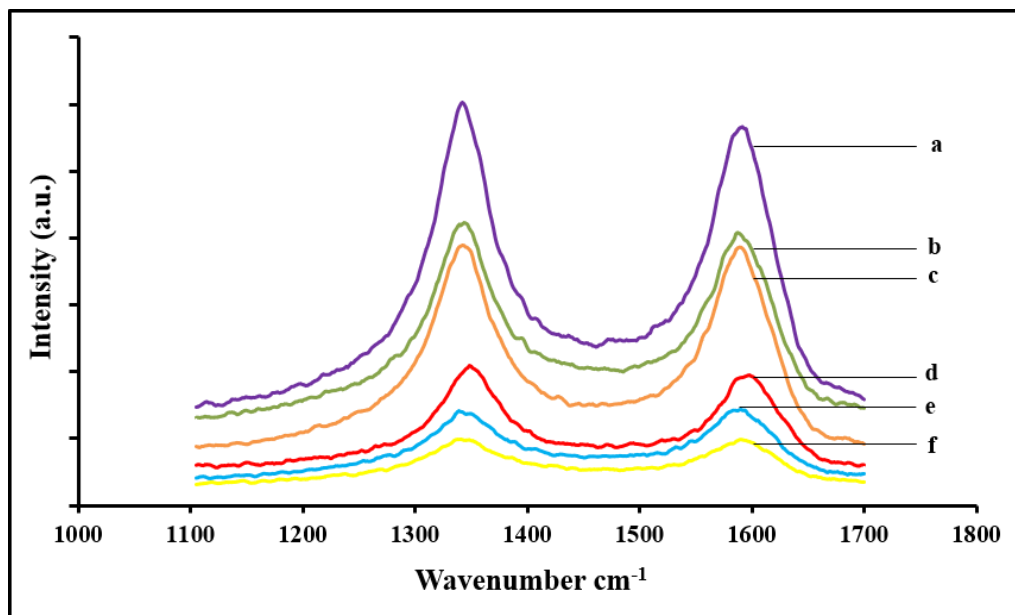


Figure 4.12 Raman spectra of pristine CNH produced at different currents; a) 80A, b) 70A, c) 90A, d) 100A, e) 50A, f) 60A.

The specific D and G band values of each CNH samples produced at different current settings and corresponding intensity ratio (I_D/I_G) of D to G band are shown in Table 4.3. The I_D/I_G ratio is typically used to quantify the quality of CNH samples and is therefore a suitable metric to measure defects that occur as a result of functionalizing CNH during the catalyst preparation stage. Table 4.3 results shows that CNH samples synthesized at 50 A have minimum defects compared to CNH samples generated from 60 A to 100 A. This can be explained by the fact that the degree of turbulence is not so rigorous at lower current settings of 50 A; hence, with such a stabilized arc the chances of defects that accompanies sporadic arcs with less uniformity in particle nucleation and growth reduces (Arora and Sharma, 2014; Charinpanitkul, 2009; Ghorui et al. 2006).

Table 4.3 Examination of pristine CNH quality based on ID/IG ratio.

Samples	D band	G band	I_D	I_G	I_D/I_G
50A CNH	1346 ± 1	1585 ± 1	851.76 ± 0.02	902.70 ± 0.02	0.94 ± 0.02
60A CNH	1346 ± 1	1586 ± 1	579.03 ± 0.02	582.03 ± 0.02	0.99 ± 0.02
70A CNH	1343 ± 1	1586 ± 1	2635.76 ± 0.02	2522.56 ± 0.02	1.04 ± 0.02
80A CNH	1342 ± 1	1588 ± 1	4302.76 ± 0.02	3998.02 ± 0.02	1.08 ± 0.02
90A CNH	1342 ± 1	1587 ± 1	2864.82 ± 0.02	2817.56 ± 0.02	1.02 ± 0.02
100A CNH	1343 ± 1	1588 ± 1	1400.26 ± 0.02	1300.80 ± 0.02	1.08 ± 0.02

4.6 Conclusions

CNH with aggregate diameter between 50 - 100 nm can be fabricated on a laboratory scale using the arc discharge method. The quantity of CNH produced can be maximized by using 5- 6 more Dewar flasks at a current setting of 90 A and a shorter processing time of 30 mins for each Dewar flask. This work demonstrates that in the arc discharge method for synthesis of CNH, there are limitations on the current setting and processing time that can be used to generate substantial amount of particles. (A case in point is that the maximum current setting of 100 A resulted in a decrease in yield and production rate of CNH. In addition, there was no appreciable increase in yield of CNH beyond a processing time of 30 mins). The quantity of CNH produced can be improved by modifying the design of the reaction setup (e.g. inclusion of baffles and extension of the length of electrodes support holder). Lack of uniformity of the arc between the two rods may impact the uniformity of CNH production (quality, amount, yield, type). Change in current impacts the textural properties, adsorption capabilities and pore size distribution as evidenced by the BET results of CNH synthesized at 50 A and 90 A. Varying current tends to have an impact on nucleation and growth of particles. The highest surface area, pore diameter and pore volume were found to be 126 m²/g, 22 nm and 0.61 cm³/g respectively and were obtained using a current setting of 90 A. Similarities in FTIR spectrum and XRD patterns irrespective of the current setting provides empirical evidence that chemical properties of CNH do not vary with current. CNH also maintain good thermal stability since the overall weight loss even at elevated temperatures of 450 °C was not more than 0.5%. The identity of CNH was confirmed by the presence of prominent D and G bands. The I_D/I_G ratios revealed that the defects in CNH as a result of the 5-member ring at the tips of CNH are inevitable. The textural properties of CNH synthesized at 90 A are desirable for use as catalyst support in hydrotreating applications.

CHAPTER 5

Functionalization and Characterization of Carbon Nanohorns (CNH) for Hydrotreating of Gas Oil

The content in this chapter was published in, Topics in Catalysis and the citation is; Aryee, E.; Dalai, A. K.; Adjaye, J. “Functionalization and Characterization of Carbon Nanohorns (CNH) for Hydrotreating of Gas Oils,” Topics in Catalysis, 2014, 57, 796 – 805.

A synopsis from this phase of work had been presented at these conferences:

- E. Aryee, A. K. Dalai, J. Adjaye, “Synthesis and characterization of carbon nanohorns for hydrotreating of gas oils,” Oral presentation at 245th American Chemical Society Conference, New Orleans, United States, April 7-11, 2013.
- E. Aryee, A. K. Dalai, J. Adjaye, “Hydrotreating of gas oils using other carbon particles generated from arc discharge of pure graphite rods,” Oral presentation at 23rd Canadian Symposium on Catalysis, Edmonton, Alberta, Canada, May 11-14, 2014.

Contributions to this phase of work

Choice of acid treatment method (liquid oxidation using HNO₃) and conditions (temperature, time or HNO₃ concentration) to vary was decided by the Ph.D. candidate, Emma Aryee. Emma Aryee was also responsible for running acid treatment experiments, characterizing solid and liquid samples, making catalysts, conducting hydrotreating experiments, processing all data and interpreting results after critical reviews, suggestions and guidance from my supervisors; Dr A.K. Dalai and Dr. J. Adjaye. Writing and revision of the manuscript for this phase of work was done by Emma Aryee. Drs. Dalai and Adjaye reviewed the manuscript and rebuttals prior to its final publication.

Contribution of this chapter to the overall Ph.D. work

The intent of this chapter was to add functionality to an otherwise inert CNH material in order to create and increase the number of oxygen-containing surface sites for anchorage of metals.

Functionalization procedure would therefore improve CNH properties. Additionally, this would enhance the hydrophilicity and reactivity of CNH. As a result, the interior cavity of CNH would become easily accessible for reactions during catalyst formulation and hydrotreating experiments. Thus, the applicability of CNH in the area of hydrotreating would be tremendously boosted. The end results from this phase would help to establish the best condition for functionalizing CNH without damaging its structure. Subsequently, this best condition would serve as a starting point in functionalizing all other carbon materials that would be used in this research to achieve high HDS and HDN activity. Characterization of all functionalized CNH would help to understand the physico-chemical properties of CNH under different acid treatment conditions.

5.1 Abstract

Improvement in the functionality of carbon nanohorns (CNH), a novel carbon nanomaterial, for hydrotreating applications is investigated in the present work. The current work was carried out by using pristine CNH synthesized by the submerged arc in liquid nitrogen and their corresponding physicochemical properties were investigated. The surface area, pore diameter and pore volume of the pristine CNH are 129 m²/g, 23.1 nm, and 0.64 cm³/g respectively. Functionalizing the CNH with 30 wt% HNO³ under reflux for 15 min to 4 h at 110 °C modified the physical and chemical properties. 30 min functionalization duration was found to be the best, and a co-impregnation method was used to load Ni (2.5 wt%) and Mo (13 wt%) onto the support. Techniques used to thoroughly characterize the properties of pristine CNH, functionalized CNH and NiMo/CNH catalyst include: Brunauer-Emmett-Teller (BET), Fourier Transform Infrared (FTIR) and Raman Spectroscopy. Type IV isotherm and mesoporous pore diameter was observed for CNH in its pristine, functionalized or catalyst form. An increase in surface area of over 500 m²/g was also attained under optimum functionalized conditions. The pore volume of acid treated CNH samples for hydrotreating increased by ~10 % as compared to the pore volume of the pristine CNH. FTIR results revealed the presence of carboxylic acid (–COOH) groups on the functionalized CNH and I_D/I_G ratios from Raman spectroscopy was used to assess the increase in defects (nanowindow) on functionalized CNH. Successful enhancement of CNH properties via functionalization raises the prospect that CNH can be used as a catalyst support for hydrotreating.

5.2 Introduction

Hydrotreating is a catalytic hydrogenation reaction that removes sulfur, nitrogen, oxygen, metal atoms and unsaturated hydrocarbons from gas oils. Global scarcity in regular crudes and high cost of oil supplies necessitates an upgrade via, hydrotreating of Athabasca bitumen which contains heavier and higher amount of contaminants (e.g. 2 - 4 times higher amounts of sulfur, nitrogen and aromatic compounds) for desired end products (Jarullah et al. 2011; Leliveld and Eijssbouts, 2008; Valavarasu et al. 2003; Grange and Vanhaeren, 1997). One way of optimizing the hydrotreating performance is to enhance the hydrotreating catalyst (e.g. carbon supported catalyst) by fine tuning their porosity and chemical properties for a specific experimental goal (Ferdous et al. 2006; Furimsky, 1998). To date, examples of carbon-supported material that have been used in hydrotreating include activated carbon, carbon black, mesoporous carbon, carbon nanotubes (CNT) (Hussain and Ihm, 2009; Sigurdson et al. 2009; Hynaux et al. 2007; Sano et al. 2004).

Pristine CNH are usually inert and hydrophobic. CNH is a porous nanocarbon material and mainly consist of fully enclosed nanoscale spaces. The pores in aggregated CNH can also be divided into two i.e. internanohorn and interstitial pores found between the tubes that make up the nanohorn aggregate, and intranahorn pores found inside the hollow interior spaces (i.e. spaces behind the tip) of the individual tubes, and therefore available after nanowindows have been etched on the surface via oxidation. The size and number of nanowindows are influenced by the oxidation conditions (Krungleviciute et al. 2008; Ajima et al. 2004; Bekyarova et al. 2005; Yudasaka et al. 2008). Although CNH have hexagonal geometry which is similar to graphene, research shows that the side wall, tip and bent sides of CNH consist of pentagonal and heptagonal rings that are major defective sites on CNH and are therefore more likely to be opened at the onset of functionalization. In terms of the pore size, a CNH aggregated structure consist of micropores and mesopores since its interhorn wall distance of 0.4 nm is greater than the 0.335 nm interlayer spacing of graphite (Ajima et al. 2004; Bekyarova et al. 2002; Murata et al. 2001; Lordi et al. 1999). Metals impregnated on the support during catalyst formulation get deposited on the external walls as well as the inside of the nanohorn tubes after going through the opened pores. High resolution TEM images from some studies show clear details of the pores before and after metal deposition (Krungleviciute et al. 2008; Ajima et al. 2004; Bekyarova et al. 2005; Yudasaka et al. 2008).

Functionalization of CNH can be accomplished through chemical oxidation. Examples include gas phase oxidation (with air, O₂, CO₂ or Cl₂), liquid phase oxidation (by treating with

acids under reflux) and electrochemical oxidation. With gas phase oxidation, defect formation and presence of functional groups are less pronounced compared with liquid oxidation. Thermal oxidation can be carried out by oxidizing the CNH samples for 10 - 15 min at 350 - 700 °C at a heating rate of 10 °C/min. In addition, thermal oxidation in CO₂ at higher temperatures (> 850–900 °C) can reduce the oxygen content of nanotubular structures due to thermal decomposition and evolution of oxygenated groups on CNH walls as the reaction proceeds (Bekyarova et al. 2003). Examples of commonly used oxidants in liquid oxidation are HNO₃, H₂O₂, HCl and H₂SO₄. Functionalization enhances the surface chemistry of CNH due to attachment of oxygenated groups (–OH, –C=O and –COOH) on CHN surfaces. Functionalization also improves the solubility of CNH in aqueous and organic medium. Oxidized CNH are highly dispersed due to the hydrophilic nature of the pore edges after functionalization, and as a result the adsorption rates become much more pronounced when CNH are used in their highly dispersed state (Pagona et al. 2009; Hou et al. 2008; Pagona et al. 2006; Bekyarova et al. 2002;)

Carbon nanohorns exhibit certain unique properties that make them useful in applications such as hydrogen storage, drug delivery, fuel cell, and biosensors (Brandao and Passeira, 2011; Liu et al. 2010; Ajima et al. 2005; Nisha et al. 2000). For instance, the high surface area (1006–1464 m²/g), high pore volume (0.47–1.05 mL/g) and high nanospace porosity exhibited by CNH make them useful in gas adsorption processes. CNH rough external structures coupled with its inhomogeneous structure and inherent pores (i.e. internal and interstitial pores) renders CNH beneficial when used as catalyst support (Yuge et al. 2012; Itoh et al. 2008; Utsumi et al. 2005; Yang et al. 2004; Murata et al. 2001). Use of CNH as potential support for hydrotreating has therefore garnered interest in this study since some of these unique properties possessed by CNH may be beneficial for hydroprocessing application. This phase of work seeks to develop a novel CNH support for hydrotreating of gas oils. The optimum liquid oxidation condition for functionalizing pristine CNH support material is also investigated.

5.3 Experimental method

5.3.1 CNH functionalization, catalyst preparation and hydrotreating experiment

The pristine CNH support material used in the present work was synthesized at a constant current setting of 90 A by using the submerged arc discharge in liquid nitrogen method (Aryee et al. 2017). In order to improve the functional or surface properties of as-synthesized CNH, the

pristine CNH samples were magnetically stirred in a flat bottom flask and oxidized using 7 M HNO₃ at 110 °C under reflux for 15, 30 min, 1, 2, and 4 h. After acid treatment, the resulting solution was filtered and the residue was thoroughly rinsed with de-ionized water until a neutral pH of filtrate was attained. Filtration of acid treated CNH samples was done using MF-Millipore membrane filters of 1.2 µm pore size (Millipore, Canada). The residue was then air dried for at least 24 h before catalyst preparation and further characterization. Since all functionalized samples were initially produced under a constant current setting of 90A, oxidized samples are denoted as 90A CNH_T where, T represents the time taken to functionalize the samples i.e. 15, 30 min, 1, 2 and 4 h.

To prepare the catalyst, co-incipient wetness impregnation method was used to disperse 2.5 wt% Ni and 13 wt% Mo onto CNH support from their respective aqueous metal precursor solutions i.e. ammonium heptamolybdate [(NH₄)₆Mo₇O₂₄H₂O] and nickel nitrate [Ni(NO₃)₂·6H₂O]. The resulting impregnated sample was oven-dried at 110 °C for 5 h before calcining it in a fine powdered form at 450 °C for 5 h. Calcination was done in a vertical furnace under an argon flow of 50 mL/min. 5 mL of NiMo/CNH catalyst diluted with 12 mL of 90 mesh size (SiC) was then loaded into a trickle-bed reactor (Figure 1.1). This packed combination of diluted CNH catalyst and 90 mesh SiC (catalyst bed) was positioned in between layers of SiC comprising of different mesh sizes at the top and bottom of the reactor. A precise loading pattern is described in Chapter 1 of this thesis. The hydrotreating reactor was pressurized to 8.8 MPa, and 2.9 vol% butanethiol in straight run gas oil (VOLTESSO 35) was prepared as sulfiding feed solution for the initial stage of the experiment. The reason for sulfidation of the catalyst after catalyst preparation and calcination is that at this point, the catalyst exists in an oxide form and therefore must be sulfided before the commencement of any hydrotreating experiments to make it active to catalyze HDS and HDN reactions. Sulfidation also makes the catalyst selective to perform their expected cuts. Thus, once the catalyst had been loaded into the reactor, 100 mL of the sulfiding feed solution was used to wet the catalyst. The pre-wetted catalyst was initially sulfided at 193 °C for 24 h such that, a liquid hourly space velocity (LHSV) of 2 h⁻¹ was achieved. A second sulfidation step was carried out for another 24 h at a temperature and LHSV of 343 °C and 2 h⁻¹, respectively. Following this second sulfidation period, the sulfiding solution feed was replaced with the real gas oil feed (i.e. coker light gas oil also referred to as CLGO derived from Athabasca

bitumen). The fully sulfided catalyst was then precoked with CLGO for 3 days at a temperature of 370 °C and a constant LHSV and pressure of 2 h⁻¹ and 8.8 MPa, respectively.

Hydrogen flow to the reactor was kept constant at 50 mL/min and a gas to oil ratio of 600 mL/mL was used. Hydrodesulfurization (HDS) and Hydrodenitrogenation (HDN) activity studies at three different temperatures i.e. 370, 350 and 330 °C began as soon as the precoking duration was completed. Each temperature study lasted 1.5 days. CLGO-hydrotreated samples were collected every 12 h and a stabilization period of 12 h was also allowed in between the different experimental conditions. Thus, samples were discarded at the end of the stabilization period to ensure the next 12 h sample collection was processed at the desired set point. All samples collected were stripped with nitrogen for 2 h to remove any dissolved ammonia and hydrogen sulfide. Stripped hydrotreated liquid products were analyzed using an Antek 9000 NS analyzer to determine the nitrogen and sulfur conversion. ASTM D4629 and ASTM D5463 methods were used to analyze total nitrogen and sulfur content, respectively. Sulfur content analysis is based on fluorescence whereas, the total nitrogen analysis is based on chemiluminescence.

5.4. Characterizations

In order to get a better understanding of the effect of functionalization on CNH properties and their consequent effect on hydrotreating performance, acid treated and/or non-treated solid samples, were analyzed using BET, HRTEM, FTIR, Raman spectroscopy, XRD, TGA and Boehm titration. Treated and non-treated gas oil samples were also analyzed using an NS analyzer. A summary of these techniques and sample analysis procedure are reported in Chapter 3 of this thesis.

5.5 Results and discussion

5.5.1 BET analysis of pristine and functionalized CNH and NiMo/CNH catalyst

The textural properties of pristine CNH, functionalized CNH and NiMo/CNH catalyst are shown in Table 5.1. These results are based on three replicates. Compared to the pristine CNH sample synthesized at 90A, a general observation from Table 5.1 shows that functionalization results in an increase in surface area and a decrease in pore diameter. In addition, the pore volume of functionalized samples could be less or more than the pristine sample depending on the functionalization processing time. A close look at the surface area results in Table 5.1 shows that a steady increase in surface area occurs as the functionalization time increased from 15 to 30 min

however, increase in functionalization time from 1 to 4 h resulted in a steady decrease in the surface area from the optimum value of 547 m²/g for samples treated at 30 min to 298 m²/g for samples treated for 4 h. According to Murata *et al.* (2001) a drop in the surface area is attributed to the appearance of nanosized voids that merge together to form macroscopic voids.

Table 5.1 Textural properties of pristine and functionalized CNH and NiMo/CNH catalyst.

Samples	Surface Area (m²/g)	Pore Diameter (nm)	Pore Volume (cm³/g)
90A CNH	129 ± 2	23.1 ± 0.1	0.64 ± 0.01
90A CNH_15min	448 ± 2	14.7 ± 0.2	0.78 ± 0.01
90A CNH_30min	547 ± 2	12.3 ± 0.2	0.70 ± 0.01
90A CNH_1h	454 ± 2	9.7 ± 0.2	0.41 ± 0.01
90A CNH_2h	399 ± 2	9.7 ± 0.2	0.34 ± 0.01
90A CNH_4h	298 ± 2	9.6 ± 0.1	0.26 ± 0.01
NiMo/CNH	445 ± 2	12.5 ± 0.1	0.45 ± 0.01

In the case of the pore diameter there was a steady decrease in pore diameter as the functionalization time increased from 15 min to 4 h. As evidence in Table 5.1, the pore volume of the pristine CNH samples increased after 15 to 30 min of acid treatment but dropped significantly as the acid treatment duration increased from 1 to 4 h. The steady drop in pore volume beyond functionalization time of 1 h is attributed to the breaking of pore walls as a result of over oxidation (Utsumi *et al.* 2005). This also supports the coalesced TEM images observed for samples treated with acid for more than 1 h. The surface area and pore volume results of samples functionalized for 15 and 30 min also agrees closely to literature reports that showed an enhanced surface area and pore volume after functionalization due to the formation of nanowindows on the surfaces of the acid treated CNH (Pagona *et al.* 2009; Utsumi *et al.* 2005). Increase in surface area as a result of an enhanced nanowindows formation on CNH is expected since, the openings or windows make it possible to access internal nanopores of CNH in addition to the interstitial pores and external surface (Utsumi *et al.* 2005). Overall, mesoporous pore diameter was also observed for as-synthesized CNH, functionalized CNH and NiMo/CNH catalyst. In Figure 5.1, the BET isotherms of pristine CNH, functionalized CNH and NiMo/CNH catalyst reveal that all the isotherms are Type IV which is consistent with mesoporous material with H3 hysteresis loop (Lynch 2003; Sing *et al.* 1985). In general, N₂ adsorption capacity of CNH was improved by acid treatment and, the adsorbed amount by NiMo/CNH catalyst and CNH functionalized for 15 and 30 min were at least thrice that of the pristine CNH sample as seen in Figure 5.2. This is because with acid treated

samples, a remarkable increase in surface areas occurs and consequently, more surface area becomes available for reactions. As such, increased surface area leads to an increase in the adsorption capacity of the samples as evident from their isotherms having higher surface areas than pristine CNH (Figure 5.2).

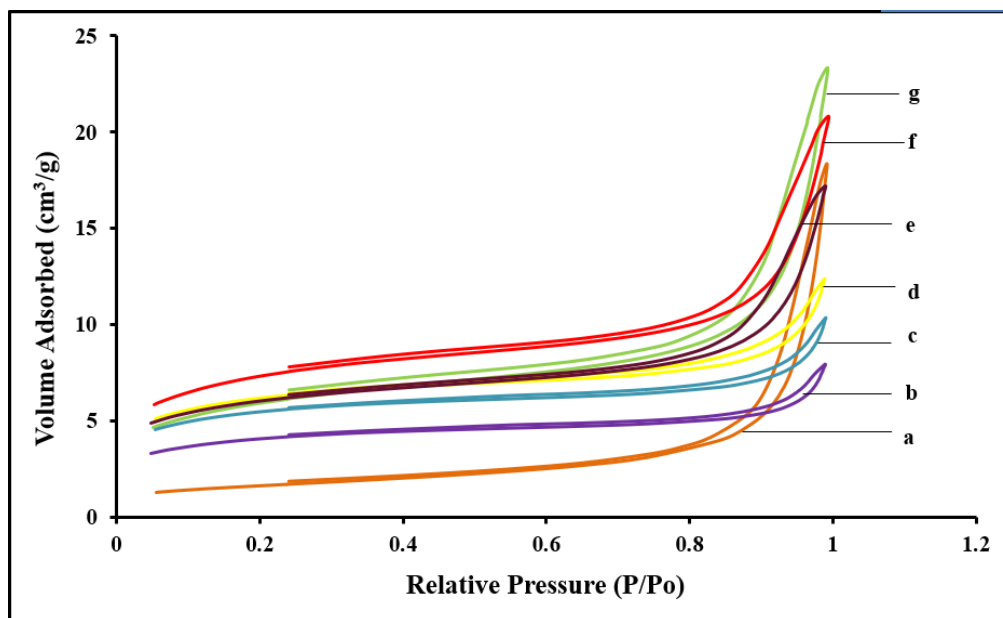


Figure 5.1 BET Isotherms of; a) 90A CNH, b) 90A CNH_4 h, c) 90A CNH_2 h, d) 90A CNH_1 h, e) NiMo/CNH, f) 90A CNH_30 min, g) 90A CNH_15 min.

Functionalized CNH samples also adsorb better than pristine CNH samples since their pores are available once nanowindows have been created on the surfaces (Utsumi, et al. 2005). The adsorption capacity of NiMo/CNH catalyst may drop due to an interaction (blocking) of the metal precursors with the support. This explains why the adsorption isotherms for samples functionalized for 15 and 30 min were higher than the NiMo/CNH catalyst (Itoh et al. 2008). The shortness of the adsorption and desorption branch in P/P_0 regions beyond 0.8 for samples functionalized for 1 to 4 h as compared with the results for the NiMo/CNH catalyst and CNH samples functionalized for 15 and 30 min signifies structural changes associated with harsh acid treatment as revealed by TEM image (see Figure 5.4c) (Bekyarova et al. 2002). From Figure 5.2, the pore sizes of pristine CNH are bigger and have similar profile as that of the NiMo/CNH catalyst and samples functionalized for 15 and 30 min. On the contrary, the pore sizes became smaller/flatter with longer functionalization processing time (1–4 h) and therefore implies that

some pores have collapsed as a result of prolonged acid treatment. This is also evident in the fused TEM images of the acid treated samples (e.g. Figure 5.3c) (Utsumi et al. 2005; Murata et al. 2001).

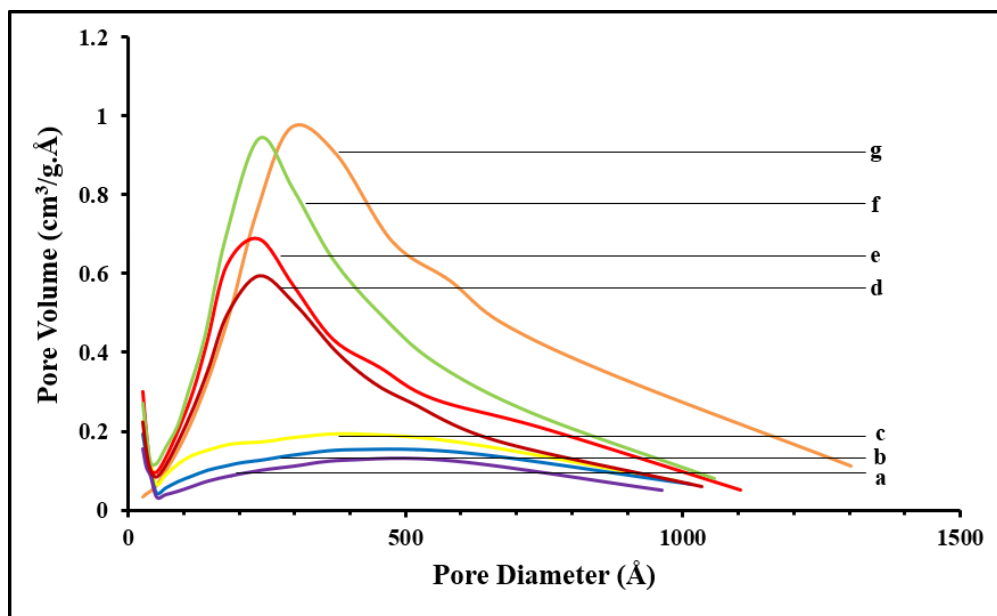


Figure 5.2 Pore size distribution of; a) 90A CNH_4 h, b) 90A CNH_2 h, c) 90A CNH_1 h, d) NiMo/CNH catalyst, e) 90A CNH_30 min, f) 90A CNH_15 min, g) 90A CNH.

5.5.2 Morphology of pristine and functionalized CNH and NiMo/CNH catalyst

Common CNH assemblies such as budlike and dahlia-like CNH were seen in the TEM images (see Figure 5.3a–e). From our results, an aggregated CNH size within the range of 50–110 nm was consistent with published results in literature (Yuge et al. 2007; Wang et al. 2004; Yamaguchi et al. 2004; Iijima et al. 1999). The TEM image represented in Figure 5.3c shows that longer acid treatment duration causes the aggregated SWNH structure to coalesce after treatment compared to the rest of the TEM images in Figure 5.3 that showed loose aggregated particles. The presence of nanowindows on CNH as a result of acid treatment was not clearly visible from the TEM images since the resolution was not strong enough to locate and capture these on CNH. However, the occurrence of nanowindows on the surfaces of functionalized CNH and most especially on the 15, and 30 min functionalized samples has already been established from an enhancement of surface area and pore volume of those samples as well as the nature of their isotherms as compared to the pristine samples. Figure 5.3d and e shows the presence of dark clumped spots which were not present in the pristine sample (Figure 5.3a) and therefore suggest

that Ni and Mo have been incorporated into 90A CNH_30 min support in a fairly disperse state after impregnation of this support with the metal precursors of choice. Figure 5.3d and e shows that some distinct aggregate shapes and sizes were still retained in NiMo/CNH catalyst prior to hydrotreating, and this finding validates the results from other researchers who proved the robustness of the horns and the inability to separate these individual horns (Azami et al. 2008; Iijima et al. 1999).

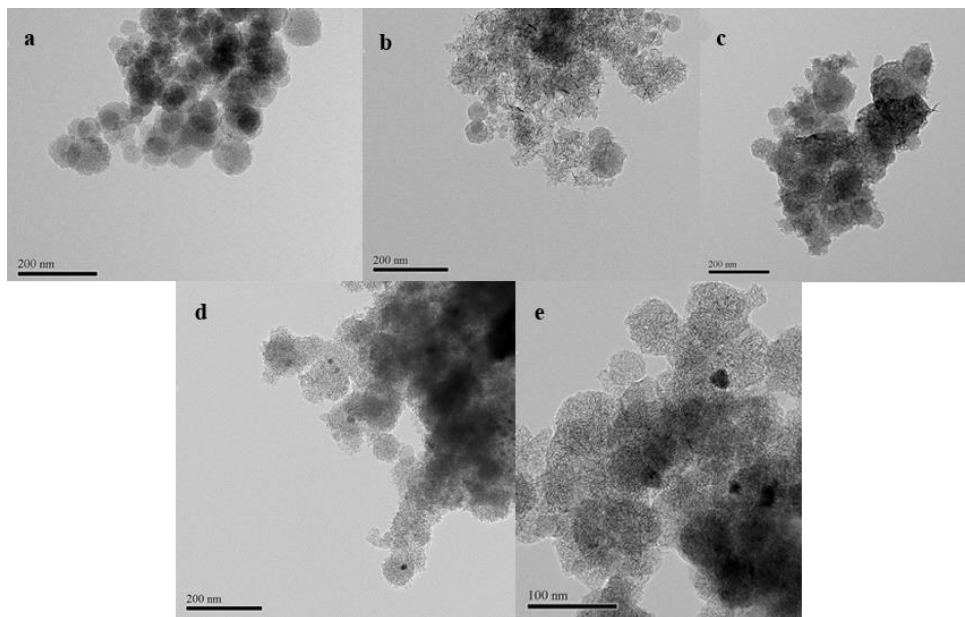


Figure 5.3 TEM images of; a) 90A CNH, b) 90A CNH_30 min, c) 90A CNH_1 h, d) NiMo/CNH (low magnification), e) NiMo/CNH (high magnification).

5.5.3 Thermal stability of pristine and functionalized CNH and NiMo/CNH catalyst

Results of the thermal stability of pristine CNH, CNH functionalized for 30 min and NiMo/CNH catalyst are shown in Figure 5.4. Overall, a total weight loss of less than 8 % was obtained for all three samples. In addition, an initial weight loss from room temperature to approximately 100 °C for all three samples ascribes to the evolution of physically adsorbed water on the surfaces of respective CNH. Following this as evidenced by other researchers, a weight loss at temperatures less than 400 °C for all three samples is due to the loss of amorphous carbon whereas, residual graphitic structures are contributing factors to the weight loss at temperatures greater or equal to 600 °C (Battiston et al. 2009; Azami et al. 2008; Utsumi et al. 2005).

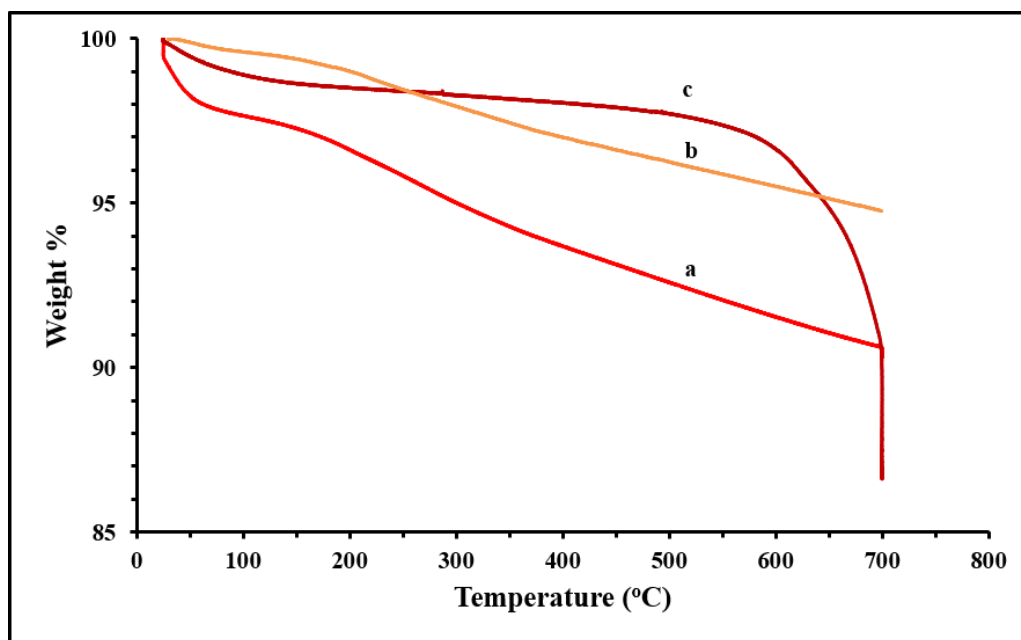


Figure 5.4 TGA analysis of; a) 90A CNH_30 min, b) 90A CNH and c) NiMo/CNH catalyst.

From Figure 5.4, it can be observed that there was a drastic drop in weight for the NiMo/CNH sample at about 700 °C and this can be related to the findings from Bekyarova *et al.* (2002) which showed that at higher temperatures of at least 700 °C, CNH was prone to burn-off due to instability. For the NiMo/CNH catalyst, the drastic thermal degradation around 700 °C could also be linked to deactivation by sintering, which causes a loss of catalytic activity as a result of a loss of active surface area resulting from prolonged (> 500 °C) exposure to high-gas phase temperatures. Loss of active surface area can be attributed to growth of metals deposited on the support, support collapse, crystal agglomeration, clogging of pores inside the catalyst pellet or surface recrystallization (Fogler, 2006; Bartholomew, 2001). In the case of the pristine and functionalized CNH, no drastic weight loss as a result of sintering was observed around 700 °C. Comparison of the thermal stability results of the samples shown in Figure 5.4 reveals that CNH functionalized for 30 min exhibited the greatest weight loss and this suggests that the functionalized samples have some oxygenated groups which get decomposed as time progresses (Bekyarova *et al.* 2003). In (2004), Zhang *et al.* added that the thermal stability of acid treated samples may decrease as the nitric acid processing time increases and this is possible because higher nitric acid processing time or over oxidation already causes some degree of degradation in CNH as confirmed by our BET results (e.g. collapse of pore walls at higher acid treatment duration)

hence, with higher temperature heat treatment the tendency for degradation to worsen is also on the ascendency. Thus, although the shape of the TGA graph for pristine and functionalized CNH looks similar, the functionalized CNH experienced a greater weight loss due to decomposition of oxygenated group as time progresses. In the case of the catalyst, drastic weight loss at around 700 °C was attributed to both, a burn-off of CNH due to instability and deactivation by sintering. TGA of all the three samples shown in Figure 5.4 indicates that the thermal stability of NiMo/CNH catalyst in a typical hydrotreater is practicable since the weight loss for NiMo/CNH catalyst was less than 2.5 % at 450 °C compared to the 90A CNH (pristine) and 90A CNH_30 min (functionalized) that showed weight losses of about 3.5 and 6.9 % respectively at 450 °C. Usually for hydrotreating runs, operating temperatures do not exceed 425 °C.

5.5.4 XRD analysis of pristine CNH and NiMo/CNH catalyst

Broad angle X-ray diffractogram patterns of the pristine CNH and NiMo/CNH catalyst samples are shown in Figure 5.5. For the 90A CNH sample shown in Figure 5.5b, a sharp peak at two theta degree of approximately 26° is representative of a graphite (002) framework. The existence of two other graphitic broad peaks were also confirmed at two theta degrees of 42° (100) and 44° (101) (Battiston et al. 2009; Anderson et al. 1998). The presence of graphite is attributed to the single layer of graphenic wall from which CNH are made of (Georgakilas et al. 2015; Ajima et al. 2004).

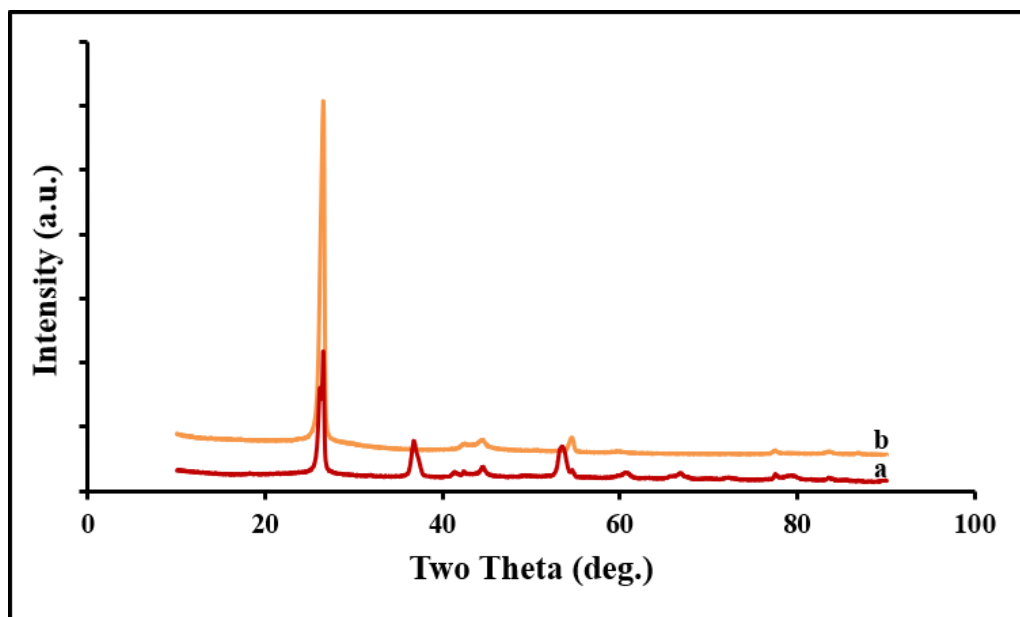


Figure 5.5 XRD analysis of; a) NiMo/CNH catalyst, b) 90A CNH.

From Figure 5.5a, a sharp peak on NiMo/CNH catalyst at approximately 26° but with much lesser intensity than the same peak on pristine CNH (Figure 5.5b) indicates that MoO_3 has superimposed the graphitic finger print resonating from the CNH support (Badoga et al. 2012). A close look at Figure 5.5a shows a mixture of both crystalline and amorphous phase, and the emergence of additional sharp peaks at 36° and 52° confirms a fair dispersion after NiO and MoO_3 have been impregnated on the 90A CNHs_30 min support as already been observed from the TEM images of the NiMo/CNH catalyst.

5.5.5 FTIR analysis of pristine and functionalized CNH

The FTIR spectra of pristine and functionalized samples are shown in Figure 5.6. From these spectra since, the KBr pellet method was used, the band at $1,640\text{ cm}^{-1}$ corresponds to water that had been absorbed on the KBr. The spectra of functionalized samples show an additional $\text{C}=\text{O}$ band. The $\text{C}=\text{O}$ band indicative of stretching vibration in carboxyl, ketones and aldehydes groups emerged at $1,780\text{ cm}^{-1}$. However, due to the appearance of a small peak at $1,420\text{ cm}^{-1}$ the band at $1,780\text{ cm}^{-1}$ is more representative of carboxyl acid groups. From Boehm titration, the acid strength of the carboxylic acid groups on the optimum functionalized support (90A CNHs_30 min) surface was found to be 0.25 mmol/g . The FTIR spectra also shows a band at approximately $3,500\text{ cm}^{-1}$ that signifies phenolic O–H stretching vibrations conjugated with $\text{C}=\text{O}$ whereas a band at

about $1,270\text{ cm}^{-1}$ is assigned to the bending modes of O–H (Teng and Tang, 2008; Xiao and Thomas, 2004; Fanning and Vannice 1993). The presence of carboxylic acid groups on the surfaces of functionalized CNH samples highlights our success in introducing oxygenated functional groups at the defect sites of CNH, and this has already been proven based on our findings from BET, TGA and Raman analyses.

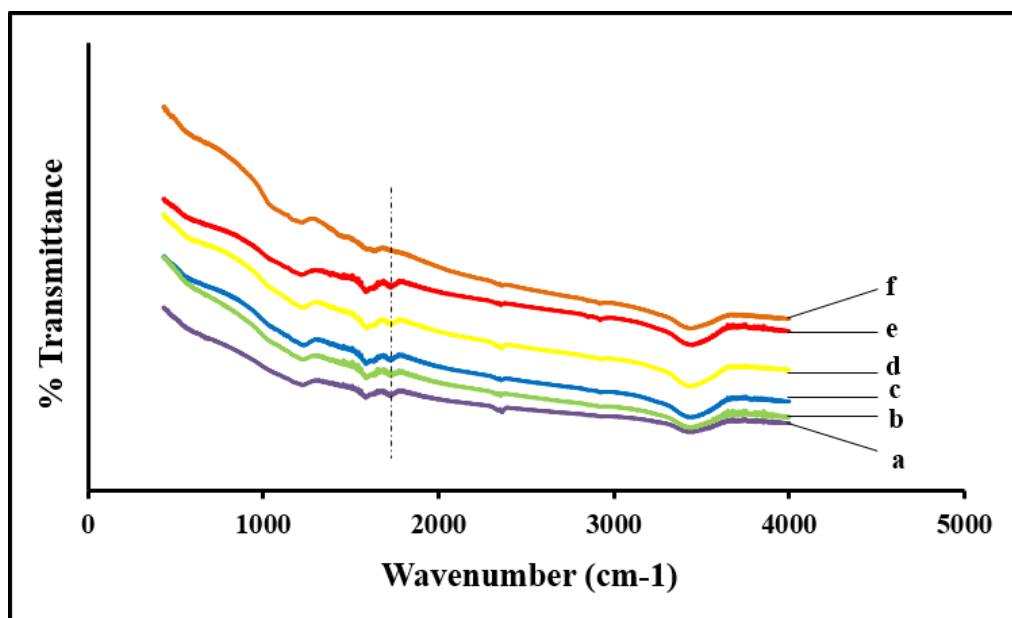


Figure 5.6 FTIR analysis of; a) 90A CNH_4 h, b) 90A CNH_15 min, c) 90A CNH_2 h, d) 90A CNH_1 h, e) 90A CNH_30 min, f) 90A CNH.

5.5.6 Raman spectroscopy of pristine and functionalized CNH

From Figure 5.7, Raman spectroscopy results of both the pristine CNH sample and all functionalized CNH samples showed two significant bands associated with CNH i.e. the D and G bands which occurred between the wavenumbers of $1,330\text{--}1,380$ and $1,580\text{--}1,600\text{ cm}^{-1}$, respectively however, specific D and G values for each sample are shown in Table 5.2. The D band corresponds to the degree of disorderliness disorder (defects) in graphitic structures whereas, the G band corresponds to the stretching mode of sp^2 graphite bonds. The presence of defects in pristine and functionalized CNH was further elucidated by use of Raman spectroscopy. The intensity ratio of the D band relative to the G band (I_D/I_G) signifies the presence of defective sites in the graphitic carbon. Wen *et al.* (2010) reported that a value of about 0.91 confirms that the surface of CNH has significant defect sites. An I_D/I_G ratio of 0.97 for the 90A CNH sample

validates the generality of the fact that CNH has defective sites (tips and bent areas) composed of pentagonal and heptagonal rings as mentioned earlier (Aijima et al. 2004; Bekyarova et al. 2002; Murata et al. 2001; Lordi et al. 1999). For each sample results in Table 5.2, the analysis was conducted 3 times and repeatable results were obtained. The error margin for the D and G band was ± 2 whereas, that for the I_D and I_G was ± 0.02 .

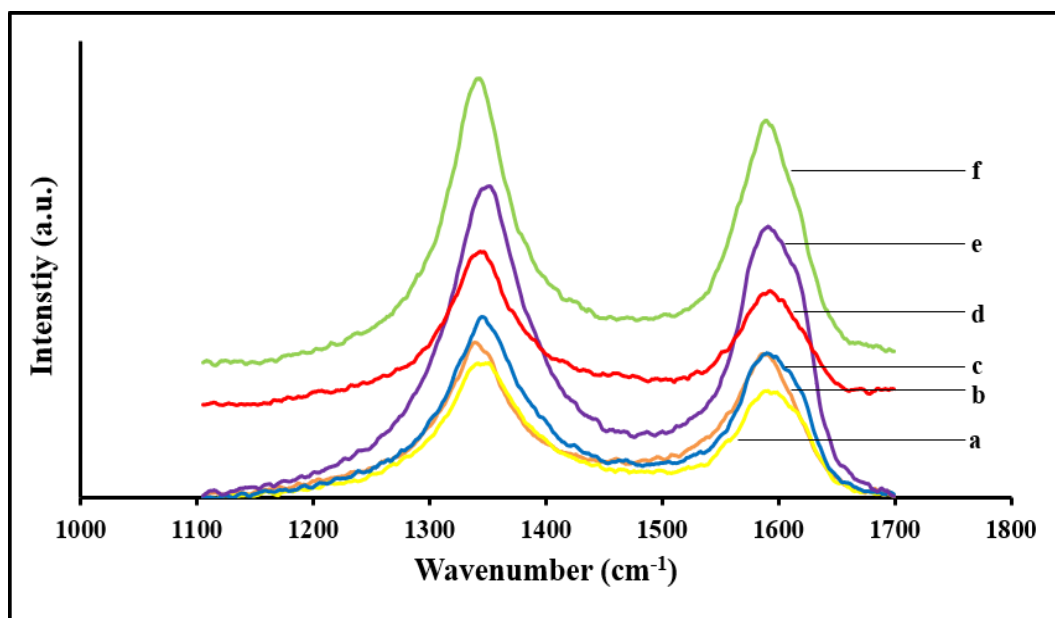


Figure 5.7 Raman spectra of pristine CNH produced at different currents; a) 90A CNH_1 h, b) 90A CNH, c) 90A CNH_2 h, d) 90A CNH_30 min, e) 90A CNH_4 h, f) 90A CNH_15 min.

However, the I_D/I_G ratios increased to 1.20 and 1.41 when pristine CNH were functionalized for 15 and 30 min respectively. This strongly suggests that significant defects (nanowindows) occurred on pristine CNH at the optimum functionalization time of 30 min which is important for catalyst development in hydrotreating application. From Table 5.2, compared to the pristine CNH sample an increase ($\sim 18\%$) in the I_D/I_G ratio as the functionalization time increased from 15 to 30 min indicates that the number of defects and consequently the presence of functional groups occupying defective sites has increased with increasing functionalization time. Increase in I_D/I_G ratio with oxidation agrees with the findings made by Pagona *et al.* (2009) that, an increase in defect occurs after oxidation treatment due to creation of defective sites that gets occupied with carboxylic acid groups.

Table 5.2 Examination of pristine and functionalized CNHs quality based on I_D/I_G ratio.

Samples	D Band	G Band	I_D	I_G	I_D/I_G
90A CNH	1340	1586	1879.12	1937.24	0.97
90A CNH_15min	1342	1590	3541.68	2951.77	1.20
90A CNH_30min	1344	1592	2243.02	1591.43	1.41
90A CNH_80°C_30min	1343	1595	2154.06	1659.40	1.30
90A_CNH_1 h	1345	1591	5082.81	4969.48	1.02
90A_CNH_2 h	1346	1596	1897.75	1793.57	1.06
90A_CNH_4h	1349	1595	2571.27	2398.90	1.07

Contrary to the aforementioned observation for CNH functionalized for up to 30 min, the I_D/I_G ratio for CNH functionalized for 1, 2, and 4 h were approximately 1.02, 1.06 and 1.07 respectively. This suggests that increasing functionalization time does not significantly increase the amount of defects and/or oxygenated functional groups on CNH at all times and therefore, supports our earlier findings from BET and TEM that over oxidation from 1 to 4 h have negative impact on the pristine CNH e.g. collapse of pore walls, decrease in pore volume, decrease in surface area and fusing of distinct CNH structures. From Table 5.2, it is likely that the pentagon and heptagon rings at the tips and bent sites of pristine CNH mainly contributes to the defects (I_D/I_G of ~ 1) exhibited by the 90A CNH_1 h, 90A CNH_2 h and 90A CNH_4 h samples and not significant additional defects or nanowindows resulting from acid treatment.

5.5.7 Catalytic activity of NiMo/CNH catalyst

Figure 5.8 shows HDS and HDN results on our preliminary hydrotreating studies using the novel NiMo/CNH catalyst with CLGO feed. Based on calibrations with standard solutions of known composition, the instrumental error for both N and S analysis was $\pm 3\%$. From Figure 5.8, the effect of different temperatures i.e. 370, 350, and 330 °C on the activity of the catalyst at a constant LHSV of 2 h^{-1} shows that, in general, the HDS activity was always higher than the HDN activity for each temperature under study. This is because nitrogen-based compounds in feedstock poses bigger challenge in hydrotreating compared to sulfur-based compounds due to steric hindrance, and the complexity of their kinetic and conversion (Zeuthen et al. 2001).

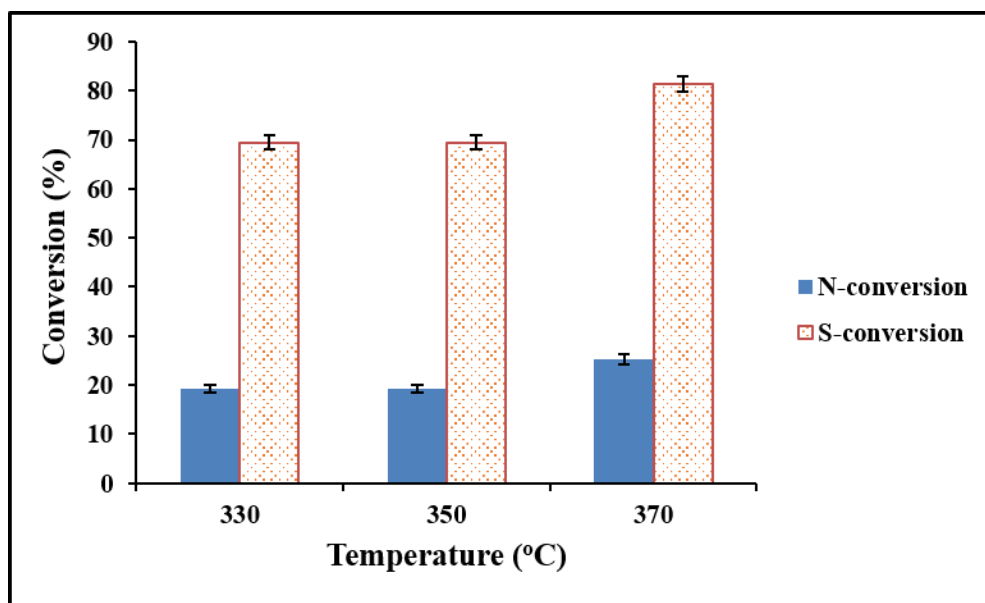


Figure 5.8 HDN and HDS activities of NiMo/CNH catalyst using Bitumen derived LGO at various temperatures. (Catalyst volume = 5cm³, P= 8.8 MPa LHSV = 2h⁻¹ and H₂/oil ratio = 600 (v/v)).

In addition, clear observations show that for both HDN and HDS reactions the optimum activity occurred at the highest temperature of 370 °C and decreased steadily as the temperature decreased from 370 to 330 °C. Activity increases with temperature because, the stability of the catalyst performance and effectiveness of HDS reaction are attained at high temperatures (Stanislaus et al. 2010). Since the hydrotreating experiments were all performed using light gas oil with less contaminant molecules as compared to heavy gas oil, these temperatures were selected in order not to cause any hydrocracking as a result of excessive temperature.

From Figure 5.8, the HDS conversions at 370, 350, and 330 °C are; 80.9, 69.5, and 54.3 %. Similarly, the HDN conversions are 24.0, 19.2, and 10.8 %. This implies that the best HDS and HDN conversions were found to be 80.9 and 24.0 %. These low HDS and HDN conversions may be due to the low dispersion of Ni and Mo on the functionalized support as confirmed by the TEM images of Figure 5.3d and e. Based on these preliminary results, the optimization of the metal loading capacity on novel CNH support, pelletization of CNH for hydrotreating and the effect of operating conditions on HDS and HDN reactions will be further investigated.

5.6 Conclusions

The textural properties of pristine CNH can be improved by acid treatment as evident from samples functionalized with 30wt % of HNO₃ for 30 min. Samples produced at the optimum functionalization condition exhibited a surface area of 547 m²/g, pore diameter of 12.3 nm and pore volume of 0.70 cm³/g. In comparison to pristine CNH samples, ~ 320 % increase in surface area and ~10 % increase in pore volume was achieved for the optimum 90A CNH_30 min sample. The optimum functionalization condition resulted in ~ 46 % drop in pore diameter as compared with the pristine samples. Higher acid treatment duration (≥ 1 h) causes a reduction in textural properties of CNH and fusing of CNH as confirmed by the BET, TEM, and Raman results. FTIR analysis showed that oxygenated functional groups such as carboxylic acid groups are introduced onto the surface of pristine CNH after acid treatment based on the occurrence of a band at approximately 1,780 cm⁻¹ in the FTIR spectra of all functionalized samples. Raman spectroscopy showed prominent D band at 1,340–1,350 cm⁻¹ and G band at 1,580–1,600 cm⁻¹. For all the functionalized samples, the intensity of the D band was higher than the G band. Functionalization introduced defects on the samples as evident from the high I_D/I_G ratio of 1.41 at the optimum acid treatment condition. CNH can be successfully functionalized by liquid oxidation. Characterization results of the optimum functionalized CNH shows unique desirable properties for hydrotreating. Effect of temperature on HDS and HDN activity shows a higher HDS activity at all temperatures under study compared with HDN activities. The optimum HDN and HDS occurred at 370 °C and were found to be 80.9 and 24.0 % respectively.

CHAPTER 6

Comparative Studies of Carbon Nanomaterial and Gamma-alumina as Supports for Ni-Mo Catalyst in Hydrotreating of Gas Oils

Majority of the content of the chapter has been submitted to the journal, Fuel. The author's information are as follows; Aryee, E.; Essilfie-Dughan, J.; Dalai, A.K.; Adjaye, J. "Comparative Studies of Carbon Nanomaterial and Gamma-alumina as Supports for Ni-Mo Catalyst in Hydrotreating of Gas Oils" (submitted for publication).

Some content of this phase of work had been presented at these conferences:

- E. Aryee, A. K. Dalai, J. Adjaye, "Comparative studies of carbon nanohorns and other carbon particles as supports for Ni-Mo in hydrotreating of gas oils," Poster presentation at Oil Sands, 2014, Edmonton, Alberta, Canada, April 28 – 30, 2014.
- E. Aryee, A. K. Dalai, J. Adjaye, "Hydrotreating of gas oils using other carbon particles generated from arc discharge of pure graphite rods," Oral presentation at 23rd Canadian Symposium on Catalysis, Edmonton, Alberta, Canada, May 11-14, 2014.
- E. Aryee, A.K. Dalai, J. Adjaye, "Comparative studies of carbon nanohorns and other carbon particles as support for Ni-Mo in hydrotreating of gas oils," Oral presentation at 24th Canadian Symposium on Catalysis, Ottawa, Ontario, Canada, May 8-11, 2016.

Contributions to this phase of work

Emma Aryee, the Ph.D. candidate prepared and characterized five different support materials that were used in making catalyst under this phase. Emma Aryee designed the experimental plan for this study, and executed all work including; functionalization of different carbon supports, synthesis of various catalysts, loading and unloading of hydrotreating reactors, hydrotreating experiments, characterization of catalysts and liquid samples, data processing and results interpretation. Emma Aryee wrote the manuscript, worked on some rebuttals prior to the submission of manuscript to Fuel. All CLS work (XAS experiments and data processing) were

carried out by Dr. J. Essilfie-Dughan however, for the benefit of each other Emma Aryee and Dr. J. Essilfie-Dughan occasionally had discussions as the data were being processed. My supervisors Dr A. K. Dalai and Dr. J. Adjaye monitored the progress of this study, critically reviewed the experimental plan and findings, and provided guidance and suggestions when necessary. Additionally, Dr. A. K. Dalai and Dr. J. Adjaye reviewed the manuscript and rebuttals before submission. Dr. J. Essilfie-Dughan also provided valuable information for the XAS part of the document and reviewed that section as well.

Contribution of this chapter to the overall Ph.D. work

The chapter aimed at investigating how different carbon-supported catalysts and gamma-alumina-supported catalyst influence hydrotreating performance. This chapter would provide information and an improved understanding of the properties of various carbon-supported catalysts, and how their properties vary from the traditional gamma-alumina catalyst. This chapter would clarify the different behaviours of carbon-supported and gamma alumina-supported catalysts towards achieving higher hydrotreating performance. As such, knowledge would be gained about the influence of various supports on hydrotreating. The results from this study would help to determine the type of carbon material that should be selected as a support for further research, pilot study or commercial hydrotreating application.

6.1 Abstract

Carbon nanohorns (CNH), other carbon particles (OCP), fine fractions of other carbon particles (OCP_f), carbon nanotubes (CNT) and gamma-alumina ($\gamma\text{-Al}_2\text{O}_3$) were utilized as support materials for Ni-Mo catalyst in this study to; test the influence of the support on hydrotreating efficiency using real feed, and identify the cause of disparity in activity from these various catalyst supports. OCP and OCP_f are the main by-products obtained during the production of CNH. The influence of the support on the hydrotreating catalyst are significant and include enhancement of; textural properties, active phase dispersion and catalyst reducibility. Among all the carbon-supported catalysts used, the NiMo/CNH catalyst exhibited outstanding physico-chemical properties and as such its catalytic activity dominated that of NiMo/ OCP_f , NiMo/OCP, and NiMo/CNT catalysts. The pore volume, pore diameter and surface area of NiMo/CNH catalyst was $0.42\text{ cm}^3/\text{g}$, 10.9 nm and $350\text{ m}^2/\text{g}$ respectively. The percentage metal dispersion of

NiMo/CNH catalyst was also 8.0% and was about twice that of NiMo/OCP_f and NiMo/CNT catalysts. XAS analysis confirmed that the carbon-supported catalysts exhibited a distorted octahedral Mo coordination environment whereas, the NiMo/ γ -Al₂O₃ catalyst exhibited a tetrahedral Mo coordination environment. Hydrotreating activities of all the different-supported catalysts with light gas oil are also presented in this study.

6.2 Introduction

Oil refineries worldwide are constantly being challenged to hydrotreat petroleum fractions and residues that are characterized by high contaminants such as nitrogen, sulfur, aromatics, asphaltenes and metals into valuable liquid products that can meet tighter environmental regulations, and the demand for high quality cleaner fuels. In the US and Canada, the current environmental regulation is aimed at limiting the amount of sulfur in diesel oils to less than 15 ppm whereas, in EU this limit is set to less than 10 ppm. Due to this, a significant improvement in the hydrotreating process is required to meet these environmental regulations. As a result, refineries are therefore seeking a highly active hydrotreating catalyst that can be used to achieve deep hydrodesulfurization (HDS) of diesel feed to ultra-low-level sulfur. Factors that mainly affect the hydrotreating process include; the type of catalyst, feed, and hydrodynamics of the system (Al-Dalama et al. 2011; HARTENERGY, 2014; Ancheyta et al. 2005). Since the typical hydrotreating catalyst comprises of active metals, promoters and a support, a more active and stable catalyst can be developed further by: varying the support, using different impregnation methods during catalyst preparation, improving the active metal components on the support, using secondary additives, and tuning the catalyst acidity (Yao et al. 2012; Al-Dalama and Stanislaus, 2011; Okamoto et al. 2003; Satterfield, 1991).

Based on the preceding information, the focus of this study is to investigate how a new hydrotreating catalyst support, and precisely carbon-based support would impact hydrotreating activities. The type of catalyst support used can result in a tremendous impact on HDS and hydrodenitrogenation (HDN) activities since, the textural properties of the support can determine how desirable the catalyst porosity and surface area are for enhanced hydrotreating effect. Additionally, depending on the type of support used there is the ability to control the metal-support-interaction that consequently influences the stabilization and dispersion of metallic particles on the support as well as the extent to which catalytic centers are reduced (Lynch, 2003;

Acres, 1980). The support also affects the promotional effect on the catalyst by changing the allowable number of promoted atoms at its edges, and this directly controls the promoted site energetics. (Ancheyta et al. 2005; Okamoto et al. 2003; Prins et al. 1997). Commercially, the preferable support used in industry for HDS of sulfur compounds is γ -Al₂O₃. However, the downside of using gamma alumina is that, extensive research has shown that during the initial stages of catalyst preparation, a strong interaction occurs between the support and metallic precursors which makes it difficult for the supported metal oxides to undergo complete sulfidation (Carrier et al. 1997; Vissers et al. 1987). This drawback in complete sulfidation eventually has a negative effect on hydrotreating since, a sulfided catalyst in its active form may likely have oxides that might prevent it from working at its fullest potential. Metal-support-interaction have a significant impact on HDS efficiency, and moderate metal-support-interaction is normally favored (Xia et al. 2017).

Other than the conventional γ -Al₂O₃ support, the use of alternative supports such as carbon, titania, silica, silica-alumina and zirconia have gained a lot of research attention not only because they have been proven to yield outstanding hydrotreating performances but also because, the use of these alternative support (especially carbon) will circumvent the major challenge encountered with γ -Al₂O₃ support (Sakanishi et al. 2000; Martín-Gullón et al. 1993; Luck, 1991; Segawa et al. 1990). To buttress this point, in (1976) de Beer and his group demonstrated that by using different supported metal sulfides the HDS catalytic activity for thiophene increased in this order; alumina < silica < carbon. Research work by Boahene, (2017) related to the conversion of syngas to higher alcohols also showed that use of CNH as a catalyst support resulted in higher conversion than that of ordered mesoporous carbon, CNT, OCP_f and OCP. A study by Vissers *et al.* (1987) also revealed that Mo/C catalyst demonstrated a higher activity than Mo/Al₂O₃ due to the structural phases that occurred after sulfidation as well as the interaction between the various support and the phases (Vissers et al. 1987; Duchet et al. 1983; deBeer et al. 1976). The interest in the use of carbon-based support for this study sparked off because carbon; is ubiquitous in nature, not prone to nitrogen poisoning and possesses high surface area, controlled pore volume and size. Improved selectivity plus activity with less coke formation can be attained by using a carbon-supported catalyst in hydrotreating. Other benefits of carbon-supported catalyst include; the tendency to modify the surface chemistry and porosity for a suitable application, and the ability to exclusively conduct extensive structural studies on the effect of active metals on hydrotreating due to the inert nature

of carbon (Ancheyta et al. 2005; Sakanishi et al. 2000; Rodriguez-Reinoso et al. 1998; Martín-Gullón et al. 1993; deBeer et al. 1984; Duchet et al. 1983). Therefore, this present work is aimed at comparing the performances of different carbon catalysts versus gamma-alumina catalyst in hydrotreating, and to decipher the influence of the catalysts physico-chemical properties on hydrotreating activities of light gas oil (LGO).

6.3 Experimental method

6.3.1 Catalyst preparations and hydrotreating experiments

The CNH and OCP carbon-supports used in this study were simultaneously generated from the arc discharge process and these supports were distinguished based on a filtration process after an arc discharge experiment. A current setting of 90 A was used and detailed information about the experimental setup and reaction conditions have been previously reported (Aryee et al. 2017). US No. 50 standard sieve series which corresponds to 300-micron average particle diameter was used to set the cut-off for OCP_f (i.e. fine fraction of OCP) support. CNT was purchased from U.S. Research Nanomaterials Inc. whereas γ -Al₂O₃ was purchased from Alfa Aesar. All carbon supports were functionalized by means of nitric acid (HNO₃) to, create oxidized functional groups on the surfaces of the carbon supports for better anchorage of metals and enhanced hydrophilicity during catalyst preparation. The reflux time for functionalization was 30 mins (Aryee et al. 2014; Wang et al. 2010). Functionalization of γ -Al₂O₃ was not required since, γ -Al₂O₃ has excellent surface properties (acidic and basic sites, hydroxyl groups (Al-OH) and oxide groups (Al-O)) that aids with reactions or metal impregnation (Digne et al. 2004; Satterfield 1991).

A co-incipient wetness impregnation method with aqueous solution of nickel nitrate [Ni(NO₃)₂.6H₂O] and ammonium heptamolybdate [(NH₄)₆Mo₇O₂₄.4H₂O] was used in preparing the different NiMo catalysts. For all the supported-NiMo catalysts, Ni and Mo concentrations were kept constant at 2.5 wt % and 13 wt % respectively. The resulting wet catalysts were placed in an oven to dry overnight at 110 °C prior to getting calcined. A vertical furnace conditioned at 450 °C for 5 hours under 50 ml/min argon flow was used in calcining all carbon catalysts whereas; the gamma-alumina supported catalyst was subjected to 5 hours calcination treatment at 550 °C. A diluted combination consisting of 5 ml of each calcined catalyst and approximately 12 ml silicon carbide was alternately packed into a micro scale trickle bed hydrotreater in 10 parts (1/10th) before the commencement of any activity test. On the average, 5 mL volume of catalyst was equivalent

to approximately 4.00 g for γ -Al₂O₃, 2.20 g of CNH, 2.00 g of CNT, 3.00 g of OCP and 2.50 g of OCP_f.

For micro-reactors, use of this diluent proportion was paramount since, it averts problems related to complete wetting of the catalyst, wall effect, liquid maldistribution and backmixing of liquid that might occur by using such a small volume of catalyst. This dilution, therefore, leads to maximization of hydrotreating performance in a trickle bed reactor and generates reasonable data to test a commercial catalyst. Additionally, the top and bottom of the reactor was packed with requisite quantity of silicon carbide and glass beads for proper mixing of inlet and exit streams (Bej et al. 2001; Bej et al. 2000). After the reactor loading had been completed, the reactor was pressurized with helium (He) at 9.3 MPa and left under the pressurized condition for 24-hours to be clear of leakages. Two connecting scrubbers at the lower section of the reactor were also filled with about 50 ml of deionized water to absorb traces of ammonium sulphide from the effluent stream. After this step, the catalyst was wetted with approximately 100 ml of a mixture of 2.9 vol% butanethiol in 500 ml of insulating oil (Voltesso 35). In situ activation of the catalyst then proceeded using the existing butanethiol and insulating oil mixture. The sulfidation process was carried out in two stages i.e. at 193 and 343 °C at an LHSV of 2 hr⁻¹ for a period of 24 hours each. After sulfidation, light gas was used as a substitute for the sulfiding solution and then stabilization of the catalyst activity via precoking was done for 3 days at an LHSV of 2 hr⁻¹ before, proceeding with the hydrotreating experiments. This LHSV was maintained throughout the hydrotreating reaction. The gas (H₂) to oil (LGO feed) ratio, and reactor operating pressure were maintained constant at 600 mL/ml and 9.0 MPa, respectively. Liquid hydrotreated products collected from a gas-liquid separator were stripped using nitrogen (N₂) for 2 hours to eliminate traces of hydrogen sulphide and ammonia that had been absorbed. The effects of temperature (330 - 370 °C) on the nitrogen and sulfur content of liquid products were examined using Antek 9000 NS analyzer based on a combustion-chemiluminescence or combustion-fluorescence technique, and in combination with the ASTM D4629 method.

6.4. Characterizations

Solid samples (different-supported catalysts) were characterized with BET, XRD, HRTEM, Py-FTIR, TGA, CO-chemisorption, TPR and XAS to help with results interpretation about the influence of different-supported catalysts (with possibly differing properties) on

hydrotreating performance. Both treated and non-treated gas oil liquid samples from all hydrotreating experiments were characterized using NS analyzer. Chapter 3 of this thesis contains a summary of these techniques and sample analysis procedures for reference.

6.5 Results and discussion

6.5.1 Morphology of arc-discharge materials

TEM images of as-synthesized carbon materials (CNH, OCP_f and OCP) are shown in Figure 6.1. The morphology of the particles in Figure 6.1a, was that of CNH and is homogenous in nature with aggregate diameter ranging from 50 to 110 nm. Figure 6.1b, contains particles with morphology identical to CNH and CNT and in Figure 6.1c, the pristine OCP material is made of CNH, CNT and other unknown structures which could be amorphous carbon, graphene foils and graphite sub-micron particles. The TEM micrographs in Figure 6.1 confirm that the products from the arc discharge experiment consist of different carbon nanostructure particles (Berkmans et al. 2015; Fan et al. 2005; Iijima et al. 1999). Raman results in Appendix C also confirms that the OCP_f material comprises of CNH and CNT.

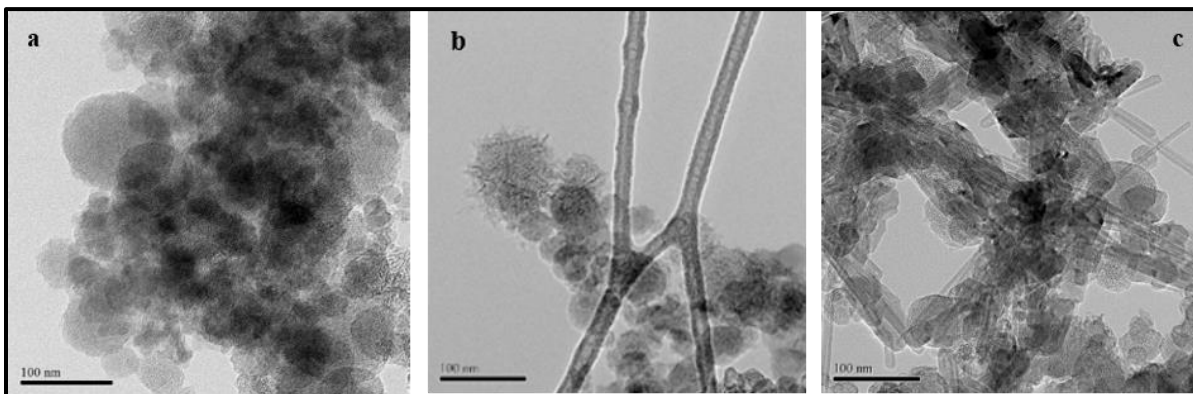


Figure 6.1 TEM images of different carbon materials from arc-discharge experiment; a) pristine CNH, b) pristine OCP_f, and c) pristine OCP.

6.5.2 Textural properties of catalysts

The textural properties of all the catalysts used in this study is highlighted in Table 6.1. From this table, the NiMo/CNH catalyst demonstrated a higher surface area than that of NiMo/ γ -Al₂O₃ catalyst as well as the remaining three carbon-supported catalysts used. The higher surface area of NiMo/CNH catalyst over the rest of the carbon-supported catalysts stems from the

enhanced surface area (546 m²/g) of CNH support after 30 minutes functionalization, and prior to impregnation of support with desirable metals. Functionalization of pristine OCP_f, OCP and CNT materials led to a surface area of 177, 23, and 168 m²/g respectively. Check Appendix B for information about the effect of functionalization on the textural properties of OCP and OCP_f support materials. Typically, the preferred industrial alumina support has a surface area that ranges between 150 – 250 m²/g (Kaluža and Zdražil, 2001). A drop in surface area of all functionalized carbon-supports and γ -Al₂O₃ support after metal impregnation was due to the plugging of pores and micro channels with metals after catalyst preparation. On the average, the pore volume of NiMo/CNH, NiMo/CNT and NiMo/ γ -Al₂O₃ catalysts were approximately 0.49 cm³/g whereas, the pore volumes of NiMo/OCP_f and NiMo/OCP catalysts were negligible. The low surface area and pore volume values exhibited by NiMo/OCP_f and NiMo/OCP catalysts were due to the rigid-crust-like nature of the original support material used in making these catalysts (Yeh et al. 2016). From Table 6.1, overall observation of all catalysts revealed mesoporous pore diameters according to IUPAC specifications.

Table 6.1 Textural properties of all the different supported Ni-Mo catalysts.

Sample	BET Surface Area (m²/g)	Pore Volume (cm³/g)	Pore Diameter (nm)
NiMo/CNH	350 ± 2	0.42 ± 0.01	10.8 ± 0.1
NiMo/OCP _f	52 ± 2	0.09 ± 0.01	14.3 ± 0.1
NiMo/OCP	-	-	-
NiMo/CNT	117 ± 2	0.50 ± 0.01	17.4 ± 0.1
NiMo/ γ -Al ₂ O ₃	223 ± 2	0.55 ± 0.01	7.3 ± 0.1

The high surface area exhibited by the NiMo/CNH catalyst is of importance since, it enables the active species to become highly dispersed for the formation of more active sites. According to Vissers *et al.* (1987), another advantage of using a catalyst with a high surface area is that the possibility of sintering of the active phase is minimized and this, consequently enhanced HDS activity. Martín-Gullón *et al.* (1993) discovered that, the adsorption of heptamolybdate solution is improved with high surface area and pore volume thus, causing an enhancement in Mo loading. In (1998), a review article by Furimsky emphasized the importance of using a catalyst with small pore diameters and large surface area for hydroprocessing of light feeds with porosity not being too critical as likened to the hydroprocessing of heavy feed. The catalyst pore structure is beneficial since, it controls the amount of feed that diffuses into the catalyst pellet, and a

reasonable pore diameter also facilitates the elimination of diffusion resistances likely to occur during hydrotreating. As such, easier accessibility of big molecules inside the catalyst internal pores leads to higher rate of conversion and a reduction in diffusional limitation that accompanies feedstock with large molecules. The capability for metal deposition also varies depending on the pore volume (Jarullah et al. 2011; Furimsky, 1998). Information on textural properties of OCP and OCP_f before and after functionalization can be found in Appendix B. Additionally, the adsorption capabilities behaviour of all catalysts used in this study can be found in Appendix C.

6.5.3 Thermal stability of catalysts

TGA thermograms of the five catalysts used in this study are presented in Figure 6.2. The TGA profiles in Figure 6.2 shows that, NiMo/OCP and NiMo/CNT catalysts are thermally stable from room temperature to 550 °C. The profiles for NiMo/CNH and NiMo/OCP_f were similar, and their respective plots from room temperature till approximately 150 °C shows that after about 2% drop in weight as a result of moisture loss or physically adsorbed water, a diminutive weight drop occurred again till 550 °C, followed by 3 - 7% weight loss up to 700 °C. The NiMo/OCP_f catalyst registered a lesser weight loss than the NiMo/CNH catalyst as a result of more inherent graphitic particles that are more likely resistant to combustion. With the exception of NiMo/OCP catalyst all carbon-supported catalyst experienced rapid decomposition at 700 °C. In the case of the NiMo/ γ -Al₂O₃ catalyst, the initial drop in weight attributed to the loss of moisture, was about 4 %. Later on, a weight loss of approximately 3% occurred up to 450 °C because of the loss of chemisorbed water as well as the decomposition of precursors before stabilizing till 700 °C. The operating temperatures explored in this study were 330, 350 and 370 °C hence, based on these TGA findings, the thermal stability of all the catalysts under these temperature conditions are guaranteed after the initial weight loss due to moisture.

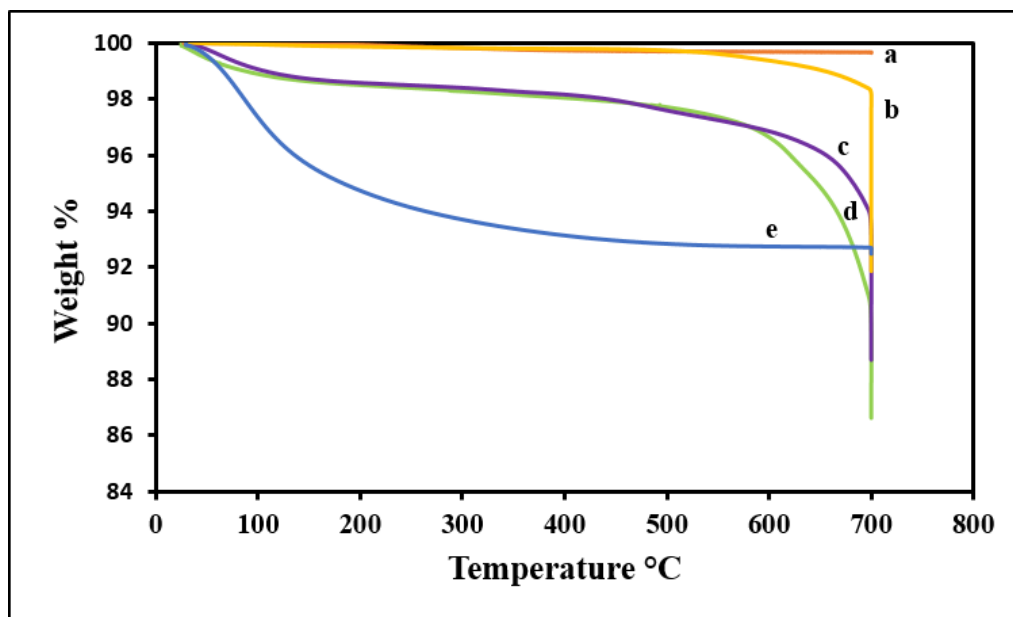


Figure 6.2 TGA thermograms of the different supported catalysts; a) NiMo/OCP, b) NiMo/CNT, c) NiMo/OCP_f, d) NiMo/CNH, and e) NiMo/ γ -Al₂O₃.

6.5.4 Examination of XRD patterns

XRD is essential in determining the catalysts structure, the various phases on the catalyst that are crystalline as well as the extent of homogeneous dispersion. Low angle XRD results (not shown) confirmed that the NiMo/CNH, NiMo/OCP_f, NiMo/CNT and NiMo/ γ -Al₂O₃ catalysts exhibited a hexagonal mesoporous structure with a well resolved strong and weak peak at $2\theta = 0.9$ and $2\theta = 1.7$, respectively. Peak indexes at d (100) and d (110) were realized, and the intensities of the peak were similar for all catalysts under study, which inferred that the mesoporous hexagonal structure was retained despite the type of support used in catalyst preparation. The wide angle XRD domain of NiMo/CNH, NiMo/OCP_f, NiMo/CNT and NiMo/ γ -Al₂O₃ catalysts are shown in Figure 6.3. Information from JCPDS card number 10-0425, shows that γ -Al₂O₃ characteristic diffraction peaks usually occurs at $2\theta = 37.60^\circ$, 45.84° and 67.30° , whereas, MoO₃ characteristic diffraction peaks are present at $2\theta = 23.33^\circ$, 25.70° , 27.33° , 33.13° , 33.73° , 38.97° , 39.65° and 46.28° according to JCPDS card number 05-0508. Information about characteristic diffraction peaks corresponding to NiO and NiAl₂O₄ crystal phases can also be found from JCPDS card numbers 78-0429 and 78-0552, respectively. NiMoO₄ related crystalline phase signals can be identified at $2\theta = 14^\circ$, 26° , 29° , 33° , 45° , 47° and 54° using JCPDS card number 33-0948 (Garg et al. 2016; Calderon-Magdaleno et al. 2014).

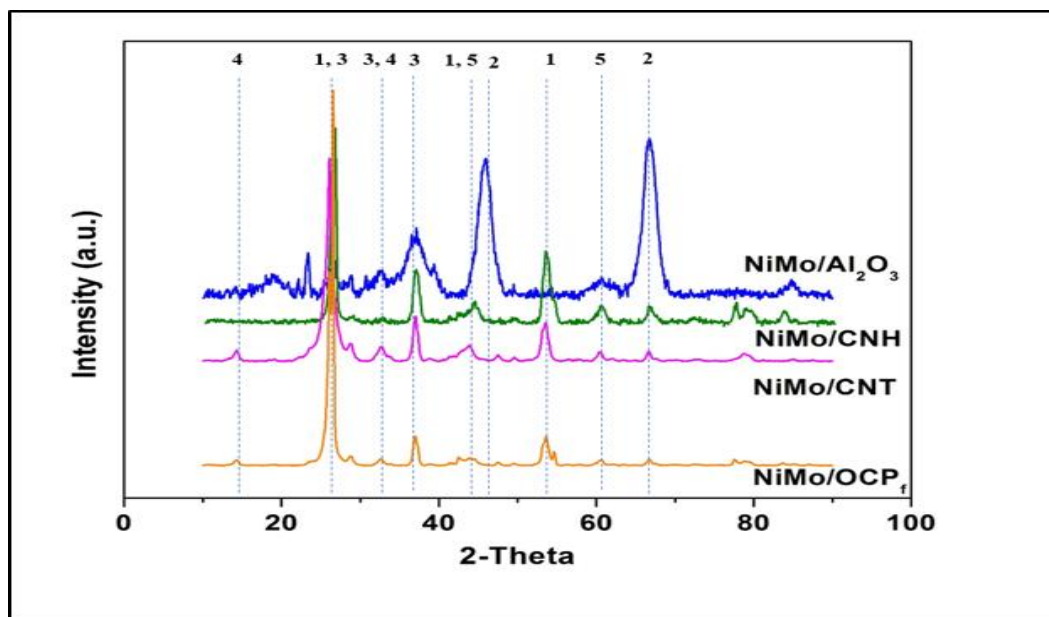


Figure 6.3 XRD patterns of different supported catalysts: a) NiMo/ γ -Al₂O₃, b) NiMo/CNH, c) NiMo/OCP_f, and d) NiMo/CNT.

This implies that from Figure 6.3, the two sharp peaks centered around $2\theta = \sim 46^\circ$ and 67° and designated as 2 on the NiMo/ γ -Al₂O₃ catalyst are γ -Al₂O₃ characteristic peaks. For the carbon-supported catalysts, the sharpest peak with highest intensity at $2\theta = \sim 26^\circ$ corresponds to (002) diffraction plane and is attributed to regularly stacked graphenic layer. Other characteristic peaks relating to carbon were noticeable at $2\theta = \sim 43^\circ$ and 55° and designated as 1 on all the carbon-supported catalysts. Characteristic MoO₃ peaks at $2\theta = \sim 26^\circ$, 34° and 38° and designated as 3 were observed on all catalysts used in this study, however for the carbon-supported catalysts the, MoO₃ peak at $2\theta = \sim 26^\circ$ overlapped with the diffraction from the (002) graphitic plane. The sharpness of the MoO₃, 2θ peak at $\sim 38^\circ$ on all three carbon-supported catalysts as compared to its broad peak on the NiMo/ γ -Al₂O₃ catalyst connotes that, dispersion of MoO₃ on all the carbon-supported catalysts were less than that on the NiMo/ γ -Al₂O₃ catalyst. The broadness of the small intensity NiO peak (designated as 5) on NiMo/ γ -Al₂O₃ catalyst at $2\theta = \sim 63^\circ$ compared to that on all carbon-supported catalysts also signifies that NiO is less dispersed on a carbon-supported catalyst than on a NiMo/ γ -Al₂O₃ catalyst. For all the carbon-supported catalysts the peak at $\sim 54^\circ$ corresponding to a graphenic layer may have overlapped with NiMoO₄ characteristic peak which also occurs at $2\theta = \sim 54^\circ$ and at (510) diffraction plane. No NiMoO₄ characteristic peaks were however, observed on the NiMo/ γ -Al₂O₃ catalyst.

6.5.5 Dispersion behaviour of catalysts

CO chemisorption analysis was conducted to determine the extent at which metal particles in the catalyst are dispersed on the support surface thus, providing information about the number of exposed active sites on catalyst. Table 6.2 gives information about the CO chemisorption results of all the catalysts used in this study. The deviation for % metal dispersion, metallic surface area, CO absorbed, and crystallite size were; ± 0.1 , ± 0.3 , ± 2 and ± 0.2 respectively. These results suggest that, for the carbon-supported catalysts, NiMo/CNH catalyst showed higher degree of dispersion compared to the NiMo/OCP_f and NiMo/CNT catalysts, and agrees with the wide angle XRD results mentioned earlier in Figure 6.3. The higher degree of dispersion exhibited by NiMo/CNH catalyst compared to the remaining carbon-supported catalysts was attributable to the high stability of MoS₂ particles on CNH-carbon support which, allowed smaller crystallites with reduced stacking to be maintained on the support with concomitant improvement in dispersion (Berhault et al. 2001). Improved dispersion of molybdenum sulfide on the support also have a positive impact on catalytic activities since, more edges of MoS₂ layer are exposed for reactions leading to higher conversions.

From all the catalysts under study in Table 6.2, though, the NiMo/ γ -Al₂O₃ catalyst displayed the highest dispersion, the dispersion of the NiMo/CNH catalyst was also high as compared to the rest of the other carbon supported catalyst. The order of dispersion decreased as follows: NiMo/ γ -Al₂O₃ > NiMo/CNH > NiMo/CNT > NiMo/OCP_f > NiMo/OCP. Since the same metal loading composition was impregnated on all the supports, a decrease in the degree of dispersion among the carbon-supported catalysts certainly had to do with a decline in surface area based on the type of support used and a corresponding increase in metal-support-interaction (Ancheyta et al. 2005; Okamoto et al. 2003). The bigger crystallite size NiMo particles in the NiMo/OCP catalyst relative to the remaining catalysts accounted for the negligible surface area exhibited by NiMo/OCP catalyst, and contributed to the poor dispersion of NiMo particles on the OCP-carbon support. Observation of the results in Table 6.2, also revealed that it would be more effective to disperse and stabilize NiMo particles on γ -Al₂O₃ support than on a carbon support as a result of the resulting small crystallite size of NiMo particles in NiMo/ γ -Al₂O₃ catalyst.

Table 6.2 CO chemisorption results of different NiMo-supported catalysts.

Catalyst	Metal Dispersion (%)	Metallic Surface Area (m ² /g of sample)	CO Absorbed (μmol/g)	Crystallite Size (nm)
NiMo/Al ₂ O ₃	12.2	9.3	217	10.1
NiMo/CNH	8.0	6.1	141	15.6
NiMo/OCP _f	4.8	3.6	84	26.2
NiMo/OCP	1.3	1.0	23	95.8
NiMo/CNT	5.2	4.0	92	23.8

6.5.6 Reducibility of catalysts

Figure 6.4 shows the TPR profiles of the five catalysts utilized in this study. Overall observation from this figure implied that all the species can undergo reduction irrespective of the type of support used, and reduction of MoO₃ occurred in two steps i.e. low and high-temperature reduction. Low temperature reduction could be associated with partial reduction of heteropolymolybdates (octahedral Mo species) or multilayered Mo oxides that are highly defective and amorphous, and this phenomenon generally relates to the presence of Ni-Mo-S precursor active type-II phase (Henker et al. 1991; Arnoldy et al. 1985). On the other hand, reduction of tetrahedral Mo species such as Mo oxides that require intense reduction, highly dispersed MoO₃ monolayer as well as the crystalline phases of orthorhombic MoO₃ and Al₂(MoO₄) that get formed as a result strong metal support interaction are associated with high-temperature reduction.

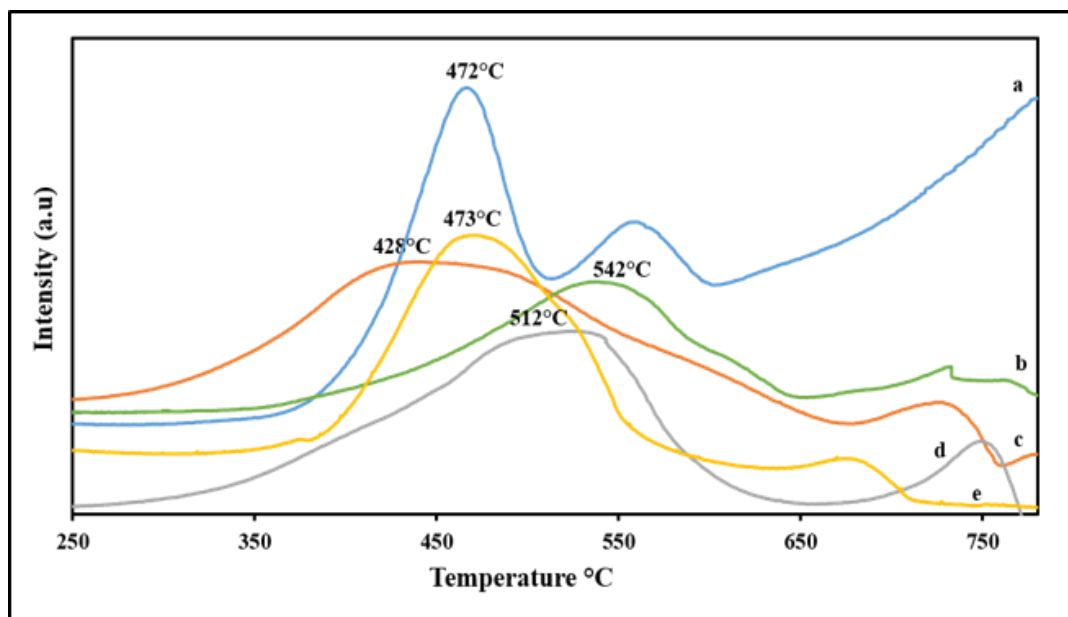


Figure 6.4 TPR profiles of different supported catalysts; a) NiMo/ γ -Al₂O₃, b) NiMo/OCP, c) NiMo/CNH, d) NiMo/OCP_f, and e) NiMo/CNT.

The pattern in Figure 6.4, suggests a Mo⁶⁺ to Mo⁴⁺ reduction for the first peak followed by a reduction of Mo⁴⁺ to Mo⁰⁺ in the second peak (Marzari et al. 1995; Rajagopal et al. 1994; Arnoldy et al. 1985). Based on the profiles in Figure 6.4, the carbon-supported catalysts displayed two apparent reduction peaks that ranged from 350 – 625 °C and 650 – 775 °C. All the carbon supported catalysts, showed broad peaks with the first reduction peak of NiMo/CNH catalysts occurring at a much-reduced temperature compared with the rest of the carbon-supported catalysts. This also signified minimal metal oxide interaction using a CNH-carbon support as compared to the rest of the carbon-supports. The shoulder peak immediately following the first reduction peak of all the carbon-supported catalysts was caused by reduction of NiMoO₄ or bulk NiO kind of species (Eswaramoorthi et al. 2008; Damyanova et al. 1995).

The first reduction temperature of NiMo/OCP catalyst occurred at a comparatively higher temperature than the remaining carbon-supported catalysts and based on CO chemisorption results, this is ascribed to the presence of bigger NiMo active phase particles within this catalyst that required higher temperature for reduction. Similarly, Figure 6.4 also confirms that NiMo/CNH catalyst consisted of smaller particles since, catalyst with smaller NiMo particles have also been proven to be reduced at lower temperatures. The disclosure of smaller particles presence in NiMo/CNH catalyst using TPR was also consistent with Table 6.2 CO-chemisorption results

which, revealed a high degree of dispersion for NiMo /CNH catalyst as a result of the smaller NiMo particles that existed in the catalyst (Eswaramoorthi et al. 2008). From Figure 6.4, it is obvious that the first reduction peak of NiMo/ γ -Al₂O₃ is sharper and with a much higher intensity than all the carbon-supported catalysts, and the reason behind this is that NiMo/ γ -Al₂O₃ contains more exposed highly dispersed MoO₃ that can consume more hydrogen and be readily converted to Ni-Mo-S type-II phases. The TPR profiles therefore indicates that reducibility from oxidic to sulfidic molybdenum species was higher for NiMo/ γ -Al₂O₃ and NiMo/CNH compared to the rest of the catalyst, and reducibility of the various catalysts clearly increased as follows: NiMo/OCP < NiMo/OCP_f < NiMo/CNT < NiMo/CNH < NiMo/ γ -Al₂O₃.

6.5.7 Acidity measurements

Enhanced catalytic activities have been achieved with Lewis and Bronsted acid sites since, some studies have shown that Lewis and Bronsted acid sites with weak and intermediate strength have contributed positively to the hydrotreating performance. Usually, Lewis acid sites promote hydrogenolysis reactions whereas, Bronsted acid sites accelerates hydrogenation reactions. In addition, the acidic nature of the catalyst can directly enhance HDS reactions by boosting hydrogenation properties, and isomerization reactions that accelerates the transformation of refractory sulfur compounds into highly reactive compounds. High HDN activities have also been linked to an increase in the hydrotreating catalyst acidity due to saturation of aromatic rings by Lewis acid sites and cleavage of C – N bond on strong Bronsted acid sites (Perot, 2003; Prins et al. 1997; Kwart et al. 1982). Figure 6.5a and b shows the pyridine-FTIR spectra of NiMo/CNH, NiMo/OCP_f, NiMo/CNT and NiMo/ γ -Al₂O₃. Usually FTIR bands that occur at 1450 and 1610 cm⁻¹ depicts an adsorbed pyridine on Lewis acid sites. Pyridine adsorbed on Bronsted acid sites also corresponds to a band around 1540 cm⁻¹. However, the appearance of a 1490 cm⁻¹ band relates to pyridine that is co-adsorbed on both Lewis and Bronsted acid sites (Wang et al. 2015; Connell and Dumesic, 1985).

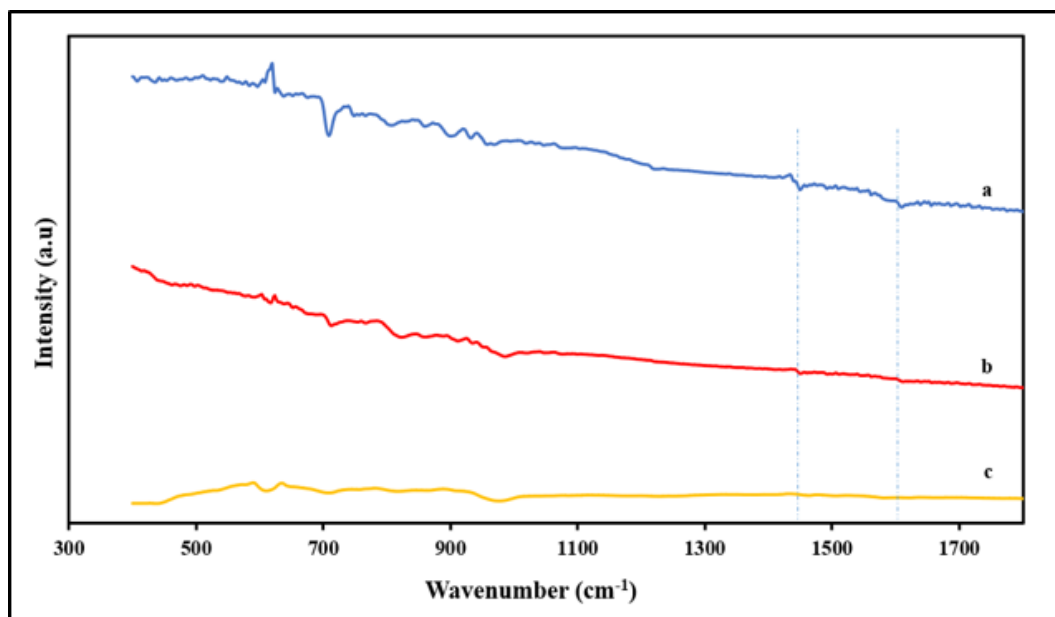


Figure 6.5 Pyridine FTIR images of samples; a) NiMo/CNH, b) NiMo/OCP_f, and c) NiMo/CNT.

For the carbon-supported catalysts in Figure 6.5 apparent pyridine peaks adsorbed only on Lewis acid sites were seen on the NiMo/CNH and NiMo/OCP_f catalysts at approximately 1450 and 1610 cm⁻¹ whereas, the NiMo/CNT catalyst barely exhibited any Lewis and / Bronsted type acid sites under the characteristic window of concern. From Figure 6.6, the pyridine-FTIR spectra of NiMo/ γ -Al₂O₃ showed pyridine bonded onto Lewis acid sites at 1446 and 1594 cm⁻¹ along with pyridine bonded to Bronsted acid sites at 1544 cm⁻¹. In Figure 6.6 an additional band at 1496 cm⁻¹ is allocated to pyridine adsorbed on both Bronsted and Lewis acid sites. The slight shift in the NiMo/ γ -Al₂O₃ band may be due to ongoing metal-support-interaction. Overall results therefore indicated that, although the key acid-type sites present in all the catalyst under study were Lewis acid sites, the NiMo/ γ -Al₂O₃ catalyst has additional Bronsted acid sites that could possibly give it an extra edge in attaining excellent hydrotreating activities. The peaks intensities on the NiMo/ γ -Al₂O₃ catalyst was also more pronounced than that of all the carbon-supported catalysts.

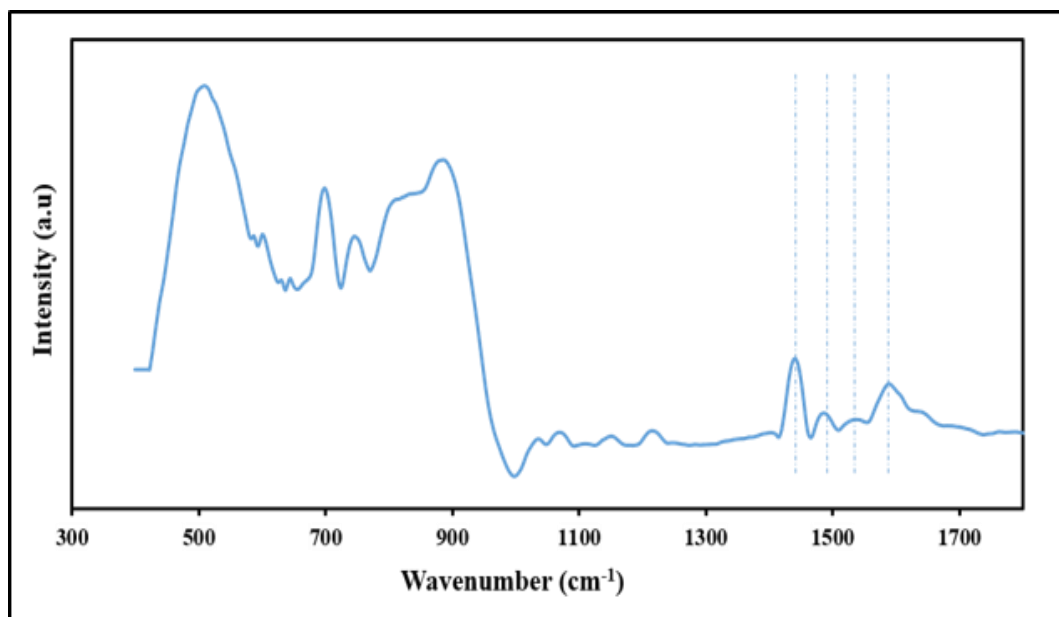


Figure 6.6 Pyridine FTIR image of NiMo/ γ -Al₂O₃.

6.5.8 XAS analysis

Plots in Figure 6.7 shows normalized Mo-K edge XANES spectra of catalyst samples (NiMo/ γ -Al₂O₃, NiMo/OCP_f, NiMo/CNH) and reference compounds (i.e. pure Ammonium heptamolybdate [(NH₄)₆Mo₇O₂₄·4H₂O], Na₂MoO₄, and MoO₃). The spectra show well defined characteristics over the energy range 19950 – 20200 eV, and XANES analysis was performed to determine the oxidation state of the absorbing atom that is caused by a positional shift in the absorption edge of the acquired XANES spectra (Kelly et al. 2008; George and Pickering, 2007). Normally, Mo in the ground state i.e. Mo⁰ (Mo Foil) has a Mo K-edge excitation potential of 20000 eV, and this value increases or decreases depending on the oxidation state. The increase in edge energy shifts is linked with an absorber atom that maintains a higher oxidation state but have less electrons than protons. This phenomenon causes slight lowering of the energy states of the electrons, and contrarily leads to an increase in the absorption edge energy (Pickering et al. 1995).

After comparing the XANES spectra edge positions of the various analyzed samples to that of the reference compound, it was inferred that Mo in all the catalysts has Mo⁶⁺ oxidation state. This signifies that Mo⁶⁺ in the starting reagent [(NH₄)₆Mo₇O₂₄·4H₂O], did not undergo any change in oxidation state during and after all catalyst preparations.

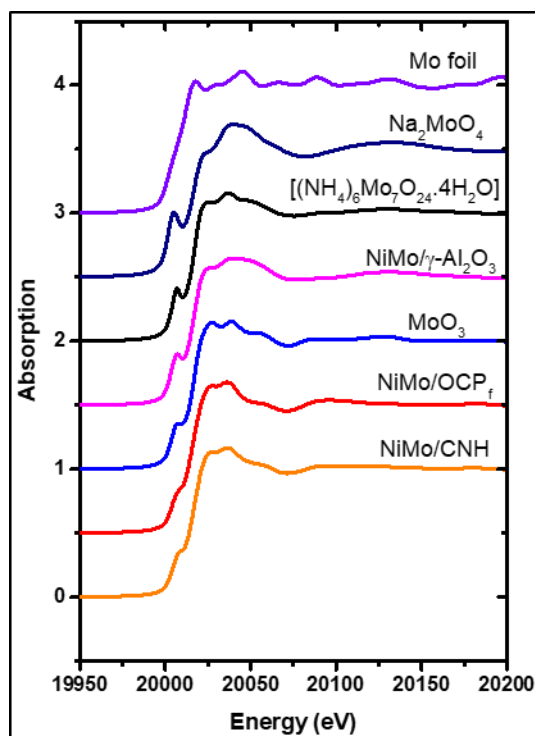


Figure 6.7 Mo K-edge XANES spectra of: Mo foil, Na_2MoO_4 , $[(\text{NH}_4)_6\text{Mo}_7\text{O}_{24} \cdot 4\text{H}_2\text{O}]$, NiMo/ γ - Al_2O_3 , MoO_3 , NiMo/ OCP_f , and NiMo/CNH.

The XANES portion of the XAS spectra also provides information about the coordination environment (geometrically arranged bonded atoms) around the Mo absorber atom (Kelly et al. 2008; George and Pickering, 2007). As can be seen in Figure 6.7, the NiMo/ γ - Al_2O_3 catalyst pre-edge feature at approximately 20010 eV was more pronounced than the pre-edge features in the NiMo/CNH and NiMo/ OCP_f catalysts. Additionally, the intensity and sharpness of the pre-edge feature in the NiMo/ γ - Al_2O_3 catalyst was the same as that of $(\text{NH}_4)_6\text{Mo}_7\text{O}_{24} \cdot 4\text{H}_2\text{O}$ and Na_2MoO_4 and relates to a tetrahedral Mo coordination environment whereas, the intensity or sharpness of the peak in the NiMo/CNH and NiMo/ OCP_f catalysts bears resemblance to that in MoO_3 reference sample and indicate a possibly distorted octahedral coordination environment. This pre-edge feature is a result of $1s \rightarrow 4d$ electron transition from core electrons to higher-level vacant orbital. Such an excitation is solely tolerable in a tetrahedral field but, strongly prohibited in an octahedral field. However, due to the presence of distorted octahedral coordination environment of Mo in compounds like MoO_3 , a less intense pre-edge feature is also observable because of the admixing of the 4d levels and p orbitals of Mo in the distorted octahedral field (Essilfie-Dughan et al. 2017; Wharton et al. 2003). This resulting information meant that Mo in XANES samples existed in two

coordination environments (tetrahedral and octahedral), and that during the preparation of the catalysts, the coordination environment of Mo changed from tetrahedral in $(\text{NH}_4)_6\text{Mo}_7\text{O}_{24}\cdot 4\text{H}_2\text{O}$ to a distorted octahedral in NiMo/CNH and NiMo/OCP_f catalysts. With regards to metal-support-interaction, results in Figure 6.7 indicates that metal-support-interaction was less in the NiMo/CNH and NiMo/OCP_f catalysts because of their less pronounced pre-edge feature and distorted octahedral Mo coordination environment. The advantage of having octahedral coordinated Mo species with less pronounced pre-edge feature is that, they produce precursors that enhance the creation of more active sites by reason of the increase in number of molybdenum species that are easily reducible during sulfidation, and which subsequently results in an enhancement of catalytic hydrogenation activities (Badoga et al. 2014). To this effect in (1996), Topsoe and his group reported that weak interactions between molybdenum species and carbon support resulted in high activity since, the degree of sulfidation became higher and was ascribed to the likely creation of active Type II Co-Mo-S phase. On the other hand, work by Maity and co-workers also revealed that molybdenum oxide in the form of tetrahedral species are extremely hard to get reduced based on the strong interaction formed with the support as compared with molybdenum species present as octahedral species (Maity et al. 2000).

Analyzation of the EXAFS part of the XAS spectra was conducted to obtain information on bonded atoms, bond distances and coordination numbers relative to the Mo atom. Figure 6.8 (a & b) illustrates the $(\chi(k)k^3)$ in k-space (\AA^{-1}) together with the Fourier transform radial structure function (FT RSF) in R-space (\AA) of $[(\text{NH}_4)_6\text{Mo}_7\text{O}_{24}\cdot 4\text{H}_2\text{O}]$, NiMo/ γ -Al₂O₃, NiMo/OCP_f, and NiMo/CNH. The resulting k-space spectra came about based on backscattering from bonded atoms in all the absorber atom (i.e. Mo) coordination shells. Backscattering from distant bonded atom (i.e. Mo-Al/Mo) were also noticeable in the form of peak splitting and shoulders on the wave pattern. Although the k-space of NiMo/ γ -Al₂O₃ and $(\text{NH}_4)_6\text{Mo}_7\text{O}_{24}\cdot 4\text{H}_2\text{O}$ share some similarities in Figure 6.8 (a), as a result of both having a tetrahedral coordinated Mo environment, the increase intensity of peaks at 3, 5.5, 8 and 9 \AA^{-1} as well as, shift in the positions of the peaks at 10 and 11 \AA^{-1} of the k-space spectra of NiMo/ γ -Al₂O₃ compared to that of $(\text{NH}_4)_6\text{Mo}_7\text{O}_{24}\cdot 4\text{H}_2\text{O}$ suggest that the tetrahedral molybdate is bonded to the γ -Al₂O₃ in NiMo/ γ -Al₂O₃. As shown in Figure 6.8 (b), these features of the k-space spectra can be clearly deduced from the FT in R-space spectra because, that can give estimated bond distances existing between the central absorber atom (Mo) and its closest adjacent atoms.

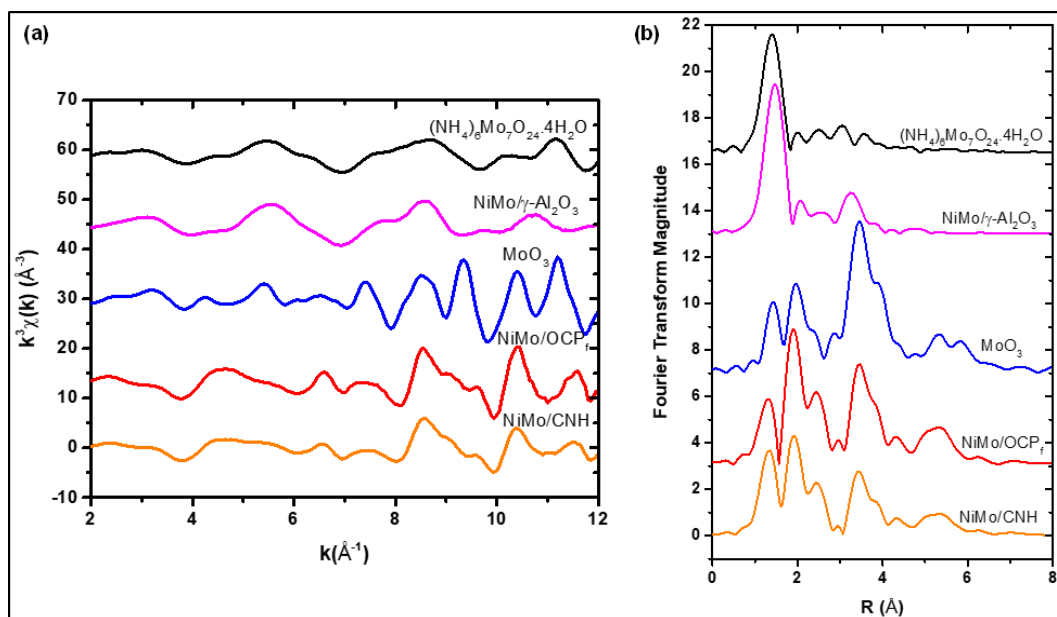


Figure 6.8 (a) Mo K-edge k^3 -weighted EXAFS, and (b) Fourier transform (FT) spectra for a k interval of 2-12 \AA^{-1} of $(\text{NH}_4)_6\text{Mo}_7\text{O}_{24}\cdot 4\text{H}_2\text{O}$, $\text{NiMo}/\gamma\text{-Al}_2\text{O}_3$, MoO_3 , NiMo/OCP_f , and NiMo/CNH .

In the FT in R-space spectra of $(\text{NH}_4)_6\text{Mo}_7\text{O}_{24}\cdot 4\text{H}_2\text{O}$ and $\text{NiMo}/\gamma\text{-Al}_2\text{O}_3$ catalysts, the first distinct peak at $\sim 1.7 \text{\AA}$ (uncorrected for phase shifts) signifies scattering from oxygen atoms that are directly attached to the Mo atom tetrahedrally. Additionally, the peak at $\sim 3.0 \text{\AA}$ (uncorrected for phase shifts) for the FT in R-space of the $\text{NiMo}/\gamma\text{-Al}_2\text{O}_3$ catalyst is attributed to the bond distance between the Mo in the tetrahedral molybdate and the Al in $\gamma\text{-Al}_2\text{O}_3$ (Radhakrishnan et al. 2001; Shimada et al. 1992). From Figure 6.8 (a), the k -space spectra of NiMo/OCP_f , and NiMo/CNH catalysts were found to be similar and identical to that of MoO_3 but, were notably different from the k -space spectra of $\text{NiMo}/\gamma\text{-Al}_2\text{O}_3$ catalyst and $(\text{NH}_4)_6\text{Mo}_7\text{O}_{24}\cdot 4\text{H}_2\text{O}$ reference compound. The FT in R-space spectra of NiMo/OCP_f and NiMo/CNH catalysts (Figure 6.8b) show two major peaks (split peak) at ~ 1.7 and 2.0\AA and a third peak with a shoulder at ~ 3.5 (uncorrected for phase shifts) and also identical to the FT in R-space spectra of MoO_3 . This implies that, in NiMo/OCP_f and NiMo/CNH catalysts, the oxygen atoms are octahedrally bonded to Mo atom (Lv et al. 2015; Wharton et al. 2003; Shi et al. 2001). The spectra features observed in the EXAFS analysis regarding the tetrahedral coordinated Mo atom in the $\text{NiMo}/\gamma\text{-Al}_2\text{O}_3$ catalyst and octahedral coordinated Mo atom in NiMo/OCP_f and NiMo/CNH catalysts also concurs with the XANES results.

6.5.9 Determination of catalytic activity

Figures 6.9 and 6.10 shows the HDS and HDN results of the catalytic activities for NiMo/CNH, NiMo/OCP_f, NiMo/OCP, NiMo/CNT and NiMo/ γ -Al₂O₃ catalysts measured as percentage conversion at operating temperatures of 370, 350, and 330 °C. The HDS and HDN activities of all the catalysts under study increased in this order: NiMo/OCP < NiMo/CNT < NiMo/OCP_f < NiMo/CNH < NiMo/ γ -Al₂O₃. This implied that among the carbon-supported catalysts, improved HDS and HDN conversions were achieved with NiMo/CNH catalyst as compared with the NiMo/OCP_f, NiMo/OCP and NiMo/CNT catalysts. Also, an enhanced product quality was generally observed for all the catalysts at higher temperatures. Compared to the remaining carbon-supported catalysts, the high surface area and moderated pore volume exhibited by NiMo/CNH catalyst contributed to its high activity since, such properties allow the active metals to be efficiently dispersed in the pores. This was also in accordance with the information by Ancheyta *et al.* (2005) that a highly disperse active phase is one of the key factors in attaining high conversions. In addition, Song (1992) discovered that fine particles with increased surface areas enhance conversions because of an improvement in mass transfer.

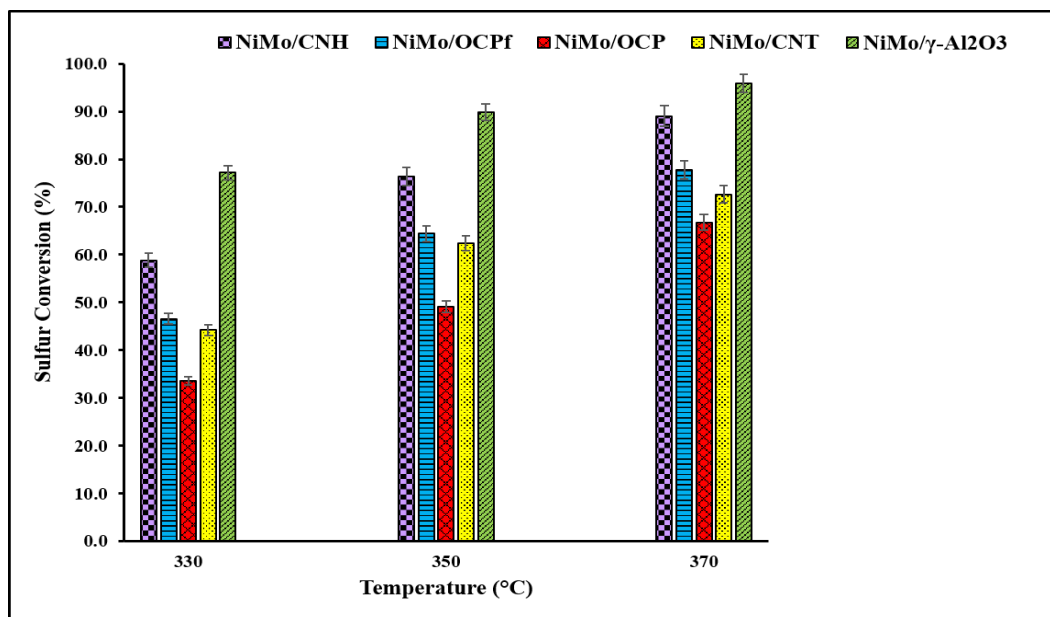


Figure 6.9 HDS activities of carbon and gamma alumina-supported NiMo catalysts using LGO at 370, 350, and 330 °C (Catalyst = 5 cm³, LHSV = 2 hr⁻¹, P = 9.0 MPa, and H₂ / oil ratio = 600 (v/v)).

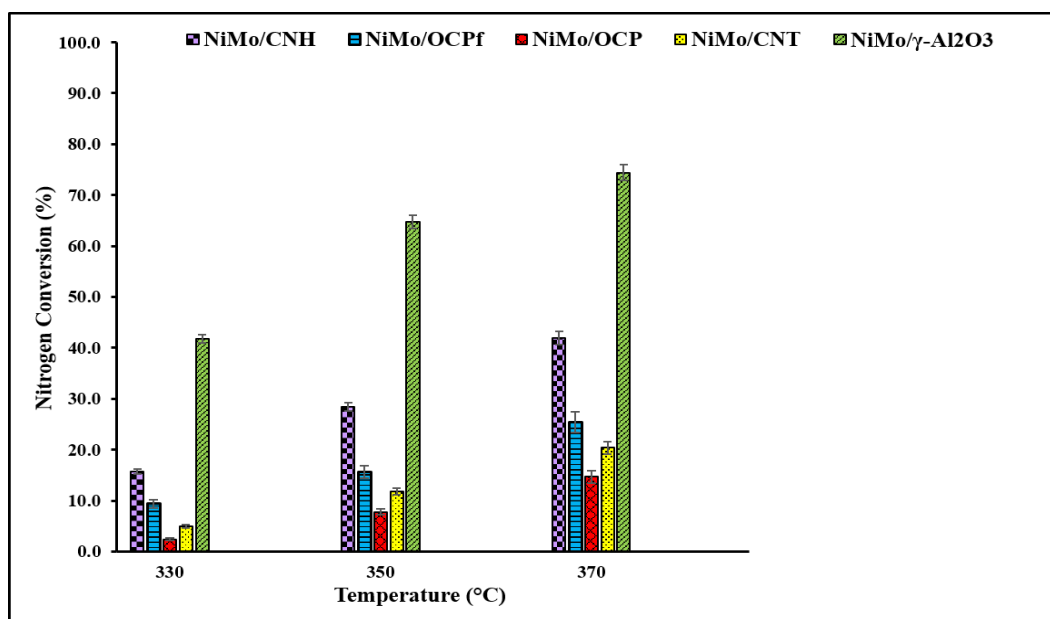


Figure 6.10 HDN activities of carbon and gamma alumina-supported NiMo catalysts using LGO at 370, 350, and 330 °C (Catalyst = 5 cm³, LHSV = 2 hr⁻¹, P = 9.0 MPa, and H₂ / oil ratio = 600 (v/v)).

The mesoporous diameter exhibited by all the catalysts was favorable since that ensured that, the ability of the catalyst to accommodate big molecules that takes part in reactions is retained thereby minimizing diffusional limitations. On the contrary, use of NiMo/CNT catalyst with larger mesoporous diameter (17.4 nm) relative to all the other catalysts used in this study may be disadvantageous in hydrotreating applications because, large molecules may diffuse in and out of the catalyst surface without having adequate contact to react and cause an improvement in HDS and HDN conversions. This may also be the reason why the NiMo/CNT catalyst registered lower HDS and HDN activities than the NiMo/OCP_f catalyst despite the fact that; (i) the surface area of NiMo/CNT catalyst was at least twice that of the NiMo/OCP_f catalyst, (ii) reducibility was easier with NiMo/CNT catalyst than with the NiMo/OCP_f catalyst, and (iii) about 8% improvement in dispersion was also realized with NiMo/CNT catalyst as compared to the NiMo/OCP_f catalyst. Besides, 30 minutes functionalization may also not be enough for etching oxygenated groups on CNT support since, CNT comprises of multi-walls that may limit effective functionalization and hinder the ability of the metals to anchor on support which can consequently have a negative impact on active metal dispersion, catalyst reducibility and eventually catalytic activity.

From XRD and CO-chemisorption results, the greater dispersion capability of metal oxide precursors on NiMo/CNH catalyst as compared to the remaining carbon-supported catalysts also contributed significantly to it having the highest activity among the carbon-supported catalysts. The higher dispersion effect and CO uptake was directly linked to the smaller crystallite size metal particles in the NiMo/CNH catalyst. In addition, translation of higher CO uptake and smaller crystallite size particles to higher HDS and HDN activities as demonstrated by NiMo/CNH catalyst occurred since, report indicates that smaller crystallite size particles not only decrease the presence of undesired diffusion limitations but, eventually causes reaction rate to increase (Hussain et al. 2011; Yin et al. 2011; Rodriguez-Reinoso, 1998). Based on TPR analysis, the easily reducible Mo species formed in the NiMo/CNH catalyst in comparison to NiMo/CNT, NiMo/OCP_f and NiMo/OCP catalysts had a tremendous effect on the highest activity outcome displayed by the NiMo/CNH catalyst since, easily reducible Mo species are normally the precursors needed for the formation of more active sites that enhances HDS activities. Based on Figure 6.5, another underlying reason why NiMo/CNH catalyst showed higher activity than the NiMo/OCP_f and NiMo/CNT catalysts is that, the NiMo/CNH catalyst showed prominent Lewis acid sites than NiMo/OCP_f and NiMo/CNT catalysts which facilitated C-N bond cleavage and led to further

improvement in HDN activities. Although some of the physico-chemical properties (e.g. textural properties, catalyst reducibility and dispersion of the active phase) results for NiMo/OCP_f catalyst were lower in value than that of NiMo/CNT catalyst, from Figures 6.9 and 6.10, the high HDS plus HDN activities of NiMo/OCP_f over NiMo/CNT catalyst may be due to the contribution from the superior-quality CNH particles embedded in the OCP_f support as shown in the TEM images of Figure 6.1. Additionally, from Figure 6.5, the discernible Lewis acid sites on NiMo/OCP_f compared to the unnoticeable acid sites on NiMo/CNT catalyst greatly influenced the higher activity displayed by the NiMo/OCP_f catalyst.

The lowest activity demonstrated by the NiMo/OCP catalyst was not surprising and was accounted for by its; negligible textural properties, lowest degree of dispersion consistent with CO-chemisorption and XRD results, as well as; its difficulties in getting reduced as revealed in Figure 6.4, TPR results. The low activity displayed by NiMo/OCP catalyst can also be linked to the functionality of OCP-carbon support, which was not encouraging since no apparent oxygenated groups were seen from its FTIR analysis (Figure not shown). OCP support was also found to be refractory and that reflected in its ability to resist thermal degradation as observed from TGA analysis. The absence of oxygenated functional groups certainly has a negative impact on hydrotreating activities due to the inability of the metals to anchor on the support during the catalyst preparation, and consequently the effect of this lack of requisite amount of catalyst metal composition on sulfidation, the active phase and catalytic activity. This is in agreement with inputs from various researchers who have testified that, these oxygenated functional groups which are equivalent to active sites, have significant impact on the characteristics of the support surface by likely influencing the metal-support-interaction as well as catalytic activities of carbon-supported catalysts (Hussain et al. 2011; Rodriguez-Reinoso, 1998). The low catalytic performance of NiMo/OCP catalyst can further be attributed to bigger crystallite size Ni-Mo particles in the NiMo/OCP catalyst that, leads to poor dispersion and a resulting negative influence in hydrotreating activities.

At operating temperature conditions of 330, 350 and 370 °C, the HDS activities of NiMo/ γ -Al₂O₃ catalyst were found to be 96%, 90% and 77%, whereas, the HDN activities were 74%, 65% and 42%. From Figures 6.9 and 6.10, HDS and HDN activities of NiMo/ γ -Al₂O₃ catalyst was found to be the highest among all the catalysts under study although, from Table 6.1 the textural properties NiMo/CNH catalyst (best catalyst among the carbon-supported catalysts) showed

higher textural properties and appeared to have weaker metal-support-interaction (XANES results) than NiMo/ γ -Al₂O₃ catalyst. This means that catalytic activity is not solely dependent on the catalyst's textural properties nor the metal-support-interaction but, its also influenced by other factors such as the degree to which metal components are dispersed on the catalyst, the way Ni and Mo catalyst species are reduced and the type and amount of acid sites. Therefore, the highest NiMo/ γ -Al₂O₃ catalytic activity from this present study can be correlated to; the highest degree of dispersion of its metal components (12.2%), the easily reducible Mo and Ni species (Figure 6.4) with easier possibility of being sulfided as well as, the occurrence of both Bronsted and Lewis acid sites on the NiMo/ γ -Al₂O₃ catalyst. A study by Wang *et al.* (2015) also confirmed that high amounts of acid sites results in easier cleavage of C-N bond which is of additional benefit to the enhancement of HDN efficiency. Check Appendix B for information about the effect of 15 minutes CNH functionalization on HDS and HDN activities using NiMo/CNH catalyst with Ni composition of 2.5 wt%, and Mo composition of 13 wt%.

6.6 Conclusions

Findings from this study reveals that among the carbon-supported catalysts, NiMo/CNH catalyst possesses excellent physico-chemical properties than NiMo/OCP_f, NiMo/OCP and NiMo/CNT. For the carbon supported catalysts, the highest HDS and HDN activities with real LGO feed were achieved with the NiMo/CNH catalyst with catalytic activity decreasing in this order: NiMo/CNH > NiMo/OCP_f, > NiMo/CNT > NiMo/OCP. Factors that contributed to the highest HDS and HDN activities of NiMo/CNH catalyst in comparison to the remaining carbon-supported catalyst include: homogeneity and structure of the CNH-carbon support, the superior textural properties of its functionalized support and catalyst, the easier reducibility of Ni and Mo species from their oxidic to sulfidic form, and the appearance of strong Lewis acid sites on NiMo/CNH catalyst. Therefore, overall, the selectivity of carbon-supported sulfide catalysts for hydrotreating reactions can be influenced by the type of carbon being used since, catalyst supported on CNH gave higher activity than that supported on OCP_f, OCP and CNT materials. For all the catalysts under study, catalytic activity using NiMo/ γ -Al₂O₃ was superior compared to the analogous carbon-supported catalysts and some factors that impacted its activity were it high percentage dispersion, and the presence of both Bronsted and Lewis acid sites (that enhances both hydrogenation and hydrogenolysis reactions). Although XANES analysis confirmed that the

coordination environment of Mo species in NiMo/CNH catalyst is a distorted octahedral environment implying that, it had less metal-support-interaction and more likely to create Type II Ni-Mo-S structures having enhanced activity, the effect from the Mo octahedral coordinated environment may not be significant since, the NiMo/ γ -Al₂O₃ catalyst with Mo tetrahedral environment and supposedly strong metal support still demonstrated the highest activity over all catalysts used in this study. In addition to NiMo/ γ -Al₂O₃ catalyst, NiMo/CNH catalyst can also be a suitable candidate to consider for deep HDS processes due to the higher catalytic activities achieved with NiMo/CNH catalyst from this study.

CHAPTER 7

Determination of a suitable NiMo/OCP_f catalyst with varying Ni and Mo loadings for hydrotreating of light gas oils

An article on this phase of work is being prepared for submission to a suitable journal (Microporous and Mesoporous Materials). Some aspects of this study have been presented at the following conferences:

- E. Aryee, A. K. Dalai, J. Adjaye, “Optimization of NiMo/OCP_f catalyst for hydrotreating of gas oils,” Oral presentation at 64th Canadian Chemical Engineering Conference, Niagara Falls, Ontario, Canada, October 19-22, 2014.
- E. Aryee, A. K. Dalai, J. Adjaye, “Determination of the best NiMo/OCP_f catalyst for hydrotreating: Effects of varying metal compositions in catalyst formulation,” Oral presentation at 66th Canadian Chemical Engineering Conference, Quebec City, Quebec, Canada, October 16-19, 2016.

Contributions to this phase of work

The Ph.D. candidate, Emma Aryee planned, designed and carried out the experiments under this phase of work. The work included, synthesizing CNH, differentiating the OCP_f material from the entire OCP material, determining the best functionalization condition for OCP_f, formulating different catalysts with combinations of metal compositions, and running all hydrotreating experiments. In addition, characterization of solid (pristine OCP_f, functionalized OCP_f, and OCP_f-supported catalysts) and liquid (treated and untreated gas oil) samples, data processing and interpretation, and documentation of the work were done by Emma Aryee. Dr. Philip Boahene, and Dr. Sandeep Badoga occasionally assisted Emma Aryee to trouble shoot the reactor. My supervisors Drs. A. K. Dalai and J. Adjaye, critically reviewed the experimental plan, provided suggestions and monitored the progress of work.

Contribution of this chapter to the overall Ph.D. work

This chapter would provide answers as to whether the hydrotreating performance of OCP_f-supported NiMo catalyst could be enhanced by impregnating metals and varying the metals composition since, the previous work in Chapter 6 proved that use of OCP_f as a support material was feasible. In addition, knowledge would be gained about the effects of different combinations of Ni and Mo metal compositions on catalytic properties, and their subsequent effects on HDS and HDN activities. OCP_f material comprises of CNH and other carbon particles. Hence, due to the low yield of CNH in comparison to the OCP_f material, information from this chapter would also aid to streamline the experimental plan for the final phase of work involving CNH catalyst development for high HDN and HDS activities.

7.1 Abstract

The by-products collected during the synthesis of carbon nanohorns (CNH) via the arc-discharge method is comprised of other carbon particles. Preliminary investigations (from Chapter 6) using the fine fraction of these other carbon particles (OCP_f) with 13 wt% Mo and 2.5 wt% Ni in hydrotreating light gas oil resulted in an HDS conversion of ~78 %, and HDN conversion of 25%. Variation of the metal compositions in catalyst formulation was therefore considered in this study to enhance the hydrotreating activity of OCP_f - supported catalyst, and to determine if the best NiMo/OCP_f catalyst achieved from this study could be a viable catalyst for hydrotreating applications. Prior to catalyst preparation, pristine OCP_f were functionalized using 30 wt% HNO₃ refluxed at 110°C for 30 mins. The co-incipient wetness impregnation method was used in preparing the catalysts and the Ni and Mo loadings investigated were within the range of (2.5 - 5.0 wt%) and (13 - 26 wt%) respectively. Techniques that were used to characterize the catalysts include; BET, TGA, XRD, CO-chemisorption, and TPR. BET data suggests mesoporous pore diameter (~10-13 nm) and CO-chemisorption results showed that at constant Mo loading of 13 wt% and 19 wt%, there was a surge in metal dispersion with increasing Ni concentration. Overall, the catalyst samples with maximum Ni loading of 5.0 wt%, and Mo loadings of either 13 or 19 wt% showed higher dispersion and the possibility of forming a type-II Ni-Mo-S phase with enhanced activity. All catalyst samples were tested in a trickle-bed micro reactor and the effects of the different metal compositions on both HDS and HDN activities are reported in this study.

7.2 Introduction

Hydrotreating is a catalytic hydrogenation process that is globally used to upgrade highly contaminated crude oil into high quality products with reduced sulfur, nitrogen, oxygen and metal content. The hydrotreating process also leads to the conversion of aromatics and olefins in the crude oil into saturated products. Hydrotreating therefore helps to meet the demands for cleaner environment and stricter regulations. Since this process is catalytically driven, development of a hydrotreating catalyst is one way of achieving optimal hydrotreating effect. Apart from the support, other key components of the catalyst are the active metals and promoters. Commonly used hydrotreating catalysts are supported-CoMo and -NiMo sulfides, and typical metal loading compositions for Ni (Co) and Mo are within the range of (3 - 8 wt%) and (10 - 30 wt%), respectively (Robinson and Dolbear, 2007). For a hydrotreating catalyst such as NiMo/Al₂O₃ the main catalytic active sites are the MoS₂ edges, and addition of a Ni promoter aids in increasing vacant sites by lowering the binding energy of sulfur present at the edges of MoS₂ (Afanasiev and Bezverkhyy, 2007; Grimbolt, 1998; Byskov et al. 1997). To some extent, some research work has revealed that the final sulfided phase of the active catalyst is dependent on the extent to which the supported NiMo catalyst in its oxide form becomes sulfided since, sulfidation partially converts these oxide species into their equivalent active Ni (Co)-Mo-S structures. As a result, during catalyst formulation it is important to use a suitable metal composition that would optimize the metal loading on the support, and consequently result in the achievement of maximum hydrotreating activity (López and López, 2000; Furimsky, 1998; Prins et al. 1989).

The Ni (Co)-Mo-S structure exist in two forms (Type I and Type II). Usually, the Type II structure is more active than the type I structure because, it is rarely attached to the support via Mo-O-Al linkages unlike, the Type-I structure which is more bonded to the support. For the Type II phase, Van der Waals forces of attraction exist between the support and the active phase. The linkages with the support create some steric hindrances during reactions. Hence, in the case of the Type II structure due to its less linkage with support, there is less effect from steric hindrance which makes it easier for reactant molecules to access the catalytic active sites. Comparatively, reactant molecules are more hindered from getting to the catalytic active sites in a Type I structure than a Type II structure. Also, the presence of Type II structures can result in high activities because of their weak metal-support-interactions. Therefore, an increase in temperature during

sulfidation favors a Type II structure since, stacking is enhanced as temperature increases which further creates a highly active Type II structure (Van Veen et al. 1993; Vissers et al. 1987).

The sulfiding temperature impacts the formation of different phases since high temperature sulfidation causes the MoS₂ particles that are parallel to the basal planes to grow in their size and transition from a two-dimensional structure (Type I) to a three-dimensional structure (Type II). For Type I structures, due to the strong bond that exists between Mo-O-Al linkages with the support, transition to Type II structures would require a breakage of these Mo-O-Al linkages. For certain catalysts (e.g. carbon-supported catalyst) that possess low or minimal support interaction after preparation, sulfidation of these catalysts using low temperature conditions can readily lead to the formation of Type II structures. For NiMo/ γ -Al₂O₃ catalysts that form strong metal support interaction with the support, apart from high sulfidation temperatures, transition to Type II structures can be obtained by using high metal loading or calcining the catalyst at high temperatures prior to hydrotreating. The properties at the active sites can be impacted by Mo loading and therefore low Mo loading are dominated by Type I structures whereas, higher Mo loadings are dominated by Type II structures. The MoS₂ crystallites are normally oriented in such a way that their basal planes are parallel to the support although there are rare cases whereby the basal planes of MoS₂ crystallites are oriented perpendicularly to the support (Scheffer et al. 1986; Candia et al. 1984).

Use of carbon as a support in heterogenous catalysis has attracted numerous attentions as a result of its relative chemical inertness, high porosity, high surface area, retention of its structural integrity, existence in various physical forms and ability to functionalize the carbon material to enhance catalytic activity. When given the choice to use carbon as a hydrotreating catalyst support, most researchers resort to carbon black or activated carbon as a result of their mass availability, low cost and high surface area. In recent times a plethora of research related to the use of carbon in catalysis is centred around carbon nanotubes and fullerenes, and investigations about their properties and possible applications are still in progress. Use of CNH as a catalyst support is also in the limelight. (Lam and Luong, 2014; Titirici and Antonietti, 2010; Falcao and Wudl, 2007; Rodriguez-Reinoso, 1998). As mentioned in previous chapters of this thesis, the arc-discharge method which is well-known for producing CNH is accompanied by the formation of a chunk by-product (termed OCP), and its fine fraction denoted as OCP_f. For anodic type of arc's in which ablation of the anode is prevalent, these by-products usually form on the cathode and fall off or

build up with time. Keidar *et al.* (2011) also added that for anodic arc, a carbonaceous deposit (~60-70% of the ablated material) inevitably forms on the cathode surface as a result of low thermal conductivity. This carbonaceous deposit can be described as having a crust-like texture with an inner black core that could contain carbon nanotubes, carbon nanoparticles and some graphitic particles. It is also noted to consist of a greyish metallic hard shell on the exterior with no nanotubes present. The appearance of this by-products after an arc experiment was also noted by Saito *et al.* (1993). In their work, they mentioned that a carbonaceous deposit made up of graphitic tubules and polyhedral particles accumulated on the face of the cathode electrode. (Keidar et al. 2011; Tang et al. 2005; Saito et al. 1993; Ebbesen and Ajayan, 1992). Gattia *et al.* (2006) were of the view that the deposits collected on the cathode after conducting arc-discharge experiments comprised of CNH, CNT, amorphous carbon and carbon nanocages, and their results were not far-fetched from the observations from many arc discharge experiments that mentioned the formation of a rich MWCNT among the deposits on the surface of the cathode (Zhang et al. 2019; Yeh et al. 2016; Arora and Neha, 2014; Ng and Raites.; 2014; Gattia et al. 2006).

The properties and characteristics of the OCP produced and used in this phase of work are similar to that described here. Thus, with the right operating conditions identified for the synthesis of CNH via the arc discharge method, OCP of similar characteristics will be generated. Yeh *et al.* (2016) also added that during the arc discharge process, the deposited carbonaceous material on the surface of the cathode and the walls of the reactor vessel contributed to the formation of nanoparticles by acting as an effective cathode electrode that sustained the arc discharge and reaction process. Results from their work also showed that a strong correlation exists between the radial distribution of the arc discharge current, temperature at the surface of the cathode deposit and the various morphologies of the deposits formed on the cathode. The complex nature of the formed nanoparticles are attributed to spatial variations of particle, plasma and heat fluxes from the arc to the deposit. The purity of the nanoparticles within the core area of the deposit are dependent on particle and heat flux from the plasma. The effective diameter of the cathode deposit is usually more than the anode diameter, and the deposit builds up at the center of the cathode due to the accumulation of more material (Yeh et al. 2016).

Laboratory synthesis of CNH shows that the yield of OCP_f was more than twice the CNH material of interest. Moreover, a comparative study from our previous work (phase 3 or Chapter 6) confirmed the feasibility of using OCP_f as a hydrotreating catalyst with Ni and Mo compositions

of 2.5 wt.% and 13 wt.% respectively, and this study resulted in HDS and HDN activities of ~78% and 25%, respectively. Thus, knowing the benefits of using carbon as a support, and having been convinced from other researches that the by-products are mainly carbon-based particles our goals were to (i) enhance the hydrotreating performance of NiMo/OCP_f catalyst by experimenting with different combinations of Ni and Mo compositions that would lead to higher HDS and HDN activities and (ii) to add value to an otherwise by-product which has not been used in any hydrotreating applications as far as we know. In addition, since the OCP_f material contains CNH materials, results from this study would henceforth help to determine the best conditions to focus on in an effort to develop the best NiMo/CNH catalyst for hydrotreating.

7.3 Experimental method

7.3.1 Catalyst preparations and hydrotreating experiments

The OCP_f material used as hydrotreating catalyst support in this study was obtained after separation following a CNH arc discharge synthesis. Thereafter, the size of the OCP_f support material that was used in making the various catalysts was classified by means of the US standard series No. 60 which is equivalent to 250-micron average particle diameter. In preparation for catalyst formulation, oxygenated functional groups were created on the OCP_f support by liquid oxidation. This step is important because it enhances their solubility and guarantees efficient wettability for metal anchorage because, catalyst preparation involved contacting the OCP_f material with catalyst precursor metals in solution. 30 minutes functionalization time emerged as the best duration for functionalizing OCP_f support material based on the results of a series of experimental runs to determine the best condition for OCP_f functionalization. Thus, all OCP_f support material were functionalized for 30 minutes using the same method from a previous description (Aryee et al. 2013). The functionalized supports were then impregnated with desired Ni (2.5, 3.5 and 5.0 wt%) and Mo (13, 19, 26 wt%) solutions via the incipient wetness co-impregnation method to form oxidic catalysts. Depending on the Ni and Mo loading combination, their respective nickel nitrate hexahydrate [Ni(NO₃)₂·6H₂O], and ammonium heptamolybdate tetrahydrate [(NH₄)₆Mo₇O₂₄·4H₂O] weights were used in making the metal precursor solutions. For easy referencing with regards to this study, the prepared catalysts were named as xNiyMo/OCP_f where; x is the wt% Ni composition and y is the wt% Mo composition used.

The wet catalysts that were formulated were oven dried at 110 °C overnight. Subsequently, each dried oxidic catalysts was ground, and calcined in a furnace at 450 °C for 5 hours using argon as a carrier gas at 50 mL/min flow rate. Prior to hydrotreating experiments, 5ml of each powdered catalyst was diluted with 12 ml of 90 mesh inert silicon carbide by way of loading into the reactor in 10-12 layers. Loading was done by alternating between catalyst and SiC. The top and bottom of the diluted catalyst mix was also packed with 3 mm glass beads, and different mesh sizes (16, 46, 60) of silicon carbide. The packing was done in such a way that the diluent size increased as it approaches the top and bottom end of the reactor. After the reactor had been loaded, it was sealed firmly, and then transferred and mounted into the hydrotreater assembly. The hydrotreater was pressurized to ~ 9.3 - 9.7 MPa with helium and tested for leaks over 24 hours.

In preparation for the hydrotreating experiments, the operating pressure was reduced to 9.0 MPa and kept constant throughout all experimental runs. The catalyst was wetted with a mixture of approximately 100 ml butanethiol (2.9 vol%) and insulating oil (500 ml). A sulfidation process continued for two consecutive days (48 hrs) after completion of catalyst wetting. Sulfidation temperatures of 193 and 343 °C, respectively were used for each of the days, and an LHSV of 1 hr⁻¹ was maintained throughout the sulfidation process. Once sulfidation was complete, the sulfiding solution was switched to light gas oil and the catalyst was precoked for 3 days at an LHSV of 2 hr⁻¹ and a temperature of 370 °C. Thereafter, the hydrotreating tests were executed at three different temperatures (i.e. 330 °C, 350 °C or 370°C). Each experimental temperature condition was run for 1.5 days and a constant LHSV and pressure of 2 hr⁻¹ and 9.0 MPa, respectively were maintained for all the runs. Hydrotreated liquid samples were collected after every 12 hours. However, a change in experimental temperature condition led to the discarding of collected samples for the initial 12 hours of run before any further storage was done. The collected samples were stripped for 2 hours with N₂ gas to eliminate the presence of any residual traces of NH₃ and H₂S in the liquid sample. Sulfur and nitrogen concentrations in the stripped liquid products were further analyzed with the Antek 9000 NS analyzer.

7.4. Characterizations

In order to have a better insight about the properties of the various NiMo/OCP_f catalysts used in this study, BET, TGA, XRD, CO-chemisorption, HRTEM, and TPR techniques were used to characterize the solid catalyst samples. Additionally, these techniques helped to interpret the

results on the impact of varying Ni and Mo loadings on HDS and HDN activities. The S and N compositions for both untreated and treated gas oil samples were determined using the Antek 9000 NS analyzer. Chapter 3 may be referred for information about these techniques and their corresponding sample analysis procedures.

7.5 Results and discussion

7.5.1 BET analysis of pristine OCP_f, functionalized OCP_f and OCP_f-supported NiMo catalysts

Table 7.1 shows the surface area, pore volume and pore diameter of as-synthesized OCP_f, functionalized OCP_f, and NiMo/OCP_f catalysts with varying Ni and Mo compositions. Similar to the CNH material, the functionalized OCP_f material was of higher surface area and pore volume than the pristine OCP_f due to the presence of defects after functionalization. Contrarily, a decrease in pore diameter was observed as the pristine OCP_f material was functionalized, and this was due to the breaking of bigger pores, with the average pore diameter being more representative of smaller pores (Karousis et al. 2016). For the different catalysts, it was observed that the surface area and pore volume of all the catalysts decreased from the functionalized material due to the plugging of pores by metals. An increment in pore diameter however, occurred after the functionalized OCP_f samples had been impregnated with metals to form different catalysts.

Table 7.1 BET analysis of pristine OCP_f, functionalized OCP_f, and NiMo/OCP_f catalysts.

Sample	BET Surface Area (m ² /g)	Pore Volume (cm ³ /g)	Pore Diameter (nm)
Pristine OCP _f	41 ± 2	0.15 ± 0.01	22.1 ± 0.2
Functionalized OCP _f	177 ± 2	0.19 ± 0.01	9.3 ± 0.1
2.5wt%Ni13wt%Mo/OCP _f	97 ± 1	0.12 ± 0.01	10.1 ± 0.2
2.5wt%Ni19wt%Mo/OCP _f	99 ± 2	0.14 ± 0.01	12.8 ± 0.1
3.5wt%Ni13wt%Mo/OCP _f	96 ± 2	0.12 ± 0.01	9.6 ± 0.1
3.5wt%Ni19wt%Mo/OCP _f	81 ± 2	0.12 ± 0.01	11.1 ± 0.1
5.0wt%Ni13wt%Mo/OCP _f	106 ± 2	0.12 ± 0.01	10.6 ± 0.1
5.0wt%Ni19wt%Mo/OCP _f	89 ± 2	0.12 ± 0.01	10.9 ± 0.1
5.0wt%Ni26wt%Mo/OCP _f	78 ± 2	0.12 ± 0.01	12.6 ± 0.2

There was no significant change in surface area at constant Ni composition of 2.5 wt% as Mo composition was raised from 13 wt% to 19 wt%. On the other hand, as the Ni loading was

kept constant at higher compositions (either 3.5 wt% or 5.0 wt%), increased in Mo composition from 13 wt% to 19 wt% resulted in ~16% decrease in surface area. This is because more pores were blocked as higher Mo loadings were impregnated on the support. Lower Mo loading of 13 wt % did not bring about any significant change in surface area and pore diameter at Ni compositions of 2.5 wt% and 3.5 wt%. At a constant Mo loading of 19 wt%, both the surface area and pore diameter decreased steadily as Ni compositions increased from 2.5 to 5.0 wt%. Overall all the catalyst exhibited mesoporous pore diameters and constant pore volume. From BET results it can be deduced that low Ni (2.5 wt%) and Mo (13 wt%) composition have less impact on the textural properties. However, at a higher Mo loading of 19 wt%, the impact on the surface area and pore diameter were significant and consistent as Ni compositions increased steadily from 2.5 – 5.0 wt%. The catalyst with the highest Ni and Mo compositions (5.0wt%Ni26wt%Mo/OCP_f) had the lowest surface area since its pores (most especially micropores) were filled with metals having higher weight compositions during catalyst formulation. Consequently, its pore diameter was high since, it was more likely for its micropores to be blocked making its mesopores the major representative of its pore diameter.

7.5.2 TGA analysis of the OCP_f-supported NiMo catalysts

Since all OCP_f catalysts were prepared from a by-product support and there is an instant negativity surrounding by-products, the thermal stability of the catalysts under hydrotreating temperature conditions (330, 350 and 370 °C) being experimented had to be tested with TGA to ensure that the catalysts would not burn out during the hydrotreating process but, can be able to resist thermal degradation. The TGA profiles of all the OCP_f-supported NiMo catalysts utilized in this study are displayed in Figure 7.1.

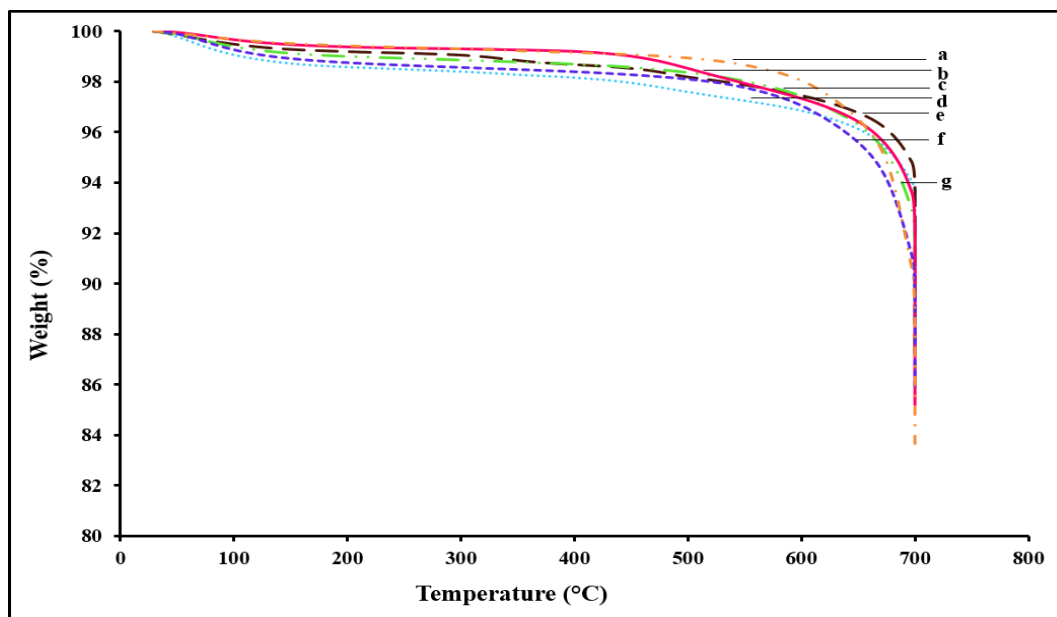


Figure 7.1 TGA profile of OCP_f -supported NiMo catalysts; a) 5.0wt%Ni19wt%Mo/ OCP_f , b) 3.5wt%Ni19wt%Mo/ OCP_f , c) 3.5wt%Ni13wt%Mo/ OCP_f , d) 2.5wt%Ni13wt%Mo/ OCP_f , e) 2.5wt%Ni19wt%Mo/ OCP_f , f) 5.0wt%Ni13wt%Mo/ OCP_f , g) 5.0wt%Ni12wt%Mo/ OCP_f .

From Figure 7.1, the desorption of water that had been physically adsorbed (due to the ability of the catalysts to adsorb water during the handling of catalysts) led to a weight loss of about 1% up to 120 °C. Afterwards, the weight loss was almost constant up to about 400 °C and mostly stable until ~ 600 °C. The stability of the thermal properties from 120 – 400 °C may be due to less concentration of surface defects on the catalysts. A slight loss in weight from 120 – 400 °C can be attributed to the loss of impurities that remain on the sample after catalyst preparation, or loss due to MoO_3 decomposition into MoO_2 or Mo_4O_{11} intermediate compounds (Serp, 2003; Spevack and McIntyre, 1992). Beyond 500 °C to 700 °C carbothermal reductive decomposition of NiO or NiMoO_4 may contribute to the weight loss (Lebukhova and Karpovich, 2008). The drastic drop in weight for the NiMo/ OCP_f catalyst samples at about 700 °C can also be attributed to the findings from Bekyarova *et al.* (2002) which showed that at higher temperatures of at least 700 °C, carbon nanomaterials are prone to burn-off due to instability. An inert gas (nitrogen) was used to carry out the TGA experiments. However, for a typical hydrotreating experiment, the reactive gas is hydrogen and since this gas is not inert the catalyst may not be stable in a hydrogen environment because of the possibility of reduction. On the other hand, the thermal stability of the catalyst in terms of thermal sintering is the same irrespective of the gas environment (inert or H_2)

since exposure to higher ($> 500\text{ }^{\circ}\text{C}$) gas-phase temperatures is the main factor that influences catalyst deactivation by thermal sintering (Fogler, 2016; Bartholomew, 2001). Based on the above information, the thermal stability of all the catalysts in terms of thermal sintering is assured for the hydrotreating temperatures ($330 - 370\text{ }^{\circ}\text{C}$) under study.

7.5.3 XRD analysis of the OCP_f -supported NiMo catalysts

Low angle XRD profile patterns of all the different NiMo/ OCP_f catalysts displayed in Figure 7.2 shows that a hexagonal mesoporous structure with well resolved strong ($2\theta = 0.9$) and weak ($2\theta = 1.7$) peaks were observed that were identical for every catalyst used in this study. The peaks were indexed at $d(100)$ and $d(110)$. This identical characteristic implied that variation in metal loading composition did not influence the hexagonal mesoporous structure. Figure 7.3 shows the high angle XRD profile patterns of all the NiMo/ OCP_f catalysts. All the samples exhibited crystalline phases. The 2θ diffraction peak at $\sim 26^{\circ}$ represents, (002) plane characteristic of a hexagonal carbon structure. This 2θ diffraction peak at $\sim 26^{\circ}$ also corresponds to an intense MoO_3 peak. Thus, the peak at this position can be associated to an overlap of MoO_3 and carbon (OCP_f) material. Other small intensity peaks occurred at $\sim 37^{\circ}$ and $\sim 54^{\circ}$ which corresponded to NiO and NiMoO_4 , respectively. The appearance of these characteristic crystalline peaks relating to MoO_3 , NiO and NiMoO_4 on the OCP_f -supported NiMo catalysts implied that the metals were not well dispersed on the support. A small diffraction peak relating to molybdenum carbide (Mo_2C) was also observed at $2\theta = \sim 62^{\circ}$ (Liu et al. 2011; Gattia D et al. 2006; Quanli et al. 2003). From Figure 7.3, it was also realized that, the crystalline peak intensities for the 5.0wt%Ni13wt%Mo/ OCP_f , 5.0wt%Ni19wt%Mo/ OCP_f , 3.5wt%Ni13wt%Mo/ OCP_f and 2.5wt%Ni13wt%Mo/ OCP_f catalysts were smaller than the rest of the catalysts and therefore, it is expected that the dispersion of the metal components in these catalysts would be much improved compared to the remaining OCP_f -supported NiMo catalysts used in this study.

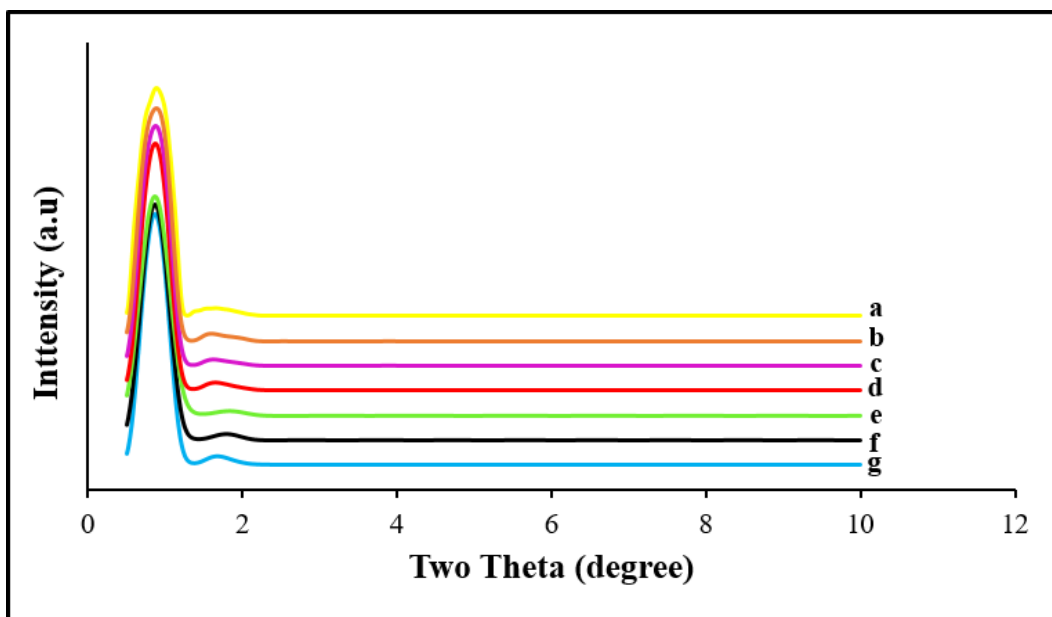


Figure 7.2 Low angle XRD pattern of OCP_f-supported NiMo catalysts;

- a) 5.0wt%Ni26wt%Mo/OCP_f b) 5.0wt%Ni19wt%Mo/OCP_f c) 5.0wt%Ni13wt%Mo/OCP_f
 d) 3.5wt%Ni19wt%Mo/OCP_f e) 3.5wt%Ni13wt%Mo/OCP_f f) 2.5wt%Ni19wt%Mo/OCP_f
 g) 2.5wt%Ni13wt%Mo/OCP_f.

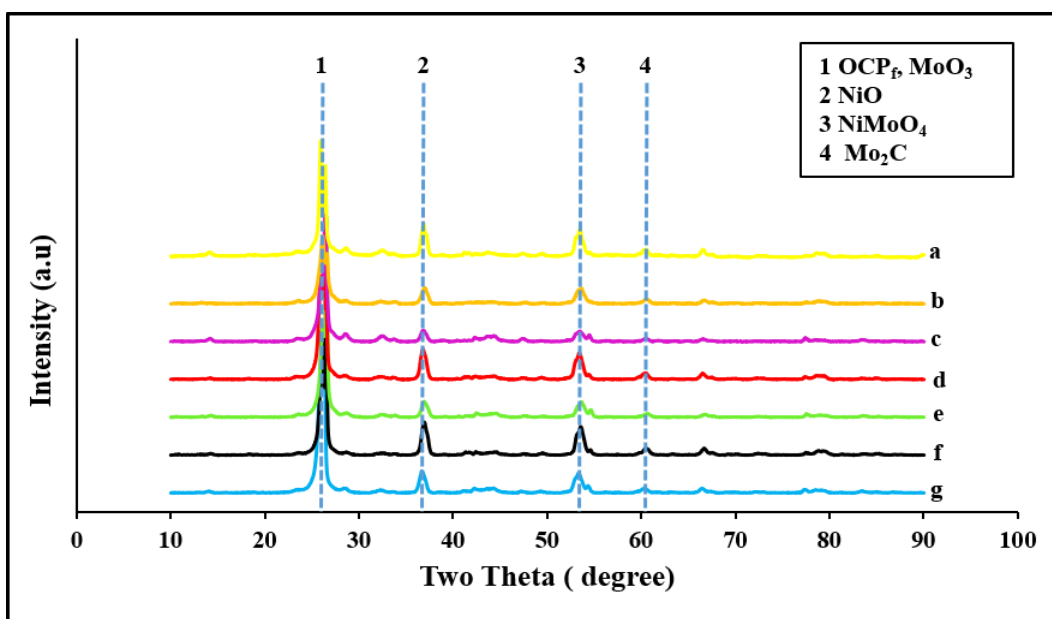


Figure 7.3 High angle XRD pattern of OCP_f-supported NiMo catalysts;

- a) 5.0wt%Ni26wt%Mo/OCP_f b) 5.0wt%Ni19wt%Mo/OCP_f c) 5.0wt%Ni13wt%Mo/OCP_f
 d) 3.5wt%Ni19wt%Mo/OCP_f e) 3.5wt%Ni13wt%Mo/OCP_f f) 2.5wt%Ni19wt%Mo/OCP_f
 g) 2.5wt%Ni13wt%Mo/OCP_f.

7.5.4 CO chemisorption analysis of the OCP_f-supported NiMo catalysts

Results from CO chemisorption analysis are displayed in Table 7.2, and these results shows that at constant Mo loadings of 13 wt% or 19 wt%, metal dispersion and CO uptake increased steadily with increasing Ni compositions from 2.5 to 5.0 wt%. This positive impact is ascribed to the fact that increase in Ni loadings increases the amount of Ni release during sulfidation, and this effect simultaneously enhances the redistribution of MoO₃ which further results in a decrease in crystallite size with a corresponding increase in metal dispersion (Badoga et al. 2014). However, at constant Ni composition of 2.5 and 5.0 wt% increasing Mo composition from 13 wt% to 19 wt% resulted in a decrease in dispersion. However, no change in dispersion occurred at constant Ni composition of 3.5 wt% as the Mo varied from 13 to 19 wt% even though there was an increase in the amount of CO absorbed. Additionally, so far as CO uptake was concerned, at constant Ni composition of either 2.5, 3.5 or 5.0 wt%, CO uptake increased with increasing Mo composition from 13 wt% to 19 wt%. These results indicate that a significant improvement in metal dispersion and CO uptake can be achieved by using a high Ni composition (3.5 and 5.0 wt%) and high Mo composition of 19 wt%. From Table 7.2, the 5.0wt%Ni13wt%Mo/OCP_f and 5.0wt%Ni19wt%Mo/OCP_f catalysts exhibited maximum metal dispersions whereas, the 5.0 wt%Ni26wt%Mo /OCP_f catalyst showed the least metal dispersion since, the Mo loadings of 26 wt% was too high for the 5.0 wt% Ni to have any positive influence on the redistribution of MoO₃ to form smaller crystallite size with enhanced dispersion.

Table 7.2 CO-chemisorption analysis of OCP_f-supported NiMo catalysts.

Catalysts	Metal Dispersion (%)	CO absorbed (μmol/g)	Crystallite Size (nm)
2.5wt%Ni13wt%Mo/OCP _f	5.8 ± 0.2	102 ± 2	21.6 ± 0.2
2.5wt%Ni19wt%Mo/OCP _f	4.4 ± 0.2	106 ± 1	28.5 ± 0.2
3.5wt%Ni13wt%Mo/OCP _f	6.2 ± 0.2	121 ± 2	19.7 ± 0.2
3.5wt%Ni19wt%Mo/OCP _f	6.2 ± 0.2	158 ± 2	20.1 ± 0.2
5.0wt%Ni13wt%Mo/OCP _f	9.3 ± 0.2	205 ± 2	12.9 ± 0.2
5.0wt%Ni19wt%Mo/OCP _f	7.8 ± 0.1	221 ± 2	15.7 ± 0.2
5.0wt%Ni26wt%Mo/OCP _f	3.8 ± 0.2	135 ± 1	32.6 ± 0.3

7.5.5 HRTEM examination of the morphology of the various OCP_f-supported NiMo catalysts

The morphology of the different NiMo/OCP_f catalysts used for this study are displayed in Figure 7.4. The TEM micrographs of all the catalysts showed dark spots that signified that metals have been impregnated on the support. However, the micrographs suggest that metals were not evenly dispersed on the support. Additionally, apart from CNH structures, some of the catalysts also revealed CNT and other embedded structures typical of an OCP_f material.

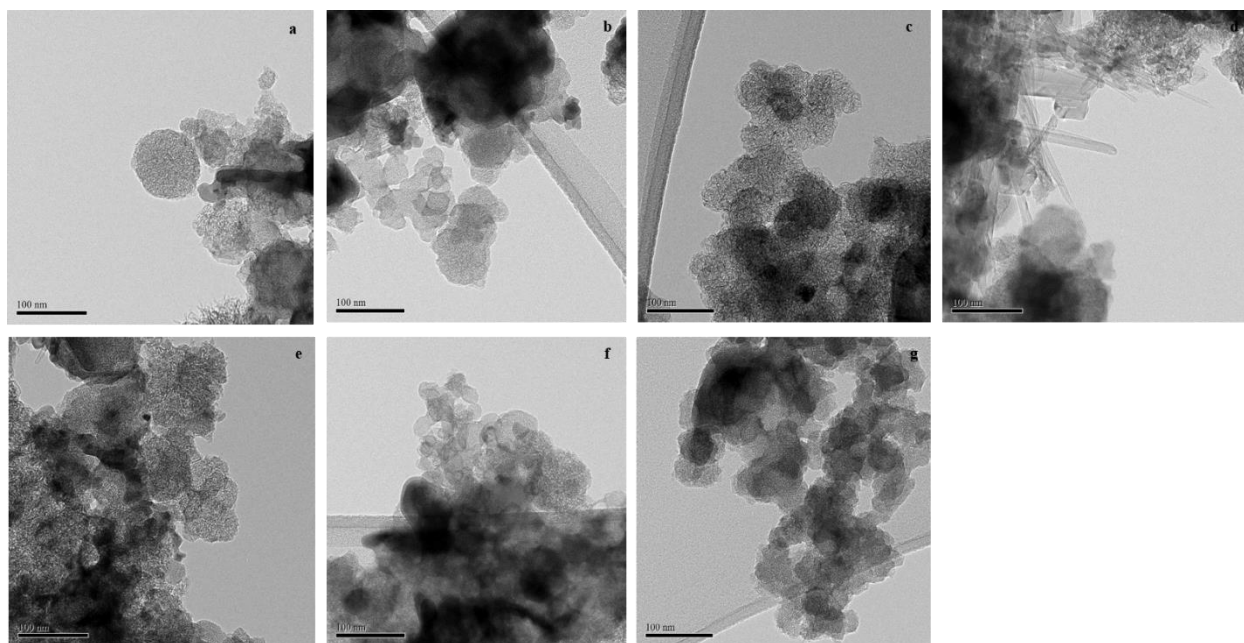


Figure 7.4 Morphology of different NiMo/OCP_f catalysts; a) 2.5wt%Ni13wt%Mo/OCP_f, b) 2.5wt%Ni19wt%Mo/OCP_f, c) 3.5wt%Ni13wt%Mo/OCP_f, d) 3.5wt%Ni19wt%Mo/OCP_f, e) 5.0wt%Ni13wt%Mo/OCP_f, f) 5.0wt%Ni19wt%Mo/OCP_f, g) 5.0wt%Ni26wt%Mo/OCP_f.

7.5.6 TPR analysis of the various OCP_f-supported NiMo catalysts

The TPR results of all the NiMo/OCP_f catalysts are shown in Figure 7.5. Two reduction peaks at low (250 to 480 °C) and high (580 to 660 °C) were detected. As mentioned in previous chapters, the first peak corresponded to a partial reduction of Mo⁶⁺ to Mo⁴⁺ whereas the second peak was from a combination of a complete reduction of Mo⁶⁺ to Mo⁴⁺ and Mo⁴⁺ to Mo⁰⁺. Reduction of Ni²⁺ also contributed to the low temperature reduction peak in the range of 250 to 375 °C whereas, NiMoO₄ also contributed to the reduction peak that ranged from 375 to 480 °C (Calafat et al. 1996; Brito et al. 1989; Hurst, 1982). Due to the low temperature peak reduction

observation in the vicinity of the first reduction peak, metal support interaction between the metallic oxides and the OCP_f support is expected to decrease and consequently cause an increase in hydrotreating performance (Qu et al. 2003).

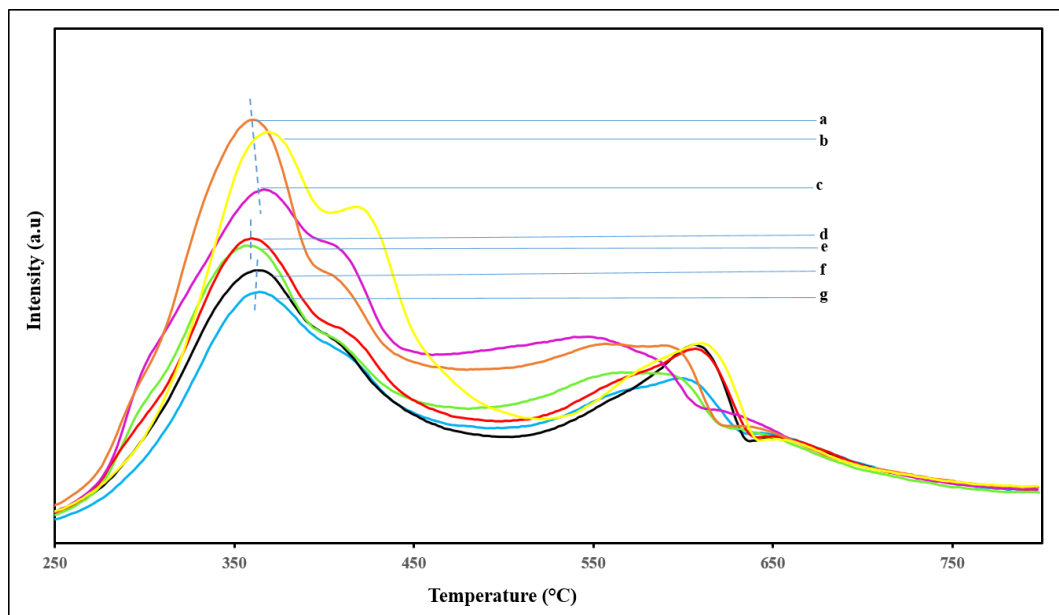


Figure 7.5 TPR results of NiMo/ OCP_f catalysts; a) 5.0wt%Ni19wt%Mo/ OCP_f , b) 5.0wt%Ni26wt%Mo/ OCP_f , c) 5.0wt%Ni13wt%Mo/ OCP_f , d) 3.5wt%Ni19wt%Mo/ OCP_f , e) 3.5wt%Ni13wt%Mo/ OCP_f , f) 2.5wt%Ni19wt%Mo/ OCP_f , g) 2.5wt%Ni13wt%Mo/ OCP_f .

For all the catalysts under study, variation of Ni and Mo in any of the catalyst combination only resulted in a slight change in the peak reduction temperature which was around 360 °C on the average. However, the hydrogen consumption intensity increased drastically as Ni compositions increased from 2.5 to 5.0 wt% as compared to the slight jump in hydrogen consumption intensity with increasing Ni composition from 2.5 to 3.5 wt%. From Figure 7.5, it was obvious that with the exception of the 5.0wt%Ni26wt%Mo/ OCP_f the hydrogen consumption intensities were higher at high Mo composition of 19 wt% for all catalysts under study as compared to the catalysts with low Mo composition of 13 wt%. Overall, the catalyst with the highest Ni and Mo composition (5.0wt%Ni26wt%Mo/ OCP_f) exhibited the greatest difficulty in reduction. Also, though the reduction temperature for the catalysts with 5.0 wt% Ni composition were higher in comparison, to the remaining catalysts and therefore signified high metal support interaction, on the contrary these catalysts are expected to result in high HDS and HDN activities because, their highest

hydrogen consumption intensities with sharp peaks especially in the case of the 5.0wt%Ni19wt%Mo/OCP_f catalyst renders MoO₃ in these catalysts to be readily transformed to a type-II Ni-Mo-S phase associated with enhanced activity (Yin et al. 2011; Park et al. 1997). Due to a slight change (increase or decrease) in their first peak reduction temperatures irrespective of the metal combination type any significant effect on the activity can therefore be attributed to the hydrogen consumption intensity.

7.5.7 HDS and HDN activities of the various OCP_f-supported NiMo catalysts

Figures 7.6 and 7.7 show the effects of temperature on the HDS and HDN activities of all the different catalysts used in this study. In all cases, the HDS and HDN activities increased with increasing temperature. A rise in HDS and HDN activities with increasing temperature is attributed to higher reaction rates and conversions with increasing temperature (Speight, 2000). Thus, maximum HDS and HDN activities were obtained at the highest operating temperature of 370 °C. Overall, for all the catalysts the HDS processes exhibited higher activities than the HDN processes under the different temperature conditions. This trend is acceptable because, it is much easier to convert sulfur compounds with less refractory linkages than total nitrogen compounds comprising of the most refractory compounds. Total nitrogen compounds in gas oils exist in two forms i.e. basic and non-basic nitrogen compounds. In terms of activity, the non-basic nitrogen compounds contribute to the low activities exhibited by total nitrogen compounds since they are less reactive (Sano et al. 2004; Botchwey et al. 2001; Laredo et al. 2001).

Results from Figure 7.6 show that at 370 °C, the HDS activities for the 2.5wt%Ni19wt%Mo/OCP_f, 3.5wt%Ni13wt%Mo/OCP_f, and 3.5wt%Ni19wt%Mo/OCP_f catalysts were almost the same (~85%). However, these catalysts exhibited a steady increase in HDN activities as their metal loading compositions increased. Also, from Figure 7.6, doubling the compositions of Ni and Mo in the 2.5wt%Ni13wt%Mo/OCP_f catalyst and 5.0wt%Ni26wt%Mo/OCP_f catalyst did not double the conversions as in a direct scale up manner. For HDS activities, a slight decrease (~1%) in conversion occurred when the Ni and Mo compositions were doubled. Whereas, a slight increase (~4%) in HDN activities occurred by doubling the metal compositions. This implies that doubling the metal compositions have insignificant impact on the conversions and not a good choice in catalyst formulation. The 2.5wt%Ni13wt%Mo/OCP_f catalyst which has the same composition as the OCP_f-supported NiMo

catalyst used in phase 3 (Chapter 6) exhibited an enhanced HDS and HDN activity of 89% and 41% due to an improvement in both the textural properties, and percentage dispersion as well as a reduction in the extent of reducibility. The improvement in textural properties may be attributed to the reduction in particle size from sieving, since more chunk materials were eliminated with the US No 60 standard series sieve used in this study versus the US No 50 standard series sieve used in previous study. Additionally, the improvement in dispersion and reducibility may be due to the LHSV value of 1 hr^{-1} , which was used in sulfiding the catalyst in this phase of work compared to LHSV value of 2 hr^{-1} used in sulfiding the catalysts in phase 3. Less LHSV means more contact time between the catalyst and liquid during sulfidation, and this increases the active sites with subsequent increase in activities.

Among all the catalysts, maximum HDS and HDN activities of 90% and 50%, respectively were attained with the 5.0wt%Ni19wt%Mo/OCP_f catalyst due to its high ability to consume hydrogen (TPR results), and that translates to easier formation to a type II Ni-Mo-S phase with enhanced activity (Yin et al. 2011; Park et al. 1997). The minimum HDS (84%) and HDN (42%) conversions were also obtained with the 2.5wt%Ni19wt%Mo/OCP_f catalyst because, of its low percentage dispersion (4.4%) coupled with it having the highest pore diameter (~13nm). Even though this pore diameter was the highest amongst all the catalysts, it may not be the optimal. This is because, it would allow reactant molecules to access the catalytic sites without making maximum contact at the active sites for maximum activity results. Although the 5.0wt%Ni26wt%Mo/OCP_f catalyst exhibited; the lowest percentage metal dispersion of 3.8 %, highest reducibility temperature and had the lowest surface area of $\sim 78 \text{ m}^2/\text{g}$, these properties did not have any negative impact on its corresponding HDS and HDN activities as a result of its high hydrogen consumption intensity from TPR results. High hydrogen consumption translates to high ability to form a type-II Ni-Mo-S phase. Hence, the 5.0wt%Ni26wt%Mo/OCP_f catalyst had a high propensity of forming a type-II Ni-Mo-S with enhanced activity as confirmed by Yin et al. 2011 (Yin et al. 2011; Park et al. 1997).

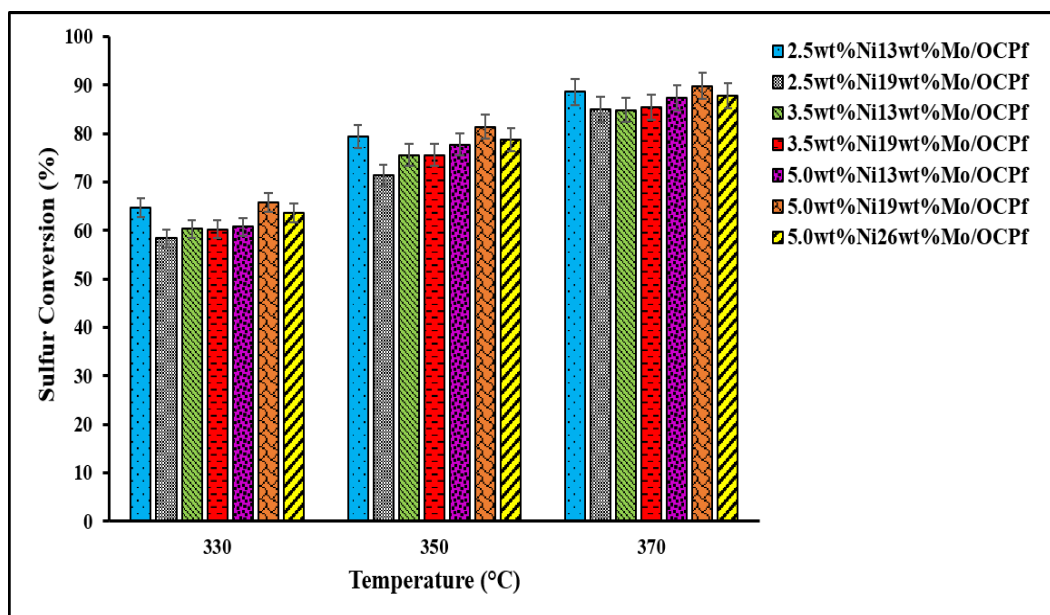


Figure 7.6 HDS activities of NiMo/OCP_f catalysts with LGO at 370, 350, and 330 °C (Catalyst = 5 cm³, LHSV = 2 hr⁻¹, P = 9.0 MPa, and H₂ / oil ratio = 600 (v/v)).

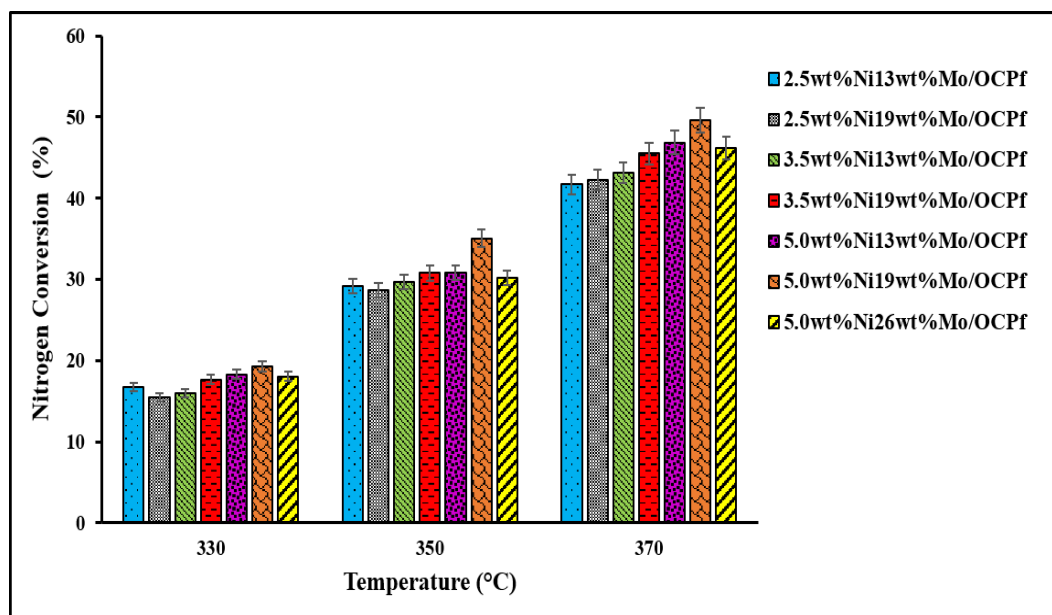


Figure 7.7 HDN activities of NiMo/OCP_f catalysts with LGO at 370, 350, and 330 °C (Catalyst = 5 cm³, LHSV = 2 hr⁻¹, P = 9.0 MPa, and H₂ / oil ratio = 600 (v/v)).

7.6 Conclusions

Variation in metal loading composition did not have any significant effect on the surface area at low Ni composition of 2.5 wt% and Mo composition of either 13 or 19 wt% percent. Beyond this, a decrease in surface area was obtained at constant Ni compositions (3.5 and 5.0 wt%) as Mo composition increased from 13 to 19 wt%. Similar pore volumes ($\sim 0.12 \text{ cm}^3/\text{g}$) together with mesoporous pore diameter ranging from (10 -13 nm) were attained irrespective of the catalyst combination type. All the different combinations of catalyst made from the arc discharge by-products showed, high thermal stability with low weight loss (1%) within the hydrotreating operating temperature conditions (330-370 °C) of interest. From CO-chemisorption results it was observed that an increased in Ni composition of 5.0 wt% played a dominant role in enhancing both the percentage metal dispersion and CO uptake as well as decreasing the crystallite sites. TPR analysis also showed that even though the catalysts with high Ni composition of 5.0 wt% demonstrated slight difficulties in reducibility due to their increasing reduction temperature peak, the influence from their corresponding high hydrogen consumption surpassed that of the effect from metal support interaction. Hence, they showed HDS and HDN activities comparable to the remaining catalysts used in the study. Subsequently, the 5.0wt%Ni19wt%Mo/OCP_f demonstrated the highest HDS and HDN activities of 90% and 50%, respectively at 9.0 MPa pressure, 370°C and 2 hr⁻¹ LHSV with light gas oil. On the other hand, the 2.5wt%Ni19wt%Mo/OCP_f catalyst also displayed the lowest HDS and HDN activity for same experimental conditions.

CHAPTER 8

Development of the NiMo/CNH catalyst for hydrotreating: Characterization, statistical, hydrodynamics, mass transfer and kinetic studies

The content of this chapter has not been communicated with the external scientific community in any form (oral presentation, poster presentation or journal article). This chapter will be expatiated further for submission to two Journal articles (i.e. one involving the characterization of catalysts and corresponding hydrotreating activity results, and the other involving the Design of Experiments, mass transfer, kinetics and deactivation study).

Contributions to this phase of work

Emma Aryee, the Ph.D. candidate prepared and characterized all the catalysts and conducted hydrotreating experiments under this study. Emma Aryee used central composite design (CCD) method to design experiments for the optimization of hydrotreating operation variables. Characterization of liquid samples, data processing, results interpretation, maintenance and troubleshooting of hydrotreator were also done by Emma Aryee. Emma Aryee consulted with Majak Mapiour on mass transfer and kinetic calculations. The experimental plan was critically reviewed by my supervisors, Dr. A. K. Dalai and Dr. J. Adjaye. Drs Dalai and Adjaye also provided suggestions and monitored the progress of this study through discussions and meetings.

Contribution of this chapter to the overall Ph.D. work

The main goal of this study is to develop the best NiMo/CNH catalyst for hydrotreating, optimize hydrotreating process parameters and to study the hydrodynamics of the system as well as, mass transfer resistances and kinetics involved in HDS and HDN reactions. First, the best CNH supported catalyst was tested in a pelletized form to determine if there is any variation in activity between the powdered and pelletized catalyst. Second, the effect of a secondary additive, phosphorus (P) in the best catalyst was tested further to investigate its impact on HDS and HDN activities. As a result, this chapter would provide information on how different Ni and Mo

combinations on CNH-supported catalysts affects hydrotreating performance. In addition, the effects of pelletization on hydrotreating activities using the best NiMo/CNH catalyst would be insightful. The role of a secondary additive (P) on the hydrotreating performance would also be evaluated. Information from this chapter would also help to determine if a carbon-supported catalyst would satisfy the hydrodynamics of a trickle-bed reactor in hydrotreating applications. Mass transfer calculation results would provide awareness as to whether the HDS and HDN reaction rates are limited by mass transfer or not. Information about kinetic parameters such as rate constant, order of reaction and activation energy would be made available through the evaluation of the Power Law model. This chapter would also provide information on the long-term (≥ 45 days) stability of the best NiMo/CNH catalyst for HDS and HDN reactions.

8.1 Abstract

A co-impregnation method was used to formulate three different catalysts loaded with Ni and Mo for hydrotreating of light gas oil. Mo loading was maintained constant at 19 wt% whereas, the Ni concentrations varied from 2.5 to 5.0 wt% in these catalysts. The 3.5Niwt%19wt%Mo/CNH catalyst gave the highest HDS and HDN activities of 95% and 66%, respectively after hydrotreating. However, lower HDS (91%) and HDN (57%) activities were obtained using this same catalyst in a pelletized form, indicating mass transfer resistances in the pelletized catalyst. A phosphorus-doped catalyst prepared with similar Ni and Mo loading on the best catalyst but having (phosphorus as an additive) resulted in HDS and HDN activities of 89% and 75% respectively. This indicated that, the additive significantly increased the HDN reaction by creating new Bronsted acid sites that enhanced C-N bond breaking which happens to be the rate determining step in HDN reactions. The hydrodynamics of the reactor using the powdered 3.5Niwt%19wt%Mo/CNH catalyst was tested, and it was found that the effect of high back mixing, poor catalyst wetting, and wall effect could be negligible. A central composite design of experiment was used in determining the optimum process condition for hydrotreating using the best catalyst formulation. The order of reaction and activation energy for HDS and HDN reactions were found to be 1.4 and 64 kJ/mol, and 1.0 and 92 kJ/mol, respectively.

8.2 Introduction

Hydrotreating is one of the most common technologies used in the refinery to generate cleaner fuels. Hydrotreating processes continue to progress due to increasing demand to process feedstocks heavily contaminated with impurities such as nitrogen, sulfur, and aromatic compounds as well as, the need to meet stricter environmental regulations. Since the hydrotreating process is catalytically driven, refineries and researchers are compelled to develop active catalyst that could be effectively used to achieve better hydrotreating activities. Transition metal sulfides such as Mo, Co, Ni, and W are the most common components present in a hydrotreating catalyst due to their availability, low cost, and their ability to yield higher hydrodenitrogenation (HDN), hydrodesulfurization (HDS), and hydrogenation (HYD) activities over years (Leliveld and Eijsbouts, 2008). A typical commercial hydrotreating catalyst is made up of promoted MoS₂ or WS₂ particles that are spread on a high surface area support. Under typical hydrotreating operating conditions, these highly active MoS₂ crystallites occur as single layer S-Mo-S and their average size is approximately 2-3 nm. Addition of small fraction of either Ni and Co relative to the amount of Mo used, increases the reactivity of the catalyst. Determining the optimal combination of Ni and Mo compositions in a hydrotreating catalyst is a positive step towards catalyst development. Secondary promoters (phosphorus, boron and fluorine) are sometimes added to the catalyst systems to enhance the catalysts activity and selectivity (Sigurdson et al. 2008; Maity et al. 2005; Klimov et al. 2018). The catalysts physicochemical properties can be strongly affected after the addition of phosphorus since, numerous research work over the years have demonstrated that addition of phosphorus to the catalyst can alter the catalysts structural properties, modify the type of Ni in the catalyst by enhancing the octahedral nickel present in the catalyst and improve hydrotreating activities by transforming Type I Ni-Mo-S phase to a Type II Ni-Mo-S phase. Addition of phosphorus has been known to enhance the reducibility and dispersion of metal species (Mo, Ni (Co)) and increases both the number of stacks and MoS₂ slab size (Maity et al. 2003; Antanasova et al. 1997; Eijsbouts et al. 1991; Zeuthen et al. 1991; Spojakina et al. 1989; Atanasova et al. 1988).

Due to the complexity of the hydrotreating process and the interdependence of hydrotreating operating parameters like temperature, pressure and LHSV on HDS and HDN activities, the central composite design method can be used to study the impact of operating parameters on hydrotreating activities. The presence of both internal and external mass transfer

resistances can have constraining effects on the reaction rate, rate of conversion, product formation and on the overall hydrotreating performance. Ability to disregard both internal and external mass transfer resistances is important to efficiently evaluate the intrinsic kinetics in a trickle-bed reactor. Catalyst deactivation is also a crucial problem to deal with since they affect the longevity of the active catalyst. For instance, it is known that promoter metals such as Ni or Co starts to detach from Mo once, sulfidation is completed and subsequent utilization of the catalyst progresses. It is therefore important to have a catalyst that could endure longer cycle lengths whilst achieving clean fuel specification goals (Vogelaar et al. 2010, Leliveld and Eijsbouts, 2008). This present work therefore addresses (i) the best Ni and Mo combination that can enhance HDS and HDN activities (ii) the effect of using a catalyst in a powdered vs pelletized form on hydrotreating performance (iii) the consequences of using a phosphorus doped catalyst for hydrotreating (iv) the optimized operating variables that can enhance HDS and HDN activities and (iv) whether the negligibility of mass transfer resistances assumption in HDS and HDN reactions is valid.

8.3 Experimental Method

8.3.1 Catalyst preparations, hydrotreating experiments and statistical analysis method

Four catalysts were prepared using CNH material that had already been functionalized by the method and conditions described in Chapters 5 and 6. An incipient wetness co-impregnation method was used in impregnating respective compositions of metals on the functionalized CNH support. For the series of NiMo/CNH catalysts that were produced, Ni concentration was varied from 2.5 to 5.0 wt% whereas, the Mo loading was kept constant at 19 wt%. Ammonium heptamolybdate $[(\text{NH}_4)_6\text{Mo}_7\text{O}_{24}\cdot 4\text{H}_2\text{O}]$ and nickel nitrate $[\text{Ni}(\text{NO}_3)_2\cdot 6\text{H}_2\text{O}]$ were used as precursor solutions. Once catalyst formulation, drying and calcination were done, the samples were stored in a vial in preparation for the corresponding hydrotreating experiments. The prepared catalysts were designated as xNi_yMo/CNH where x, and y are the wt% of Ni and Mo impregnated on the support. The catalysts were further calcined to transform the OH groups that occurred as a result of catalyst formulation into oxide groups. After running a series of hydrotreating experiments with these calcined powdered catalysts, the HDS and HDN activities of these catalyst demonstrated that higher hydrotreating performance was achieved with the 3.5wt%Ni19wt% Mo/CNH catalyst. The d50 value for the powdered 3.5wt%Ni19wt% Mo/CNH catalyst was found to be approximately 0.1 mm, and this particle size was used for hydrodynamics and mass transfer calculations since it was

equivalent to the average particle size. The particle size distribution of the 3.5wt%Ni19wt%Mo/CNH catalyst is also shown in Figure 8.1. This was determined using a Mastersizer instrument. A pelletized form of the 3.5wt%Ni19wt%Mo/CNH catalyst was made after, compressing some quantity of its calcined catalyst in powdered form into a form of a disc using a Carver hydraulic press. Approximately 67000 N force was exerted, and no binder was used during pelletization. Thereafter, pellets were made using the US number 12 standard sieve series. The size of the pellets was approximately 1.8 mm. The pelletized catalyst was denoted as xNiyMo/CNH (pel) where, x and y are the wt% of Ni and Mo which was the same as the concentrations in the best catalyst whereas, pel means pelletized.

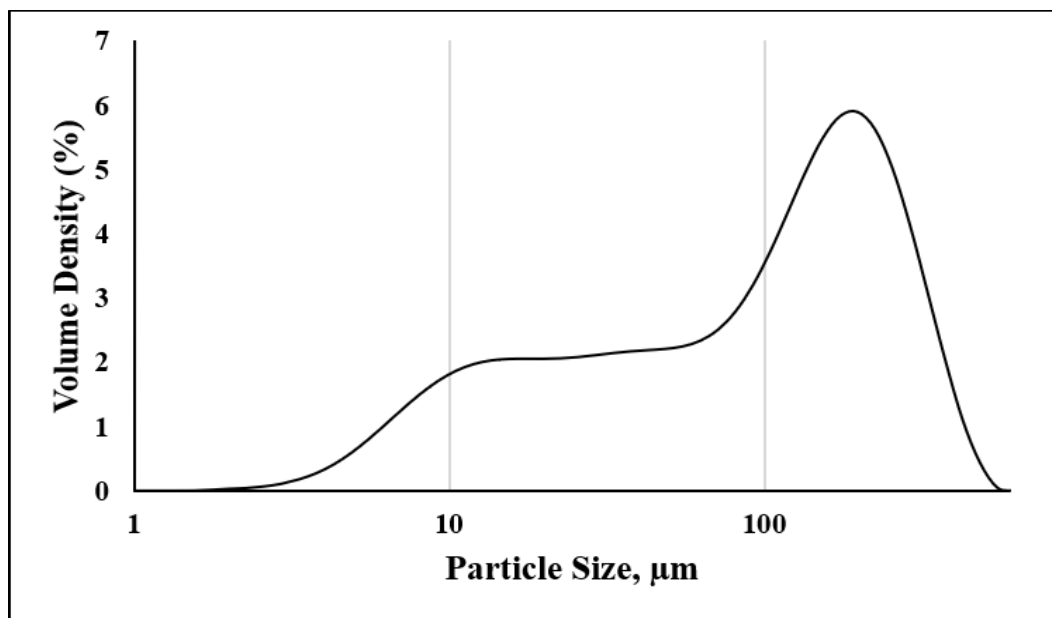


Figure 8.1 Particle size distribution of 3.5wt%Ni19wt%Mo/CNH catalyst.

A phosphorus doped catalyst was subsequently prepared with similar Ni and Mo compositions as the 3.5wt%Ni19wt%Mo/CNH catalyst but having an additional secondary promoter (P). For this catalyst, the concentration of phosphorus used was 2.0 wt% hence, required amounts of nickel nitrate, ammonium heptamolybdate and phosphoric acid (H_3PO_4) were co-impregnated on a functionalized CNH support material. The prepared catalyst was denoted as xNiyMozP/CNH where x, y, z represented the wt% of Ni, Mo and P, respectively, on the catalyst. For each of the hydrotreating experiments, 5 ml of the catalyst that had been prepared was loaded in a micro-trickle bed reactor. The hydrotreating feed was light gas oil. Details on catalyst

preparation method and hydrotreating experimental method can be found in Chapters 5, 6, and 7. A schematic of the hydrotreater is also shown in chapter 1.

Optimization of hydrotreating process variables was done with the aid of a response surface methodology (i.e. the central composite design of experiment method) in Minitab18. Three design factors were considered i.e. temperature ($^{\circ}\text{C}$), pressure (MPa) and LHSV (hr^{-1}), and the response variables for this design were the percent sulfur and nitrogen removal after the hydrotreating of light gas oil. 50 mL/min of hydrogen flow rate was kept constant for all the runs. Table 8.1 shows the coded levels and actual values of designed factors. Based on the design factors, 20 hydrotreating experimental runs were conducted.

Table 8.1 Design levels (coded and uncoded) for design of experiment.

Variable	Symbol	Coded level		
		-1	0	1
Temperature ($^{\circ}\text{C}$)	T	330	350	370
Pressure (MPa)	P	8.3	9.0	9.7
Liquid hourly space velocity (hr^{-1})	LHSV	1	1.5	2

8.4 Characterization

Characterization of the catalyst samples were accomplished with CO-chemisorption, BET, XRD, and TPR techniques. Antek NS analyzer was used to determine the N and S content in gas oils before and after hydrotreating with the ASTM D4629 and ASTM D5463, respectively. Information about these techniques and sample analysis procedures can be found in Chapter 3 of this thesis. The samples were analyzed multiple times to establish average values and, the standard deviation, given in Results and Discussion section.

8.5 Results and discussion

8.5.1 Textural properties of pristine CNH, functionalized CNH and NiMo/CNH and P-doped NiMo/CNH catalysts

The textural properties result of all catalysts used in this study can be found in Table 8.2. Comparison of the pristine CNH to the functionalized CNH, shows that functionalization resulted in an increase in pore volume and surface area as well as a decline in pore diameter. This trend was similar to, those observed and presented in Chapters 5 and 6 about the effect of functionalization on pristine CNH samples. Relative to the functionalized CNH sample, an increase in pore diameter and a decrease in both surface area and pore volume were obtained for

all the catalyst samples. Mesopores were obtained for all catalysts with the exception of the phosphorus doped catalyst. All the catalysts showed an average pore volume of $\sim 0.48 \text{ cm}^3/\text{g}$. The 40% decrease in pore volume for the P-doped catalyst can be attributed to the collapse of pore walls as a result of the harsh impact from the phosphoric acid precursor used in preparing the P-doped catalysts. This consequently led to a reduction in surface area of the P-doped catalyst as compared to the 3.5wt%Ni19wt%Mo/CNH catalyst without P. The pore diameter of the 3.5wt%Ni19wt%Mo/CNH catalyst however remained the same with and without phosphorus. From, Table 8.2 it was observed that for the NiMo/CNH catalysts, increasing Ni loading from 2.5 to 5.0 wt% resulted in an increase in surface area, and this is ascribed to the formation of small crystallite size MoO_3 with higher Ni loadings (Badoga et al. 2014).

Table 8.2 Textural properties of pristine CNH, functionalized CNH and NiMo/CNH and P-doped NiMo/CNH catalysts.

Samples	BET SA (m^2/g)	Pore Volume (cm^3/g)	Pore diameter (nm)
Pristine CNH	158 ± 1	0.65 ± 0.01	20.1 ± 0.1
Functionalized CNH	724 ± 1	0.88 ± 0.01	11.7 ± 0.1
2.5wt%Ni19wt%Mo/CNH	240 ± 2	0.49 ± 0.02	15.6 ± 0.2
3.5wt%Ni19wt%Mo/CNH	250 ± 2	0.47 ± 0.01	14.6 ± 0.1
5.0wt%Ni19wt%Mo/CNH	345 ± 2	0.49 ± 0.01	13.5 ± 0.2
3.5wt%Ni19wt%Mo2.0wt%P/CNH	197 ± 2	0.29 ± 0.01	14.7 ± 0.1

8.5.2 Examination of XRD patterns

The XRD patterns of all the catalysts can be seen in Figure 8.2. The strong characteristic peak with highest intensity at $2\theta = \sim 26^\circ$ corresponded to an overlapped peak characteristic of either carbon or MoO_3 . The thin width of this predominant $2\theta = \sim 26^\circ$ peak on the P-doped catalyst as compared to the remaining catalyst under study indicates that, this peak is more representative of just a carbon characteristic peak since, overall metal dispersion was highly enhanced on P-doped catalyst as compared to the remaining catalysts under study. Unlike the P-doped catalyst, other small distinct characteristic peaks were observed from all the remaining catalysts at $2\theta = \sim 37^\circ$, 44° and 54° . The peaks at $2\theta = \sim 37^\circ$ and $\sim 44^\circ$ are related to NiO characteristic diffraction peaks whereas, the peak at $2\theta = \sim 54^\circ$ corresponded to NiMoO_4 characteristic diffraction peak (JCPDS card numbers: 78-0429, 33-0948). The peak at $2\theta = \sim 44^\circ$ was even more pronounced on the 5.0wt%Ni19wt%Mo/CNH catalyst as compared to the 2.5wt%Ni19wt%Mo/CNH and

3.5wt%Ni19wt%Mo2wt%/CNH catalyst. Based on these observations it can be inferred that dispersion of NiO and NiMoO₄ were not well dispersed on the 2.5wt%Ni19wt%/CNH and 3.5wt%Ni19wt%/CNH catalysts and even poorly dispersed on the 5.0wt%Ni19wt%/CNH catalyst relative to the P-doped catalyst.

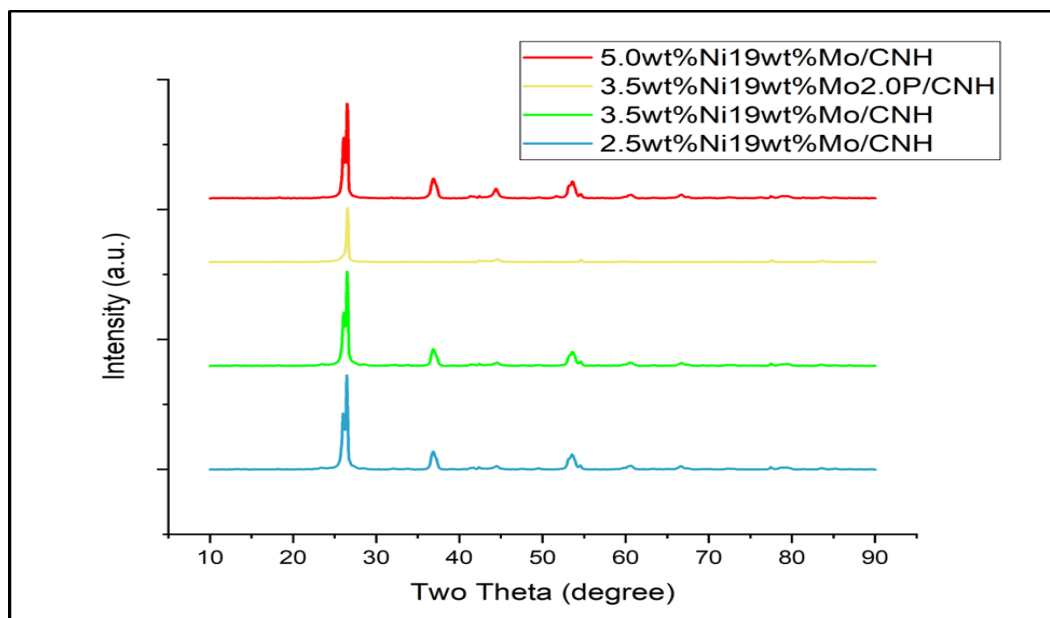


Figure 8.2 XRD patterns of NiMo/CNH and P-doped NiMo/CNH catalysts.

8.5.3 CO-chemisorption analysis of catalysts

Table 8.3 shows the results of CO-chemisorption analysis of all catalysts used in this study. For each sample the analysis was conducted 3 times and the results were repeatable. From Table 8.3 it can be inferred that at constant Mo composition, increasing Ni loading from 2.5 to 3.5 wt% enhanced both the redistribution of MoO₃ and formation of small crystallite since, the metal dispersion and co-uptake increased with increasing Ni content whereas, the crystallite size decreased with increasing Ni loading (Badoga et al. 2014). Additional increase in Ni loading from 3.5 to 5.0 wt% as (e.g. the 5.0wt%Ni19wt%Mo/CNH catalyst), counteracted the enhanced dispersion effect caused by increasing Ni loading. This is because although MoO₃ dispersion might have been improved, the high 5.0 wt% Ni content in the catalyst was an added disadvantage to the catalyst since, it led to a poor dispersion of NiO and NiMoO₄ as confirmed by the XRD analysis. Thus, the decrease in dispersion and increase in crystallite size as Ni loading increased from 3.5 wt% to 5.0 wt% can be associated with the poor dispersion of NiO and NiMoO₄. Results from

Table 8.3 also showed that there was better metal dispersion, CO uptake and smaller crystallite size for the P-doped 3.5wt%Ni19wt%Mo/CNH catalyst and agrees with the XRD results in Figure 8.1.

Table 8.3 CO chemisorption results of various NiMo/CNH catalysts.

Catalyst	Metal Dispersion (%)	CO Adsorbed ($\mu\text{mol/g}$)	Crystallite Size (nm)
2.5wt%Ni19wt%Mo/CNH	8.5 ± 0.2	206 ± 2	14.6 ± 0.2
3.5wt%Ni19wt%Mo/CNH	9.3 ± 0.1	238 ± 1	13.3 ± 0.1
5.0wt%Ni19wt%Mo/CNH	7.1 ± 0.1	202 ± 1	17.1 ± 0.1
3.5wt%Ni19wt%Mo2.0wt%P/CNH	9.2 ± 0.1	238 ± 1	13.4 ± 0.1

8.5.4 TPR analysis of catalysts

The TPR analysis of all the catalysts used in this work is shown in Figure 8.3. From Figure 8.3 it was noted that reducibility of MoO_3 occurred in two steps. The first step with low reduction peak temperature was in the range of ~ 330 to 400 °C whereas, the second step with high reduction peak temperature was found within the range of ~ 480 to 600 °C. The two-step mechanism for MoO_3 reduction is illustrated as follows: (i) $\text{MoO}_3 + \text{H}_2 \rightarrow \text{MoO}_2 + \text{H}_2\text{O}$ (ii) $\text{MoO}_2 + 2\text{H}_2 \rightarrow \text{Mo} + 2\text{H}_2\text{O}$ (Brito and Laine, 1989). Based on the first reduction peak, the reducibility of all catalysts under study decreased in this order:

3.5wt%Ni19wt%Mo2.0wt%P/CNH (~ 348 °C) > 3.5wt%Ni19wt%Mo/CNH (~ 351 °C)
 > 5.0wt%Ni19wt%Mo/CNH (~ 358 °C) > 2.5wt%Ni19wt%Mo/CNH (~ 357 °C).

The trend implied that the P-doped catalyst, which exhibited the lowest peak temperature, was more likely to form reducible species with possibly less metal support interaction as compared to the rest of the catalysts. Additionally, From Figure 8.3, it was observed that the 3.5wt%Ni19wt%Mo/CNH had a larger peak area which translates to higher hydrogen consumption. Thus, with its lowest reduction peak of ~ 351 °C, it is more likely to form highly dispersed and reducible Ni and Mo species as compared to, the other remaining catalysts that were not doped with phosphorous. Formation of easily reducible species have a weakening effect on metal-support-interaction since, this phenomenon enhances the stacking of synergetic NiMoS phases (Shan et al. 2018).

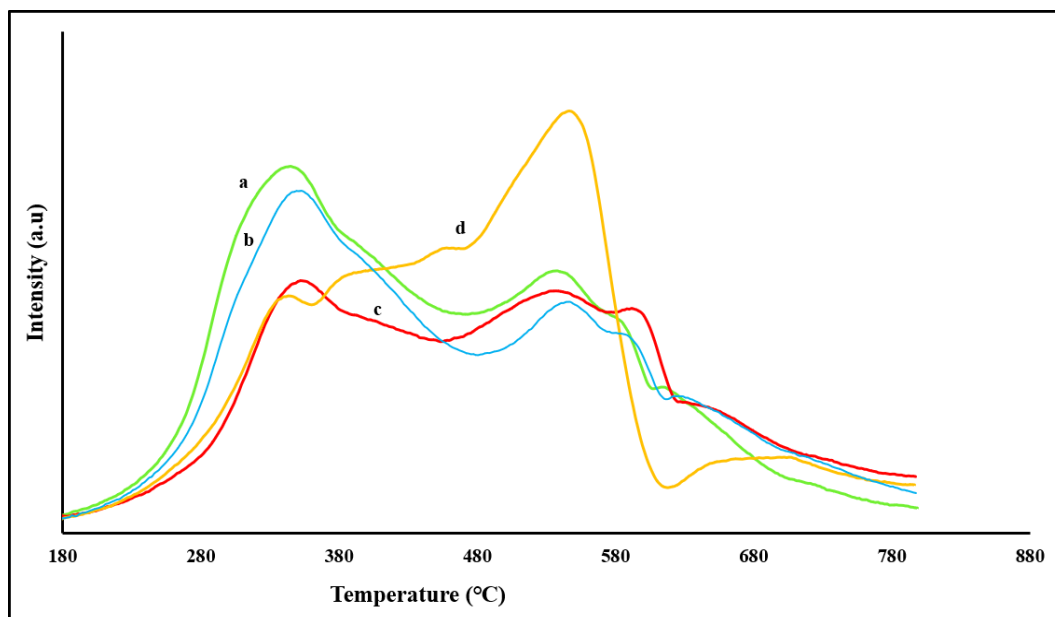


Figure 8.3 TPR profiles of a) 3.5wt%Ni19wt%Mo/CNH, b) 2.5wt%Ni19wt%Mo/CNH, c) 5.0wt%Ni19wt%Mo/CNH and d) 3.5wt%Ni19wt%Mo2.0wt%P/CNH.

8.5.5 HDS and HDN activities

The HDS and HDN results of the catalysts are shown in Figures 8.4 and 8.5. In general, among the catalysts that were not doped with phosphorus, the highest HDS and HDN activities were achieved with the 3.5wt%Ni19wt%Mo/CNH. This catalyst was therefore identified as the best formulated catalyst. The high HDS and HDN activities demonstrated by the 3.5wt%Ni19wt%Mo/CNH catalyst as compared to the rest of the catalyst without phosphorus doping can be attributed to the highest % dispersion displayed by this catalyst as well as its ability to form easily reducible species with enhanced stacking of NiMoS phases. The 5.0wt%Ni19wt%Mo/CNH catalyst exhibited the lowest HDS and HDN activities among all the catalysts and this was due to its poor metal dispersion revealed by both CO-chemisorption and XRD analysis. Besides, even though the peak reduction temperatures of the 5.0wt%Ni19wt%Mo/CNH and 2.5wt%Ni19wt%Mo/CNH catalysts were almost the same, the large reduction peak area in the 2.5wt%Ni19wt%Mo/CNH catalyst which signified high hydrogen consumption and easier formation of a Type II NiMoS phase caused both HDS and HDN activities for the 2.5wt%Ni19wt%Mo/CNH catalyst to surpass that of the 5.0wt%Ni19wt%Mo/CNH. From CO chemisorption results, the 2.5wt%Ni19wt%Mo/CNH catalyst showed high dispersion than the 5.0wt%Ni19wt%Mo/CNH catalyst. Thus, the high dispersion also influenced the achievement of

enhanced HDS and HDN activities for the 2.5wt%Ni19wt%Mo/CNH catalyst over the 5.0wt%Ni19wt%Mo/CNH catalyst.

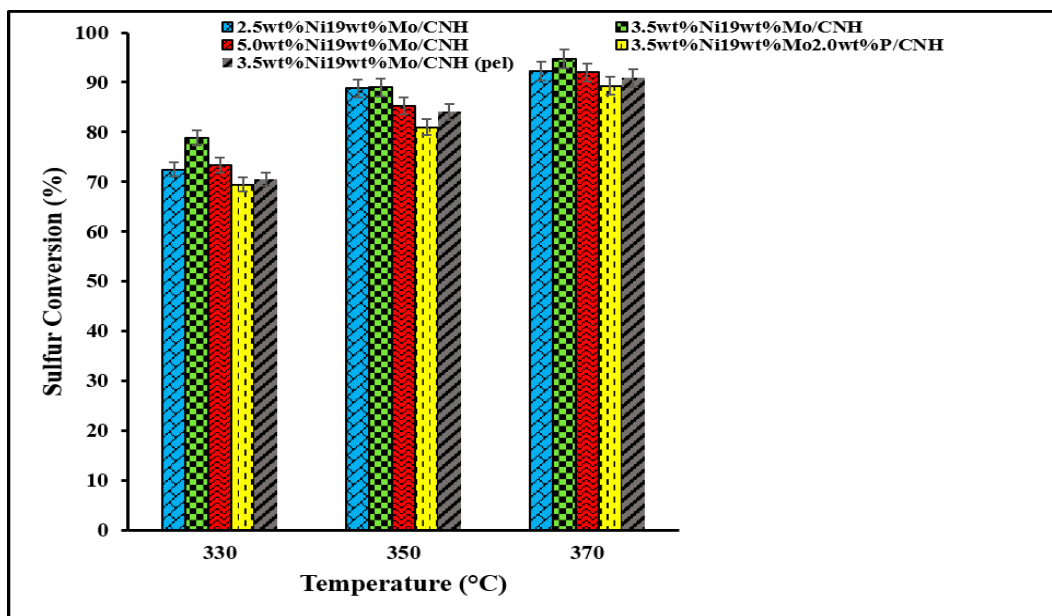


Figure 8.4 HDS activities of a) 2.5wt%Ni19wt%Mo/CNH, b) 3.5wt%Ni19wt%Mo/CNH, c) 5.0wt%Ni19wt%Mo/CNH and d) 3.5wt%Ni19wt%Mo2.0wt%P/CNH and e) 3.5wt%Ni19wt%Mo/CNH (pel) catalysts using LGO at 370, 350, and 330 °C (Catalyst = 5 cm³, P = 9.0 MPa, LHSV = 2 hr⁻¹, and H₂ / oil ratio = 600 (v/v)).

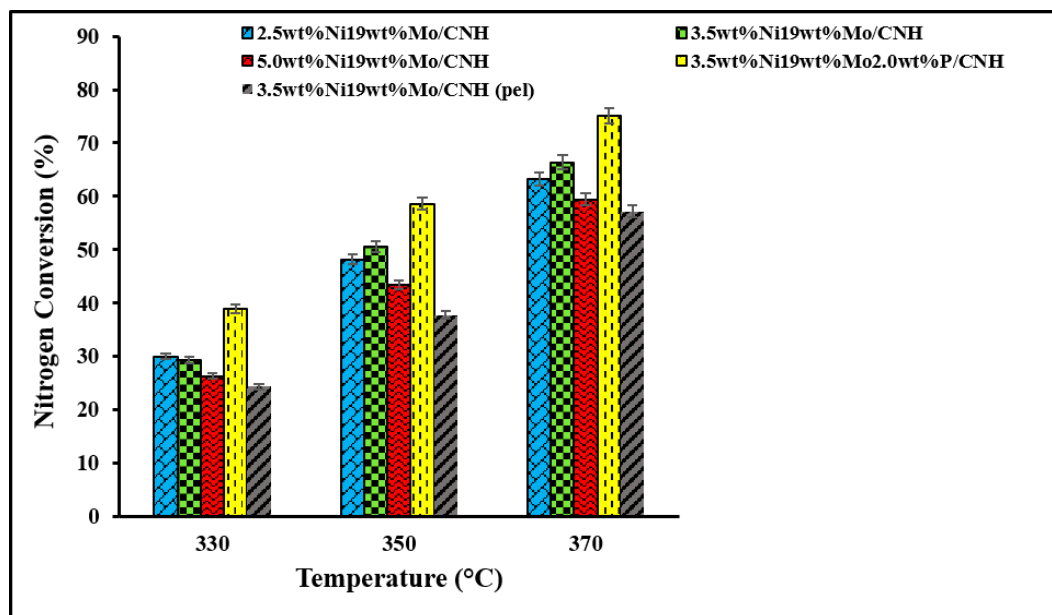


Figure 8.5 HDN activities of a) 2.5wt%Ni19wt%Mo/CNH, b) 3.5wt%Ni19wt%Mo/CNH, c) 5.0wt%Ni19wt%Mo/CNH and d) 3.5wt%Ni19wt%Mo2.0wt%P/CNH and e) 3.5wt%Ni19wt%Mo/CNH (pel) catalysts using LGO at 370, 350 and 330 °C (Catalyst = 5 cm³, P = 9.0 MPa, LHSV = 2 hr⁻¹, and H₂ / oil ratio = 600 (v/v)).

From Figures 8.4 and 8.5, HDS and HDN activities of a pelletized form of the best catalyst (3.5wt%Ni19wt%Mo/CNH) resulted in a reduction in both HDS and HDN activities. The decrease was also more pronounced for the HDN activity than the HDS activity. Since no binder was used in pelletizing this catalyst, the reason behind the decrease in HDS and HDN activities could be because, the normalized BET surface area (NS_{BET}) of the 3.5wt%Ni19wt%Mo/CNH catalyst in powdered form was higher than that of the pelletized catalyst. As demonstrated by Boahene et al. 2014, the normalized BET can be used to estimate the possibility of pore blockage during metal loading and a value close to unity corresponds to minimal probability of pore blockage. From their work, the NS_{BET} of their pelletized catalyst without binder showed less NS_{BET} value than the powdered form of the catalyst, and therefore had a high ability to experience pore blockage. Pore blockage causes diffusional limitations during hydrotreating and subsequently have a negative impact on hydrotreating activities. Therefore, the low HDS and HDN activities demonstrated by the pelletized 3.5wt%Ni19wt%Mo/CNH catalyst justify the reason why it was not necessary to run the all catalyst under this research study in a pelletized form. Compared to a pelletized catalyst,

this information also debunks the idea that with time, the activity of the powdered catalyst would decrease since the powder may be washed off before the catalyst loses its activity.

The phosphorus doped catalyst showed a reduction in HDS activity and a notable increase in HDN activities as compared to the best catalyst without phosphorus. As revealed by the study done by Sigurdson *et al.* (2008), the reason behind the high HDN activity of the phosphorus doped catalyst in comparison to all the catalyst under study was more related to enhanced acidity than the increase in dispersion accompanied with increase number of surface acid sites from a P-doped catalyst. In their work, it was noted that the addition of phosphorus to the catalyst affected the mechanism as well as the rate determining step of the HDS and HDN reaction. The HDS and HDN mechanisms are governed by two key steps that is hydrogenation (HYD) and hydrogenolysis (C-S or C-N bond breaking). These steps however happen on different sites because, HYD is known to occur on metal sulfide sites having sulfur vacancies whereas, hydrogenolysis occurs on Bronsted acid sites that could originate from the contribution from the phosphate promoter or H₂S adsorption of on metal sulfide. For HDN reactions, the C-N bond breaking is the rate determining step because it is the slowest step. Meanwhile, the C-S bond in HDS reactions mainly originated from organic sulfur compounds, which are comparatively weaker than C-N bonds and therefore not the rate limiting step. Due to the simultaneous HDS and HDN reactions that occur during hydrotreating, it was realized that use of a P-doped catalyst created additional new Bronsted acid sites that enhanced C-N bond breaking which is the rate limiting step and consequently boosted the activity of HDN to a upper level than the HDS activity (Sigurdson et al. 2008). In other findings, a phosphorus doped catalyst enhanced both HDS and HDN reactions since, it resulted in an enhancement of octahedrally coordinated Ni²⁺ that are usually the precursors to the active phase in HDS and HDN (Jones et al. 1995: Antanasova and Halachev, 1989). Appendix H also contains information about the effect of using the best catalyst (3.5wt%Ni19wt%Mo/CNH) and heavy gas oil on HDS and HDN activities.

8.5.6 Statistical analysis

The results of the experimental runs are shown in Table 8.4. As noted in Table 8.4, the repeated runs (5, 6, 14, 16, 17, 20) were conducted at the same operating conditions. However, there was a slight deviation in their respective % nitrogen and % sulfur removal which can be attributed to the instrumental error of $\pm 4\%$ from analysis. For run 17, the 73% nitrogen removal

value compared to the values from the other runs at similar conditions is an indication that this value is an outlier which is likely based on experimental error.

Table 8.4 Results of nitrogen removal and sulfur removal percentages based on DOE.

RunOrder	Temperature (°C)	Pressure (MPa)	LHSV (hr ⁻¹)	% Nitrogen removal	%Sulphur removal
1	330	8.3	1.0	48.2	72.5
2	316	9.0	1.5	33.8	63.9
3	350	9.0	0.7	92.5	88.8
4	370	8.3	2.0	65.7	87.8
5	350	9.0	1.5	64.7	84.5
6	350	9.0	1.5	67.9	85.5
7	330	9.7	1.0	66.1	81.7
8	330	9.7	2.0	39.1	70.2
9	370	9.7	2.0	78.0	91.3
10	370	9.7	1.0	96.0	95.2
11	370	8.3	1.0	87.5	90.5
12	350	9.0	2.3	52.6	81.0
13	350	7.8	1.5	57.7	83.2
14	350	9.0	1.5	65.1	83.9
15	350	10.1	1.5	71.5	86.5
16	350	9.0	1.5	69.7	88.1
17	350	9.0	1.5	73.4	86.9
18	384	9.0	1.5	93.4	95.1
19	330	8.3	2.0	31.8	68.2
20	350	9.0	1.5	66.9	83.8

An initial test for normality to determine if the data follows a normal distribution showed that the % nitrogen removal results gave a P-value of 0.339 and therefore normally distributed (P-value > 0.05). In the case of % sulfur removal the test for normality gave a P-value of 0.03 which was close to normality. Box-cox transformation was therefore applied on the % sulfur removal results using lambda (λ) values of 0.5 (square root), 0 (log) and -1 (inverse) to ensure that the data provided a reliable lack of fit test results. These λ values gave equivalent P-values of 0.017, 0.009 and < 0.005. Other values of λ that were tried included the optimal λ value of, 4.54, which gave uncharacteristically high standard deviations (> than 10^3). This implies that Box-cox transformation is not always the panacea for all model problems. Based on box-cox transformation results, the original % sulfur removal data generated from experiment was used in constructing the model. The experimental results gathered for both % nitrogen and % sulphur removal was analyzed

with the aid of a response surface methodology in Minitab 18. The lack of fit test aimed at determining the reliability of the nitrogen and sulfur models was evaluated using ANOVA.

The Pareto chart results for both % sulfur and nitrogen removal in Appendix D which was based on an initial lack-of-fit test results with all terms included in the model, validated that only four of the horizontal blocks were above the Pareto threshold of 2.23 and implied that these were the significant factors. In terms of the level of significance of the main independent factors, the Pareto charts (Figure D.1 and D.2) also showed that A (Temperature) was the most significant factor, followed by C (LHSV), and then B (pressure). As a result of this information, after the insignificant terms had been dropped, the quadratic regression models that were finally fitted to the experimental data for % sulfur and % nitrogen removal can be represented by Equations 8.1 and 8.2.

$$\% \text{ Sulfur Removal} = -767 + 4.322 T + 2.606 P - 5.23 \text{ LHSV} - 0.00552 T^2 \quad \dots 8.1$$

$$\% \text{ Nitrogen Removal} = -908 + 4.50 T + 7.23 P - 22.01 \text{ LHSV} - 0.00517 T^2 \quad \dots 8.2$$

where,

T = Temperature (°C)

P = Pressure (MPa)

LHSV = Liquid hourly space velocity (hr⁻¹)

The empirical correlations (Equation 8.1 and 8.2) imply that % sulfur removal and % nitrogen removal are dependent on temperature, LHSV, and pressure. Out of these factors, the catalyst used depend on temperature and pressure since prolonged exposure to temperature can lead to loss of catalytic activity due to thermal sintering. Additionally, use of powdered catalyst can cause clogging and excessive pressure drop during reaction (Fogler 2006; Satterfield 1991). The parity plots for % sulfur and nitrogen removal can be found in Appendix D.

Tables 8.5 and 8.6 shows the ANOVA results obtained for the lack-of-fit test for % sulfur and nitrogen removal. The lack-of-fit test signifies whether the constructed model can best be described with the experimental data. From statistical perspective, the p value columns in both tables is important since, it helps to determine the importance of the factors contributing to the

model. Independent and dependent variables with p values greater than 0.05 have insignificant contribution to the model, and therefore can be eliminated from the model at 95% confidence interval.

Table 8.5 ANOVA analysis results for response surface quadratic model of % sulfur removal with 3.5Ni19Mo/CNH catalyst.

HDS					
Source	Degree of Freedom	Sum of Squares	Mean Squares	F value	P value
Model	4	1347.6	336.9	94.7	0.000
T	1	1137.2	1137.2	319.6	0.000
P	1	45.4	45.4	12.8	0.003
LHSV	1	93.4	93.4	26.3	0.000
T*T	1	71.6	71.6	20.1	0.000
Lack of fit	10	38.4	3.8	1.3	0.416
Pure error	5	15.0	3.0		
Total	19	1401.0			
Model summary of R-squared statistics					
R-sq	0.96				
R-sq (Adj)	0.95				
R-sq (Pre)	0.93				

Table 8.6 ANOVA analysis results for response surface quadratic model of % nitrogen removal with 3.5Ni19Mo/CNH catalyst.

HDN					
Source	Degree of Freedom	Sum of Squares	Mean Squares	F value	P value
Model	4	6364.85	1591.21	120.89	0.000
T	1	4297.17	4297.17	326.46	0.000
P	1	350.25	350.25	26.61	0.000
LHSV	1	1654.73	1654.73	125.71	0.000
T*T	1	62.70	62.70	4.76	0.045
Lack of fit	10	144.41	14.44	1.36	0.386
Pure error	5	53.04	10.61		
Total	19	6562.9			
Model summary of R-squared statistics					
R-sq	0.97				
R-sq (Adj)	0.96				
R-sq (Pre)	0.94				

This suggests that from Table 8.5 and 8.6, temperature, pressure, LHSV, and temperature squared are significant factors that should be included in the model. The lack-of-fit p-value is also a vital parameter since, a value of less than 0.05 is significant and means that there is a statistical

evidence that there is no fit between the model and data at 95% confidence interval. This implies that the model does not adequately describe the data at this level. From Table 8.5 and 8.6, The p values for the lack-of-fit for % sulfur and nitrogen removal were 0.416 and 0.386, respectively and therefore an indication that lack-of-fit is not significant. This implies that the models for both % sulfur and nitrogen removal are good and fit the experimental data well.

Also, the results from Table 8.5 and 8.6 as well as the Pareto charts in Appendix D indicated that independent variables like temperature, pressure or LHSV had significant impact on % sulfur and nitrogen removal regression models due to their p values which were less than 0.05. The presence of square terms in Tables 8.5 and 8.6 with significant p values ≤ 0.05 such as (T*T) point out that, that there is slight curvature in the data (model). Central composite design normally captures curvature inside and outside of the design cube due to the addition of center points augmented with axial points. The R-squared statistics value is also used to assess the extent of the goodness of fit for the developed model and signifies the overall variability percentage in the response variable that is predicted by independent variable(s). In terms of the model, a fit that matches the experimental data perfectly gives an R^2 value close to 1. As shown in Table 8.5 and 8.6 the R-squared values for both % sulfur (0.96) and % nitrogen (0.97) removal were nearly 1 and therefore indicates that the model agrees well with the experimental data. In addition, the respective R^2 values meant that 96% of the sulfur removal results are being predicted by the independent variables whereas 97% of the nitrogen removal results are being predicted by the independent variables. The ratio of mean square for individual term to the mean square for the residuals gives the F-value for the model, and the null hypothesis can be tested using the probability of the F-statistics value (prob > F value) (Ferdous et al. 2005; Sadhukhan et al. 2016).

From Figure 8.6, the main effects plots for % sulfur removal indicates that temperature has a pronounced effect on % sulfur removal. Increasing temperature also increases % sulfur removal drastically. Variation of pressure had minimal impact on the % sulfur removal. It was also observed variation of LHSV had a slight impact on % sulfur removal although, the % sulfur removal decreased steadily with increasing LHSV. As shown in Figure 8.7, temperature and LHSV had a major impact on % nitrogen removal. Additionally, % nitrogen removal increased drastically with an increase in temperature and a decrease in LHSV. Variation in pressure also had a minimal effect on the % nitrogen removal. Check Appendix D for the interaction plots for both % sulfur and nitrogen removal.

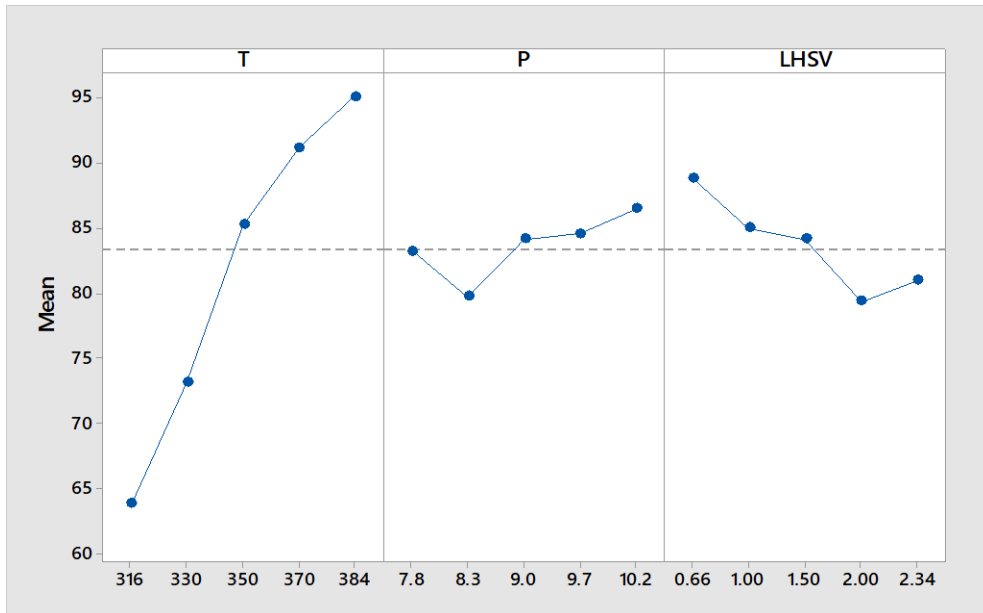


Figure 8.6 Main effects plot for % sulfur removal.

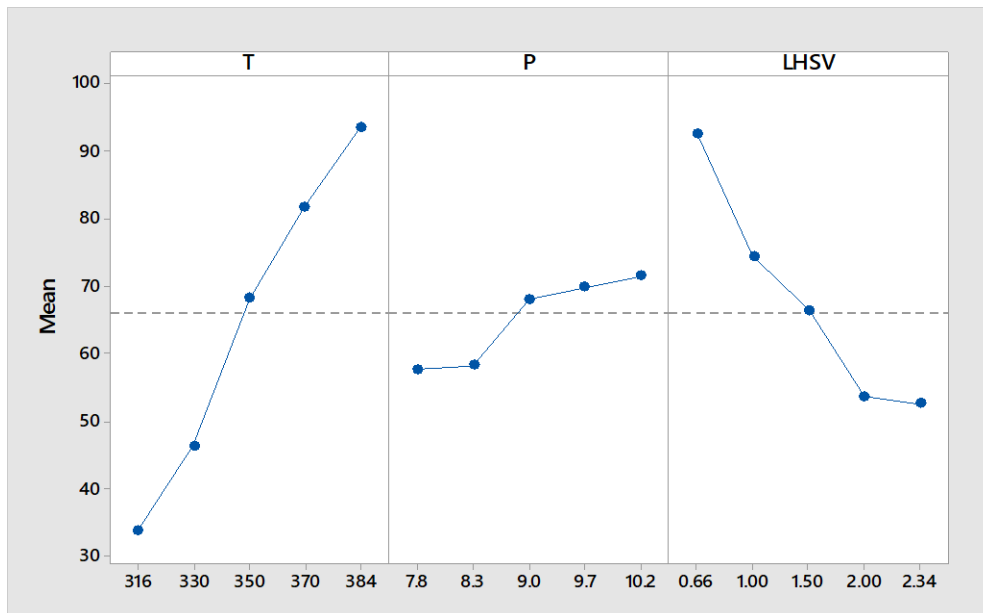


Figure 8.7 Main effects plot for % nitrogen removal.

The contour plots in Figures 8.8 and 8.9 show that % sulfur and nitrogen removal are high at the following combinations of conditions i.e. high temperature and high pressure, high temperature and low LHSV as well as high pressure and low LHSV.

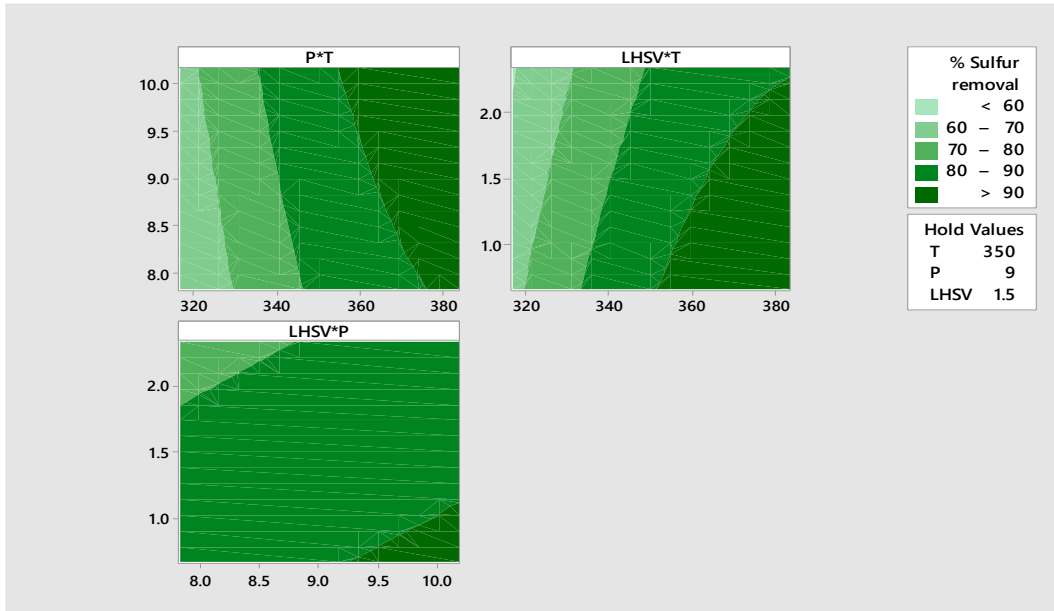


Figure 8.8 Contour Plots for % sulfur removal.

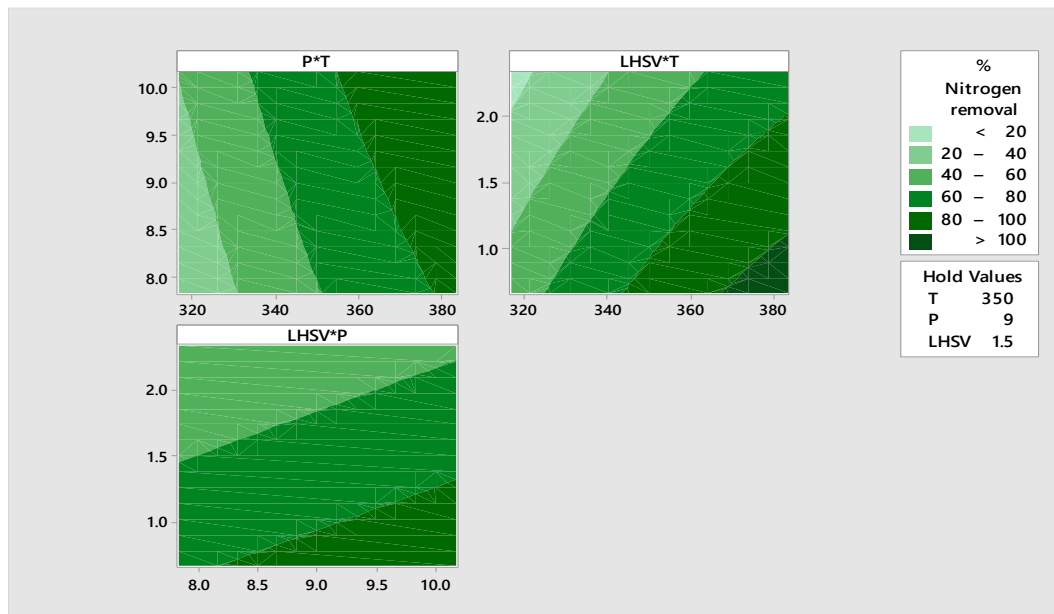


Figure 8.9 Contour plots for % nitrogen removal.

Table 8.7 includes the optimized hydroprocessing variables that could maximize the HDS and HDN activities in hydrotreating. The original optimized variables for 95% HDS and 96% HDN from the regression models were a temperature of 384 °C, pressure of 10.1 MPa and LHSV of 0.66 hr⁻¹. Although this reasonable temperature and less LHSV may lead to more conversion and more product quantity, the pressure seems to be excessive and may impact the hydrotreating process negatively. The high pressure might also not be cost effective in commercial hydrotreating. As such other recommended scenario for achieving 95% HDS and 98% HDN reactions have been highlighted in Table 8.7.

Table 8.7 Optimum operating condition for maximization of sulfur and nitrogen removal.

	HDS	HDN	HDS	HDN
Target	95%	96%	95%	98%
Temperature (°C)	384		369	
Pressure (MPa)	10.1		9.0	
LHSV (hr ⁻¹)	0.66		0.82	

8.5.7 Hydrodynamics of a trickle-bed reactor

Kinetic studies are usually conducted under the basic assumption that operating system satisfies plug flow and isothermal conditions. However, hydrodynamics related factors such as backmixing, catalyst wetting, and wall effects can significantly cause trickle-bed reactors (laboratory- scale) to deviate from conditions of isothermality and plug flow. As a result, during catalyst loading, the catalyst bed was diluted with an inert material such as silicon carbide (SiC) to limit these hydrodynamic effects (Bej et al. 2001). Axial dispersion or backmixing especially, when not checked in a liquid phase for hydrotreating process conducted in a micro reactor with high conversion and small catalyst bed length, could have a negative impact on the catalyst screening results and further kinetics analysis based on plug flow conditions. The effect could contribute to serious deviations in reactor scale up. Complete wetting of the catalyst ensures that during the hydrotreating process reaction only occurs between the reacting components that are in the liquid phase and are in contact with the surface of the catalyst. Ability to have all the catalyst particles in the reactor completely covered by the flowing liquid as in complete wetting additionally, maximizes the utilization of the catalyst during reaction. A partially wet catalyst could lead to feed by-pass and restricts the catalyst performance. Wall effect is usually not a major

problem in commercial hydrotreating since, the reactor diameter is excessively larger than the size of the catalyst particles.

Presence of wall effect becomes worrisome when pilot-plant reactors with relatively large catalyst particle size is used in small reactors (Chen et al. 2009). An evaluation of the hydrodynamics of the reactor with the 3.5wt%Ni19wt%Mo/CNH catalyst, with and without SiC was done based on the criteria's enumerated in Table 8.8. Complete wetting of catalyst and plug flow condition was determined using Gierman's criteria whereas, the criteria determined by Chuzf and Ng, 1989 was used to calculate the wall effect (Chen et al. 2009; Carberry 1963, Gierman, 1988, Chuzf and Ng, 1989). From Table 8.8, it can be inferred that backmixing, wetting, and wall effects are negligible since they satisfied the conditions of the criteria. In addition, plug flow condition can be assumed to exist. All calculations that were used in testing the various criterions in Table 8.8 can be found in Appendix E.

Table 8.8 Hydrodynamics of a trickle-bed reactor using a carbon (CNH)-supported catalyst.

Phenomena	Criteria	Calculated results under undiluted conditions	Calculated criteria under diluted conditions	Remarks: Negligibility of this criteria under diluted conditions
Backmixing	$\frac{L_B}{d_{pe}} > 100$	1000	613	Yes, negligible
Wetting	$W = \frac{\mu_L u_L}{\rho_L d_{pe}^2 g} > 5$ $* 10^{-6}$	$4.16 * 10^{-4}$	$1.57 * 10^{-4}$	No, Complete wetting
Wall effect	$\frac{D_R}{d_{pe}} > 25$	140	86	Yes, negligible
Plug flow	$\frac{L_B}{d_{pe}} > \frac{8n}{P_{eL}} \ln \frac{1}{(1-x)}$	1000>441(HDS) 1000>277(HDN)	613>441(HDS) 613>277(HDN)	No, plug flow exist

8.5.8 Mass transfer resistances for the HDS/HDN reactions

In heterogeneous catalysis, the catalytic reaction steps in a trickle bed reactor can be described by the seven steps listed below (Fogler, 2006).

1. Mass transfer (diffusion) of reactant (s) from the bulk of the fluid to the outer surface of the catalyst pellet.
2. Diffusion of the reactant from the catalyst pore mouth, through the pores of the catalyst and to

the immediate environment of the catalyst internal surface.

3. Adsorption of reactant onto the surface of the catalyst.
4. Reaction on the catalyst surface.
5. Desorption of the products from surface of the catalyst.
6. Diffusion of the products from the interior of the pellet, through the pore mouth and to the external surface of the catalyst.
7. Mass transfer of the products from the external surface of the pellet to the bulk fluid.

From the catalytic steps enumerated above, steps 1, 2, 6, and 7 are diffusion steps whereas, steps 3, 4 and 5 are the reaction steps (Fogler, 2006). In order to get reliable kinetic data, it is important to eliminate the effects of external and internal mass transfer resistances since the overall kinetic is governed by both reaction rates and mass transfers. The external and internal mass transfers effects on the hydrotreating process using NiMo/CNH catalyst were evaluated based on the methodology and criterions gleaned from the work by Sigurdson, (2009). The assessment was done in two part i.e. (i) determination of external mass transfer and (ii) determination of internal mass transfer.

8.5.8.1 External mass transfer

External mass transfer resistances come into play during the diffusion of reactant molecules from the bulk of the fluid to the surface of the catalyst. The external mass transfer was determined using the criterion developed by Satterfield *et al.* (1969). Satterfield criterion evaluates whether the rate determining step of the overall hydrotreating reactions is dependent on the rate of hydrogen conversion in HDS and HDN reactions or rate of hydrogen mass transfer (diffusion) through the liquid (LGO) phase to the catalyst (Sigurdson, 2009; Satterfield, 1969). Satisfaction of the equation 8.3 implied that in the overall reaction, hydrogen conversion dominated that of hydrogen mass transfer. Equation 8.3 concludes that mass transfer from the gas phase to the catalyst pellets outer surface is significant once Equation 8.3 is satisfied (Satterfield 1969).

$$\left(\frac{10d_p}{3C_{H_2}}\right) \cdot \left(\frac{-1}{V_c} \cdot \frac{dn}{dt}\right) > k_{OVR} \quad \dots 8.3$$

where;

k_{OVR} = Overall mass transfer coefficient for hydrogen, cm/s

C_{H_2} = Hydrogen concentration in the liquid phase at equilibrium, mol/mL

$\left(\frac{-1}{V_c} \cdot \frac{dn}{dt}\right)$ = Rate of hydrogen conversion in the reaction, mol/(s.mL)

V_c = Volume of the loaded catalyst = 5 mL

d_p = Average diameter of the catalyst particles

The steps involve in estimating equation 8.3 calculation are shown in the Appendix F section of the thesis. After solving for the left-hand side (LHS) and right-hand side (RHS) of Equation 8.3 for HDS and HDN reactions from 330 - 370 °C using the best catalyst (3.5wt%Ni19wt%Mo/CNH), the following results were obtained:

Hydrodesulfurization calculation of left- and right-hand side of Satterfield's criterion:

Left hand side of Satterfield's criterion = 1.16×10^{-4} cm/s to 1.40×10^{-4} cm/s

Right hand side of Satterfield's criterion = 1.72×10^{-6} cm/s to 1.94×10^{-6} cm/s

Hydrodenitrogenation calculations of left- and right-hand side of Satterfield's criterion:

Left hand side of Satterfield's criterion = 1.57×10^{-7} cm/s to 1.09×10^{-6} cm/s

Right hand side of Satterfield's criterion = 1.72×10^{-6} cm/s to 1.94×10^{-6} cm/s

These results therefore implied that for HDS reactions Satterfield criterion was satisfied whereas for HDN reactions Satterfield criterion was not satisfied for all reaction conditions. Based on these findings, it can be concluded that mass transfer from the gas phase to the catalyst surface is significant for the overall hydrodesulfurization reaction whereas, mass transfer from the gas phase to the catalyst surface is negligible for the overall hydrodenitrogenation reaction. Although the HDS reaction was mass transfer controlled, it was still necessary to evaluate and report kinetics for a reaction that was mass transfer controlled because, some kinetic information was required to complete the evaluation of mass transfer limitation. Moreover, until the mass transfer evaluation was determined there was no knowledge that either the HDS and/or HDN reaction was mass transfer controlled.

Also, from equation F.21 and F.22 in Appendix F, the rate of hydrogen (H₂) consumption for HDS and HDN reactions were found to be 5.54 x 10⁻⁶ and 1.42 x 10⁻⁶ mol.H₂/(mL.s), respectively. Therefore, about 4 times hydrogen was consumed for the overall HDS process as compared to HDN process. This suggests that higher hydrogen consumption is required for the HDS reaction as compared to the HDN reaction, and the high demand for hydrogen for HDS reaction is attributed to the high sulfur concentration in the crude oil feedstock as compared to the nitrogen concentration in the feedstock.

8.5.8.2 Internal mass transfer

Internal mass transfer resistances are encountered as reactant molecules move from the catalyst surface to the internal parts of the catalyst particles. In determining the internal mass transfer resistances, the preliminary calculation was done to evaluate whether isothermality within the catalyst pellets could be assumed. Each catalyst particle degree of isothermality could be examined in two ways. Either by finding the highest potential rise in temperature between the core and the surface of the catalyst particles or by confirming Anderson's criterion (Fogler, 2006; Anderson, 1963). The highest potential rise in temperature between the core and the surface of the catalyst particle (ΔT_{MAX}) was calculated using Equation 8.4.

$$\beta = \frac{\Delta T_{MAX}}{T_S} = \frac{\Delta H_{R,i} \cdot D_i \cdot [C_i]_s}{k_t \cdot T_S} \quad \dots 8.4$$

where,

$\Delta H_{R,i}$ = Heat of HDS/HDN reaction, kJ/mol

$[C_i]_s$ = Catalyst surface concentration of sulfur/nitrogen species, mol/mL

k_t = Thermal conductivity of the NiMo/CNH catalyst powder particle.

$k_t = 0.155$ W/(cm.K) (assumption: pure CNH powder particle,
(Yang et al.2002)

T_S = Pellet catalyst or powder particle surface temperature = 603 to 643 K
(reaction temperature)

In estimating the surface concentration of sulfur or nitrogen species, an assumption was made that in the absence of mass transfer limitation, the surface concentration was equivalent to the bulk concentration of sulfur or nitrogen species. All the steps involved in estimating Equation 8.4 are shown in the Appendix G section of this thesis. A calculated ΔT_{MAX} value ranging from 0.014 to 0.021 K for the simultaneous hydrotreating process (HDS and HDN) indicates that isothermallity can be assumed for both conditions since ΔT_{MAX} could never exceed 0.05K.

The Anderson's criterion method of determining isothermallity is shown in equation 8.5.

$$\frac{\Delta H_{R,i} \cdot \{R_i\} \cdot d_p^2}{k_t \cdot T_s} < \frac{3 \cdot T_s \cdot R}{E_i} \quad \dots 8.5$$

where,

$\{R_i\}$ = Global reaction rate: HDS/HDN, mol/(s.mL)

k_t = Catalyst thermal conductivity = 0.155 W/(m.K) or W/(cm.°C)

R = Universal gas constant = 8.314 J/(mol.K)

E_i = Activation energy: HDS/HDN, J/mol

In terms of data manipulation as mentioned earlier, a central composite design of experiment was used to obtain optimum regression model for sulfur and nitrogen removal and this information was further used to determine the order of reaction and activation energy for HDS and HDN reactions. The Arrhenius equation was however used in evaluating the activations energies for HDS and HDN reactions. For the HDS reaction, the order of reaction and activation energy were 1.4 and 64 kJ/mol, respectively whereas, that for the HDN reaction were 1 and 92 kJ/mol, respectively. The heat of reaction for HDS was estimated using the heat of reaction for most thiophene molecules (63 to 66 kJ/mol) and an assumed stoichiometric value of 4. In the case of the HDN reaction, the heat of reaction for HDN was estimated using the heat of reaction for most quinoline molecules (65 to 68 kJ/mol) and an assumed stoichiometric value of 5. The global reaction rate was calculated using, the apparent rate constant, bulk concentration and order of reaction of the sulfur and nitrogen. Knowing the diameter (0.01 cm) of the powder catalyst and the operating temperatures (330 °C – 370 °C), the left and right hand side of the Anderson's criterion

were calculated to test the criterion (Fogler, 2006; Ancheyta and Speight, 2007; Satterfield and Cocchetto, 1981).

For the trickle-bed reactor that was used in carrying out the hydrotreating experiments, variation in concentration was considered by assuming that all compositions were uniformly distributed, there was minimum leaching, and by ensuring that average concentration values for sulfur and nitrogen species were used. The reaction rates and kinetic parameters determined were apparent results and not intrinsic therefore, the effects of diffusion as a result of mass transfer limitations were considered. Additionally, the variation in concentration was accounted for by ensuring that the residence time was constant during reactions and the focus was on the overall conversion at the end of the reaction. The hydrotreating reaction satisfied plug flow conditions based on satisfaction of the plug flow criterion in Table 8.8. Moreover, the effect of backmixing was found to be negligible (Table 8.8).

Based on the range of operating conditions tested, the values for the left- and right-hand side of Anderson's criterion were found to be:

Left hand side of Anderson's criterion (HDS) = 1.39×10^{-8} to 3.82×10^{-8}

Right hand side of Anderson's criterion (HDS) = 0.235 to 0.250

Left hand side of Anderson's criterion (HDN) = 1.56×10^{-9} to 6.62×10^{-9}

Right hand side of Anderson's criterion (HDN) = 0.163 to 0.174

The results from these calculations on the hydrotreating process using the 3.5wt%Ni19wt%Mo/CNH catalyst suggests that assumption of isothermal behaviour is valid when evaluating internal mass transfer resistances. Additionally, From Equation 8.6, the rates of reaction for HDS and HDN were found to be 5.6×10^{-8} mol/mL.s and 5.14×10^{-5} mol/mL.s respectively. Therefore, in terms of speed, the rate of HDN reaction was faster than the HDS reaction. The calculations leading to the results of the catalyst pellet isothermality can be found in Appendix G section.

8.5.9 Kinetics

For hydrotreating of real feedstock, the rate of hydrodesulfurization and hydrodenitrogenation can be expressed using two main models i.e. the power law and the

Langmuir-Hinshelwood kinetic models (Girgis and Gates, 1991; Ancheyta et al. 2002). The power law model is frequently used because of its simplicity and determination of only a few parameters. The power law model provides information about the overall rate law for the different reactions that occur in HDS and HDN reactions. Unlike the Langmuir-Hinshelwood kinetic model, the power law model does not incorporate the inhibition effects from certain potential molecules that are present in the feedstock. A combination of the power law and Langmuir-Hinshelwood kinetic models provides adequate prediction of the performance of a hydrotreating system (Majak et al. 2010; Sigurdson et al. 2011). Knowledge about the kinetic model is important since it aids in pilot plant study, design of commercial reactors and improvement in process and operating conditions. A suitable kinetic model or expression can be used to predict the effects of operating conditions such as temperature, LHSV, pressure on the hydrotreating performance of the catalyst.

The power law model for both HDS and HDN can be described by the rate expression below:

$$-r_i = -\frac{dC_i}{dt} = k_i C_i^n \quad \dots .8.6$$

where,

C_i = concentration of species i (either S or N) in the petroleum feedstock,

k_i = apparent rate constant of species i ,

n = order of reaction and t = residence time.

Based on the value of n the plausible solution to equation 8.6 are as follows:

$$C_f - C_p = \frac{k_i}{LHSV} \quad \text{for } n = 0 \quad \dots .8.7$$

$$\ln\left(\frac{C_p}{C_f}\right) = -\frac{k_i}{LHSV} \quad \text{for } n = 1 \quad \dots .8.8$$

$$\left[\frac{1}{C_p^{n-1}} - \frac{1}{C_f^{n-1}}\right] = (n-1) \frac{k_i}{LHSV} \quad \text{for } n \neq 0, 1 \quad \dots .8.9$$

where,

C_p = concentration of species i in the product, wt%;

C_f = concentration of species i in the feed, wt%

$LHSV$ = liquid hourly space velocity, h^{-1}

The order of reaction (n) and apparent rate constant (k_i) are the main kinetic parameters that can be deduced from the power law model. The order of reaction is dependent on the type of catalyst and feedstock composition being used and, ranges from 0.5 to 1.5 for HDN of gas oil, whereas, for HDS of gas oils it is typical to have the order of reaction ranging from 1.0 to 2.5. Additionally, it has been noted that the rate of nitrogen removal is mostly determined by using an order of reaction equivalent to 1.0 (Ancheyta et al. 2002; Bej et al. 2001; Aoyagi et al. 2003; Callejas and Martinez, 1999). Use of the apparent rate constant in the above kinetic equations accounts for the effects of diffusion as a result of mass transfer limitations. The Arrhenius equation given in Equation 8.10 can be used to obtain the activation energy.

$$k_i(T) = k_o e^{-E/RT} \quad \dots 8.10$$

where:

k_o = pre-exponential factor or Arrhenius constant

E = activation energy, (kJ/mol)

R = gas constant, (kJ/mol.K)

T = temperature, K

From equations 8.7, 8.8 and 8.9, the apparent rate constant (k_i) can be found from the slope of a straight-line plot of the left-hand side of these equations versus $1/LHSV$ at constant temperature and pressure. Another way of determining k_i is to, calculate k_i at constant pressure, $LHSV$ and varying temperatures after establishing the right power law equation that would fit the experimental or predicted values.

The initial approach used in determining n for the HDS and HDN reactions in this study was to calculate the sulfur and nitrogen conversions using the regression models (Equation 8.1 and 8.2) for % sulfur and nitrogen removal at varying $LHSV$ (0.66-2.34 hr^{-1}), and a constant pressure

and temperature of 9 MPa and 384 °C, respectively. Following this, an initial n value was used to compute values for the left-hand side of equation 8.9 whereas, the LHSV was used to compute values for the right-hand side of equation 8.9. These computed values were used to generate a plot similar to Figure 8.10 (for HDS) and Figure 8.11 (for HDN). A trial and error method was further applied to test different values of n in order to find out about the value of n that would provide the best fit (highest regression coefficient, R^2) for the predicted data. For HDS, an average n value of 1.4 provided a best fit for the predicted data whereas, for HDN the best fit for the predicted value was obtained with an n value of 1.0. The R^2 values for HDS and HDN were 1.00 and 0.96, respectively.

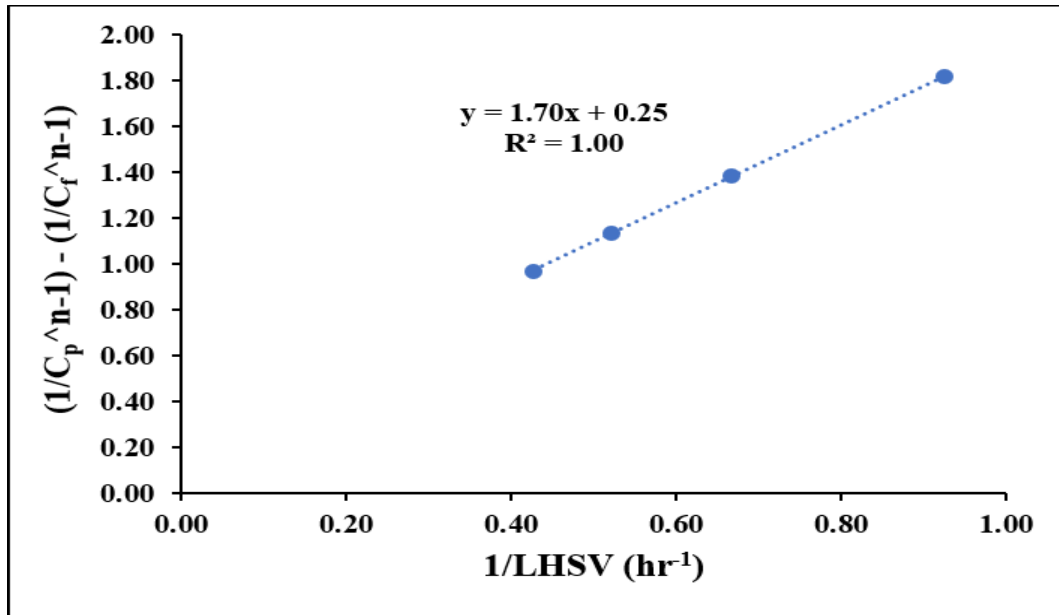


Figure 8.10 Determination of R^2 for HDS of light gas oil with $n = 1.4$.

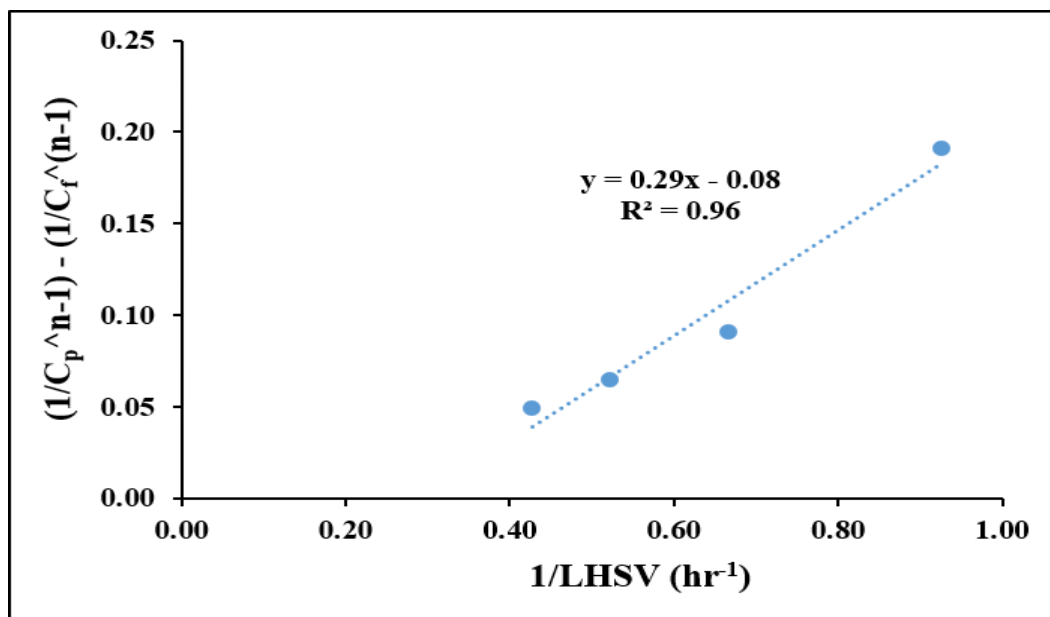


Figure 8.11 Determination of R^2 for HDN of light gas oil with $n = 1.0$.

Following this, the next step was to determine k_i and E . Hence, for the HDS reaction where $n = 1.4$, equation 8.9 was used to calculate different values of k_i at varying temperatures ranging from 350 to 370 °C, and at a constant pressure and LHSV of 9 MPa and 2 hr⁻¹, respectively. In the case of the HDN reaction where $n = 1$, equation 8.8 was used to calculate k_i at the same operating conditions. Once a series of these k_i values had been generated, Arrhenius equation was further used to determine the activation energy from a plot of $\ln(k_i)$ versus $1/T$ based on the slope ($-E/R$) of the graph. Figures 8.12 and 8.13 show the activation energy plots for HDS and HDN reactions. The activation energies for HDS and HDN for this study were found to be 64 kJ/mol and 92 kJ/mol, respectively. This implies that the reactant nitrogen molecules must overcome more energy or a higher energy barrier for the reaction to occur as compared to the reactant sulfur molecules. These results are also in agreement with the low nitrogen conversion relative to the sulfur conversion obtained after hydrotreating the light gas oil with the 3.5wt%Ni19wt%Mo/CNH catalyst.

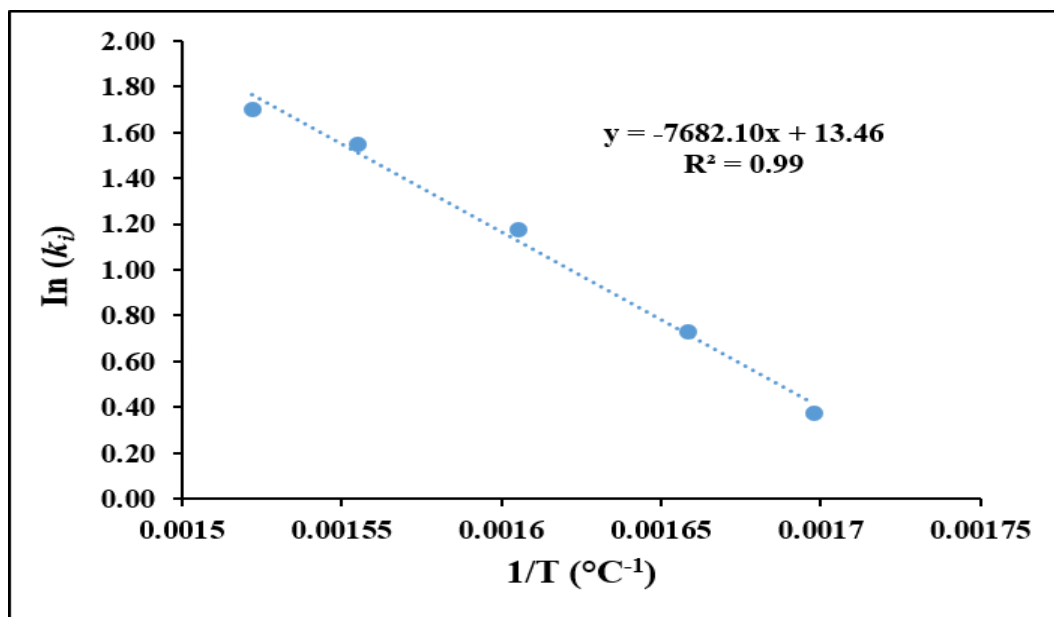


Figure 8.12 Determination of activation energy for HDS reaction with $n = 1.4$.

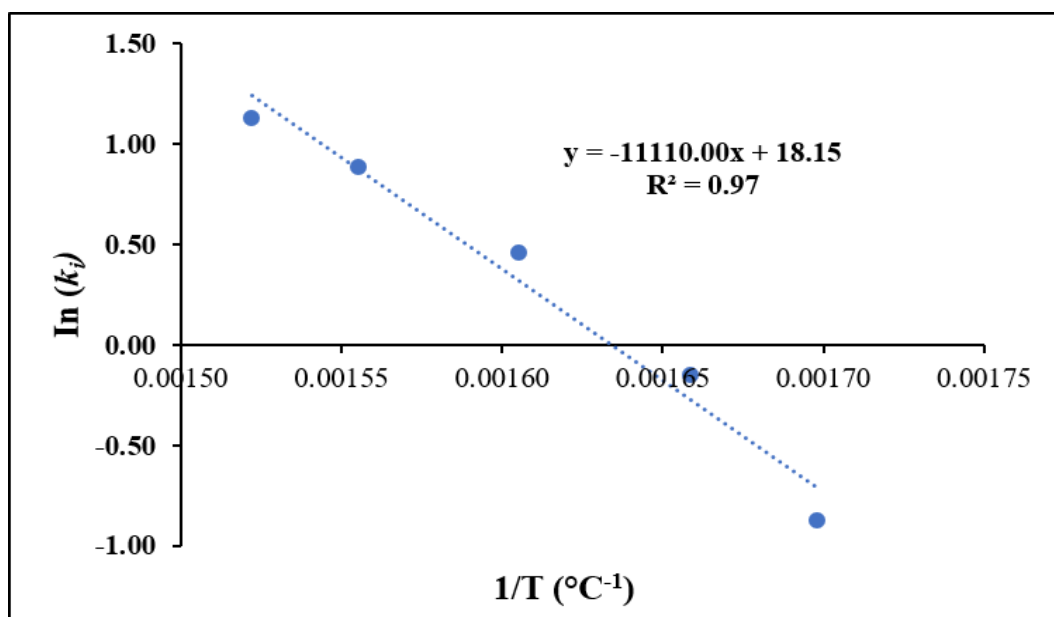


Figure 8.13 Determination of activation energy for HDN reaction with $n = 1.0$.

8.5.10 Catalyst Stability Study

Catalyst stability study results shown in Figure 8.14 was investigated using the best catalyst (3.5wt%Ni19wt%Mo/CNH catalyst) with light gas oil. The study began once all the design of experiment runs had been completed, and certain targeted conditions for optimum % sulfur and

nitrogen removal had been tested. The experiment was conducted for 45 days, and samples were consistently collected every 24 hours till the end of this duration. Hydrotreating temperature, pressure and LHSV of 370 °C, 9.0 MPa and 2 hr⁻¹, respectively were used. The catalyst was precoked for 3 days to attain some stability before, the actual experiment proceeded. From the onset of the experiment, it was noted that the initial 95% sulfur and 77% nitrogen removal values dropped steadily to 90% sulfur and 67% nitrogen removal till the fifth day of experiments. Following this, the HDS and HDN remained nearly steady at average values of 90% and 67% of the stability runs. For both HDS and HDN, the margin of error was ± 1 %. This implies that long term stability of the 3.5wt%Ni19wt%Mo/CNH catalyst can be guaranteed for at least 45 days.

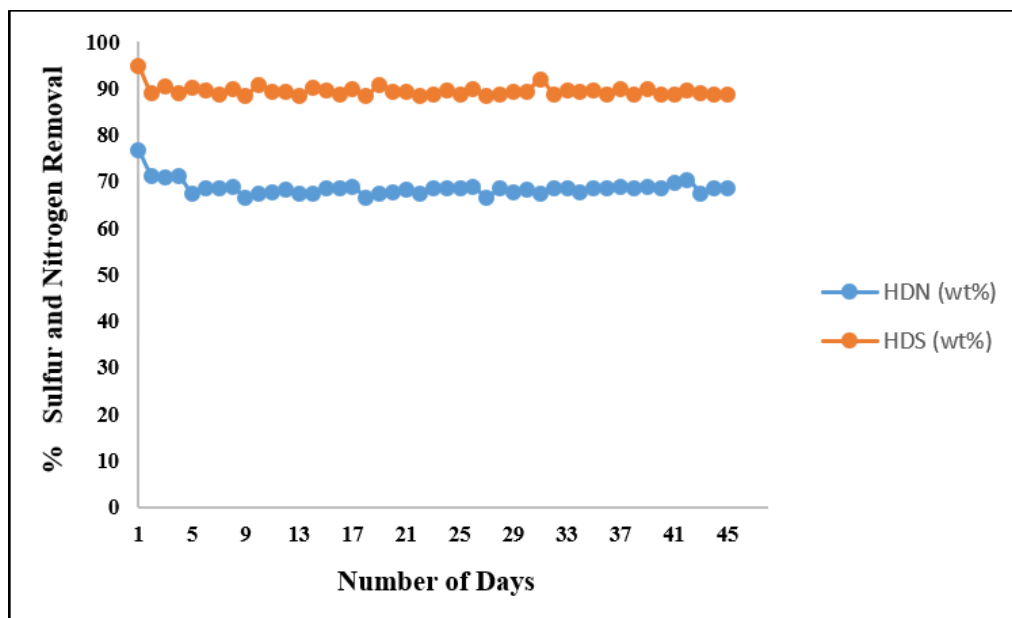


Figure 8.14 HDS and HDN long-term stability study with 3.5wt%Ni19wt%Mo/CNH catalyst using LGO at 370 °C (Catalyst = 5 cm³, P = 9.0 MPa, LHSV = 2 hr⁻¹, and H₂ / oil ratio = 600 (v/v)).

8.6 Conclusions

In conclusion, HDS and HDN activities were impacted by variation of Ni and Mo loading on the catalysts since, the 3.5wt%Ni19wt%Mo/CNH catalyst exhibited the highest HDS catalyst based on its superior properties (e.g. improved dispersion and reducibility). Pelletization of catalyst can result in a decrease in activity due to pore plugging which could lead to mass transfer resistances during reaction. A P doped catalyst (3.5wt%Ni19wt%Mo2.0wt%P/CNH) can cause

significant improvement in dispersion, reducibility and an enhancement of HDN activities. Operating variables such as temperature, pressure and LHSV have a significant impact on HDS, and HDN reactions. From the statistical analysis, the effect of temperature on both HDS and HDN reactions is more drastic as compared to LHSV. Variation of pressure also had a minimal effect on both HDS and HDN reactions. External mass transfer resistance can be neglected in HDN reactions but not in HDS reactions. Internal mass transfer resistances can however be ignored in both HDS and HDN reactions. The reaction order and activation energy for the hydrotreating reactions using power law model was found to be 1.4 and 64 kJ/mol for HDS and 1 and 92 kJ/mol. Catalyst deactivation study for over 45 days showed that with the best catalyst a steady HDS and HDN activity of 90% and 67% is attainable.

Although CNH may be expensive and not a good support as γ -Al₂O₃, it has exhibited remarkable physiochemical properties than certain carbon materials such as CNT, OCP, OCP_f and ordered mesoporous carbon. Consequently, compared to other carbon materials, the use of CNH in applications such as hydrotreating and conversion of syngas to higher alcohols have yielded outstanding results. Use of CNH for fundamental research pertaining to catalysis may be beneficial since, other better capabilities and applications of CNH can be explored. In a scenario where there is the option of choosing and receiving free supplies of carbon materials such as CNH or CNT for some research work, the choice would certainly be CNH since, this research work have confirmed that CNH demonstrates high hydrotreating performance compared to other carbon materials.

CHAPTER 9

Conclusions and Recommendations

9.1 Overall conclusions

The overall conclusions based on sub-objectives given in the introduction section of this thesis are as follows:

1. The arc discharge in liquid nitrogen can be used to produce CNH in the laboratory with aggregate diameters ranging from 50-110 nm. The process also generates CNT and OCP. The yield of the CNH generated from this arc discharge synthesis method is very low (~ 3 wt%) compared to the OCP by-product (~ 48 wt%), and these values are repeatable based on the numerous reactions and measurements that were carried out. System modification resulted in ~ 73% increase in production rate since, the production rate was 0.13 g/hr and 0.075 g/hr, respectively before and after system modification. Change in current, processing time and system modification impacted CNH production, and this work also validates that there are limitations on exact current and processing time for producing CNH. However, the effect of these conditions on the yield is not significant since, particle loss continued to be a huge challenge with the process. Defects in CNH as well as the identity of CNH were confirmed via Raman analysis based on the I_D/I_G ratio and the position and intensity of the D and G bands. Ability to build CNH setup and generate CNH in the laboratory to carry out research activities was one of the most important results. Without this achievement, completion of the different phases of work would not have been possible.

2. CNH can be functionalized using nitric acid. A functionalization duration of 30 mins or less (15mins) is efficient for introducing oxygen containing group (carboxylic acid groups) on CNH surface as evidenced from FTIR analysis. Through functionalization the surface characteristics of the carbon supports were altered from an otherwise inert material. Results from our functionalization work confirms that functionalization improves the surface area and pore volume of the catalyst. Additionally, enhancement of defect sites on the carbon support can be achieved with functionalization. From BET, TEM and Raman results it was found that, variation of functionalization time has an impact on the textural properties and quality of CNH. However, there

is a limit to which functionalization can be done since, over oxidation can cause CNH particles to coalesce and degrades their properties. CNH supports functionalized for 15 or 30 minutes can be used to achieve reasonable hydrotreating activities as revealed in Chapter 5 and Appendix B. Ability to establish that with short functionalization times (15-30 mins), CNH surface properties can be enhanced in preparation for catalyst formulation is another contribution that was made.

3. From the carbon-supported catalysts used in this study, NiMo/CNH catalyst exhibited superior properties compared to the remaining carbon-supported catalysts (NiMo/CNT, NiMo/OCP_f, NiMo/OCP) and subsequently this led to the high hydrotreating performance exhibited by NiMo/CNH relative to the rest of the carbon supported catalysts. Factors that contributed to the high HDS and HDN activity of NiMo/CNH catalyst include; homogeneity and structure of the CNH-carbon support, higher dispersion and reducibility of Ni and Mo species. Although, it was confirmed from XAS analysis that metal support interaction (MSI) was lower for the carbon-support catalysts (e.g. NiMo/CNH and NiMo/OCP_f) than for the NiMo/ γ -Al₂O₃ catalyst, the hydrotreating performance of the NiMo/ γ -Al₂O₃ catalyst was still the highest among all the catalyst under study. This implied that MSI is not always the determining factor on the hydrotreating performance. With respect to the NiMo/ γ -Al₂O₃ catalyst properties such as type of acid sites, and extent of reducibility may have contributed to its excellent hydrotreating performance. This work demonstrates that the type of support used in hydrotreating has an impact on the HDS and HDN activities. The realization that CNH-supported catalyst proved to be a superior catalyst over other carbon (CNT, OCP, OCP_f) -supported catalysts that were tested in hydrotreating application was another major contribution to science.

4. The hydrotreating performance of NiMo/OCP_f catalyst can be enhanced by increasing the Ni and Mo compositions from their initial 2.5 wt% and 13 wt%, respectively to a Ni composition of 5.0 wt% and a Mo composition of 19 wt%. As a result, the 5.0wt%Ni19wt%Mo/OCP_f catalyst gave the highest HDS and HDN activities. The high nickel concentration of 5 wt% in this best catalyst enhanced its dispersion and hydrogen consumption capacity which are some of the factors that impact HDS and HDN activities positively. Variation of metal loading compositions have an influence on the physico-chemical properties at higher loadings. All the different combinations of NiMo/OCP_f catalysts showed high thermal stability within the hydrotreating temperature of

interest. HDS and HDN activities were affected depending on the type of Ni and Mo compositions in the supported catalyst.

5. Hydrotreating of light gas oils with different combinations of Ni and Mo loadings on carbon-supported catalysts, revealed that highest HDS and HDN activities were achieved with the 3.5wt%Ni19wt%Mo/CNH catalyst and key factors that led to this are the higher dispersion abilities of the metals species in this catalyst as well as the high ability of forming a highly active Type II phase based on its hydrogen consumption capacity. Utilization of a pelletized catalyst can cause a reduction in both HDS and HDN activities due to pore blockage and consequent effect on mass transfer resistances during hydrotreating reactions. Use of a P-doped catalyst resulted in a drastic enhancement of the HDN activity as compared to its analogous HDS activity, and this was partly due to the enhancement of C-N bond breaking which happens to be the rate determining step of the process. Statistical analysis using design of experiment showed that variation in operating variables like temperature and LHSV have a major impact on sulfur and nitrogen conversion. On the other hand, pressure variation has minimal impact on sulfur and nitrogen removal. Additionally, statistical parameter results such as p and r-squared values supported the reliability of the generated HDS and HDN process models. External mass transfer resistances cannot be totally ignored for HDS unlike HDN reactions. Negligibility of internal mass transfer for both HDS and HDN reactions is reasonable. Results from the power law model for both HDS and HDN reaction showed that an order of reaction (n) value of 1.4 for HDN, and 1 for HDS gave the best fit for the predicted data. Kinetic calculations using the power law model resulted in an activation energy of 64 kJ/mol for HDS reaction, and 92 kJ/mol for HDN reactions. Catalyst deactivation studies over 45 days confirmed the stability of the catalyst life-cycle is reliable since HDS and HDN reactions remaining nearly steady at average values of 90% and 67% during this duration.

9.2 Recommendations for future research work

1. The low yield of CNH generated in this research is frustrating and worrisome since a substantial quantity is required to make catalysts for all hydrotreating experiments. A lot of CNH material was lost in a form of a plume during synthesis. TEM micrographs of collected particles that settled on the floor, fume hood and lab bench validated that the collected particles were purely CNH

particles. Hence, to trap these lost particles and maximize the quantity of CNH produced, use of a bag house or bag filter can be considered to capture the lost particles. Due to the inconsistencies involved in maintaining a constant arc and gap between the anode and cathode electrode rods, ability to ensure that there is a non-fluctuating arc and a stable plasma is another factor that limits the yield of CNH generated. This can therefore be improved by using a proportional-integral-derivative (PID) controller to automatically adjust the gap between the anode and cathode electrodes based on, the feedback mechanism of this closed loop. The volume of the Dewar flask used in carrying out the arc discharge experiment was 4.5 L hence, use of a bigger reaction vessel could be considered to give more room for particles to settle within the vessel as they are being generated. The effect of other process parameters such as, current density and applied potential on the yield should be investigated since they could impact the amount, size and shape of nanostructure materials collected. Better still, it is highly recommended that commercial CNH when available should be purchased and used for this research to save time. The low yield limits the scope to which CNH can be explored for enhanced hydrotreating performance.

2. Parameters such as the oxidation agent, oxidation time and temperature have been known to have an impact on the type and amount of surface sites produced after functionalization. Hence, a design of experiment (DOE) considering these factors would provide thorough information about how these process variable affects the properties of CNH both independently and combined. The DOE results will help in identifying the optimized condition that would enhance CNH properties for hydrotreating application.

3. Since sulfidation of all catalysts prior to hydrotreating were done using an LHSV of 2 hr^{-1} , all the catalysts could be sulfided using an LHSV of 1 hr^{-1} to investigate if hydrotreating activity could be enhanced further. Conducting an HRTEM characterization on all the sulfided catalysts (i.e. NiMo/CNH, NiMo/CNT, NiMo/ γ -Al₂O₃, NiMo/OCP_f, NiMo/OCP) would be beneficial since it would provide additional insight into the structure of the various catalysts and how the active metals (MoS₂) are dispersed. This information (including stacking results from HRTEM) would be significant in interpreting hydrotreating activity data in the development of more active catalysts. NMR analysis should be repeated on all the hydrotreated liquid products in order to find how the different supports affects HDA activities. It is highly recommended to use CNH as a

catalyst support if the production yield is very good. Apart from the fact that CNH possesses superior qualities, results from this research showed that HDS and HDN activities are higher when a NiMo/CNH catalyst is used in place of NiMo/CNT or NiMo/OCP_f indicating that the CNH is an alternative good catalyst support.

4. Use of simulated distillation method in determining the boiling point range as well as the resulting composition of the gas oil products should be considered. Molecular carbon range from C5 to C60 could be analyzed and this range should be broken down to three categories, carbon numbers up to 15 ($C \leq 15$), carbon numbers between 15 and 20 ($15 < C < 20$) and carbon numbers above 20 ($C \geq 20$). This category breakdown would aid in establishing a direct relation between the different combinations of metals on the OCP_f support and the carbon numbers. NMR analysis should be done on all the liquid products in order to gain valuable information about how variation of metal compositions affect HDA reactions. It is also recommended that TGA experiments should be conducted under safe operating conditions using hydrogen to mimic the thermal degradation during hydrotreating with hydrogen gas.

5. HRTEM analysis on the catalysts used in phase five is highly recommended to examine the stacking of MoS₂ in order to experimentally validate the hydrogen consumption effect on Type II NiMoS structure. It is recommended that kinetics should be performed on the HDS and HDN processes for the pelletized 3.5wt%Ni19wt%Mo/CNH catalyst using light gas oil. It would be worthwhile to conduct a DOE and assess the mass transfer resistances and kinetics on HDS and HDN processes for the phosphorus-doped catalyst using light gas oil.

References

- Abbas, S.; Maqsood, Z.; Ali, M. "The demetallization of residual fuel oil and petroleum residue," *Petroleum Science and Technology*, **2010**, 28, 1770 - 1777.
- Acres, J. "The characterization of catalysts. A survey of present industrial practice," *Platinum Metals Review*, **1980**, 24, 14 - 25.
- Afanasiev, P.; Bezverkhyy, I. "Ternary transition metals sulfides in hydrotreating catalysis," *Applied Catalysis A General*, **2007**, 322, 129 - 141.
- Ahmed, T. "Hydrocarbon phase behavior," *Contributions in Petroleum Geology and Engineering*, 7, Gulf Publishing Company, Houston, **1989**.
- Ajima, K.; Yudasaka, M.; Murakami, T.; Maigne, A.; Shiba, K.; Iijima, S. "Carbon nanohorns as anticancer drug carriers," *Molecular Pharmaceutics*, **2005**, 2, 475 - 480.
- Ajima, K., Yudasaka, M., Suenaga, K., Kasuya, D., Azami, T., Iijima, S., "Material storage mechanism in porous nanocarbon," *Advance Materials*, **2004**, 16, 397 - 401.
- Akiladevi, D.; Basak, S. "Carbon nanotubes (CNTs) production, characterization and its applications," *International Journal of Advances in Pharmaceutical Sciences*, **2010**, 1, 187 - 195.
- Al-Dalama, K.; Stanislaus, A. "Temperature programmed reduction of SiO₂-Al₂O₃ supported Ni, Mo and NiMo catalysts prepared with EDTA" *Thermochimica Acta* **2011**, 520, 67 - 74.
- ALothman, Z. "A review: Fundamental aspects of silicate mesoporous materials," *Materials*, **2012**, 5, 2874 - 2902.
- Ancheyta, J.; Speight, J. "Hydroprocessing of heavy oils and Residua," *Chemical Industries: A Series of Reference Books and Textbooks*, Speight J. G. (ed), Taylor & Francis Group, **2007**.
- Ancheyta, J.; Rana M.; Furimsky, E. "Hydroprocessing of heavy petroleum feeds: Tutorial," *Catalysis Today* **2005**, 109, 3 - 15.
- Anderson, O.; Prasad, B.; Sato, H.; Enoki, T.; Hishiyama, Y.; Kaburagi, Y. "Structure and electronic properties of graphite nanoparticles," *Physical Review B*, **1998**, 58, 16387 -16395.
- Antisari, M.; Marazzi, R.; Krsmanovic, R. "Synthesis of multiwall carbon nanotubes by electric discharge in liquid environments" *Carbon*, **2003**, 41, 2393 - 2401.

- Antolini, E. "Carbon supports for low-temperature fuel cell catalysts," *Applied Catalysis B: Environmental*, **2009**, 88, 1 - 24.
- Arepalli, S. "Laser ablation process for single-walled carbon nanotube production," *Journal of Nanoscience and Nanotechnology*, **2004**, 4, 317 – 325.
- Arnoldy, P.; de Jonge, J.; Moulijn, J. "Temperature-programmed reduction of MoO₃ and MoO₂," *The Journal of Physical Chemistry* **1985**, 89, 4517 - 4526.
- Arora, N.; Sharma, N. "Arc discharge synthesis of carbon nanotubes: Comprehensive review," *Diamond & Related Materials*, **2014**, 50, 135 - 150.
- Aryee, E.; Dalai, A.; Adjaye, J. "Maximization of carbon nanohorns production via the arc discharge method for hydrotreating application," *Journal of Nanoscience and Nanotechnology*, **2017**, 17, 4784 - 4791.
- Aryee, E.; Dalai, A.; Adjaye, J. "Functionalization and characterization of carbon nanohorns (CNH) for hydrotreating of gas oils," *Topics in Catalysis*, **2014**, 57, 796 - 805.
- Atanasova, P.; Tabakova, T.; Vladov, C.; Halachev, T.; Lopez Agudo, A. "Effect of phosphorus concentration and method of preparation on the structure of the oxide form of phosphorus-nickel-tungsten/alumina hydrotreating catalysts," *Applied Catalysis A: General*, **1997**, 161, 105 - 119.
- Atanasova, P.; Halachev, T.; Uchytel, J.; Kraus, M. "Effect of phosphorus on the surface concentration of molybdenum and nickel in the oxide form of nickel-molybdenum/alumina catalysts and on their hydrodesulfurization activity," *Applied Catalysis*, **1988**, 38, 235 - 240.
- Azami, T.; Kasuya, D.; Yuge, R.; Yudasaka, M.; Iijima, S.; Yoshitake, T.; Yoshimi, K. "Large scale production of single-wall carbon nanohorns with high purity," *The Journal of Physical Chemistry C*, **2008**, 112, 1330 - 1334.
- Babich, I.; Moulijn, J. "Science and technology of novel processes for deep desulfurization of oil refinery streams: A Review," *Fuel*, **2003**, 82, 607 - 631.
- Badoga, S.; Sharma, R.; Dalai, A.; Adjaye, J. "Hydrotreating of heavy gas oil on mesoporous zirconia supported NiMo catalyst with EDTA," *Fuel*, **2014**, 128, 30 - 38.
- Bandow, S.; Kokai, F.; Takahashi, K.; Yudasaka, M.; Qin, L.; Iijima, S. "Interlayer spacing anomaly of single-wall carbon nanohorn aggregate," *Chemical Physics Letters*, **2000**, 321, 514 - 519.

- Bartholomew, C. "Mechanism of catalyst deactivation," *Applied Catalysis A: General*, **2001**, 212, 17 - 60.
- Barzetti, T.; Selli, E.; Moscotti, D.; Forni, L. "Pyridine and ammonia as probes for FTIR analysis of solid acid catalysts," *Journal of the Chemical Society, Faraday Transactions*, **1996**, 92, 1401 - 1407.
- Battiston, S.; Bolzan, M.; Fiameni, S.; Gerbasi, R.; Meneghetti, M.; Miorin, E.; Mortalo, C.; Pagura, C. "Single wall carbon nanohorns coated with anatase titanium oxide," *Carbon*, **2009**, 47, 1321 - 1326.
- Bej, S.; Dalai, A.; Maity, S. "Effect of diluent size on the performance of a micro-scale fixed bed multiphase reactor in up flow and down flow modes of operation," *Catalysis Today*, **2001**, 64, 333 - 345.
- Bej, S.; Dabral, R.; Gupta, P.; Mittal, K.; Sen, G.; Kapoor, V.; Dalai, A. "Studies on the performance of a microscale trickle bed reactor using different sizes of diluent," *Energy & Fuels* **2000**, 14, 701 - 705.
- Bekyarova, E.; Hashimoto, A.; Yudasaka, M.; Hattori, Y.; Murata, K.; Kanoh, H.; Kasuya, D.; Iijima, S.; Kaneko, K. "Palladium nanoclusters deposited on single-walled carbon nanohorns," *The Journal of Physical Chemistry B Letters*, **2005**, 109, 3711 - 3714.
- Bekyarova, E.; Kaneko, K.; Yudasaka, M.; Kasuya, D.; Iijima, S.; Huidobro, A.; Rodriguez-Reinoso, F. "Controlled opening of single-wall carbon nanohorns by heat treatment in carbon dioxide" *Journal of Physical Chemistry B*, **2003**, 107, 19, 4479 - 4484.
- Bekyarova, E.; Murata, K.; Yudasaka, M.; Kasuya, D.; Iijima, S.; Tanaka, H.; Kahoh, H.; Kaneko, K. "Single-wall nanostructured carbon for methane storage" *The Journal of Physical Chemistry B*, **2003**, 107, 4681 - 4684.
- Bekyarova, E.; Hanzawa, Y.; Kaneko, K.; Silvestre-Albero, J.; Sepulveda-Escribano, A.; Rodriguez-Reinoso, F.; Kasuya, D.; Yudasaka, M.; Iijima, S. "Cluster-mediated filling of water vapor in intratube and interstitial nanospaces of single-wall carbon nanohorns," *Chemical Physics Letters*, **2002**, 366, 463 - 468.
- Bekyarova, E.; Kaneko, K.; Kasuya, D.; Murata, K.; Yudasaka, M.; Iijima, S. "Oxidation and porosity evaluation of budlike single-wall carbon nanohorn aggregates," *Langmuir*, **2002**, 18, 4138 - 4141.
- Bera, D.; Johnston, G.; Heinrich, H.; Seal, S. "A parametric study on the synthesis of carbon

- nanotubes through arc-discharge in water,” *Nanotechnology*, **2006**, 17, 6, 1722 - 1730.
- Bera, D.; Perrault, J.; Heinrich, H.; Seal, S. “Defect studies on as-synthesized and purified carbon nanostructures produced by arc-discharge in solution process,” *Journal of Nanoscience and Nanotechnology*, **2006**, 6, 1084 - 1091.
- Bergeret, G.; Gallezot, P. “Particle size and dispersion measurements,” *Handbook Heterogenous Catalysis*, **2008**, 6, 6965 - 6976.
- Berhault, G.; Mehta, A.; Pavel, A. C.; Yang, J.; Rendon, L.; Yacaman, M. J.; Araiza, L. C.; Moller, A. D.; Chianelli, R. “The role of structural carbon in transition metal sulfides hydrotreating catalysts,” *Journal of Catalysis*, **2001**, 198, 9 - 19.
- Berkmans, A.; Jagannatham, M.; Reddy, D.; Haridoss, P. “Synthesis of thin bundled single walled carbon nanotubes and nanohorn hybrids by arc discharge technique in open air atmosphere,” *Diamond & Related Materials*, **2015**, 55, 12 - 15.
- Berthomieu, C.; Hienerwadel, R. “Fourier transform infrared (FTIR) spectroscopy,” *Photosynthesis Research*, **2009**, 101, 157 - 170.
- Bessel, C.; Laubemds, K.; Rodriguez, N.; Baker, R. “Graphite nanofibers as an electrode for fuel cell application,” *Journal of Physical Chemistry B*, **2001**, 105, 1115 - 1118.
- Boahene, P. “Catalyst development for the conversion of syngas to higher alcohols using alkali-promoted MoS₂-based catalyst over carbon supports,” *Doctorate Thesis, University of Saskatchewan*, **2017**.
- Boahene, P.; Surisetty, V.; Sammynaiken, R.; Dalai, A. “Higher alcohol synthesis using K-doped CoRhMoS₂/MWCNT catalysts: Influence of pelletization, particle size and incorporation of binders. *Topics in Catalysis*, **2014**, 57, 538 - 549.
- Boehm, H. “Surface oxides on carbon and their analysis: a critical assessment,” *Carbon*, **2002**, 40, 145 - 149.
- Boehm, H. “Some aspects of the surface chemistry of carbon blacks and other carbons,” *Carbon*, **1994**, 32, 759 - 769.
- Borodziński, A.; Bonarowska, M. “Relationship between crystallite size and dispersion on supported Metal Catalysts.” *Langmuir*, **1997**, 13, 5613 - 5620.
- Bose, D. “Design parameters for a hydro desulfurization (HDS) unit for petroleum naphtha at 3500 barrels per day,” *World Scientific News*, **2015**, 99 - 111.
- Botchwey, C.; Dalai, A.; Adjaye, J. “Product selectivity during hydrotreating and mild

- hydrocracking of bitumen-derived gas oil.” *Energy & Fuels*, **2003**, 17, 1372 - 1381.
- Brandao, L.; Passeira, C. “Use of single wall carbon nanohorns in polymeric electrolyte fuel cells,” *Journal of Material Science*, 2011, 46, 7198 - 7205.
- Breysse, M., Afanasiev, P., Geantet, C., Vrinat, M. “Overview of support effects in hydrotreating catalysts,” *Catalysis Today*, **2003**, 86, 5 - 16.
- Brito, J. L.; Laine, J.; Pratt, K. C. “Temperature-Programmed reduction of Ni-Mo oxides,” *Journal of Materials Science*, **1989**, 24, 2, 425 - 431.
- Broekhoff, J.C.P. “Mesopore determination from nitrogen sorption isotherms: Fundamentals, scope, limitations,” *Studies in Surface Science and Catalysis*, **1979**, 3, 663 – 684.
- Bumrah, G.; Sharma, R. “Raman spectroscopy-Basic principle, instrumentation and selected applications for the characterization of drugs of abuse,” *Egyptian Journal of Forensic Sciences*, **2016**, 6, 209 - 215.
- Byskov, L.; Hammer, B.; Nørskov, J., Clausen B.; Topsøe, H. “Sulfur bonding in MoS₂ and Co-Mo-S structures,” *Catalysis letters*, **1997**, 47, 177 – 182.
- Calafat, A.; Laine, J.; LopezAgudo, A.; Palacios, J. M. “Effect of surface oxidation of the support on the thiophene hydrodesulfurization activity of Mo, Ni, and NiMo catalysts supported on activated carbon,” *Journal of Catalysis*, **1996**, 162, 1, 20 - 30.
- Calderon-Magdalenos, M.; Mendoza-Nieto, J.; Klimova, T. “Effect of the amount of citric acid used in the preparation of NiMo/SBA-15 catalysts on their performance in HDS of dibenzothiophene-type compounds,” *Catalysis Today*, **2014**, 220-222, 78 - 88.
- Cançado, L. G.; Takai, K.; Enoki, T.; Endo, M.; Kim, Y. A.; Mizusaki, H.; Pimenta, M. A. “General equation for the determination of the crystallite size La of nanographite by Raman spectroscopy,” *Applied Physics Letters*, **2006**, 88, 16, 163106 - 1 – 16106 3.
- Candia, R.; Sorensen, O.; Villadsen, J.; Topsoe, N.; Clausen, B.; Topsoe, H. “Effect of sulfiding temperature on activity and structures of CoMo/Al₂O₃ catalysts,” *Bulletin des Societes Chimiques Belges*, **1984**, 93, 763 - 773.
- Carberry, J. J.; Wendel, M. M. “A computer model of the fixed bed catalytic reactor: The adiabatic and quasi-adiabatic cases,” *American Institute of Chemical Engineers Journal*, **1963**, 9, 1, 129 – 133.

- Carrier, X.; Lambert, J.; Che, M. "Ligand-promoted alumina dissolution in the preparation of MoOx/ γ -Al₂O₃ catalyst: Evidence for the formation and deposition of an anderson-type alumino-heteropolymolybdate," *Journal of American Chemical Society*, **1997**, 119, 10137 - 10146.
- Chao, G. W.; Luo, X. H.; Liu, Z. H.; He, J. H. "Preparation and characterization of hydrotreating catalysts: I Preparation of MoNiP/Al₂O₃ and effect of promoters," *Chinese Journal of Catalysis*, **2001**, 22, 2, 143 – 147.
- Charinpanitkuk, T.; Tanthapanichakoon, W.; Sano, N. "Carbon nanostructures synthesized by arc discharge between carbon and iron electrodes in liquid nitrogen," *Current Applied Physics*, **2009**, 9, 629 - 632.
- Che, C.; Glotch, T.; Bish, D.; Michalski, J.; Xu, W. "Spectroscopic study of the dehydration and/or dehydroxylation of phyllosilicate and zeolite minerals," *Journal of Geophysical Research*, **2011**, 116, 1 - 23.
- Chen, F.; Duponta, V.; Twigg, M. V. "Temperature-programmed reduction of nickel steam reforming catalyst with glucose," *Applied Catalysis A: General*, **2016**, 527, 1 - 8.
- Chen, J.; Wang, N.; Mederos, F.; Ancheyta, J. "Vapor-liquid equilibrium study in trickle-bed reactors," *Industrial Engineering Chemistry Research*, **2009**, 48, 1096 - 1106.
- Chen, J.; Wu, S. "Acid/Base-treated activated carbons: Characterization of functional groups and metal adsorptive properties," *Langmuir*, **2004**, 20, 2233 - 2242.
- Chithrani, B.; Ghazani, A.; Chan, W. "Determining the size and shape dependence of gold nanoparticle uptake into mammalian cells," *Nano Letters*, **2006**, 6, 662 - 668.
- Chuzf, C. F.; Ng, K. M. "Flow in packed tubes with a small tube to particle diameter ratio," *American Institute of Chemical Engineers Journal*, **1989**, 35, 148.
- Connell, G.; Dumesic, J. "The generation of Bronsted and Lewis acid sites on the surface of silica by addition of dopant cations," *Journal of Catalysis*, **1987**, 105, 285 - 298.
- Cullity, B.; Stock, S. "Elements of X-ray Diffraction," Third Edition, New York: Prentice Hall, **2001**.
- Damyanova, S.; Spojakina, A.; Jiratova, K. "Effect of mixed titania-alumina supports on the phase composition of NiMo/TiO₂-Al₂O₃ catalysts," *Applied Catalysis A: General*, **1995**, 125, 257 - 269.

- Das, R.; Shahnavaz, Z.; Ali, M.; Islam, M.; Hamid, S. "Can we optimize arc discharge and laser ablation for well-controlled carbon nanotube synthesis?" *Nanoscale Research Letters*, **2016**, 11, 510, 1 - 23.
- Das, S.; Essilfie-Dughan, J.; Hendry, M. "Sequestration of molybdate during transformation of 2-line ferrihydrite under alkaline conditions" *Applied Geochemistry*, **2016**, 73, 70 - 80.
- de Beer, V.; Derbyshire, F.; Grout, C.; Prins, R.; Scaroni, A.; Solar, J. "Hydrodesulfurization activity and coking propensity of carbon and alumina supported catalysts," *Fuel*, **1984**, 63, 1095 - 1100.
- de Beer, V.; van der Aalst, M.; Machiels, C.; Schuit, G. "The CoO-MoO₃- γ -Al₂O₃ catalyst: VII. Influence of the support" *Journal of Catalysis*, **1976**, 43, 78 - 89.
- Delmastro, A.; Gozzelino, G.; Mazza, D.; Vallino, M.; Busca, G.; Lorenzelli, V. "Characterization of microporous amorphous alumina boria," *Journal of Chemical Society, Faraday Transactions*, **1992**, 88, 2065 - 2070.
- Deliyanni, E.; Seredych, M.; Bandosz, T. "Interactions of 4,6-Dimethyldibenzothiophene with the surface of activated carbons," *Langmuir*, **2009**, 25, 9302 - 9312.
- Digne, M.; Sautet, P.; Raybaud, P.; Euzen, P., Toulhoat, H. "Use of DFT to achieve a rational understanding of acid-basic properties of γ -alumina surfaces," *Journal of Catalysis*, **2004**, 226, 54 - 68.
- Ding, L.; Zheng, Y.; Zhang, Z.; Ring, Z.; Chen, J. "HDS, HDN, HAD, and hydrocracking of model compounds over Mo-Ni catalysts with various acidities," *Applied Catalysis A*, **2007**, 319, 25 - 37.
- Du, J.; Liu, Z.; Li, Z.; Han, B.; Sun, Z.; Huang, Y. "Carbon onions synthesized via thermal Reduction of glycerin with magnesium," *Materials Chemistry and Physics*, **2005**, 93, 178 - 180.
- Duchet, J.; van Oers, E.; de Beer, V.; Prins, R. "Carbon-supported sulfide catalysts," *Journal of Catalysis*, **1983**, 80, 386 - 402.
- Ebbesen, T. "Cones and Tubes: Geometry in the chemistry of carbon," *Accounts of chemical research*, **1998**, 31, 558 - 566.
- Ebbesen, T.; Ajayan, P. "Large-scale synthesis of carbon nanotubes," *Nature*, **1992**, 358, 220 - 222.

- Eijsbouts, S. "On the flexibility of the active phase in hydrotreating catalysts," *Applied Catalysis A: General*, **1997**, 158, 53 - 92.
- Eijsbouts, S.; Mayo, S.; Fujita, K. "Unsupported transition metal sulfide catalysts: From fundamentals to industrial application," *Applied Catalysis A: General*, **2007**, 322, 58 - 66.
- Eijsbouts, S.; van Gestel, J.; van Veen, J.; de Beer, V.; Prins, R. "The effect of phosphate on the hydrodenitrogenation activity and selectivity of alumina-supported sulfided Mo, Ni, and NiMo catalysts," *Journal of Catalysis*, **1991**, 131, 412 - 432.
- Essilfie-Dughan, J.; Hendry, M.; Dynes, J.; Hu, Y.; Biswas, A.; Lee Barbour, S. "Geochemical and mineralogical characterization of sulfur and iron in coal waste rock, Elk Valley, British Columbia, Canada," *Science of Total Environment*, **2017**, 586, 753 - 769.
- Eswaramoorthi, I.; Sundaramurthy, V.; Das, N.; Dalai, A.; Adjaye, J. "Application of multi-walled carbon nanotubes as efficient support to NiMo hydrotreating catalyst," *Applied Catalysis A: General*, **2008**, 339, 187 - 195.
- Falcao, E. H.; Wudl, F. "Carbon allotropes: beyond graphite and diamond," *Journal of Chemical Technology & Biotechnology*, **2007**, 82, 6, 524 - 531.
- Fan, J.; Yudasaka, M.; Kasuya, D.; Azami, T.; Yuge, R.; Imai, H.; Kubo, Y.; Iijima, S. "Micrometer-sized graphitic balls produced together with single-wall carbon nanohorn," *Journal of Physical Chemistry B*, **2005**, 109, 10756 - 10759.
- Fan, J.; Yudasaka, M.; Miyawaki, J.; Ajima, K.; Murata, K.; Iijima, S. "Control of hole opening in single-wall carbon nanotubes and single-wall carbon nanohorns using oxygen," *The Journal of Physical Chemistry B*, **2006**, 110, 1587 - 1591.
- Fan, X.; Tan, J.; Zhang, G.; Zhang, F. "Isolation of carbon nanohorn assemblies and their potential for intracellular delivery," *Nanotechnology*, **2007**, 18, 195103 - 195109.
- Fanning, P.; Vannice, M. "A DRIFTS Study of the formation of surface groups on carbon by oxidation," *Carbon*, **1993**, 31, 721 - 730.
- Fay, I. W.; Seeker, A. F. "Reducibility of some metallic oxides by hydrogen and carbon monoxide," *Journal of the American Chemical Society*, **1903**, 25, 6, 641 - 647.
- Farag, H.; Mochida, I.; Sakanishi, K. "Fundamental comparison studies on hydrodesulfurization of dibenzothiophenes over Co-Mo-based carbon and alumina catalyst," *Applied Catalysis A*, **2000**, 147, 194 - 195.

- Farag, H.; Whitehurst, D.; Mochida, I. "Synthesis of active hydrodesulfurization carbon-supported Co-Mo catalysts. Relationships between preparation methods and activity/selectivity," *Industrial and Engineering Chemistry Research*, **1998**, 37, 3533 - 3539.
- Ferdous, D.; Dalai, A.; Adjaye, J. "Comparison of product selectivity during hydroprocessing of bitumen derived gas oil in the presence of NiMo/Al₂O₃ catalyst containing Boron and Phosphorus," *Fuel*, **2006**, 85, 1286 - 1297.
- Ferdous, D.; Dalai, A.; Adjaye, J. "Hydrodenitrogenation and hydrodesulfurization of heavy gas oil using NiMo/Al₂O₃ catalyst containing phosphorus: Experimental and kinetic studies," *The Canadian Journal of Chemical Engineering*, **2005**, 83, 855 - 864.
- Figueiredo, J.; Pereira, M. "The role of surface chemistry in catalysis with carbons," *Catalysis Today*, 2010, 150, 2 - 7
- Figueiredo, J.; Pereira, M.; Freitas, M.; Órfão, J. "Modification of the surface chemistry of activated carbons. Carbon," **1999**, 37, 1379 - 1389.
- Fogler, H. "Elements of chemical reaction engineering," Prentice Hall International Series, **2006**, 4th Edition.
- Froment, G.; Bischoff, K. "Chemical reactor analysis and design," New York, Wiley, **1990**.
- Furimsky, E. "Review: Selection of catalysts and reactors for hydroprocessing," *Applied Catalysis A: General*, **1998**, 171, 177 - 206.
- Furimsky, E.; Massoth, F. E. "Hydrodenitrogenation of petroleum," *Catalysis Reviews Science and Engineering*, **2005**, 47, 297 - 489.
- Gang, X.; Shen-li, J.; Zong-qian, S. "The production of carbon nano-materials by arc discharge under water or liquid nitrogen," *New Carbon Mater*, **2007**, 22, 337 - 341.
- Garg, S.; Soni, K.; Prabhu, A.; Rao, K.; Dhar, G. "Effect of ordered mesoporous Zr SBA-15 support on catalytic functionalities of hydrotreating catalysts 2. Variation of molybdenum and promoter loadings," *Catalysis Today*, **2016**, 261, 128 - 136.
- Gary, J.H.; Handwerk, G.E. "Petroleum refining: Technology and economics," Taylor & Francis, **2005**.
- Gattia, D.; Antisari, M.; Marazzi, R. "AC arc discharge synthesis of single-walled nanohorns and highly convulated graphene sheets," *Nanotechnology*, **2007**, 18, 255604 - 255611.

- Gattia, D.; Antisari, M.; Giorgi, L.; Marazzi, R.; Pilloni, L.; Contini, V.; Montone, A. "Arc-discharge synthesis of carbon nanohorns and multiwalled carbon nanotubes," *Materials Science Forum*, **2006**, 518, 23 – 28.
- Gattia, D.; Antisari, M.; Giorgi, L.; Marazzi, R.; Piscopiello, E.; Montone, A.; Bellitto, S.; Liccocchia, S.; Traversa, E. "Study of different nanostructured carbon supports for fuel cell catalysts," *Journal of Power Sources*, **2009**, 194, 243 - 251.
- Georgakilas, V.; Perman, J.; Tucek, J.; Zboril, R. "Broad Family of Carbon Nanoallotropes: Classification, chemistry, and applications of fullerenes, carbon dots, nanotubes, graphene, nanodiamonds, and combined superstructures," *Chemical Reviews*, 2015, 115, 4744 - 4822.
- George, G.; Pickering, I. "X-ray absorption spectroscopy in biology and chemistry," In: *Brilliant Light in Life and Material Sciences*, Tsakanov V, Wiedemann H (eds) Springer, Dordrecht, **2007**, 97 - 119.
- Gervasini, A. "Temperature programmed reduction/oxidation (TPR/TPO) methods, in calorimetry and thermal methods in catalysis," Edited by Auroux, A., Springer, **2013**, 175 - 197.
- Ghorui, S.; Sahasrabudhe, S.; Tak, A.; Joshi, N.; Kulkarni, N.; Karmakar, S.; Banerjee, I.; Bhoraskar, S.V.; Das, A. K. "Role of arc plasma instability on nanosynthesis," *Institute of Electrical and Electronics Engineers Transactions on Plasma Science*, **2006**, 34, 1, 121 - 127.
- Gierman, H. "Design of laboratory hydrotreating reactors scaling down of trickle-flow reactors," *Applied Catalysis*, **1988**, 43, 277.
- Goto, S.; Smith, J. "Trickle-bed reactor performance: I. Holdup and mass transfer effects," *American Institute of Chemical Engineers Journal*, **1975**, 21, 706 - 713.
- Grange P.; Vanhaeren, X. "Hydrotreating catalysts, an old story with new challenges," *Catalysis Today*, **1997**, 36, 375 - 391.
- Grimblot, J. "Genesis, architecture and nature of sites of Co(Ni)–MoS₂ supported hydroprocessing catalyst," *Catalysis Today*, **1998**, 41, 111 - 128.
- Gruia, A. "Hydrotreating," In: Jones D. S. J. S., Pujadó P.R. (eds) *Handbook of Petroleum Processing*, Springer Dordrech, **2008**.
- Hafner, J. H.; Bronikowski, M. J.; Azamian, B. R.; Niko-Laevl, P.; Rinzler, A. G.; Colbert, D. T.; Smith, K. A.; Smalley, R. E. "Catalytic growth of single-wall carbon nanotubes from

- Metal particles,” *Chemical Physics Letters*, **1998**, 296, 195 - 202.
- Harris, P. “Transmission electron microscopy of carbon: A brief history. C” *Journal of Carbon Research*, **2018**, 4, 1 - 17.
- HARTENERGY Research & Consulting. “International fuel quality standards and their implications for Australian standards,” Australian Government, Department of the Environment, Houston, TX, USA, **2014**
- Healy, M.; Wieserman, L. K.; Arnett, E.; Wefers, K. “Infrared spectroscopy and microcalorimetric investigations of δ - θ and κ Aluminas using basic probe molecules: Acetonitrile, pyridine, 2, 6 -Lutidine, and n-Butylamine,” *Langmuir*, **1989**, 5, 114 - 123.
- Helveg, S.; Lauritsen, J. V.; Laegsgaard, E.; Stensgaard, I.; Nørskov, J. K.; Clausen, B. S.; Topsøe, H.; Besenbacher, F. “Atomic-scale structure of singlelayer MoS₂ nanoclusters,” *Physical Review Letters*, **2000**, 84, 951 - 954.
- Henker, M.; Wendlandt, K.; Valyon, J.; Bornmann, P. “Structure of MoO₃/Al₂O₃-SiO₂ catalysts,” *Applied Catalysis*, **1991**, 69, 205 - 220.
- Hou, P.; Liu, C.; Cheng, H. “Purification of carbon nanotubes,” *Carbon*, **2008**, 46, 2003 - 2025.
- Hurst, N. W.; Gentry, S. J.; Jones, A.; McNicol, B. D. “Temperature programmed reduction,” *Catalysis Reviews*, **1982**, 24, 2, 233 - 309.
- Hussain, M.; Ihm, S. “Synthesis, characterization, and hydrodesulfurization activity of new mesoporous carbon supported transition metal sulfide catalysts,” *Industrial and Engineering Chemistry Research*, **2009**, 48, 698 - 707.
- Hussain, M.; Yun, J.; Ihm, S.; Russo, N.; Geobaldo, F. “Synthesis, characterization, and thiophene hydrodesulfurization activity of novel microporous and mesomacroporous carbon,” *Industrial and Engineering Chemistry Research*, **2011**, 50, 2530 - 2535.
- Hynaux, A.; Sayag, C.; Suppan, S.; Trawczynski, J.; Lewandowski, M.; Szymanska-Kolasa, A.; Djega-Mariadassou, G. “Kinetic study of the hydrodesulfurization of dibenzothiophene over molybdenum carbides supported on functionalized carbon black composite - Influence of indole,” *Applied Catalysis B: Environmental*, **2007**, 72, 62 - 70.
- Iijima, S.; Yudasaka, M.; Yamada, R.; Bandow, S.; Suenaga, K.; Kokai, F.; Takahashi, K. “Nano-aggregates of single-walled graphitic carbon nano-horns,” *Chemical Physics Letters*, **1999**, 309, 165 - 170.

- Ishigami, M.; Cummings, J.; Zettl, A.; Chen, S. "A simple method for the continuous production of carbon nanotubes," *Chemical Physics Letters*, **2000**, 319, 457 - 459.
- Itoh, T.; Urita, K.; Bekyarova, E.; Arai, M.; Yudasak, M.; Iijima, S.; Ohba, T.; Kaneko, K.; Kanoh, H. "Nanoporosities and catalytic activities of Pd-tailored single wall carbon nanohorns," *Journal of Colloid and Interface Science*, **2008**, 322, 209 - 214.
- Iwamoto, R.; Grimblot, J. "Genesis, structural, and catalytic properties of Ni-Mo-P-alumina based hydrotreating catalysts prepared by a sol-gel method," *Studies in surface science and catalysis*, **1999**, 127, 169 - 176.
- Jarullah, A.; Mujtaba, I.; Wood, A. "Improvement of the middle distillate yields during crude oil hydrotreatment in a trickle-bed reactor," *Energy and Fuels*, **2011**, 25, 773 - 781.
- Jiménez F., Kafarov V., Nunez M. "Modeling of industrial reactor for hydrotreating of vacuum gas oils: Simultaneous hydrodesulfurization, hydrodenitrogenation, and hydrodearomatization reactions," *Chemical Engineering Journal*, **2007**, 134, 200 – 208.
- Jones D.S.J. "Elements of petroleum processing," John Wiley & Sons, **1995**.
- Jonoud, S.; Jackson, D. "New criteria for the validity of steady-state upscaling," *Transport in Porous Media*, **2007**, 71, 53 - 73.
- Joo, H.; Guin, J. "Activity of noble metal-promoted hydroprocessing catalysts for pyridine HDN and naphthalene hydrogenation," *Fuel Processing Technology*, **1996**, 49, 137 - 155.
- Jori, A. "Raman Spectroscopy in graphene-based system: prototypes for nanoscience and nanometrology," *International Scholarly Research Notices, Nanotechnology*, **2012**, 234216 - 234232.
- Kaluža, L.; Zdražil, M. "Carbon-supported Mo catalysts prepared by a new impregnation method using a MoO₃/water slurry: saturated loading, hydrodesulfurization activity and promotion by Co," *Carbon*, **2001**, 39, 2023 - 2034.
- Karousis, N.; Suarez-Martinez, I.; Ewels, C. P.; Tagmatarchis, N. "Structure, properties, functionalization, and applications of carbon nanohorns" *Chemical Reviews*, **2016**, 116, 4850 - 4883.
- Kasiri, N.; Bashiri, A. "Wettability and Its Effects on Oil Recovery in Fractured and Conventional Reservoirs," *Petroleum Science and Technology*, **2011**, 29, 1324–1333.

- Kasuya, D.; Yudasaka, M.; Takahashi, K.; Kokai, F.; Iijima, S. "Selective production of single-wall carbon nanohorn aggregates and their formation mechanism," *Journal of Physical Chemistry B*, **2002**, 106, 4947 - 4951.
- Keidar, M.; Shashurin, A.; Li, J.; Volotskova, O.; Kundrapu, M.; Zhuang, T. "Arc plasma synthesis of carbon nanostructures: where is the frontier?," *Journal of Physics D: Applied Physics*, **2011**, 44, 174006.
- Kelly, S.; Hesterberg, D.; Ravel, B. "Analysis of soils and minerals using X-ray absorption spectroscopy," In: *Methods of soil analysis. Part 5, Mineralogical methods*, Ulery, L.; Drees, R.; Soil Science Society of America, Eds. Soil Science Society of America, Madison, WI, **2008**, 387 - 464.
- Keresztury, G. "Raman Spectroscopy: Theory," *Handbook of Vibrational Spectroscopy*, John Wiley & Sons, **2006**, 71 - 87.
- Klimov, O.; Vatutina, Y.; Nadeina, K.; Kazakov, M.; Gerasimov, E.; Prosvirin, I.; Larina, T.; Noskov, A. "CoMoB/Al₂O₃ catalysts for hydrotreating of diesel fuel. The effect of the way of the boron addition to a support or an impregnating solution," *Catalysis Today*, **2018**, 305, 192 - 202.
- Knözinger, H. "Infrared spectroscopy as a probe of surface acidity In: Joyner, R. W.; van Santen R. A. (eds) *Elementary reaction steps in heterogeneous catalysis*," NATO ASI Series (Series C: Mathematical and Physical Sciences), Springer Dordrecht, **1993**, 398, 267 - 285.
- Knudsen, K.; Topsoe, H.; Cooper, B. "Catalyst and process technologies for ultra-low sulfur diesel," *Applied Catalysis A*, **1999**, 189, 205 - 215.
- Kokayeff, P.; Zink S.; Roxas P. "Hydrotreating in petroleum processing. In: Treese S., Jones D., Pujado P. (eds) *Handbook of Petroleum Processing*." Springer, Cham, **2014**.
- Koningsberger, D. C.; Prins, R. (eds), "X-ray absorption: principles, applications, techniques of EXAFS, SEXAFS and XANES," Wiley, New York, **1998**.
- Korsten, H.; Hoffman, U. "Three-phase reactor model of hydrotreating in pilot tricklebed reactors," *American Institute of Chemical Engineers Journal*, **1996**, 42, 1350 - 1360.
- Koziol, K.; Boskovic, B.; Yahya, N. "Synthesis of carbon nanostructures by CVD method. In: *carbon and oxide nanostructures*," *Advanced Structured Materials*, Springer, Berlin, Heidelberg, **2010**, 5. 23 - 49.

- Krishnan, A.; Dujardin, E.; Treacy, M.; Hugdahl, J.; Lynam, S.; Ebbesen, T. "Graphitic cones and the nucleation of curved carbon surfaces," *Nature*, **1997**, 388, 451 - 454.
- Krungleviciute, V.; Calbi, M.; Wagner, J.; Migone, A.; Yudasaka, M.; Iijima, S. "Probing the structure of carbon nanohorn aggregates by adsorbing gases of different sizes," *The Journal of Physical Chemistry C*, **2008**, 112, 5742 - 5746.
- Kwart, H.; Katzer, J.; Horgan, J. "Hydroprocessing of phenothiazine catalyzed by Co-Mo/ γ -Al₂O₃," *The Journal of Physical chemistry*, **1982**, 86, 2641 - 2646.
- Lam, E.; Luong, J. "Carbon materials as catalyst supports and catalysts in the transformation of biomass to fuels and chemicals," *ACS Catalysis*, **2014**, 4, 3393 - 3410.
- Laredo, S.; De Los Reyes, J.; Luis Cano, D.; Castillo, M. "Inhibition effects of nitrogen compound on the hydrodesulfurization of dibenzothiophene," *Applied Catalysis General*, **2001**, 207, 103 - 112.
- Lebukhova, N. V.; Karpovich, N. F. "Carbothermic reduction of copper, nickel, and cobalt oxides and molybdates," *Inorganic Materials*, **2008**, 44, 8, 890 - 893.
- Lee, J.; Han, S.; Kim, H.; Koh, J.; Hyeon, T.; Moon, S. "Performance of CoMoS catalysts supported on nanoporous carbon in the hydrodesulfurization of dibenzothiophene and 4, 6 - dimethyldibenzothiophene," *Catalysis Today*, **2003**, 86, 141 - 149.
- Leliveld, R.; Eijsbouts, S. "How a 70-year-old catalytic refinery process is still ever dependent on innovation," *Catalysis Today*, **2008**, 130, 183 - 189.
- Li, H.; Zhao, N.; Wang, L.; Shi, C.; Du, X.; Li, J. "Synthesis of carbon nanohorns by the simple catalytic method," *Journal of Alloys and Compounds*, **2009**, 473, 288- 292.
- Liu, F.; Xu, S.; Chi, Y.; Xue, D. "A novel alumina-activated carbon composite supported NiMo catalyst for hydrodesulfurization of dibenzothiophene," *Catalysis Communications*, **2011**, 12, 6, 521 - 524.
- Liu, X.; Li, H.; Wang, F.; Zhu, S.; Wang, Y.; Xu, G. "Functionalized single-walled carbon nanohorns for electrochemical biosensing," *Biosensors and Bioelectronics*, **2010**, 25, 2194 - 2199.
- Lordi, V.; Ma, S.; Yao, N. "Towards probing pentagons on carbon nanotube tips," *Surface Science*, **1999**, 421, L150 - L155.
- López, C. R.; López, A. A. "Effect of water extraction on the surface properties of Mo/Al₂O₃ and NiMo/Al₂O₃ hydrotreating catalysts," *Applied Catalysis A: General*, **2000**, 202, 23 -

- Lowell, S.; Shields, J. E.; Thomas, M. A.; Thommes, M. "Characterization of porous solids and powders: Surface Area, pore size and density," Particle Technology Series, Springer Science + Business Media, **2004**.
- Luck, F. "A review of support effects on the activity and selectivity of hydrotreating catalysts," Bulletin des Societe's Chimiques Belges, **1991**, 100, 781 - 800.
- Ly, M.; Xie, W.; Sun, S.; Wu, G.; Zheng, L.; Chu, S.; Gao, C. "Activated-carbon-supported K-Co-Mo catalysts for synthesis of higher alcohols from syngas," Catalysis Science & Technology, **2015**, 5, 2925 - 2015.
- Lynch, J. "Physico-chemical analysis of industrial catalysts - A practical guide to characterization," Editions TECHNIP, **2003**, 1 - 309.
- Maity, S.; Juárez, J.; Martínez, F.; Fukuyama, H.; Terai, S.; Uchida, M. "Carbon supported catalyst for demetallation of heavy crude oil and residue," US8431018B2, **2013**.
- Maity, S.; Ancheyta, J.; Soberanis, L.; Alonso, F. "Catalysts for hydroprocessing of Maya heavy crude," Applied Catalysis A: General **2003**, 253, 125 - 134.
- Maity, S.; Ancheyta, J.; Rana, M.; Rayo, P. "Effect of phosphorus on activity of hydrotreating catalyst of Maya heavy crude," Catalysis Today, **2005**, 109, 42 - 48.
- Maity, S.; Rana, M.; Srinivas, B.; Bej, S.; Dhar, G.; Rao, T. "Characterization and evaluation of ZrO₂ supported hydrotreating catalysts," Journal of Molecular Catalysis A: Chemical, **2000**, 153, 121 - 127.
- Martín-Gullón, A.; Prado-Burguete, C.; Rodríguez-Reinoso, F. "Effect of carbon properties on the preparation and activity of carbon-supported molybdenum sulfide catalysts," Carbon, **1993**, 31, 1099 - 1105.
- Marzari, J.; Rajagopal, S.; Miranda, R. "Bifunctional mechanism of pyridine hydrodenitrogenation," Journal of Catalysis, **1995**, 156, 255 - 264.
- Mapiour, M.; Sundaramurthy, V.; Dalai, A.; Adjaye, J. "Effects of the operating variables on hydrotreating of heavy gas oil: Experimental, modeling and kinetic studies," Fuel, **2010**, 2536 - 2543.
- Maser, W.; Muñoz, E.; Benito, A.; Martínez, M.; de la Fuente, G.; Maniette, Y.; Anglaret, E.; Sauvajol, J. "Production of high-density single-walled nanotube material by a simple laser-ablation method," Chemical Physics Letters, **1998**, 292, 587 - 593.

- Mears, D. E. "The role of axial dispersion in trickle-flow laboratory reactors," *Chemical Engineering Science*, **1971**, 26, 1361 - 1366.
- Micromeritics ASAP 2020 Chemi Manual, Appendix C
- Miyawaki, J.; Yudasaka, M.; Azami, T.; Kubo, Y.; Iijima, S. "Toxicity of single-walled carbon nanohorns," *American Chemical Society Nano*, **2008**, 2, 213 - 226.
- Mochida, I.; Choi, K-H. "An overview of hydrodesulfurization and hydrodenitrogenation," *Journal of the Japan Petroleum Institute*, **2004**, 47, 3, 145 - 164.
- Moreno-Castilla, C.; López-Ramón, M.; Carrasco-Marin., "Changes in surface chemistry of activated carbons by wet oxidation," *Carbon*, **2000**, 38, 1995 - 2001.
- Murata, K.; Hirahara, K.; Yudasaka, M.; Iijima, S.; Kasuya, D.; Kaneko, K. "Nanowindow-induced molecular sieving effect in a single-wall carbon nanohorn," *Journal of Physical Chemistry B*, **2002**, 106, 12668 - 12669.
- Murata, K.; Kaneko, K.; Steele, W.; Kokai, F.; Takahashi, K.; Kasuya, D.; Hirahara, K.; Yudasaka, M.; Iijima, S. "Molecular potential structures of heat-treated single-wall carbon nanohorn assemblies," *Journal of Physics and Chemistry B*, **2001**, 105, 10210 - 10216.
- Murata, K.; Miyawaki, J.; Yudasaka, M.; Iijima, S.; Kaneko, K. "High-density of methane confined in internal nanospace of single-wall carbon nanohorns," *Carbon*, **2005**, 43, 2817 - 2833.
- Murthy, N.; Minor, H. "General procedure for evaluating amorphous scattering and crystallinity from X-ray diffraction scans of semicrystalline polymers," *Polymer*, **1990**, 31, 996 - 1002.
- Nakamura, M.; Tahara, Y.; Ikehara, Y.; Murakami, T.; Tsuchida, K.; Iijima, S.; Waga, I.; Yudasaka, M. "Single-walled carbon nanohorns as drug carriers: adsorption of prednisolone and anti-inflammatory effects on arthritis," *Nanotechnology*, **2011**, 22, 465102 - 465110.
- Nelson, N.; Levy, R. B. "The organic chemistry of hydrodenitrogenation," *Journal of Catalysis*, **1979**, 58, 3, 485 - 488.
- Ng, J.; Raites, Y. "Role of the cathode deposit in the carbon arc for the synthesis of nanomaterials," *Carbon*, **2014**, 77, 80 - 88.

- Nisha, J.; Yudasaka, M.; Bandow, S.; Kokai, F.; Takahashi, K.; Iijima, S. "Adsorption and catalytic properties of single-wall carbon nanohorns," *Chemical Physics Letters*, **2000**, 328, 381 - 386.
- Okamoto, Y.; Breyse, M.; Dhar, M.; Song, C. "Effect of support in hydrotreating catalysis for ultra clean fuels," *Catalysis Today*, **2003**, 86, 1 - 3.
- Pagona, G.; Mountrichas, G.; Rotas, G.; Karousis, N.; Pipas, S.; Tagmatarchis, N. "Properties, applications and functionalization of carbon nanohorns," *International Journal of Nanotechnology*, **2009**, 6, 176 - 195.
- Pagona, G.; Tagmatarchis, N.; Fan, J.; Yudasaka, M.; Iijima, S. "Cone-end functionalization of carbon nanohorns," *Chemistry of Materials*, **2006**, 18, 3918 - 3920.
- Park, S.; Meng, L. "Carbon Fibers: Surface treatment and sizing of carbon fibers," *Springer series in material science*, **2015**, 4, 210, 101 - 133.
- Park, Y. C.; Oh, E. S.; Rhee, H. K. "Characterization and catalytic activity of WNiMo/Al₂O₃ catalyst for hydrodenitrogenation of pyridine," *Industrial & Engineering Chemistry Research*, **1997**, 36, 5083 – 5089.
- Pawelec, B.; Navarro, R. M.; Campos-Martin, J. M.; Fierro, J. L. G. "Towards near zero-sulfur liquid fuels: A perspective review," *Catalysis Science & Technology*, **2011**, 1, 23 – 42.
- Penner-Hahn, J. "2.13 - X-ray absorption spectroscopy," *Comprehensive Coordination Chemistry II*, **2003**, 159 - 186.
- Perot, G. "Hydrotreating catalysts containing zeolites and related materials-mechanistic aspects related to deep desulfurization," *Catalysis Today*, **2003**, 86, 111 - 128.
- Pickering, I.; Brown, G.; Tokunaga, T. "Quantitative speciation of selenium in soils using x-ray absorption spectroscopy," *Environmental Science & Technology*, **1995**, 29, 2456 – 2459.
- Poonjarernsilp, C.; Sano, N.; Charinpanitkul, T.; Mori, H.; Kikuchi, T.; Tamon, H. "Single-step synthesis and characterization of single-walled carbon nanohorns hybridized with Pd nanoparticles using N₂ gas-injected arc-in-water method," *Carbon*, **2011**, 49, 4920 – 4927.
- Prado, G.; Rao, Y.; de Klerk, A. "Nitrogen removal from oil: A review," *Energy Fuels*, **2017**, 31, 14 - 36.

- Prasek, J.; Drbohlavova, J.; Chomoucka, J.; Hubalek, J.; Jasek, O.; Vojtech, A.; Kizek, R. "Methods for carbon nanotube synthesis-review," *Journal of Materials Chemistry*, **2011**, 21, 15872 - 15884.
- Prins, R.; de Beer, V.; Somorjai, G. "Structure and function of the catalyst and the promoter in Co-Mo hydrodesulfurization catalysts," *Catalysis Review Science and Engineering*, **1989**, 31, 1 - 41.
- Prins, R.; Egorova, M.; Rothlisberger, A.; Zhao, Y.; Sivasankar, N.; Kukula, P. "Mechanisms of hydrodesulfurization and hydrodenitrogenation," *Catalysis Today*, **2006**, 84 - 93.
- Prins, R.; Jian, M.; Flechsenhar, M. "Mechanism and kinetics of hydrodenitrogenation," *Polyhedron*, **1997**, 16, 3235 - 3246.
- Probst, K.; Wohlfahrt, K. "Empirical estimate of effective diffusion coefficients in porous systems," *Chemie Ingenieur Technik*, **1979**, 51, 737 - 738.
- Purohit, R.; Purohit, K.; Rana, S.; Rana, R.; Patel, V. "Carbon nanotubes and their growth methods," *Procedia Materials Science*, **2014**, 6, 716 - 728.
- Qu, L. L.; Zhang, W. P.; Kooyman, P. J.; Prins, R. "MAS NMR, TPR, and TEM studies of the interaction of NiMo with alumina and silica-alumina supports," *Journal of Catalysis*, **2003**, 215, 1, 7 - 13.
- Quanli, Z.; Bing, Z.; Jian, Y.; Jiabin, W.; Jun, Z.; Shengfu, J.; Hanqing, W. "The promotion of nickel to Mo₂C/Al₂O₃ catalyst for the partial oxidation of methane to syngas," *New Journal of Chemistry*, **2003**, 27, 1633.
- Radhakrishnan, R.; Reed, C.; Oyama, S.; Seman, M.; Kondo, J.; Domen, K.; Ohminami, Y.; Asakura, K. "Variability in the structure of supported MoO₃ catalysts: Studies using Raman and X-ray absorption spectroscopy with ab initio calculations," *The Journal of Physical Chemistry B*, **2001**, 105, 8519 - 8530.
- Raffi-Tabar, H. "Computational modeling of thermo-mechanical and transport properties of carbon nanotubes," *Physics Reports*, **2004**, 390, 235 - 452.
- Rajagopal, S.; Marini, H.; Marzari, J.; Miranda, R. "Silica-alumina-supported acidic molybdenum catalysts-TPR and XRD characterization," *Journal of Catalysis*, **1994**, 147, 417 - 428.

- Ramírez, L.; Escobar, J.; Galván, E.; Vaca, H.; Murrieta, F.; Luna, M. "Evaluation of diluted and undiluted trickle-bed hydrotreating reactor with different catalyst volume," *Petroleum Science and Technology*, **2004**, 22, 157 – 175.
- Rana, M.; Sámano, V.; Ancheyta, J.; Diaz, J. "A review of recent advances on process technologies for upgrading of heavy oils and residua," *Fuel*, **2007**, 1216 - 1231.
- Rehr, J.; Albers, R. "Theoretical approaches to X-ray absorption fine structure," *Reviews of Modern Physics*, **2000**, 72, 3, 62 - 654.
- Reid, R.; Prausnitz, J.; Poling, B. "The properties of gases and liquids," New York, McGraw-Hill, **1987**.
- Ren, Z.; Lan, Y.; Wang, Y. "Introduction to carbon. In: Aligned carbon nanotubes" *Nanoscience and Technology*. Springer, Berlin, Heidelberg, Chapter 1, **2012**, 1 - 5.
- Robinson, P. R.; Dolbear, G. E. "Hydrotreating and hydrocracking: Fundamentals," In: Hsu C.S., Robinson P.R. (eds) *Practical Advances in Petroleum Processing*. Springer, New York, **2006**, 177 - 218.
- Rodriquez-Reinoso, F. "The role of carbon materials in heterogenous catalysis," *Carbon*, **1998**, 36, 159 - 175.
- Roy, D.; Chhowalla, M.; Wang, H.; Sano, N.; Alexandrou, I.; Clyne, T.; Amaratunga, G. "Characterization of carbon nano-onions using Raman spectroscopy," *Chemical Physics Letters*, **2003**, 373, 52 - 56.
- Sadhukhan, B.; Mondal, N.; Chatteraj, S. "Optimisation using central composite design (CCD) and the desirability function for sorption of methylene blue from aqueous solution onto Lemna major," *Karbala International Journal of Modern Science*, **2016**, 2, 145 – 155.
- Sajkowski, D. J.; Miller, J. T.; Zajac; G. W.; Morrison, T. I.; Chen, H. and Fazzini, D. R. "Phosphorus promotion of Mo/Al₂O₃ hydrotreating catalysts," *Applied Catalysis*, **1990**, 62, 205 - 220.
- Saito, Y.; Yoshikawa, T.; Inagaki, M.; Tomita, M.; Hayashi, T. "Growth and structure of graphitic tubules and polyhedral particles in arc-discharge," *Chemical Physics Letters*, **1993**, 204, 3-4, 277 - 282.
- Sakanishi, K.; Nagamatsu, T.; Mochida, I.; Whitehurst, D. "Hydrodesulfurization kinetics and mechanism of 4, 6-dimethyldibenzothiophene over NiMo catalyst supported on

- carbon,” *Journal of Molecular Catalysis A: Chemical*, **2000**, 155, 101 - 109.
- Sánchez-Delgado, R. A. “Hydrodesulfurization and hydrodenitrogenation. In: Organometallic modeling of the hydrodesulfurization and hydrodenitrogenation reactions,” *Catalysis by Metal Complexes*, Springer Netherlands, **2002**, 24, 1 - 34.
- Sano, N. “Low-cost synthesis of single-walled carbon nanohorns using the arc in water method with gas injection,” *Journal of Physics D: Applied Physics*, **2004**, 37, L17 - L20.
- Sano, Y.; Choi, K.; Korai, Y.; Mochida, I. “Adsorptive removal of sulfur and nitrogen species from a straight run gas oil over activated carbons for its deep hydrodesulfurization,” *Applied Catalysis B: Environmental*, **2004**, 49, 219 - 225.
- Sano, N.; Kikuchi, T.; Wang, H.; Chhowalla, M.; Amaratunga, G. “Carbon nanohorns hybridized with a metal-included nanocapsule,” *Carbon*, **2004**, 42, 95 - 99.
- Sano, N.; Kimura, Y.; Suzuki, T. “Synthesis of carbon nanohorns by a gas-injected arc-in-water method and application to catalyst-support for polymer electrolyte fuel cell electrodes,” *Journal of Materials Chemistry*, **2008**, 18, 1555 - 1560.
- Sano, N.; Kinugasa, M.; Otsuki, F.; Suehiro, J. “Gas sensor using single-wall carbon nanohorns,” *Advanced Powder Technology*, **2007**, 18, 455 - 466.
- Sano, N.; Ukita, S. “One-step synthesis of Pt-supported carbon nanohorns for fuel cell electrode by arc plasma in liquid nitrogen,” *Materials chemistry and physics*, **2006**, 99, 447 – 450.
- Sano, N.; Wang, H.; Chhowalla, M.; Teo, K.; Amaratunga, G. “Properties of carbon onions produced by an arc discharge in water,” *Journal of Applied Physics*, **2002**, 92, 2783 – 2788.
- Sano, N.; Yoshihiro, A.; Tamon, H. “Effects of synthesis conditions on the structural features and methane adsorption properties of single-walled carbon nanohorns prepared by a gas-injected arc-in-water method,” *Journal of Applied Physics*, **2011**, 109, 124305 – 124309.
- Sano, Y.; Choi, K.; Korai, Y.; Mochida, I. “Effects of nitrogen and refractory sulfur species removal on the deep HDS of gas oil,” *Applied Catalysis Environmental*, **2004**, 53, 169 - 174.
- Sarrin, J.; Noguera, O.; Royo, H.; Perez, Z. M. J.; Scott, C.; Goldwasser, M. R.; Goldwasser, J.; Houalla, M. “Effect of the preparation method on the reducibility of molybdena-

- alumina catalysts,” *Journal of Molecular Catalysis A: Chemical*, **1999**, 144, 3, 441 – 450.
- Satterfield, C. “Heterogeneous catalysis in industrial practice,” McGraw-Hill, New York, 2nd ed, **1991**.
- Satterfield, C.; Cocchetto, J. “Reaction network and kinetics of the vapor-phase catalytic hydrodenitrogenation of quinolone,” *Industrial and Engineering Chemistry Process and Development*, **1981**, 20, 53 - 62.
- Satterfield, C.; Modell, M.; Wilkens, J. “Simultaneous catalytic hydrodenitrogenation of pyridine and hydrodesulfurization of thiophene,” *Industrial and Engineering Chemistry Process Design and Development*,” **1980**, 19, 154 - 160.
- Satterfield, C.; Pelosof, A.; Sherwood, T. “Mass transfer limitations in trickle bed reactor,” *American Institute of Chemical Engineers Journal*, **1969**, 15, 224 - 226.
- Scheffer, B.; van Oers, E.; Arnoldy, P.; de Beer, V.; Moulijn, J. “Sulfidability and HDS activity of Co-Mo/Al₂O₃ catalysts,” *Applied Catalysis*, **1986**, 25, 303 - 311.
- Sedaghat, H.; Azizmohammadi, S.; & Matthäi, K. “Numerical investigation of fracture-rock matrix ensemble saturation functions and their dependence on wettability. *Journal of Petroleum Science and Engineering*, **2017**, 159, 869 - 888.
- Segawa, K.; Soeya, T.; Kim, D. “Supported Molybdenum oxide catalyst-Structure and chemistry of oxidized, reduced and sulfide surfaces,” *Journal of Japan Petroleum Institute*, **1990**, 33, 347 - 358.
- Serp, P.; Corrias, M.; Kalck, P. “Review. Carbon nanotubes and nanofibers in catalysis” *Applied Catalysis, A: General*, **2003**, 253, 337 - 358.
- Shan, S.; Liu, H.; Shi, G.; Bao, X. “Tuning of the active phase structure and hydrofining performance of alumina-supported tri-metallic WMoNi catalysts via phosphorus incorporation,” *Frontiers of Chemical Science and Engineering*, **2018**, 12, 59 - 69.
- Shang, H.; Liu, C.; Xu, Y.; Qiu, J.; Wei, F. “States of carbon nanotube supported Mo-based HDS catalysts,” *Fuel Processing Technology*, **2007**, 88, 117 - 123.
- Shi, W.; Cai, X.; Wei, J.; Ma, J.; Hu, T.; Wu, N.; et al. “EXAFS study of molybdenum oxide on the structure Al₂O₃,” *Surface and Interface Analysis*, **2001**, 32, 202 - 204.
- Shields, J.E.; Lowell, S.; Thomas, M.A.; Thommes, M. “Characterization of porous solids and powders: Surface area, pore size and density,” Kluwer Academic Publisher: Boston,

MA, USA, **2004**, 43 – 45.

- Shimada, H.; Matsubayashi, N.; Sato, T.; Yoshimura, Y., Nishijima, A.; Kosugi, N. “XAFS study of molybdenum oxide catalysts on various support,” *Journal of Catalysis*, **1992**, 138, 746 - 749.
- Shinke, K.; Ando, K.; Koyama, T.; Takai, T.; Nakaji, S.; Ogino, T. “Properties of various carbon nanomaterial surfaces in bilirubin adsorption,” *Colloids and Surfaces B: Biointerfaces*, **2010**, 77, 18 - 21.
- Shu, Y.; Oyama, S. “Synthesis, characterization and hydrotreating activity of carbon-supported transition metal phosphides,” *Carbon*, **2005**, 43, 1517 - 1532.
- Shuihua, T.; Gongquan, S.; Jing, Q.; Shiguo, S.; Junsong, G.; Qin, X.; Haarberg, G. “Review of new carbon materials as catalyst supports in direct alcohol fuel cells,” *Chinese Journal of Catalysis*, **2010**, 31, 12 - 17.
- Sigurdson, S. “Hydrotreating of light gas oil using carbon nanotube supported NiMoS catalysts: Influence of pore diameters,” *Masters Thesis, University of Saskatchewan*, **2009**.
- Sigurdson, S.; Sundaramurthy, V.; Dalai, A.; Adjaye, J. “Effect of anodic alumina pore diameter variation on template-initiated synthesis of carbon nanotube catalyst supports,” *Journal of Molecular Catalysis A: Chemical*, **2009**, 306, 23 - 32.
- Sigurdson, S.; Sundaramurthy, V.; Dalai, A. K.; Adjaye, J. “Phosphorous promoted trimetallic NiMoW/ γ -Al₂O₃ sulfide catalysts,” *Journal of Molecular Catalysis A: Chemical*, **2008**, 291, 30 - 37.
- Sim, W.J.; Daubert, T. E. “Prediction of vapour-liquid equilibria of undefined mixtures,” *Industrial and Engineering Chemistry Process Design and Development*, **1980**, 19, 386 - 393.
- Sing, K.; Everett, D.; Haul, R.; Moscou, L.; Pierotti, R.; Rouquerol, J.; Siemieniowska, T. “Reporting physisorption data for gas/solid systems with special reference to the determination of surface area and porosity,” *Pure and Applied Chemistry*, **1985**, 57, 603 - 619.
- Sing, K.; Everett, D.; Haul, R.; Moscou, L.; Pierotti, R.; Rouquerol, J.; Siemieniowska, T. “Reporting physisorption data for gas/solid systems,” *Handbook of Heterogeneous Catalysis*, **2008**.
- Somanathan, T.; Pandurangan, A. “Towards the low temperature growth of uniform diameter

- multi walled carbon nanotubes by catalytic chemical vapour deposition technique,” *Nano-Micro Letters*, **2010**, 2, 204 - 212.
- Song, C. “Influence of pore structure and chemical properties of supported Mo catalysts on their performance in upgrading heavy coal liquids,” *Energy & Fuels*, **1992**, 6, 619 - 628.
- Spevack, P. A.; McIntyre, N. S. “Thermal reduction of MoO₃,” *Journal of Physical Chemistry* **1992**, 96, 22, 9029 - 9035.
- Spojakina, A.; Damyanova, S.; Petrov, L. “Effect of phosphorus on the surface state of alumina-supported nickel-molybdenum catalysts for hydrodesulphurization,” *Applied Catalysis*, **1989**, 56, 163 - 176.
- Stach, E. A. “Real-time observations with electron microscopy,” *Materials Today*, **2008**, 11, 50 - 58.
- Stagg-Williams, S.; Noronha, F.; Fendley, G.; Resasco, D. “CO₂ reforming of CH₄ over Pt/ZrO₂ catalysts promoted with La and Ce oxides,” *Journal of Catalysis*, **2000**, 194, 240 - 249.
- Stanislaus, A.; Cooper, B. “Aromatic hydrogenation catalysis: A review,” *Catalysis Reviews*, **1994**, 36, 75 - 123.
- Stanislaus, A.; Marafi, A.; Rana, M. “Recent advances in the science and technology of ultra low sulfur diesel (ULSD) production,” *Catalysis Today*, **2010**, 153, 1 - 68.
- Stein, A.; Wang, Z.; Fierke, M. A. “Functionalization of porous carbon materials with designed pore architecture” *Advance materials*, **2009**, 21, 265 - 293.
- Stobinski, L.; Lesiak, B.; Kövér, L.; Tóth, J.; Biniak, S.; Trykowski, G.; Judek, J. “Multiwall carbon nanotubes purification and oxidation by nitric acid studied by the FTIR and electron spectroscopy methods,” *Journal of Alloys and Compounds*, **2010**, 501, 1, 77 - 84.
- Takikawa, H.; Ikeda, M.; Hirahara, K.; Hibi, Y.; Tao, Y.; Ruiz, P. Jr.; Sakakibara, T.; Itoh, S.; Iijima, S. “Fabrication of single-walled carbon nanotubes and nanohorns by means of a torch arc in open air,” *Physica B: Condensed Matter*, **2002**, 323, 277 - 279.
- Tanaka, A.; Umeda, K.; Yudasaka, M.; Suzuki, M.; Ohana, T.; Yumura, M.; Iijima, S. “Friction and wear of carbon nanohorn-containing polyimide composites,” *Tribology Letters*, **2005**, 19, 135 - 142.
- Tang, D.; Sun, L.; Zhou, J.; Zhou, W.; Xie, S. “Two possible emission mechanisms involved in the arc discharge method of carbon nanotube preparation,” *Carbon*, **2005**, 43, 2812 -

2816.

- Tao, X.; Zhang, X.; Cheng, J.; Liu, F. "Synthesis and characterization of Cu filled carbon nanohorns," *Materials Chemistry and Physics*, **2007**, 104, 210 - 214.
- Teng, J.; Tang, T. "IR study on surface chemical properties of catalytic grown carbon nanotubes and nanofibers," *Journal of Zhejiang University Science A*, **2008**, 9, 720 – 726.
- Ternero-Hidalgo, J.; Rosas, J.; Palomo, J.; Valero-Romero, M.; Rodríguez-Mirasol, J.; Cordero, T. "Functionalization of activated carbons by HNO₃ treatment: Influence of phosphorus surface groups," *Carbon*, **2016**, 101, 409 - 419.
- Titirici, M.-M.; Antonietti, M. "Chemistry and materials options of sustainable carbon materials made by hydrothermal carbonization," *Chemical Society Reviews*, **2010**, 39, 103 – 116.
- Thomé, A.; Peters, S.; Roessner, F. "iTPR- a new methodical approach for temperature programmed reduction of catalysts with improved sensitivity," *Catalysis Communications*, **2017**, 97, 10 - 13.
- Tong-na, Z.; Hai-liang, Y.; Shu-na, H.; Yong-ming, C.; Yun-qi, L.; Chen-guang, L. "Influences of different phosphorus contents on NiMoP/Al₂O₃ hydrotreating catalysts," *Journal of Fuel Chemistry and Technology*, **2009**, 37, 330 - 334.
- Topsoe, H.; Clausen, B.; Massoth, F. "Hydrotreating Catalysis, In: Anderson, J.; Boudart, M.; (Eds)," *Catalysis Science and Technology*, **1996**, 11, 1 - 269.
- Treacy, M.; Kilian, J. "Designability of graphitic cones," *Materials Research Society Symposium Proceedings*, **2001**, 675, W2.6.1 - W2.6.6.
- Trytten, L.C.; Gray, M.R.; Emerson, C.S. "Hydroprocessing of narrow-boiling gas oil fractions: dependence of reaction kinetics on molecular weight," *Industrial and Engineering Chemistry Research*, **1990**, 29, 725 - 730.
- Tu, Q.; Chang, C. "Diagnostic applications of Raman spectroscopy. Nanomedicine: Nanotechnology," *Biology and Medicine*, **2010**, 8, 5, 545 - 558.
- Usman,U.; Kubota, T.; Hiromitsu, I.; Okamoto, Y. "Effect of boron addition on the surface structure of Co-Mo/Al₂O₃ catalysts," *Journal of Catalysis*, **2007**, 247, 78 - 85.

- Utsumi, S.; Honda, H.; Hattori, Y.; Kanoh, H.; Takahashi, K.; Sakai, H.; Abe, M.; Yudasaka, M.; Iijima, S. "Direct evidence on C-C single bonding in single-wall carbon nanohorn aggregate," *The Journal of Physical Chemistry C Letters*, **2007**, 111, 5572 - 5575.
- Utsumi, S.; Miyawaki, J.; Tanaka, H.; Hattori, Y.; Itoi, T.; Ichikuni, N.; Kanoh, H.; Yudasaka, M.; Iijima, S.; Kaneko, K. "Opening mechanism of internal nanoporosity of single-wall carbon nanohorn," *The Journal of Physical Chemistry B*, **2005**, 109, 14319 - 14324.
- Valavarasu, G.; Bhaskar, M., Balaraman, K., "Mild Hydrocracking - a review of catalytic dewaxing," *Petroleum Science and Technology*, **2003**, 21, 1185 - 1205.
- Van Oversteeg, C.; Doan, H.; de Groot, F.; Cuk, T. "In situ X-ray absorption spectroscopy of transition metal based water oxidation catalysts," *Chemical Society Reviews*, **2017**, 46, 102 - 125.
- Van Veen, J.; Colijn, H.; Hendriks, P.; van Welsenens, A. "On the formation of type I and type II NiMoS phases in NiMo/Al₂O₃ hydrotreating catalysts and its catalytic implications," *Fuel Processing Technology*, **1993**, 35, 137 - 157.
- Vasu, K.; Pramoda, K.; Moses, K.; Govindaraj, A.; Rao, C. N. R. "Single-walled nanohorns and other nanocarbons generated by submerged arc discharge between carbon electrodes in liquid argon and other media," *Materials Research Express*, **2013**, 1, 1, 015001 – 0150013.
- Vissers, J.; Lensing, T.; de Beer, V.; Prins, R. "Carbon black composites as carrier materials for sulphide catalysts," *Applied Catalysis*, **1987**, 30, 21 - 31.
- Vissers, J.; Scheffer, B.; de Beer, V.; Moulijn, J.; Prins, R. "Effect of the support on the structure of Mo-based hydrodesulfurization catalysts: activated carbon versus alumina," *Journal of Catalysis*, **1987**, 105, 277 - 284.
- Vogelaar, B.; Eijsbouts, S.; Bergwerff, J.; Heiszwolf, J. "Hydroprocessing catalyst deactivation in commercial practice," *Catalysis Today*, **2010**, 154, 256 - 263.
- Walendziewski, J. "Properties and hydrodesulfurization activity of cobalt-molybdenum-phosphorus-alumina catalysts" *Reaction Kinetics and Catalysis Letters*, **1991**, 43, 107 - 113.
- Wang, H.; Chhowalla, M.; Sano, N.; Jia, S.; Amaratunga, G. "Large-scale synthesis of single-walled carbon nanohorns by submerged arc," *Nanotechnology*, **2004**, 15, 546 - 550.

- Wang, J.; Zhao, Y.; Niu, J. "Preparation of graphitic carbon with high surface area and its application as an electrode material for fuel cells," *Journal of Materials Chemistry*, **2007**, 17, 2251 - 2256.
- Wang, X.; Li, N.; Pfefferle, L.; Haller, G. "Pt-Co bimetallic catalyst supported on single-walled carbon nanotubes: effect of alloy formation and oxygen containing groups," *Journal of Physical Chemistry C*, **2010**, 114, 16996 - 17002.
- Wang, Z.; Fu, J.; Deng, Y.; Duan, A.; Zhao, Z.; Jiang, G.; Liu, J.; Wei, Y.; Zhao, S. "Synthesis of aluminum-modified 3D mesoporous TUD-I materials and their hydrotreating performance of FCC diesel," *The Royal Society of Chemistry*, **2015**, 5, 5221 - 5230.
- Wen, L.; Deng, L.; Zhou, M.; Guo, S.; Shang, L.; Xu, G.; Dong, S. "A biofuel cell with a single-walled carbon nanohorn-based bioanode operation at physiological condition," *Biosensors and Bioelectronics*, **2010**, 25, 1544 - 1547.
- Wharton, J.; Ross, D.; Treacy, G.; Wilcox, G.; Baldwin, K. "An EXAFS investigation of molybdate-based conversion coatings," *Journal of Applied Electrochemistry*, **2003**, 33, 553 - 561.
- Wijngaarden, R. J.; Kronberg, A.; Westerterp, K. R. "Industrial catalysis: Optimizing catalysts and processes," Weinheim; Chichester: Wiley-VCH, **1998**.
- Wilhelm, S. M. "Mercury in petroleum and natural gas: estimation of emissions from production, processing and combustion," Office of Air Quality Planning Standards, **2001**.
- Wilke, C. R.; Chang, P. "Correlation of diffusion coefficients in dilute solutions", *Chemical Engineering Progress*, **1955**, 1, 264 - 270.
- Xia, Z.; Fu, J.; Duan, A.; Han, L.; Wu, H.; Zhao, Z.; Chunming Xu C.; Wang, D.; Wang B.; Meng, Q. "Post synthesis of aluminum modified mesoporous TUD-1 materials and their application for FCC diesel hydrodesulfurization catalysts," *Catalysts*, **2017**, 141, 1 – 20.
- Xiao, B.; Thomas, K. "Competitive adsorption of aqueous metal ions on an oxidized nanoporous activated carbon," *Langmuir*, **2004**, 20, 4566 - 4578.
- Xing, G.; Shen-li, J.; Zong-qian, S. "The production of carbon nano-materials by arc discharge under water or liquid nitrogen," *New Carbon Materials*, **2007**, 22, 337 - 341.
- Yamaguchi, T.; Bandow, S.; Iijima, S. "Synthesis of carbon nanohorn particles by simple pulsed arc discharge ignited between pre-heated carbon rods," *Chemical Physics Letters*,

2004, 389, 181 - 185.

- Yang, C.; Kim, Y.; Endo, M.; Kanoh, H.; Yudasaka, M.; Iijima, S.; Kaneko, K. "Nanowindow-regulated specific capacitance of supercapacitor electrodes of single-wall carbon nanohorns," *Journal of The American Chemical Society*, **2007**, 129, 20 -21.
- Yang, C.; Kasuya, D.; Yudasaka, M.; Iijima, S.; Kaneko, K. "Microporosity development of single-wall carbon nanohorn with chemically induced coalescence of the assembly structure," *The Journal of Physical Chemistry B*, **2004**, 108, 17775 - 17782.
- Yang, C.; Noguchi, H.; Murata, K.; Yudasaka, M.; Hashimoto, A.; Iijima, S.; Kaneko, K. "Highly ultramicroporous single-walled carbon nanohorn assemblies," *Advanced Materials*, **2005**, 17, 866 - 870.
- Yang, D.; Zhang, Q.; Chen, G.; Yoon, S.; Ahn, J.; Wang, S.; Zhou, Q.; Wang, Q.; Li, J. "Thermal conductivity of multiwalled carbon nanotubes," *Physical Review B*, **2002**, 66, 165440 - 165445.
- Yang, S. H.; Satterfield, C.N. "Some effects of sulfiding of a NiMoAl₂O₃ catalyst on its activity for hydrodenitrogenation of quinoline," *Journal of Catalysis*, **1993**, 81, 168 - 178.
- Yano, J.; Yachandra, V. "X-ray absorption spectroscopy," *Photosynthesis Research*, **2009**, 102, 241 - 254.
- Yao, S.; Zheng, Y.; Ding, L.; Ng, S.; Yang, H. "Co-promotion of fluorine and boron on NiMo/Al₂O₃ for hydrotreating light cycle oil," *Catalysis Science & Technology*, **2012**, 2, 1925 - 1932.
- Yeh, W.; Raitses, Y.; Yao, N. "Structural variations of the cathode deposit in the carbon arc," *Carbon*, **2016**, 105, 490 - 495.
- Yin, H.; Zhou, T.; Liu, Y.; Chai, Y.; Liu, C. "NiMo/Al₂O₃ catalyst containing nano-sized zeolite Y for deep hydrodesulfurization and by hydrodenitrogenation of diesel," *Journal of Natural Gas Chemistry*, **2011**, 20, 441 - 448.
- Yoshida, S.; Sano, M. "Microwave-assisted chemical modification of carbon nanohorns: oxidation and Pt deposition," *Chemical Physics Letters*, **2006**, 433, 97 - 100.
- Yoshitake, T.; Shimakawa, Y.; Kuroshima, S.; Kimura, H.; Ichihashi, T., Kubo, Y.; Kasuya, D.; Takahashi, K.; Kokai, F.; Yudasaka, M.; Iijima, S. "Preparation of fine platinum catalyst supported on single-wall carbon nanohorns for fuel cell application," *Physica B: Condensed Matter*, **2002**, 323, 124 - 126.

- Yudasaka, M.; Iijima, S.; Crespi, V. H. "Single-wall carbon nanohorns and nanocones." In Carbon Nanotubes Topics in Applied Physics. Volume 111. Edited by: Jorio, A.; Dresselhaus, G.; Dresselhaus, M. S., Berlin/Heidelberg: Springer; **2008**, 605 - 629.
- Yudasaka, M.; Kokai, F.; Takahashi, K.; Yamada, R.; Sensui, N.; Ichihashi, T.; Iijima, S. "Formation of single-wall carbon nanotubes: comparison of CO₂ laser ablation and Nd: YAG laser ablation," Journal of Physical Chemistry B, **1999**, 103, 3576 - 3581.
- Yuge, R. "Single-walled carbon nanohorns: Manufacturing, material properties and applications," Smart Energy Research Laboratories, Japan, **2008**.
- Yuge, R.; Ichihashi, T.; Miyawaki, J.; Yoshitake, T.; Iijima, S.; Yudasaka, M. "Hidden caves in an aggregate of single-wall carbon nanohorns found by using Gd₂O₃ probes," Journal of Physics and Chemistry C, **2009**, 113, 2741 - 2744.
- Yuge, R.; Ichihashi, T.; Shimakawa, Y.; Kubo, Y.; Yudasaka, M.; Iijima, S. "Preferential deposition of Pt nanoparticles inside single-walled carbon nanohorns," Advanced Materials, **2004**, 16, 1420 - 1423.
- Yuge, R.; Yudasaka, M.; Iijima, S. "Catalyst-supporting carbon nanohorn composite and process for producing same," Masako Yudasaka, Sumio Iijima, Patent #: 8093174, **2012**.
- Zecchina, A.; Lamberti, C.; Bordiga, S. "Surface acidity and basicity: General concepts," Catalysis Today, **1998**, 41, 169 - 177.
- Zeuthen, P.; Blom, P.; Massoth, F. "Characterization of nitrogen on aged hydroprocessing catalysts by temperature-programmed oxidation," Applied Catalysis, **1991**, 78, 265 - 276.
- Zeuthen, P.; Knudsen, K.; Whitehurst, D. "Organic nitrogen compounds in gas oil blends, their hydrotreated products and the importance to hydrotreatment," Catalysis Today, **2001**, 65, 307 - 314
- Zhang, D.; Ye, Kai.; Yao, Y.; Liang, F.; Qu, T.; Ma, W.; Yang, B.; Dai, Y.; Watanabe, T. "Controllable synthesis of carbon nanomaterials by direct current arc discharge from the inner wall of the chamber," Carbon, **2019**, 142, 278 - 284.
- Zhang, M.; Yudasaka, M.; Iijima, S. "Diameter enlargement of single-wall carbon nanotubes by oxidation," Journal of Physical Chemistry B, **2004**, 108, 149 - 153.

- Zhang, Q.; Huang, J.-Q.; Qian, W.-Z.; Zhang, Y.-Y.; Wei, F. "The road for nanomaterials industry: A review of carbon nanotube production, post-treatment, and bulk applications for composites and energy storage," *Small*, **2013**, 9, 1237 - 1265.
- Zhang, X.; Gao, B.; Creamer, A.; Cao, C.; Li, Y. "Adsorption of VOCs onto engineered carbon materials: A review," *Journal of Hazardous Materials*, **2017**, 338, 102 - 123.
- Zhao, S.; Hong, R.; Luo, Z.; Lu, H.; Yan, B. "Carbon nanostructures production by AC arc discharge plasma process at atmospheric pressure," *Journal of Nanomaterials*, **2011**, 346206 - 346212.
- Zhao, X.S.; Lu, G.Q.; Millar, G.J. "Advances in mesoporous molecular sieve MCM-41," *Industrial & Engineering Chemistry Research*, **1996**, 35, 2075 - 2090.
- Zhu, S.; Xu, G. "Single-walled carbon nanohorns and their applications," *Nanoscale*, **2010**, 2, 2538 - 2549.

Appendix A: Arc discharge production and filtration station

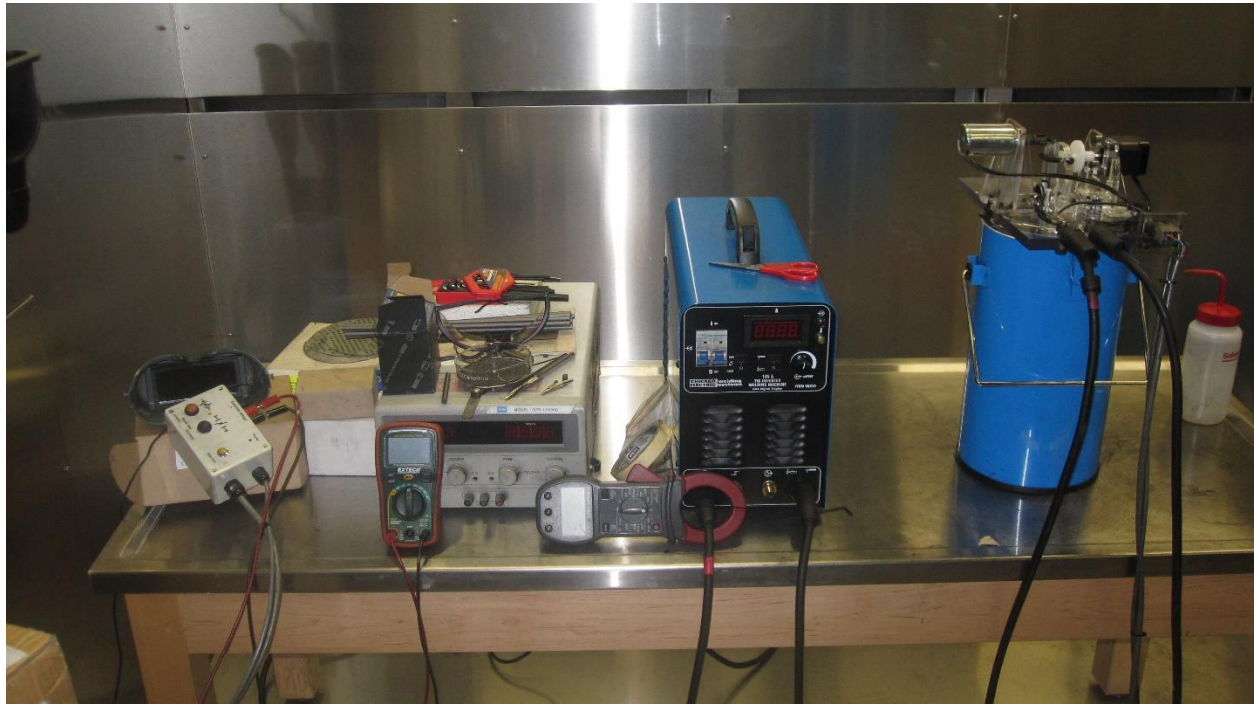


Figure A.1 Arc discharge setup and filtration area in the pilot plant.

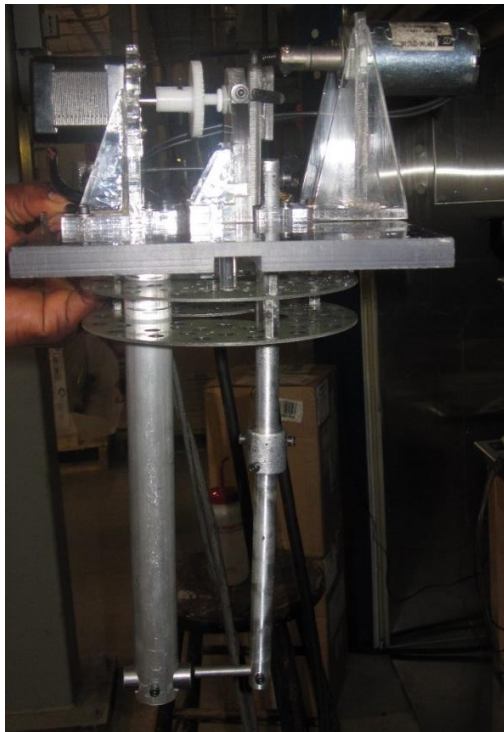


Figure A.2 Part of arc discharge setup showing mounted electrodes and some tools.

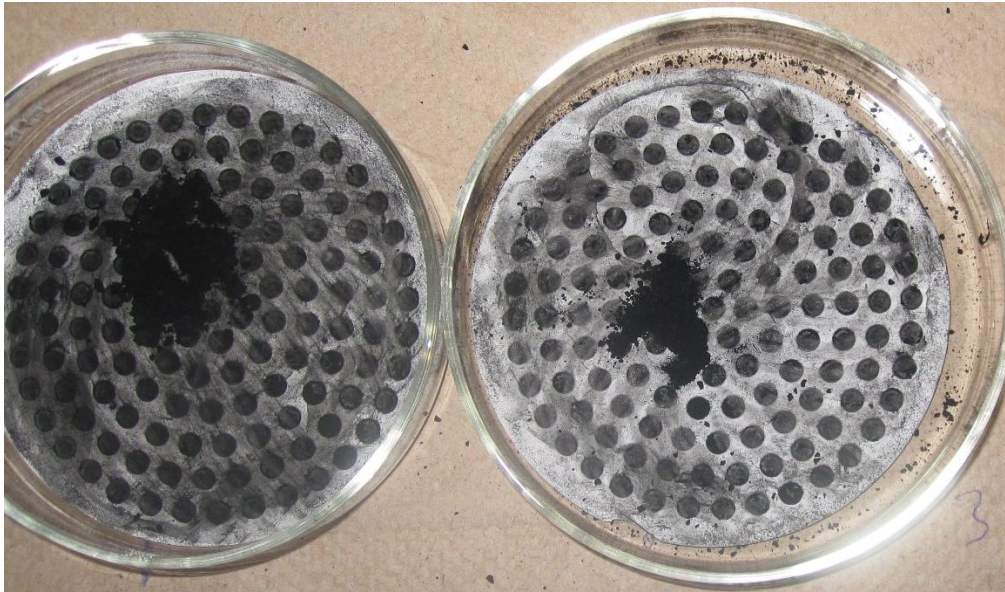
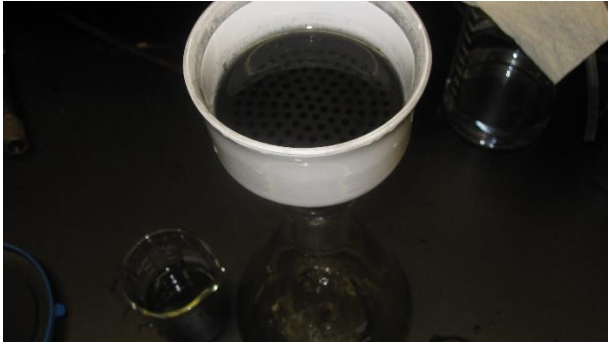


Figure A.3 Filtration, air drying of samples and sample collection.

Appendix B: Determination of best condition for OCP and OCP_f functionalization

Table B.1 Effects of functionalization on OCP (BET results).

Samples	Surface area (m ² /g)	Pore diameter (nm)	Pore Volume (cm ³ /g)
90A OCP	8 ± 2	19.4 ± 0.1	0.03 ± 0.01
90A OCP_15mins	21 ± 2	11.7 ± 0.1	0.05 ± 0.02
90A OCP_30mins	23 ± 1	11.3 ± 0.2	0.05 ± 0.01
90A OCP_1hr	23 ± 2	11.2 ± 0.1	0.04 ± 0.01
90A OCP_2hrs	21 ± 2	11.4 ± 0.1	0.04 ± 0.01
90A OCP_4hrs	27 ± 4	10.0 ± 0.2	0.06 ± 0.01

Table B.2 Effects of functionalization on OCP_f (BET results).

Samples	Surface area (m ² /g)	Pore diameter (nm)	Pore Volume (cm ³ /g)
90A OCP _f	41 ± 2	22.1 ± 0.1	0.15 ± 0.01
90A OCP _f _15mins	99 ± 2	10.5 ± 0.1	0.17 ± 0.02
90A OCP _f _30mins	177 ± 3	9.3 ± 0.2	0.19 ± 0.02
90A OCP _f _1hr	118 ± 2	7.5 ± 0.1	0.12 ± 0.01
90A OCP _f _2hrs	104 ± 2	7.8 ± 0.1	0.10 ± 0.01
90A OCP _f _4hrs	10 ± 4	6.5 ± 0.2	0.08 ± 0.01

Effects of 15 mins CNH functionalization on HDS and HDN conversions

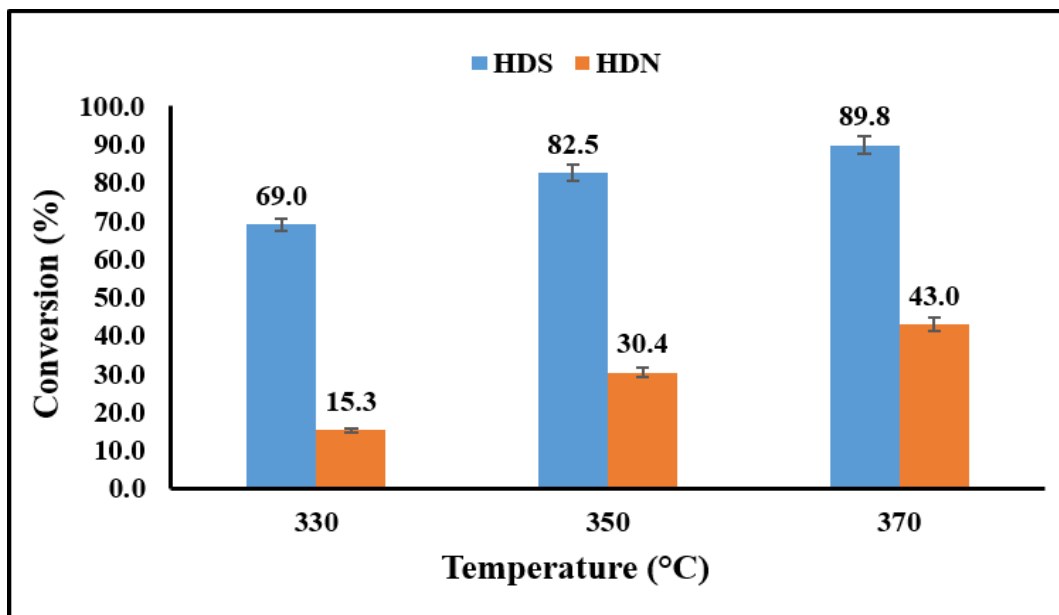


Figure B.1 HDN and HDS activities of 2.5wt%Ni13wt%Mo/CNH catalysts using LGO at 370, 350, and 330 °C (Catalyst = 5 cm³, P = 9.0 MPa, LHSV = 2 hr⁻¹, and H₂ / oil ratio = 600 (v/v)). CNH support was functionalized for 15 mins.

Comments:

- Hydrotreating was done using light gas oil and this feedstock composition was different and lower (2.7 wt% of Sulfur and 0.15 wt% Nitrogen) as compared to the composition of the light gas oil used in the main body of this thesis.
- Overall 15 mins functionalization of CNH can also be used to achieve reasonable hydrotreating performance.

Appendix C: Raman and BET results of different carbon-supported catalysts and gamma-alumina supported catalyst

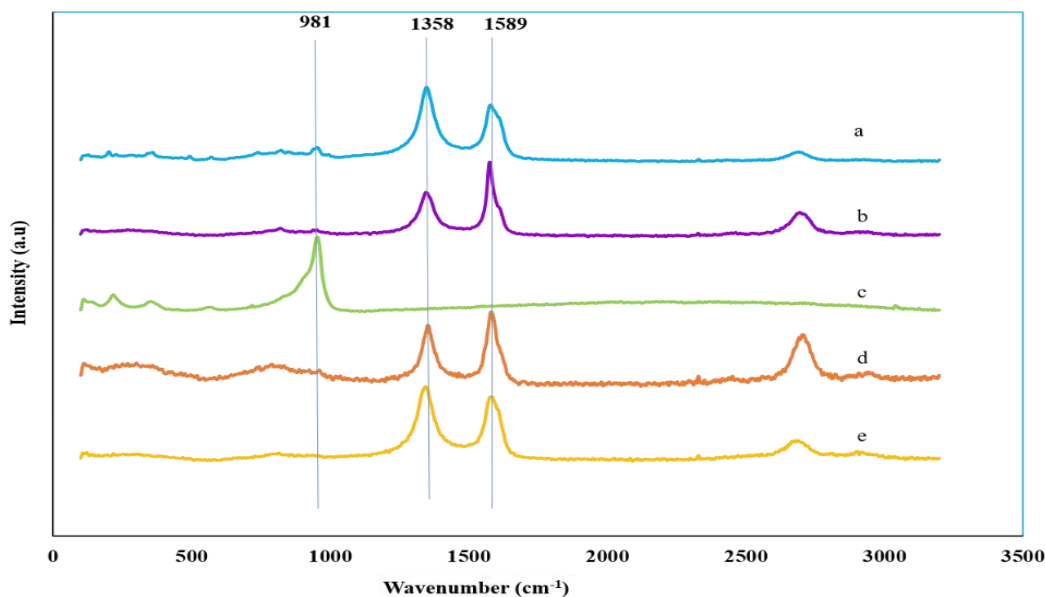


Figure C.1 Raman Spectroscopy of: a) NiMo/OCP_{f1} b) NiMo/OCP_{f2} c) NiMo/ γ Al₂O₃ d) NiMo/CNT e) NiMo/CNH.

Comments:

- These results are part of Phase 3 or Chapter 6 of the research work
- γ -Al₂O₃ catalyst showed one prominent peak at 981 cm⁻¹ attributed to Mo=O bond vibrations of the molybdenum oxide interaction with the support.
- All carbon-supported catalysts revealed two prominent bands (D and G).
- D band is of higher intensity in CNH-supported catalyst as compared to CNT-supported catalyst.
- G band is of higher intensity in CNT-supported catalyst as compared to CNH-supported catalyst.
- Raman analysis on one sample area or location of the OCP_f-supported catalyst (NiMo/OCP_{f1}) revealed a D Band, which was of higher intensity than the G band, whereas another location on the same OCP_f-supported catalyst (NiMo/OCP_{f2}) revealed a G band of higher intensity than the D band. This supports the findings that the OCP_f-supported material consists of CNH and CNT aside, the other carbon particles.

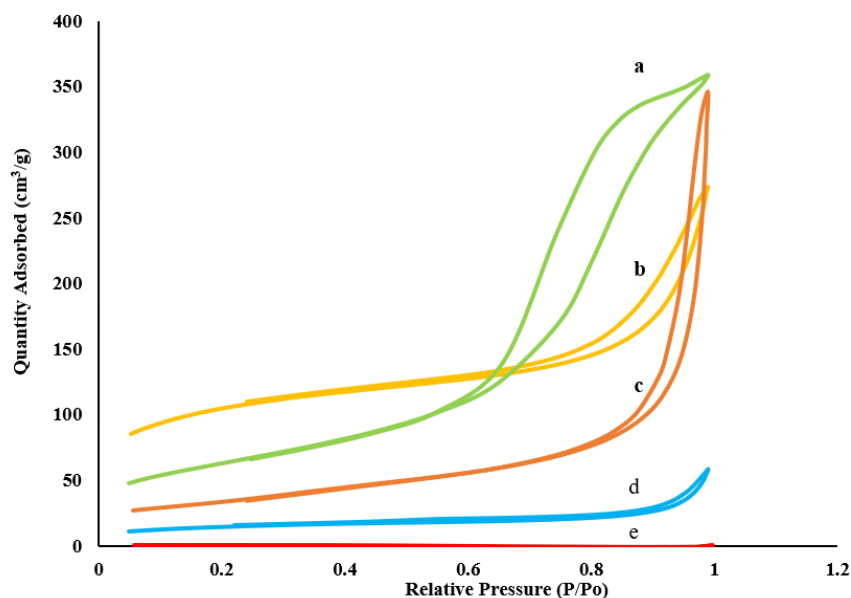


Figure C.2 Adsorption capabilities of carbon-supported catalysts and gamma-alumina supported catalyst: a) NiMo/ γ -Al₂O₃, b) NiMo/CNH, c) NiMo/CNT, d) NiMo/OCP_f, e) NiMo/OCP.

Comments:

- All catalyst samples showed the same isotherm, Type IV which is consistent with mesoporous materials. However, each sample exhibited different hysteresis loop.
- NiMo/CNH and NiMo/OCP_f showed H3 hysteresis loop.
- NiMo/ γ -Al₂O₃, exhibited H2 hysteresis loop.
- NiMo/CNT exhibited H1 hysteresis loop.
- Adsorption capability was negligible with the NiMo/OCP catalyst as such, its isotherm was flat.
- Adsorption behaviours of these catalyst would therefore differ from one another.
- The occurrence of capillary condensation in mesoporous materials leads to the formation of hysteresis loop that differ in shapes. The shape of the hysteresis loop is also associated with a unique pore structure. As a result, H1 hysteresis loop is normally linked to porous materials that comprises of agglomerates or nearly uniform compact spheres present in a fair regular arrangement and therefore have narrow pore size distribution. Type H2 loop previously has to do with the difference in condensation and evaporation process mechanisms that takes place in pores having narrow necks and wide bodies (i.e. ink bottle pores). Type H3 hysteresis loop is associated with aggregates of plate-like particles that lead to slit shaped pores whereas Type H4 hysteresis loop is related to narrow slit-like pores (Sing et al. 1985).

Appendix D: Statistical analysis

To rebuild the HDS and HDN model equations, the Pareto charts in Figure D.1 and D.2 below enabled the elimination of insignificant terms after the initial lack of fit tests for HDS and HDN experimental data had been obtained. As a result, terms lower than the Pareto threshold value of 2.23 for both HDS and HDN were dropped in rebuilding the model.

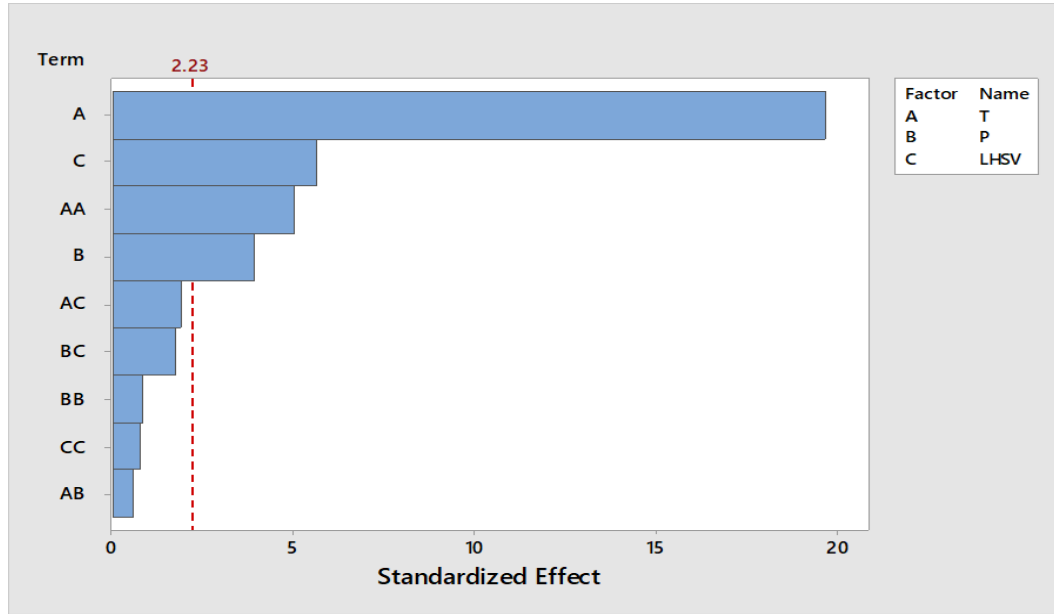


Figure D.1 Pareto Chart of the Standardized Effects (response is % Sulfur removal, $\alpha = 0.05$).

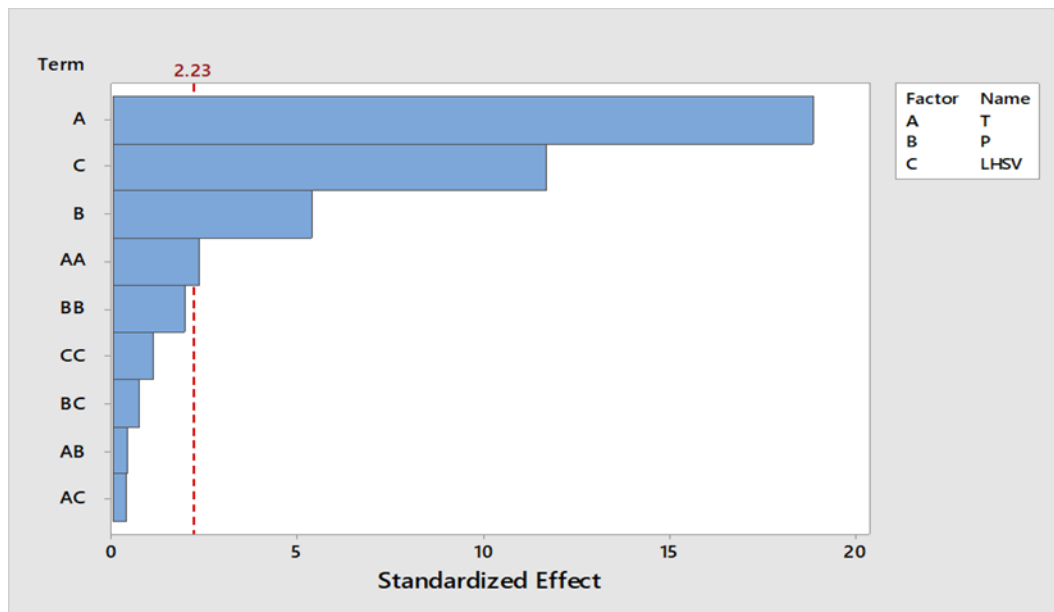


Figure D.2 Pareto Chart of the Standardized Effects (response is % Nitrogen removal, $\alpha = 0.05$).

The interaction plots in Figure D.3 and D.4 showed that there was no interaction effect between temperature and pressure as well as temperature and LHSV on both % sulfur and nitrogen removal due to the lack of cross terms. However, the interaction effect between pressure and LHSV for both % sulfur and nitrogen removal had slight impact on % sulfur and nitrogen removal. The parity plots displayed in Figure D.5 and D.6 indicates that the experimental data and predicted data are similar since the data points lie close to the line.

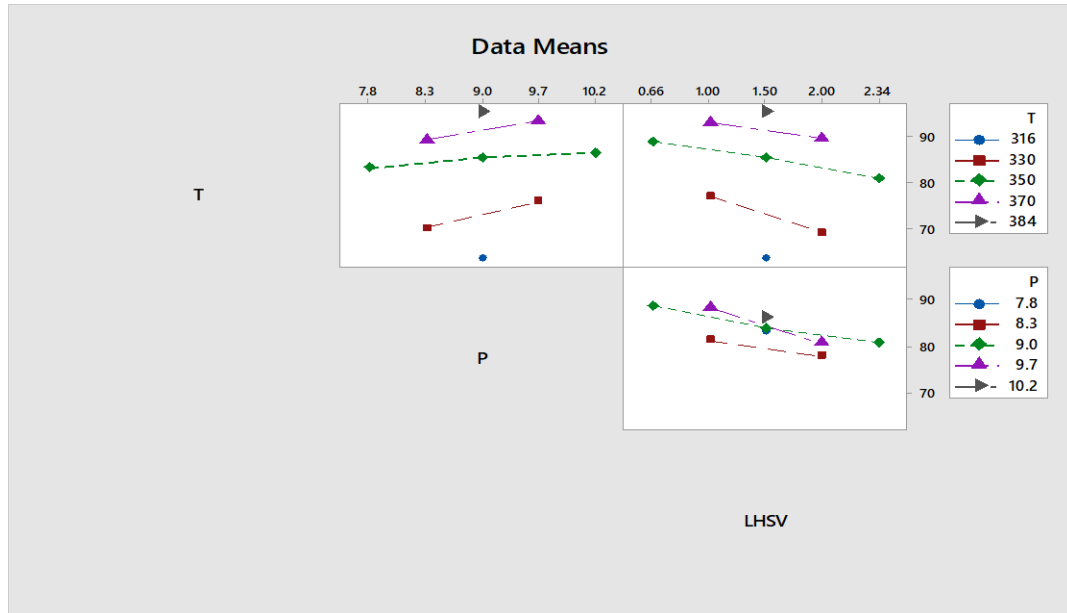


Figure D.3 Interaction plot for % sulfur removal.

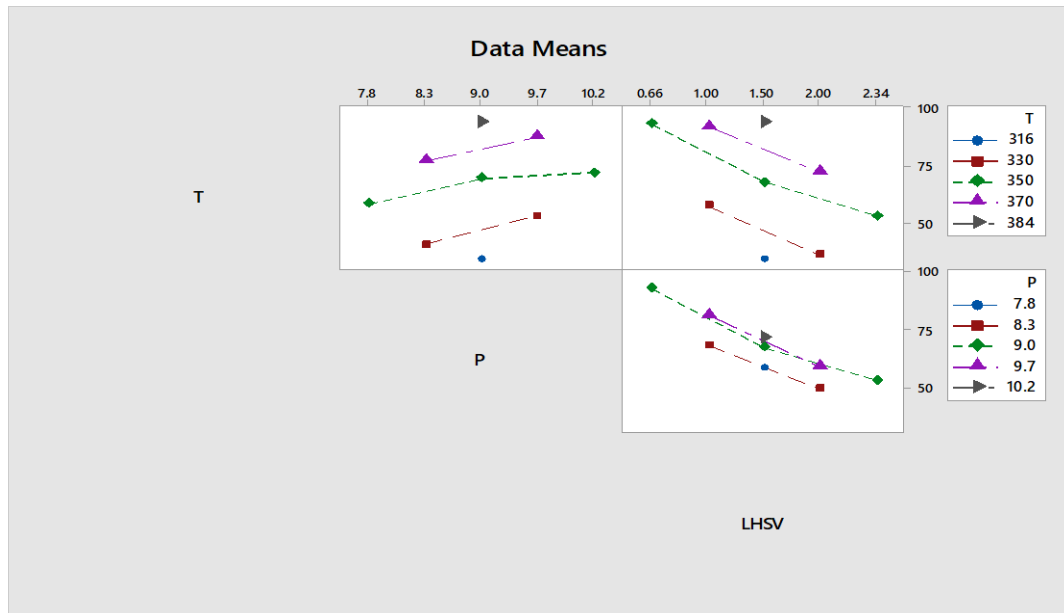


Figure D.4 Interaction plot for % nitrogen removal.

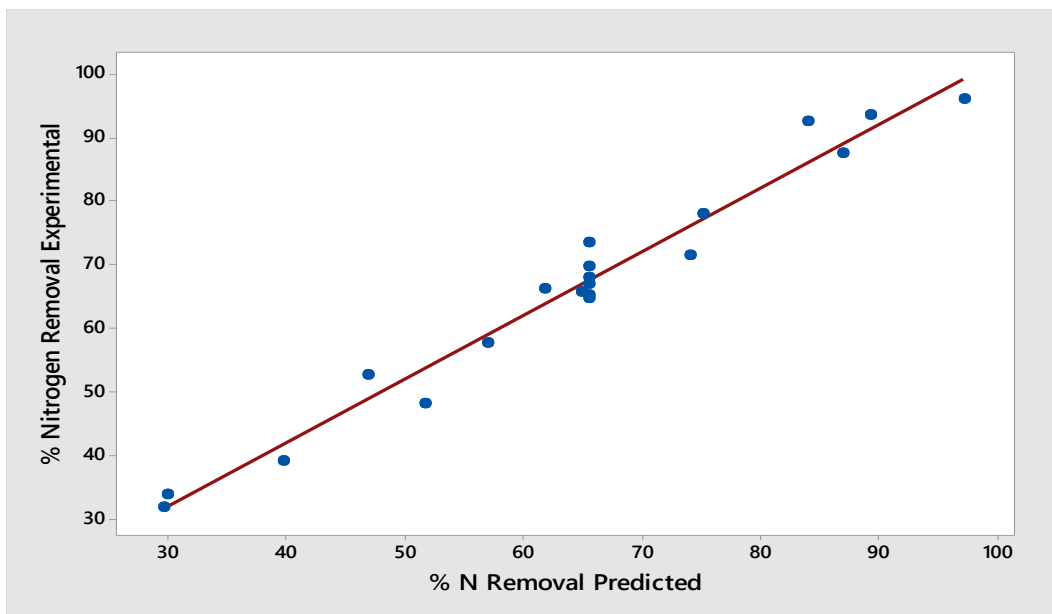


Figure D.5 Parity Plot for Sulfur Removal.

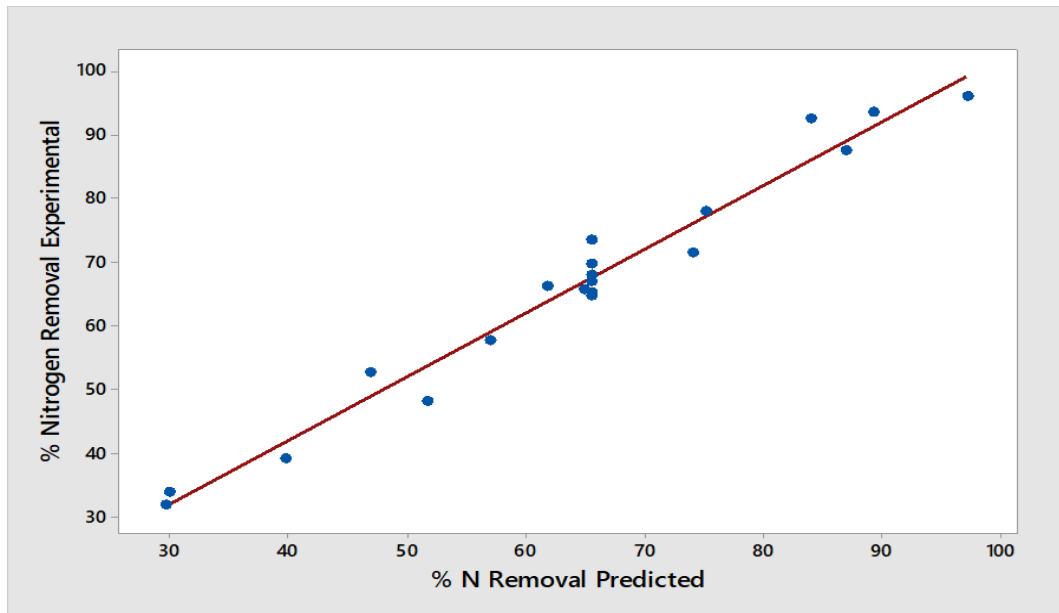


Figure D.6 Parity Plot for Nitrogen Removal.

Appendix E: Hydrodynamics calculations for hydrotreating of light gas oil using 3.5wt%Ni19wt%Mo/CNH catalyst

Back mixing

The effect of backmixing can be evaluated using a simpler form of empirical criterion below (Carberry and Wendel, 1963):

$$\frac{L_B}{d_{pe}} > 100 \quad \dots E. 1$$

where,

L = Length of the catalyst bed = 10 cm

d_{pe} = Effective catalyst particle diameter. Under undiluted conditions, d_{pe} was that of the catalyst however, under diluted case, it was assumed that d_{pe} was that of the 90 mesh particle size

Wetting efficiency

The criterion below which was proposed by Gierman, 1988 is valid for accessing the wetting efficiency:

$$\frac{\mu_L v_L}{\rho_L d_{pe}^2 g} > 5.0 \times 10^{-6} \quad \dots E. 2$$

where,

μ_L = Liquid-phase viscosity (cP) = 0.544 cP to 0.442 cP for temperature ranging from 330 °C to 370 °C

ρ_L = Liquid-phase density (g/cm³) = 0.740 to 0.756 g/cm³ for temperature ranging from 330 °C to 370 °C

g = Acceleration due to gravity (981 cm/s²)

v_L = Liquid superficial velocity (cm/s)

Wall effect

Minimum wall effects in a trickle-bed reactor can be achieved using the criterion in Equation E.3 (Chuzf and Ng, 1989):

$$\frac{D_R}{d_{pe}} > 25 \quad \dots E.3$$

where,

$$D_R = \text{Internal inside diameter of reactor} = 1.4 \text{ cm}$$

Plug flow

Deviation from plug flow can be estimated using a relaxed criterion by Gierman, 1988:

$$\frac{L_B}{d_{pe}} > \frac{8n}{Pe_L} \ln \frac{1}{(1-x)} \quad \dots E.4$$

where,

n = reaction order

x = conversion of sulfur and nitrogen species for HDS and HDN reactions

Pe_L = Peclet number, $\frac{v_L d_{pe}}{D_L}$

D_L = Liquid diffusion coefficient (cm²/s)

Note: The Peclet number is a dimensionless number and is defined as the ratio of the heat transferred by convection to the heat transferred by conduction. The Peclet number is also a parameter that describes the residence distribution of the liquid which relates to wettability (Sedagat et al. 2017; Jonoud and Jackson 2007; Kasira and Bashiri 2011).

Appendix F: External mass transfer calculation

Evaluation of the external mass transfer resistances for the HDS and HDN reactions

Satterfield criterion (F.1) was used in determining if the rate of hydrogen diffusion through the liquid oil which is an integral part of the HDS and HDN reactions was the rate determining step (Satterfield et al. 1969).

$$\left(\frac{10d_p}{3C_{H_2}}\right) \cdot \left(\frac{-1}{V_c} \cdot \frac{dn}{dt}\right) > k_{OVR} \quad \dots F.1$$

where;

k_{OVR} = Overall mass transfer coefficient for hydrogen, cm/s

C_{H_2} = Hydrogen concentration in the liquid phase at equilibrium, mol/mL

$\left(\frac{-1}{V_c} \cdot \frac{dn}{dt}\right)$ = Rate of hydrogen conversion in the reaction, mol/(s.mL)

V_c = Volume of the loaded catalyst =5 mL

d_p = Average diameter of the catalyst particles = 0.01cm

Validation of Satterfield criterion implied that in the overall reaction, hydrogen conversion was dominant over hydrogen mass transfer.

Estimation of the overall mass transfer coefficient (k_{OVR})

The overall mass transfer coefficient can be calculated using the equation below:

$$\frac{1}{k_{OVR}} = \frac{1}{k_L} + \frac{1}{k_s} \quad \dots F.2$$

where;

k_L = H₂/LGO mass transfer coefficient - gas/liquid side, cm/s

k_s = H₂/LGO mass transfer coefficient – liquid/solid side, cm/s

Calculation of the gas/liquid mass transfer coefficient (k_L)

A correlation (Equation F.3) by Goto and Smith, 1975 was used in estimating the gas/liquid mass transfer coefficient.

$$\frac{k_L a_L}{D_L} = \alpha_1 \cdot \left(\frac{L_A}{\mu_L}\right)^{\alpha_2} \sqrt{\frac{\mu_L}{\rho_L \cdot D_L}} \quad \dots F.3$$

this implies that;

$$k_L = \frac{\alpha_1 D_L}{a_L} \cdot \left(\frac{L_A}{\mu_L}\right)^{\alpha_2} \sqrt{\frac{\mu_L}{\rho_L \cdot D_L}} \quad \dots F.4$$

where;

a_L = Interfacial surface area over unit volume (cm^{-1})

$$\cong \left(\frac{6(1 - \varepsilon)}{d_p}\right)^* = 420 \text{ cm}^{-1} \quad \dots F.5$$

*Assumes that the interfacial surface area is equal to the catalyst pellet surface area.

ε = Bed porosity = 0.3 (Wijngaarden et al. 1998)

L_A = Liquid mass flow over cross-sectional area, $\text{g}/(\text{s}\cdot\text{cm}^2)$

μ_L = Viscosity of LGO at the operating temperature, $\text{g}/(\text{s}\cdot\text{cm})$

D_L = Diffusivity of hydrogen in LGO, cm^2/s

ρ_L = Density of LGO at the operating conditions, g/mL

α_1 = Constant based on the catalyst particle properties* = 0.5

α_2 = Constant based on the catalyst particle properties* = 0.4

* α_1 and α_2 values found by Korsten and Hoffman (1996) for $d_p = 0.01 \text{ cm}$

Calculation of LGO viscosity (μ_L)

The viscosity of LGO at the desired operating temperatures were estimated using the correlation developed by Glasso (Ahmed, 1989). The correlation is as follows:

$$\mu_L = 3.141 \times 10^{10} \cdot (T - 460)^{-3.144} (\log^\circ API)^a \quad \dots F. 6$$

$$a = 10.313 \cdot \log(T - 460) - 36.447 \quad \dots F. 7$$

where;

T = Operating temperature, °R

$$^\circ API = \frac{141.5}{SG} - 131.5 \quad \dots F. 8$$

SG = Specific gravity of LGO at 15.6°C standard condition = 0.901

$^\circ API \approx 25.6$

From equation F.7, $a = -7.61$ to -7.12 (for temperatures ranging from 330°C to 370°C)

From equation F.6, $\mu_L = 0.544$ cP to 0.442 cP (for temperatures ranging from 330°C to 370°C)

Calculation of LGO average molecular weight (M_{AVE}):

The average molecular weight of gas oil was calculated using a correlation developed by Winn (Sim and Daubert, 1980) and it shown below:

$$M_{AVE} = m_1 \cdot T_b^{m_2} \cdot \rho_{15.6}^\beta \quad \dots F. 9$$

where;

M_{AVE} = Average molecular weight of LGO, g/mol

T_b = Average boiling point of LGO = 299°C = 570°F

$\rho_{15.6}$ = Density of LGO at 15.6°C = 0.90 g/mL

m_1 = Empirical constant* = 2.41×10^{-6}

$$m_2 = \text{Empirical constant}^* = 2.847$$

$$\beta = \text{Empirical constant}^* = -2.13$$

*Modified Winn values for gas oil fractions from Trytten et al. 1990

$$M_{AVE} = 212 \text{ g/mol}$$

Calculation of diffusivity of hydrogen in gas oil (D_L):

The effective diffusivity of hydrogen was calculated using a correlation by Wilke and Chang, 1955 given below:

$$\frac{D_L \cdot \mu_L}{T} = (7.4 \times 10^{-8}) \cdot \frac{\sqrt{X \cdot M_{AVE}}}{V_b^{0.6}} \quad \dots F. 10$$

where;

X = Association parameter = 1 for hydrocarbon mixtures

V_b = Hydrogen molar volume at the normal boiling point

$V_b = 14.3 \text{ mL/mol}$ (Wijngaarden et al. 1998)

$D_L = 2.41 \times 10^{-4} \text{ cm}^2/\text{s}$ to $3.17 \times 10^{-4} \text{ cm}^2/\text{s}$ (for the temperature range of 330 to 370 °C)

Calculation of CLGO Density at reaction temperatures and pressures:

The density of gas oils at reactor operating conditions was calculated based on a correlation by Standing and Katz (Jiménez et al. 2007):

$$\rho_L = \rho_{15.6} - \Delta_{\rho_T} + \Delta_{\rho_P} \quad \dots F. 11$$

Δ_{ρ_T} = Temperature density correlation, lbs/ft³

Δ_{ρ_P} = Pressure density correlation, lbs/ft³

$$\Delta_{\rho_P} = [0.167 + (16.181 \times 10^{-0.0425 \rho_{15.6}})] \cdot \left[\frac{P}{1000} \right] - 0.01 \\ \cdot [0.299 + (263 \times 10^{-0.603 \rho_{15.6}})] \cdot \left[\frac{P}{1000} \right]^2 \quad \dots F. 12$$

$$\Delta\rho_T = \left[0.0133 + \left(152.4 \cdot (\rho_{15.6} + \Delta\rho_p)^{-2.45} \right) \right] \cdot [T - 520] \\ - \left[8.10 \times 10^{-6} - \left(0.0622 \times 10^{-0.764(\rho_{15.6} + \Delta\rho_p)} \right) \right] \cdot [T - 520]^2 \quad \dots F. 13$$

where;

$$P = 1100 \text{ psia to } 1500 \text{ psia}$$

$$T = 1086 \text{ }^\circ\text{R to } 1158 \text{ }^\circ\text{R (330 }^\circ\text{C to } 370 \text{ }^\circ\text{C)}$$

Based on the pressure and temperature values,

$$\Delta\rho_p = 0.25 \text{ lbs/ft}^3 \text{ to } 0.34 \text{ lbs/ft}^3$$

$$\Delta\rho_T = 9.34 \text{ lbs/ft}^3 \text{ to } 10.14 \text{ lbs/ft}^3$$

$$\rho_L = 46.4 \text{ lb/ft}^3 \text{ to } 47.1 \text{ lb/ft}^3 = 743 \text{ kg/m}^3 \text{ to } 754 \text{ kg/m}^3$$

This implies that from previous calculations,

$$k_L = 1.7 \times 10^{-6} \text{ cm/s to } 1.94 \times 10^{-6} \text{ cm/s}$$

Calculation of the liquid/solid mass transfer coefficient (k_s):

The Van Krevelen and Krekels correlation was used to estimate the liquid/solid mass transfer coefficient (Froment and Bishoff, 1990):

$$\frac{k_s}{D_L \cdot a_s} = 1.8 \cdot \sqrt{\frac{L_A}{a_s \cdot \mu_L}} \cdot \left(\frac{\mu_L}{\rho_L \cdot D_L} \right)^{1/3} \quad \dots F. 14$$

this implies that,

$$k_s = D_L \cdot a_s \cdot 1.8 \cdot \sqrt{\frac{L_A}{a_s \cdot \mu_L}} \cdot \left(\frac{\mu_L}{\rho_L \cdot D_L} \right)^{1/3} \quad \dots F. 15$$

where,

$$a_s = \text{Liquid/solid interfacial surface area} = a_L = 420 \text{ cm}^{-1}$$

therefore, using the terms determined previously,

$$k_s = 7.71 \times 10^{-3} \text{ cm/s to } 9.63 \times 10^{-3} \text{ cm/s}$$

Calculation of the equilibrium concentration of hydrogen in gas oil (C_{H_2}):

Henry's constant was used for calculating the equilibrium concentration of hydrogen in gas oil after assuming limited solubility:

$$C_{H_2} = \frac{P}{H_{H_2}} \quad \dots F.16$$

where,

$$H_{H_2} = \text{Henry's constant for hydrogen in LGO, MPa}\cdot\text{m}^3/\text{mol}$$

$$P = \text{Operating pressure} = 7.6 \text{ MPa to } 10.3 \text{ MPa}$$

The equation below can be used to calculate Henry's constant:

$$H_{H_2} = \frac{V_N}{\lambda_{H_2} \cdot \rho_L} \quad \dots F.17$$

where,

$$v_N = \text{Hydrogen molar volume at standard conditions} = 22.4 \text{ L/mol}$$

$$\rho_L = \text{Density of LGO at the operating conditions} = 743 \text{ kg/m}^3 \text{ to } 754 \text{ kg/m}^3$$

$$\lambda_{H_2} = \text{Hydrogen solubility in LGO, mL}/(\text{kg}\cdot\text{MPa})$$

The solubility of hydrogen in gas oil fractions was estimated using a correlation established by Korsten and Hoffmann, 1996:

$$\lambda_{H_2} = z_0 + z_1 \cdot T + z_2 \cdot \frac{T}{\rho_{20}} + z_3 \cdot T^2 + z_4 \cdot \frac{1}{(\rho_{20})^2} \quad \dots F18$$

where,

$$z_0 = -0.55973$$

$$z_1 = -0.42947 \times 10^{-3}$$

$$z_2 = 3.07539 \times 10^{-3}$$

$$z_3 = 1.94593 \times 10^{-6}$$

$$z_4 = 0.83578$$

$$T = \text{Operating temperature} = 330 \text{ }^\circ\text{C to } 370 \text{ }^\circ\text{C}$$

$$\rho_{20} = \text{Density of LGO at } 20 \text{ }^\circ\text{C} = 0.897 \text{ g/mL}$$

Under the desired operating conditions, the ranges below were obtained:

$$\lambda_{H_2} = 1.68 \times 10^3 \text{ mL/(kg}\cdot\text{MPa) to } 1.85 \times 10^3 \text{ mL/(kg}\cdot\text{MPa)}$$

$$H_{H_2} = 0.0179 \text{ MPa}\cdot\text{m}^3/\text{mol to } 0.0160 \text{ MPa}\cdot\text{m}^3/\text{mol}$$

$$C_{H_2} = 6.45 \times 10^{-4} \text{ mol/mL to } 4.24 \times 10^{-4} \text{ mol/mL}$$

Although equation F.18, does not include pressure, pressure affects the solubility of H₂ in gas oil. The effect of pressure on solubility of gases can be supported with Henry's Law, which shows that a direct proportionality exists between the solubility of a gas in a liquid and the partial pressure of that gas above the surface of the solution. Henry's law equation is expressed below:

$$C = k \times P_{gas} \quad \dots F. 19$$

where;

C = solubility of a gas in solvent

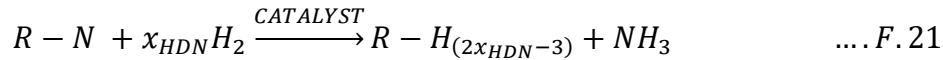
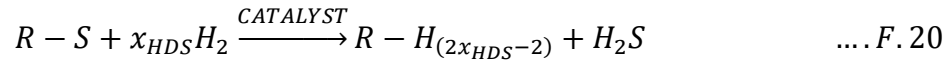
k = proportionality constant

P_{gas} = partial pressure of the gas above the solution

In addition, according to Dalton's law of partial pressures, the partial pressure of hydrogen is equivalent to the product of the mole fraction of hydrogen present and the total hydrogen pressure. This implies that from Henry's law since, hydrogen solubility is directly proportional to hydrogen partial pressure an increase in total hydrogen pressure will cause an increase in hydrogen partial pressure and a consequent increase in hydrogen solubility (Zumdahl and Zumdahl, 2010).

Calculating the hydrogen conversion rate for HDS and HDN:

The rate of hydrogen conversion for hydrodesulfurization and hydrodenitrogenation reactions were found using the simplified stoichiometric equations below:



Equations F.20 and F.21 enables the substitutions below:

HDS:

$$\left(\frac{-1}{V_c} \cdot \frac{dn}{dt}\right) = \frac{x_{HDS} \cdot r_{HDS}}{V_c} \quad \dots F. 22$$

HDN:

$$\left(\frac{-1}{V_c} \cdot \frac{dn}{dt}\right) = \frac{x_{HDN} \cdot r_{HDN}}{V_c} \quad \dots F. 23$$

where,

r_{HDS} = molar rate of sulfur removal achieved from the hydrotreating catalyst (mol/s)

r_{HDN} = molar rate of nitrogen removal achieved from the hydrotreating catalyst
(mol/s)

On assumption that sulfur removal involved hydrogenation of a 5-member thiophenic ring and nitrogen removal involved hydrogenation of a 6-member basic pyridine ring then, the stoichiometric values below can be assumed for HDS and HDN reactions of LGO.

$$x_{HDS} = 4.0 \quad ; \quad x_{HDN} = 5.0$$

Based on these assumed values for the HDS and HDN reaction, the range of values below were found for each side of the Satterfield inequality:

Hydrodesulfurization calculation of left- and right-hand side of Satterfield's criterion:

Left hand side of Satterfield's criterion = 1.16×10^{-4} cm/s to 1.40×10^{-4} cm/s

Right hand side of Satterfield's criterion = 1.72×10^{-6} cm/s to 1.94×10^{-6} cm/s

Hydrodenitrogenation calculations of left- and right-hand side of Satterfield's criterion:

Left hand side of Satterfield's criterion = 1.57×10^{-7} cm/s to 1.09×10^{-6} cm/s

Right hand side of Satterfield's criterion = 1.72×10^{-6} cm/s to 1.94×10^{-6} cm/s

Appendix G: Internal mass transfer calculation

Evaluation of internal mass transfer resistances for the HDS and HDN reactions

In determining the internal mass transfer resistances, the preliminary calculation evaluated whether isothermality within the catalyst pellets could be assumed. Each pellet's degree of isothermality could be examined in two ways. Either by finding the highest potential rise in temperature between the core and the surface of the catalyst pellet or by confirming Anderson's criterion (Fogler, 2006; Anderson, 1963).

Maximum temperature rise (ΔT_{MAX}):

$$\beta = \frac{\Delta T_{MAX}}{T_S} = \frac{\Delta H_{R,i} \cdot D_i \cdot [C_i]_s}{k_t \cdot T_S} \quad \dots G.I$$

where,

$\Delta H_{R,i}$ = Heat of HDS/HDN reaction, kJ/mol

$[C_i]_s$ = Catalyst surface concentration of sulfur/nitrogen species, mol/mL

k_t = Thermal conductivity of the NiMo/CNH catalyst pellet powder particle.

$k_t = 0.155$ W/(m. K) (assumption: pure CNH pellet powder particle, Yang et al. 2002)

T_S = Pellet Catalyst or powder catalyst particle surface temperature = 603 - 643 K (reaction temperatures)

Calculation of heats of reaction of HDS/HDN

For the light gas oil, an approximated heat of reaction range (63 to 66 kJ/mol of hydrogen consumed) for most thiophene molecules was used as the heat of reaction for hydrodesulfurization (Ancheyta and Speight, 2007). Whereas, an approximated heat of reaction range of (65 to 68 kJ/mol of hydrogen consumed) for most quinoline molecules was used as the heat of reaction for hydrodenitrogenation (Satterfield and Cocchetto, 1981). Based on the stoichiometric coefficients x_{HDS} and x_{HDN} , discussed in Appendix F, the respective heat of reaction units were converted to kJ/mol of sulfur/nitrogen removal.

Therefore,

$$\Delta H_{R,HDS} = 63 \text{ to } 66 \text{ kJ/mol of H}_2 \text{ consumed}$$

$$\Delta H_{R,HDS} = 252 \text{ to } 264 \text{ kJ/mol of sulfur}$$

$$\Delta H_{R,HDS} = 65 \text{ to } 68 \text{ kJ/mol of H}_2 \text{ consumed}$$

$$\Delta H_{R,HDS} = 325 \text{ to } 340 \text{ kJ/mol of nitrogen}$$

Calculating the effective diffusivities of organosulfur and organonitrogen compounds in

LGO ($[D_S]_F/[N]_F$):

The following equation was used to estimate the effective diffusivity of sulfur compounds:

$$[D_i]_E = \frac{\varepsilon_P \cdot D_i}{\gamma_P} \quad \dots G.2$$

where,

ε_P = Porosity of the catalyst pellets

γ_P = Tortuosity of the catalyst pellets

D_i = Bulk diffusivity of organosulfur compounds cm^2/g

The porosity and tortuosity ratio of pelletized or powdered catalyst particles was calculated using a correlation by Probst and Wohlfahrt, 1989:

$$\frac{\varepsilon_P}{\gamma_P} = \left[\frac{\varepsilon_P^m}{(2 - \varepsilon_P)^{m+1}} \right] \quad \dots G.3$$

For compressed porous catalysts (group D), m values were found to be in the range of 0.70 to 1.65. However the recommended m value of 1.05 can be used if not determined. Porosity values were found to be in the range of 0.05 to 0.65 (the average value of 0.35 was used). As a result of these conditions, the porosity and tortuosity ratio values were found to be:

$$\frac{\varepsilon_P}{\gamma_P} = 0.1190 \text{ (0.0012 to 0.4441)} \quad \dots G.4$$

Calculation of the bulk diffusivities of organosulfur and organonitrogen compounds in LGO (D_S/D_N):

Assumption: Organosulfur and organonitrogen compounds had similar average molecular weight, average boiling point, density, and average molar volume as the LGO feedstock. Tyn-Calus correlation was used in finding the bulk diffusivities of each species (Reid et al. 1987):

$$D_i = (8.93 \times 10^{-8}) \cdot \left(\frac{v_L^{0.267}}{v_i^{0.433}} \right) \cdot \left(\frac{T}{\mu_L} \right) = (8.93 \times 10^{-8}) \cdot \left(\frac{T}{\mu_L \cdot v_i^{0.166}} \right) \quad \dots G.5$$

where,

T = Operating temperature = 603 K to 643 K

μ_L = LGO viscosity at operating conditions = 0.544 cP to 0.422 cP (Check Appendix F)

v_i = Molar volume of sulfur/nitrogen molecules under standard conditions, mL/mol

v_L = Molar volume of LGO under standard conditions, mL/mol

The molar volume of the gas oil was found as follows:

$$v_i = (0.285) \cdot v_c^{1.048} \quad \dots G.6$$

where,

v_c = Critical specific molar volume of LGO, mL/mol and is given by:

$$v_c = v_c^m \cdot M_{AVE} \quad \dots G.7$$

M_{AVE} = 212 g/mol (from Appendix F)

v_c^m = Critical specific mass volume, mL/g

A correlation by Raizi and Daubert was used to calculate the critical specific mass volume (Ahmed, 1989):

$$v_c^m = (7.5214 \times 10^{-3}) \cdot T_b^{0.2896} \cdot SG^{-0.7666} \quad \dots G.8$$

where,

v_c^m = Critical specific mass volume, ft³/lb

T_b = Average boiling point temperature = 299 °C = 1030 °R

$SG_{15.6}$ = Specific gravity at 15.6 °C = 0.901

From the above, it implies that:

v_c^m = 3.79 mL/g

v_c = 804 mL/mol

v_i = 316 mL/mol

Therefore,

$D_i = D_S = D_N = 3.81 \times 10^{-5}$ cm²/g to 5.00×10^{-5} cm²/s

$[D_S]_E = [D_N]_E = 4.53 \times 10^{-6}$ cm²/g to 5.95×10^{-6} cm²/s

The calculated effective diffusivity values, resulted in these isothermality ratios:

$\beta_{HDS} = 1.70 \times 10^{-8}$ to 9.62×10^{-8}

$\beta_{HDN} = 2.38 \times 10^{-5}$ to 3.22×10^{-5}

Due to the simultaneous occurrence of HDS and HDN reactions, the overall maximum temperature change with respect to the catalyst surface temperature is the sum of the beta values.

Hence, the highest possible ΔT_{MAX} value was found to range from 0.014 to 0.021K, and therefore can be considered negligible.

Anderson's Criterion of proving isothermality:

$$\frac{\Delta H_{R,i} \cdot \{R_i\} \cdot d_p^2}{k_t \cdot T_s} < \frac{3 \cdot T_s \cdot R}{E_i} \quad \dots G.9$$

where,

$\{R_i\}$ = Global reaction rate: HDS/HDN, mol/(s.mL)

k_t = Catalyst thermal conductivity = 0.155 W/(m.K)

R = Universal gas constant = 8.314 J/(mol.K)

E_i = Activation energy: HDS/HDN, J/mol

Based on the range of operating conditions tested, the values for the left and right-hand side of Anderson's criterion were found to be:

Left hand side of Anderson's criterion (HDS) = 1.39×10^{-8} to 3.82×10^{-8}

Right hand side of Anderson's criterion (HDS) = 0.235 to 0.250

Left hand side of Anderson's criterion (HDN) = 1.56×10^{-9} to 6.62×10^{-9}

Right hand side of Anderson's criterion (HDN) = 0.163 to 0.174

These results imply that assumption of isothermal behaviour is valid during the assessment of internal mass transfer resistances of the hydrotreating process.

Appendix H: Hydrotreating performance on heavy gas oil using the best catalyst (3.5wt%Ni19wt%Mo/CNH) established from phase 5

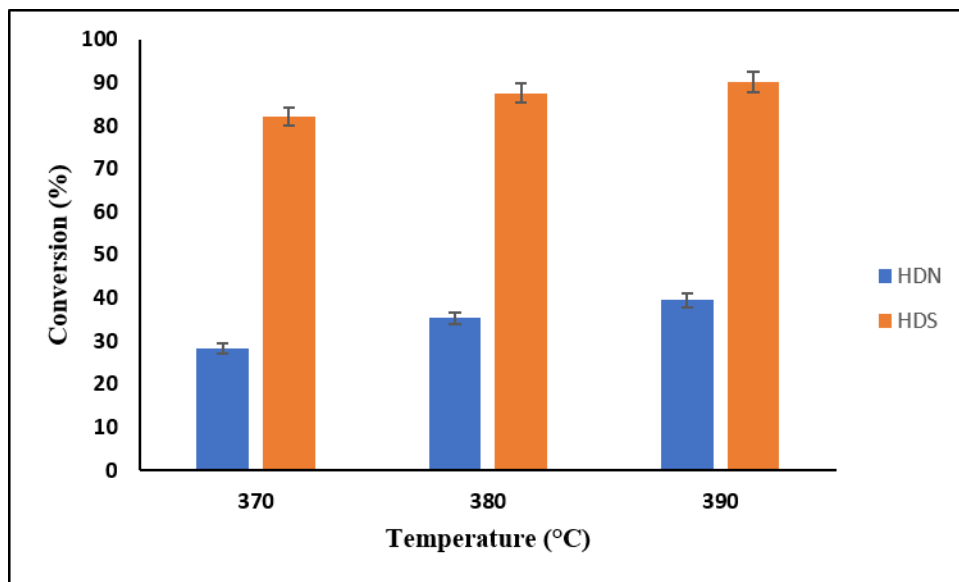


Figure H.1 HDN and HDS activities of 3.5wt%Ni19wt%Mo/CNH catalysts using HGO at 370, 380, and 390 °C (Catalyst = 5 cm³, P = 9.0 MPa, LHSV = 1 hr⁻¹, and H₂ / oil ratio = 600 (v/v)).

Comments:

- The composition of HGO was (4.3 wt% Sulfur and 0.39 wt% Nitrogen), and HDS and HDN activities were found to be 90.2% and 39.5% respectively at 390 °C.
- Although higher temperatures were experimented compared to the temperatures used for LGO, HDS and HDN activities using the best catalyst with HGO resulted in lower conversions due to the higher molecular weight of the HGO feed.

Appendix I: Permissions to Use Papers, Tables and Figures

Permission to use the following papers:

(i) Aryee, E.; Dalai, A. K.; Adjaye, J. "Maximization of Carbon Nanohorns Production via the arc discharge method for hydrotreating application" Journal of Nanoscience and Nanotechnology, 17 (2017) 4784 – 4791

"Reprinted with permission. Copyright @ American Scientific Publishers,"

Please see below

From: Dr. H. S. Nalwa <nalwa@mindspring.com>
Sent: April 18, 2019 6:59 PM
To: Aryee, Emma
Subject: RE: permission to use my article in my thesis

Just write

"Reprinted with permission. Copyright @ America Scientific Publishers".

From: Aryee, Emma [mailto:enb621@mail.usask.ca]
Sent: Thursday, April 18, 2019 4:38 PM
To: Dr. H. S. Nalwa
Subject: Re: permission to use my article in my thesis

Hi Dr. H.S. Nalwa,

Thanks for your prompt response to my mail but, please is there any form that I can fill in order to get a formal note that I can put in my thesis to show I have been granted permission by America Scientific publishers to use this full article in my thesis? Please I would appreciate if you send me a formal note to this effect.

Again, the citation is as follows: "Aryee, E.; Dalai, A. K.; Adjaye, J. "Maximization of Carbon Nanohorns Production via the arc discharge method for hydrotreating application" Journal of Nanoscience and Nanotechnology, 17 (2017) 4784 – 4791. DOI: [10.1166/jnn.2017.13447](https://doi.org/10.1166/jnn.2017.13447)"
Thanks so much.

Best regards,
Emma

(ii) Aryee, E.; Dalai, A. K.; Adjaye, J. "Functionalization and Characterization of Carbon Nanohorns (CNH) for Hydrotreating of Gas Oils," Topics in Catalysis, 2014, 57, 796 – 805.

**SPRINGER NATURE LICENSE
TERMS AND CONDITIONS**

Apr 16, 2019

This Agreement between Emma Aryee ("You") and Springer Nature ("Springer Nature") consists of your license details and the terms and conditions provided by Springer Nature and Copyright Clearance Center.

License Number	4571110536885
License date	Apr 16, 2019
Licensed Content Publisher	Springer Nature
Licensed Content Publication	Topics in Catalysis
Licensed Content Title	Functionalization and Characterization of Carbon Nanohorns (CNHs) for Hydrotreating of Gas Oils
Licensed Content Author	Emma Aryee, Ajay K. Dalai, John Adjaye
Licensed Content Date	Jan 1, 2013
Licensed Content Volume	57
Licensed Content Issue	6
Type of Use	Thesis/Dissertation
Requestor type	academic/university or research institute
Format	print and electronic
Portion	full article/chapter
Will you be translating?	no
Circulation/distribution	2,001 to 5,000
Author of this Springer Nature content	yes
Title	Hydrotreating of Gas Oils Using Ni-Mo Catalyst Supported on Carbon Nanohorns and Associated Carbon Materials
Institution name	University of Saskatchewan
Expected presentation date	May 2019
Requestor Location	Emma Aryee 805-105 Cumberland Avenue South

Saskatoon, SK S7N1L7

Canada
Attn: Emma Aryee
Total 0.00 CAD

Permission to use: Table 2.1

**SPRINGER NATURE LICENSE
TERMS AND CONDITIONS**

Mar 31, 2019

This Agreement between Emma Aryee ("You") and Springer Nature ("Springer Nature") consists of your license details and the terms and conditions provided by Springer Nature and Copyright Clearance Center.

License Number	4559480722226
License date	Mar 31, 2019
Licensed Content Publisher	Springer Nature
Licensed Content Publication	Springer eBook
Licensed Content Title	Hydrotreating and Hydrocracking: Fundamentals
Licensed Content Author	Paul R. Robinson, Geoffrey E. Dolbear
Licensed Content Date	Jan 1, 2006
Type of Use	Thesis/Dissertation
Requestor type	academic/university or research institute
Format	print and electronic
Portion	figures/tables/illustrations
Number of figures/tables/illustrations	1
Will you be translating?	no
Circulation/distribution	<501
Author of this Springer Nature content	no
Title	Hydrotreating of Gas Oils Using Ni-Mo Catalyst Supported on Carbon Nanohorns and Associated Carbon Materials
Institution name	n/a
Expected presentation date	May 2019
Portions	Table 9
Requestor Location	Emma Aryee 805-105 Cumberland Avenue South

Saskatoon, SK S7N1L7
Canada
Attn: Emma Aryee

Total 0.00 CAD

[Terms and Conditions](#)

Permission to use Figures: 2.1 – 2.7

SPRINGER NATURE LICENSE TERMS AND CONDITIONS

Mar 31, 2019

This Agreement between Emma Aryee ("You") and Springer Nature ("Springer Nature") consists of your license details and the terms and conditions provided by Springer Nature and Copyright Clearance Center.

License Number	4559471228836
License date	Mar 31, 2019
Licensed Content Publisher	Springer Nature
Licensed Content Publication	Springer eBook
Licensed Content Title	Hydrotreating
Licensed Content Author	Adrian Gruia
Licensed Content Date	Jan 1, 2008
Type of Use	Thesis/Dissertation
Requestor type	academic/university or research institute
Format	print and electronic
Portion	figures/tables/illustrations
Number of figures/tables/illustrations	6
Will you be translating?	no
Circulation/distribution	<501
Author of this Springer Nature content	no
Title	Hydrotreating of Gas Oils Using Ni-Mo Catalyst Supported on Carbon Nanohorns and Associated Carbon Materials
Institution name	n/a

Expected presentation date May 2019
Portions Images on pages:328, 329, 330, 331, 332, 333
Requestor Location Emma Aryee
805-105 Cumberland Avenue South

Saskatoon, SK S7N1L7
Canada
Attn: Emma Aryee

Total 0.00 CAD
Terms and Conditions

Permission to use: Figure 2.8

ELSEVIER LICENSE TERMS AND CONDITIONS

Mar 31, 2019

This Agreement between Emma Aryee ("You") and Elsevier ("Elsevier") consists of your license details and the terms and conditions provided by Elsevier and Copyright Clearance Center.

License Number 4559481361963
License date Mar 31, 2019
Licensed Content Publisher Elsevier
Licensed Content Publication Applied Catalysis A: General
Licensed Content Title On the flexibility of the active phase in hydrotreating catalysts
Licensed Content Author Sonja Eijsbouts
Licensed Content Date Sep 25, 1997
Licensed Content Volume 158
Licensed Content Issue 1-2
Licensed Content Pages 40
Start Page 53
End Page 92
Type of Use reuse in a thesis/dissertation
Intended publisher of new work other
Portion figures/tables/illustrations

Number of figures/tables/illustrations	1
Format	both print and electronic
Are you the author of this Elsevier article?	No
Will you be translating?	No
Original figure numbers	Fig. 1.
Title of your thesis/dissertation	Hydrotreating of Gas Oils Using Ni-Mo Catalyst Supported on Carbon Nanohorns and Associated Carbon Materials
Expected completion date	May 2019
Estimated size (number of pages)	200
Requestor Location	Emma Aryee 805-105 Cumberland Avenue South Saskatoon, SK S7N1L7 Canada Attn: Emma Aryee
Publisher Tax ID	GB 494 6272 12
Total	0.00 CAD
Terms and Conditions	

Permission to use Figure 2.9

SPRINGER NATURE LICENSE TERMS AND CONDITIONS

Apr 17, 2019

This Agreement between Emma Aryee ("You") and Springer Nature ("Springer Nature") consists of your license details and the terms and conditions provided by Springer Nature and Copyright Clearance Center.

License Number	4571140606648
License date	Apr 17, 2019
Licensed Content Publisher	Springer Nature
Licensed Content Publication	Springer eBook
Licensed Content Title	Introduction to Carbon
Licensed Content Author	Zhifeng Ren, Yucheng Lan, Yang Wang

Licensed Content Date	Jan 1, 2012
Type of Use	Thesis/Dissertation
Requestor type	academic/university or research institute
Format	print and electronic
Portion	figures/tables/illustrations
Number of figures/tables/illustrations	1
Will you be translating?	no
Circulation/distribution	2,001 to 5,000
Author of this Springer Nature content	no
Title	Hydrotreating of Gas Oils Using Ni-Mo Catalyst Supported on Carbon Nanohorns and Associated Carbon Materials
Institution name	University of Saskatchewan
Expected presentation date	May 2019
Portions	Fig. 1.1
Requestor Location	Emma Aryee 805-105 Cumberland Avenue South Saskatoon, SK S7N1L7 Canada Attn: Emma Aryee
Total	0.00 CAD

Permission to use Figure 2.10a

ELSEVIER LICENSE TERMS AND CONDITIONS

Apr 03, 2019

This Agreement between Emma Aryee ("You") and Elsevier ("Elsevier") consists of your license details and the terms and conditions provided by Elsevier and Copyright Clearance Center.

License Number	4561681281206
License date	Apr 03, 2019
Licensed Content Publisher	Elsevier
Licensed Content Publication	Chemical Physics Letters

Licensed Content Title	Nano-aggregates of single-walled graphitic carbon nano-horns
Licensed Content Author	S. Iijima, M. Yudasaka, R. Yamada, S. Bandow, K. Suenaga, F. Kokai, K. Takahashi
Licensed Content Date	Aug 13, 1999
Licensed Content Volume	309
Licensed Content Issue	3-4
Licensed Content Pages	6
Start Page	165
End Page	170
Type of Use	reuse in a thesis/dissertation
Intended publisher of new work	other
Portion	figures/tables/illustrations
Number of figures/tables/illustrations	1
Format	both print and electronic
Are you the author of this Elsevier article?	No
Will you be translating?	No
Original figure numbers	Fig. 1. (b)
Title of your thesis/dissertation	Hydrotreating of Gas Oils Using Ni-Mo Catalyst Supported on Carbon Nanohorns and Associated Carbon Materials
Expected completion date	May 2019
Estimated size (number of pages)	200
Requestor Location	Emma Aryee 805-105 Cumberland Avenue South Saskatoon, SK S7N1L7 Canada Attn: Emma Aryee
Publisher Tax ID	GB 494 6272 12
Total	0.00 CAD
Terms and Conditions	

Permission to use Figure 2.10b


Order Details

Nanotechnology

Billing Status:

N/A

Order detail ID:71869355

- **ISSN:**0957-4484
- **Publication Type:**Journal
- **Volume:**
- **Issue:**
- **Start page:**
- **Publisher:**IOP Publishing
- **Author/Editor:**Institute of Physics (Great Britain) ; American Institute of Physics
- **Permission Status:**  **Granted**
- **Permission type:**Republish or display content
- **Type of use:**Thesis/Dissertation
-

Order License Id: 4561691345748

- [Hide details](#)

○

Requestor type	Author of requested content
Format	Print, Electronic
Portion	chart/graph/table/figure
Number of charts/graphs/tables/figures	1
The requesting person/organization	Emma Aryee
Title or numeric reference of the portion(s)	Figure 4.a
Title of the article or chapter the portion is from	Isolation of carbon nanohorn assemblies and their potential for intracellular delivery
Editor of portion(s)	N/A
Author of portion(s)	Xiaobin Fan, Juan Tan, Guoliang Zhang and Fengbao Zhang
Volume of serial or monograph	N/A
Page range of portion	Page 3
Publication date of portion	17 April 2007
Rights for	Main product
Duration of use	Life of current edition
Creation of copies for the disabled	no
With minor editing privileges	no
For distribution to	United States and Canada
In the following language(s)	Original language of publication
With incidental promotional use	no

Lifetime unit quantity of new product Up to 499
Title Hydrotreating of Gas Oils Using Ni-Mo Catalyst Supported on Carbon Nanohorns and Associated Carbon Materials
Institution name University of Saskatchewan
Expected presentation date May 2019

Permission to use Figure 2.11



RightsLink®

Home

Account Info

Help



ACS Publications
Most Trusted. Most Cited. Most Read.

Title: Cones and Tubes: Geometry in the Chemistry of Carbon
Author: Thomas W. Ebbesen
Publication: Accounts of Chemical Research
Publisher: American Chemical Society
Date: Sep 1, 1998
Copyright © 1998, American Chemical Society

Logged in as:
Emma Aryee
Account #:
3000817750

LOGOUT

PERMISSION/LICENSE IS GRANTED FOR YOUR ORDER AT NO CHARGE

This type of permission/license, instead of the standard Terms & Conditions, is sent to you because no fee is being charged for your order. Please note the following:

- Permission is granted for your request in both print and electronic formats, and translations.
- If figures and/or tables were requested, they may be adapted or used in part.
- Please print this page for your records and send a copy of it to your publisher/graduate school.
- Appropriate credit for the requested material should be given as follows: "Reprinted (adapted) with permission from (Ebbesen, T. "Cones and Tubes: Geometry in the chemistry of carbon," Accounts of chemical research, 1998, 31, 558-566). Copyright (1998) American Chemical Society."
- One-time permission is granted only for the use specified in your request. No additional uses are granted (such as derivative works or other editions). For any other uses, please submit a new request.
- If credit is given to another source for the material you requested, permission must be obtained from that source.

Permission to use Figure 2.11

SPRINGER NATURE LICENSE TERMS AND CONDITIONS

Apr 04, 2019

This Agreement between Emma Aryee ("You") and Springer Nature ("Springer Nature") consists of your license details and the terms and conditions provided by Springer Nature and Copyright Clearance Center.

License Number	4561751116713
License date	Apr 04, 2019
Licensed Content Publisher	Springer Nature
Licensed Content Publication	Nature
Licensed Content Title	Graphitic cones and the nucleation of curved carbon surfaces
Licensed Content Author	A. Krishnan et al
Licensed Content Date	Jul 31, 1997
Type of Use	Thesis/Dissertation
Requestor type	academic/university or research institute
Format	print and electronic
Portion	figures/tables/illustrations
Number of figures/tables/illustrations	1
Will you be translating?	no
Circulation/distribution	<501
Author of this Springer Nature content	no
Title	Hydrotreating of Gas Oils Using Ni-Mo Catalyst Supported on Carbon Nanohorns and Associated Carbon Materials
Institution name	University of Saskatchewan
Expected presentation date	May 2019
Portions	Figure 2
Requestor Location	Emma Aryee 805-105 Cumberland Avenue South Saskatoon, SK S7N1L7 Canada Attn: Emma Aryee

Total 0.00 CAD

Terms and Conditions

Permission to use Figure 2.12

ELSEVIER LICENSE TERMS AND CONDITIONS

Mar 31, 2019

This Agreement between Emma Aryee ("You") and Elsevier ("Elsevier") consists of your license details and the terms and conditions provided by Elsevier and Copyright Clearance Center.

License Number	4559451137586
License date	Mar 31, 2019
Licensed Content Publisher	Elsevier
Licensed Content Publication	New Carbon Materials
Licensed Content Title	The production of carbon nano-materials by arc discharge under water or liquid nitrogen
Licensed Content Author	Gang XING,Shen-li JIA,Zong-qian SHI
Licensed Content Date	Dec 1, 2007
Licensed Content Volume	22
Licensed Content Issue	4
Licensed Content Pages	5
Start Page	337
End Page	341
Type of Use	reuse in a thesis/dissertation
Intended publisher of new work	other
Portion	figures/tables/illustrations
Number of figures/tables/illustrations	1
Format	both print and electronic
Are you the author of this Elsevier article?	No
Will you be translating?	No
Original figure numbers	Fig.7

Title of your thesis/dissertation	Hydrotreating of Gas Oils Using Ni-Mo Catalyst Supported on Carbon Nanohorns and Associated Carbon Materials
Expected completion date	May 2019
Estimated size (number of pages)	200
Requestor Location	Emma Aryee 805-105 Cumberland Avenue South Saskatoon, SK S7N1L7 Canada Attn: Emma Aryee
Publisher Tax ID	GB 494 6272 12
Total	0.00 CAD

Permission to use Figure 2.13

ELSEVIER LICENSE TERMS AND CONDITIONS

Apr 17, 2019

This Agreement between Emma Aryee ("You") and Elsevier ("Elsevier") consists of your license details and the terms and conditions provided by Elsevier and Copyright Clearance Center.

License Number	4571150764161
License date	Apr 17, 2019
Licensed Content Publisher	Elsevier
Licensed Content Publication	Carbon
Licensed Content Title	Some aspects of the surface chemistry of carbon blacks and other carbons
Licensed Content Author	H.P. Boehm
Licensed Content Date	Jan 1, 1994
Licensed Content Volume	32
Licensed Content Issue	5
Licensed Content Pages	11
Start Page	759
End Page	769
Type of Use	reuse in a thesis/dissertation

Intended publisher of new work	other
Portion	figures/tables/illustrations
Number of figures/tables/illustrations	1
Format	both print and electronic
Are you the author of this Elsevier article?	No
Will you be translating?	No
Original figure numbers	Fig. 1.
Title of your thesis/dissertation	Hydrotreating of Gas Oils Using Ni-Mo Catalyst Supported on Carbon Nanohorns and Associated Carbon Materials
Publisher of new work	University of Saskatchewan
Expected completion date	May 2019
Estimated size (number of pages)	200
Requestor Location	Emma Aryee 805-105 Cumberland Avenue South Saskatoon, SK S7N1L7 Canada Attn: Emma Aryee
Publisher Tax ID	GB 494 6272 12

Permission to use Figure 3.1

**JOHN WILEY AND SONS LICENSE
TERMS AND CONDITIONS**

Apr 22, 2019

This Agreement between Emma Aryee ("You") and John Wiley and Sons ("John Wiley and Sons") consists of your license details and the terms and conditions provided by John Wiley and Sons and Copyright Clearance Center.

License Number	4574341132346
License date	Apr 22, 2019
Licensed Content Publisher	John Wiley and Sons
Licensed Content Publication	Wiley Books
Licensed Content Title	Reporting Physisorption Data for Gas/Solid Systems

Licensed Content Author	Kenneth S. W. Sing, Douglas H. Everett, R. A. W. Haul, et al
Licensed Content Date	Mar 15, 2008
Licensed Content Pages	14
Type of use	Dissertation/Thesis
Requestor type	University/Academic
Format	Print and electronic
Portion	Figure/table
Number of figures/tables	2
Original Wiley figure/table number(s)	Fig. 2 and Fig. 3
Will you be translating?	No
Title of your thesis / dissertation	Hydrotreating of Gas Oils Using Ni-Mo Catalyst Supported on Carbon Nanohorns and Associated Carbon Materials
Expected completion date	May 2019
Expected size (number of pages)	200
Requestor Location	Emma Aryee 805-105 Cumberland Avenue South Saskatoon, SK S7N1L7 Canada Attn: Emma Aryee
Publisher Tax ID	EU826007151
Total	0.00 CAD
Terms and Conditions	

Permission to use Figure 3.2

ELSEVIER LICENSE TERMS AND CONDITIONS

Apr 17, 2019

This Agreement between Emma Aryee ("You") and Elsevier ("Elsevier") consists of your license details and the terms and conditions provided by Elsevier and Copyright Clearance Center.

License Number	4571640415463
License date	Apr 17, 2019
Licensed Content Publisher	Elsevier
Licensed Content Publication	Nanomedicine: Nanotechnology, Biology and Medicine
Licensed Content Title	Diagnostic applications of Raman spectroscopy
Licensed Content Author	Qiang Tu,Chang Chang
Licensed Content Date	Jul 1, 2012
Licensed Content Volume	8
Licensed Content Issue	5
Licensed Content Pages	14
Start Page	545
End Page	558
Type of Use	reuse in a thesis/dissertation
Intended publisher of new work	other
Portion	figures/tables/illustrations
Number of figures/tables/illustrations	1
Format	both print and electronic
Are you the author of this Elsevier article?	No
Will you be translating?	No
Original figure numbers	Figure 1.
Title of your thesis/dissertation	Hydrotreating of Gas Oils Using Ni-Mo Catalyst Supported on Carbon Nanohorns and Associated Carbon Materials
Publisher of new work	University of Saskatchewan
Expected completion date	May 2019
Estimated size (number of pages)	200
Requestor Location	Emma Aryee 805-105 Cumberland Avenue South Saskatoon, SK S7N1L7 Canada Attn: Emma Aryee
Publisher Tax ID	GB 494 6272 12
Total	0.00 CAD

Permission to use Figure 3.3

ELSEVIER LICENSE TERMS AND CONDITIONS

Apr 18, 2019

This Agreement between Emma Aryee ("You") and Elsevier ("Elsevier") consists of your license details and the terms and conditions provided by Elsevier and Copyright Clearance Center.

License Number	4572201319389
License date	Apr 18, 2019
Licensed Content Publisher	Elsevier
Licensed Content Publication	Elsevier Books
Licensed Content Title	Comprehensive Coordination Chemistry II
Licensed Content Author	J.E. Penner-Hahn
Licensed Content Date	Jan 1, 2003
Licensed Content Pages	28
Start Page	159
End Page	186
Type of Use	reuse in a thesis/dissertation
Intended publisher of new work	other
Portion	figures/tables/illustrations
Number of figures/tables/illustrations	1
Format	both print and electronic
Are you the author of this Elsevier chapter?	No
Will you be translating?	No
Original figure numbers	Figure 2
Title of your thesis/dissertation	Hydrotreating of Gas Oils Using Ni-Mo Catalyst Supported on Carbon Nanohorns and Associated Carbon Materials
Publisher of new work	University of Saskatchewan
Expected completion date	May 2019
Estimated size (number of pages)	200

Requestor Location	Emma Aryee 805-105 Cumberland Avenue South
	Saskatoon, SK S7N1L7 Canada Attn: Emma Aryee
Publisher Tax ID	GB 494 6272 12
Total	0.00 CAD

Permission to use Figure 5.1

JOHN WILEY AND SONS LICENSE TERMS AND CONDITIONS

Apr 24, 2019

This Agreement between Emma Aryee ("You") and John Wiley and Sons ("John Wiley and Sons") consists of your license details and the terms and conditions provided by John Wiley and Sons and Copyright Clearance Center.

License Number	4575590154686
License date	Apr 24, 2019
Licensed Content Publisher	John Wiley and Sons
Licensed Content Publication	Canadian Journal of Chemical Engineering
Licensed Content Title	Hydrodenitrogenation and Hydrodesulphurization of Heavy Gas Oil Using NiMo/Al ₂ O ₃ Catalyst Containing Phosphorus: Experimental and Kinetic Studies
Licensed Content Author	D. Ferdous, A. K. Dalai, J. Adjaye
Licensed Content Date	May 19, 2008
Licensed Content Volume	83
Licensed Content Issue	5
Licensed Content Pages	10
Type of use	Dissertation/Thesis
Requestor type	University/Academic
Format	Print and electronic
Portion	Figure/table
Number of figures/tables	1

Original Wiley figure/table number(s) Figure 1.

Will you be translating? No

Title of your thesis / dissertation Hydrotreating of Gas Oils Using Ni-Mo Catalyst Supported on Carbon Nanohorns and Associated Carbon Materials

Expected completion date May 2019

Expected size (number of pages) 200

Requestor Location Emma Aryee
805-105 Cumberland Avenue South

Saskatoon, SK S7N1L7
Canada
Attn: Emma Aryee

Publisher Tax ID EU826007151

Total 0.00 CAD

Terms and Conditions